Prediction of Ductile Crack Formation in Uncracked Bodies

by

Yingbin Bao

B.S., Engineering Mechanics, Wuhan University of Technology, 1993
M.S., Ocean Engineering, Shanghai Jiao Tong University, 1996

Submitted to the Department of Ocean Engineering
in partial fulfillment of the requirements for the degree of

Doctor of Philosophy in Applied Mechanics

at the
Massachusetts Institute of Technology
September 2003

Signature of Author .....
Department of Ocean Engineering
July 31, 2003

Certified by .....
Tomasz Wierzbicki
Professor of Applied Mechanics
Thesis Supervisor

Accepted by .....
Michael S. Triantafyllou
Professor of Ocean Engineering
Chairman, Department Committee on Graduate Students

Prediction of Ductile Crack Formation in Uncracked Bodies

Yingbin Bao

Submitted to the Department of Ocean Engineering
in July 2003, in partial fulfillment of the requirements for the degree of
Doctor of Philosophy in Applied Mechanics

ABSTRACT

One of the important challenges facing the scientific and engineering community is the development of a reliable computational tool for predicting failure of structures under extreme and/or accidental loads. Considered in the present thesis is the process of formation of ductile cracks, which may be responsible for a catastrophic structural failure. Experimental, numerical and analytical studies are carried out on the prediction of ductile crack formation in uncracked bodies on an example of 2024-T351 aluminum alloy. A methodology for ductile crack formation suitable in industrial applications is developed through the introduction of different weighting functions for different stress triaxiality ranges where different ductile crack formation mechanisms occur ("shear fracture" in negative stress triaxialities, void nucleation, growth, and linkage in high stress triaxialities, a transition mode in intermediate stress triaxialities). A cut off value at the stress triaxiality of -1/3 is discovered. Effects of stress and strain ratios, specimen size and anisotropy are also quantified. It is found that the stress triaxiality and the equivalent strain are the two most important parameters governing ductile crack formation while other parameters are probably of secondary importance. A modification to the criterion is introduced to predict crack formation in a single reversal of straining. A case study of a solid aluminum 2024-T351 beam with a smooth round notch under 3-point bending is conducted. Other cases of component validations on different materials, structures and loadings performed by colleagues in the Impact and Crashworthiness Lab are summarized. It is concluded that the proposed approach of predicting ductile crack formation holds a promise of becoming a reliable and practical calculation tool for industrial applications.

Thesis Supervisor: Tomasz Wierzbicki
Title: Professor of Applied Mechanics

Acknowledgment

First, I would like to express my deepest appreciation to my advisor, Professor Tomasz Wierzbicki, for his guidance, support, encouragement and patience during the four years of my stay at MIT. I would also like to thank Professor Frank McClintock, Professor Oral Buyukozturk, and Dr. David Burke, for serving in my dissertation committee and again to Professor Frank McClintock for his inspiring comments and discussions.

I am very grateful to Mr. Stefan Henn for giving me the opportunity to work as a summer intern at BMW R&D Center in Germany and for his valuable discussions. Thanks are also due to Mr. Stefan Rudolph for his assistance in preparing specimens and conducting tests and to Mr. Roland Treitler at BMW for his help on Fractography.

I greatfully acknowledge friendship and eadiness to help of my colleagues at the Impact and Crashworthiness Laboratory, Dr. Mulalo Doyoyo, Mr. Dirk Mohr, Mr. Young-Woong Lee, Mr. Xiaoqing Teng, Ms. Li Zheng and Mr. Liang Xue. Thanks are also extended to Ms. Sheila McNary for her assistance on administrative matters. I would also like to thank other staff members and fellow students for creating the intellectually enlightening and friendly work environment.

The work would not have been possible without the financial support by the Volpe/DOT Center Grant to MIT, the joint MIT/Industry Consortium on the Ultralight Metal Body Structure and the MURI project sponsored by ONR.

Finally, I would like to thank my wife Xiaoyan and my family who gave me the strength, ability and time to complete this study.

Contents

List of Figures

List of Tables

Nomenclature

(symbol is defined in the sequence as they appear in the text)

η_M	accumulated damage in McClintock's model
F_M	relative hole growth factor,
b	size of the hole
l_h	distance between two holes
σ_0, n	two material constants for power hardening law
$\sigma_1, \sigma_2, \sigma_3$	maximum, medium and minimum principal stress, respectively
S_1, S_2, S_3	maximum, medium and minimum principal stress deviator, respectively
$\varepsilon_1, \varepsilon_2, \varepsilon_3$	maximum, medium and minimum principal strain, respectively
$\overline{\sigma}$	von Mises equivalent stress
σ_m	mean normal stress or hydrostatic stress
$\sigma_m / \overline{\sigma}$	stress triaxiality
$\sigma_{rr}, \sigma_{\theta\theta}, \sigma_{zz}$	radius, hoop and axial stress, respectively
$\varepsilon_{rr}, \varepsilon_{\theta\theta}, \varepsilon_{zz}$	radius, hoop and axial strain, respectively
$\sigma_{ij}, \varepsilon_{ij}$	components of stress and strain tensors
σ_M, ε_M	equivalent flow stress, strain of the matrix
$\overline{\varepsilon}$	equivalent strain
f_v	void volume fraction
q_1, q_2	parameters in porosity plasticity
$f_v^*(f_v)$	function of void volume fraction
M_1, M_2	parameters governing evolution of void volume fraction

D_1	damage variable in damage mechanics
$\tilde{\sigma}$	effective stress in damage mechanics
σ_y, σ^0	yield stress
R_a	isotropic hardening scalar variable
λ, μ	Lame constants
ν	Poisson's ratio
δ_{ij}	Kronecker symbol
E	Young's modulus
F	yield function
φ	function of damage strain energy
s_{D0}, S_{D0}	material and temperature dependent parameters in damage strain energy
$\varepsilon_0, \varepsilon_c$	one-dimensional strain at damage threshold and at failure in damage mechanics
c_D, a_1, a_2, α_D	material constants in damage mechanics
δ	displacement
l_{c0}	characteristic length of the decohering zone model
Γ_0	separation work per unit area
f , g	weighting function
C	calibration constant
A	cross section area
K	stiffness
d, h	diameter and height of upsetting specimens
P	acting force
a, R	radius of the minimum cross and the circumferential notch, respectively
l_U , w_U	vertical, circumferential grid spacing of upsetting specimens
α	strain increment ratio
D	accumulated damage
p	outside hydrostatic pressure applied to specimens

σ_{pn}	the stress of the TPS zone
w_{ps}	half of the total transition zone
t, w, l	thickness, width and gauge length of specimens
$\bar{t}$	normalized thickness
d_t, l_t	diameter of the hole and ligament of the specimen for size effect
V_{cr}	critical volume.
η	degree of compression
$\boldsymbol{\sigma}$	stress tensor
$\boldsymbol{\alpha}$	backstress tensor
$\boldsymbol{S}$	deviatoric stress tensor
$\boldsymbol{\alpha}^{dev}$	deviatoric backstress tensor.
$\dot{\boldsymbol{\varepsilon}}$	rate of plastic flow tensor
C_k, γ	material constants related to kinematic hardening
Q_∞, b_i	material constants related to isotropic hardening.
β_1, β_2	constants

Chapter 1

Introduction

1.1 Background and Motivation

Failures of man-made structures, such as ships, planes, cars, trains, buildings (Fig. 1.1) under accidental loadings can lead to loss of lives and property. This becomes especially true in two recent terrorist attacks on the USS Cole and the World Trade Center Twin Towers. Those disasters proved vulnerability of man-made structures to extreme loadings. In addition, with growing legislative and market pressure, the industry is moving toward design of new generations of ships, planes, cars, trains and buildings by using novel materials and structures. Any premature failure should be fully understood and, if possible prevented. Premature failure of any key component of a system can dramatically increase the possibility of intrusion of failed members, which may risk an occupant's life and even lead to the collapse of the entire system. To alleviate the amount of damage and reduce the number of casualties engineers should understand the mechanisms of the failures and should be able to predict them.

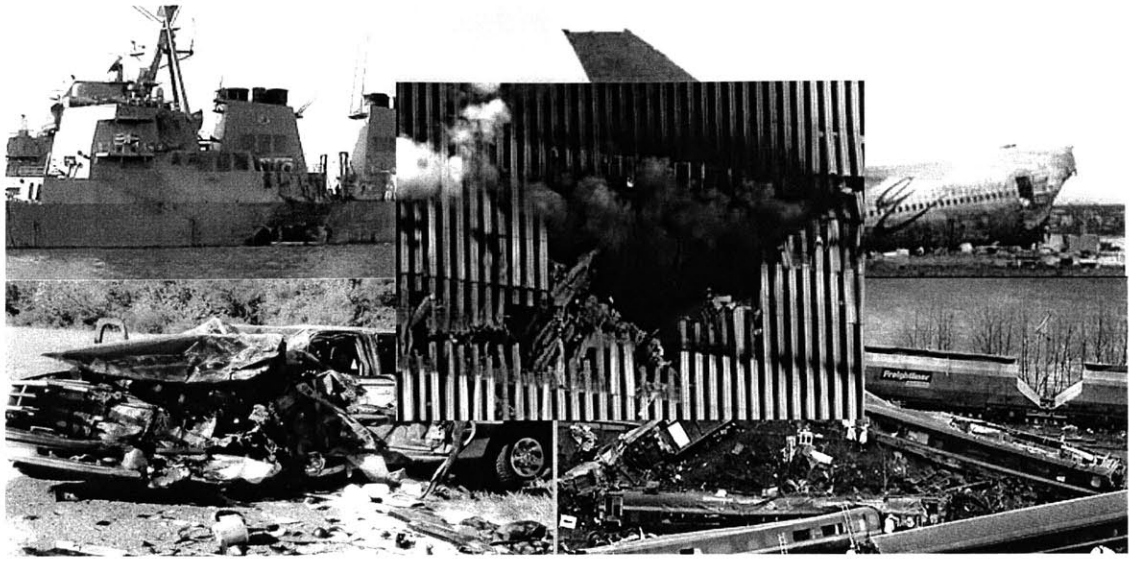

Fig. 1.1 Failures due to fracture in various structures

Fracture is one of the most important modes of failures of man-made structures. Consequently, fracture prediction becomes an important issue in the design of reliable structures, which can sustain severe loading conditions. It is well known that fracture of structures is hard to prevent once a crack initiates. In addition, with advanced manufacturing process and nondestructive damage detection techniques, structures can be produced without pre-existing cracks or crack-like defects. Most metals used in structures experience large plastic deformation before fracture occurs. Therefore, prediction of ductile crack formation (fracture initiation) in uncracked bodies appears to an important factor in the engineering design practice.

Mechanisms of crack formation are very complex and dependent on the type of material, geometry of the structure and the loading conditions. Cleavage and void nucleation, growth, and linkage are typical idealized mechanisms of fracture. According to the relation of yielding and fracture, fracture in structures can also be classified into brittle fracture and ductile fracture. Both brittle fracture and ductile fracture differs substantially at a micromechanics level experiencing intergranular and transgranular fracture patterns depending on the relation of cracks and grain boundaries. Mechanisms also differ for

crack formation in uncracked bodies, crack initiation in pre-cracked structures and continuous crack growth. Although the present study is focusing on ductile crack formation in uncracked bodies, it does not make the problem simple. The way voids nucleate, grow and link to form macrocracks is different for different materials, structures and loadings. Complicated plastic deformations such as necking, shear localization may occur prior to crack formation. Crack formation happens in different stress states such as plane strain, plane stress, and axisymmetric state, in different locations such as surface, subsurface and under different loadings such as bending, tension, shear and compression. All those factors make the ductile crack formation complicated and difficult to predict accurately.

The need of simplifying prediction of ductile crack formation is obvious for industrial applications. It is recognized that components of stress and strain tensors are basic outputs of well-developed structural analyses, such as finite element analysis using commercial codes. An ideal and also realistic goal for engineers is to develop a suitable fracture criterion in terms of the stresses and strains and possibly their gradients with certain material dependent parameters for predicting crack formation with an acceptable degree of accuracy. This criterion should be as general as possible and should apply to a broad class of materials, structures and loading conditions, which engineers have to deal with in everyday situations.

1.2 Prior Approaches to Ductile Crack Formation

Various approaches for ductile fracture have been proposed in the past. Fracture mechanics, void growth model, porous plasticity fracture model, damage mechanics, decohering zone model and empirical fracture model are the main methods that emerged to describe ductile fracture of metals. Fracture mechanics deals with crack initiation and growth in structures with a sharp crack, which is different from the topic of this thesis. A summary of methods of the calssical fracture mechanics is given in Appendix.

1.2.1 Void Nucleation, Growth, and Linkage Models

The growth of holes in tensile specimens was first observed in ductile metals around 1950's (eg. [11-13]). Studies on mechanisms of void growth have begun since then. However, before 1968, the studies were relatively empirical (eg. [14-16]). It was McClintock [3] who performed a first theoretical analysis on the void growth. In this classical paper, in order to simplify the problem, it was assumed that the principal components of stress did not rotate relative to the materials. Thus only the principal components of the stress and strain were considered. The material was assumed to contain cylindrical holes of elliptical cross-section with axes parallel to the principal directions of the applied stress and strain increment as shown in Fig.1.2. For a power law plastic hardening material, the increment of the accumulated damage can be expressed as

$$\frac{d\eta_M}{d\bar{\varepsilon}}(\ln F_M) = \frac{\sqrt{3}}{2(1-n)}\sinh\frac{\sqrt{3}(1-n)(\sigma_1+\sigma_1)}{2\bar{\sigma}} + \frac{3}{4}\frac{\sigma_1-\sigma_1}{\bar{\sigma}} \qquad (1.1)$$

where η_M is an accumulated damage $= d(\ln F_M)/\ln {F_M}^f$, n is the hardening exponent, σ_1 and σ_2 are principal transverse stresses, σ_1 being the largest, $\bar{\sigma}$ the von Mises or equivalent stress, F_M is a relative hole growth factor $= (b/l_h)/(b_0/l_{h0})$, where b is the size of the hole and l_h is the distance between two holes, b_0 and l_{h0} are the initial values of b and l_h, respectively, ${F_M}^f = (1/2)/(b_0/l_{h0})$, fracture occurs when $F_M = {F_M}^f$.

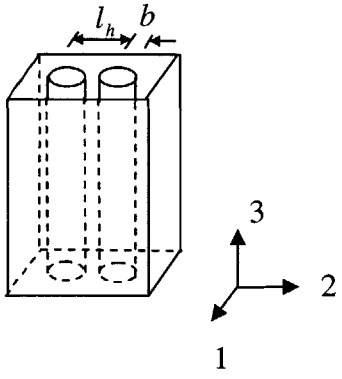

Fig. 1.2 Geometry of McClintock's hole growth model

Another important study on void growth is the one by Rice and Tracey [17]. They found that for any remote strain rate field, the enlargement rate of spherical voids was amplified over the remote strain rate by a factor of an exponential function of the stress triaxiality by studying the growth of a spherical void in a general remote field. The stress triaxiality parameter is defined as $\sigma_m / \overline{\sigma}$, where σ_m is the mean stress or hydrostatic stress. The volume changing contribution to void growth was found to override the shape changing part when the stress triaxiality was large.

In the case of shear deformation, there is rotation of the material elements at large distances from the hole. Rotation of holes in a shear band was clearly observed in a necked copper tensile specimen by Bluhm and Morrissey [2]. McClintock et al. [18] assumed that large numbers of holes were scattered uniformly throughout a material and divided the solid in to a number of elements, each containing a single centrally-located hole. Fracture was assumed to occur when the hole just touches the boundary of the deforming element in which it lies.

Void nucleation and interaction between voids were not considered in the above studies. LeRoy et al. [19] modified the theory of Rice and Tracey by allowing for a change in void shape and proposed a simple void nucleation and void linkage model. As mentioned by the authors, the mechanism of void nucleation and linkage has not been well developed. The main purpose of their study was to serve as a guideline in trying to investigate the problem instead of developing a criterion applicable to commercial materials. Recently, numerical simulations have been used in studies of void growth and linkage (eg. [20-24]). However, due to the complexity of the process of nucleation, growth, and linkage, which will be described in Chapter 2, no criterion has been developed so far to capture all the stages of the fracture processes.

1.2.2 Porous Plasticity Fracture Models

Porous plasticity fracture model is also called the Gurson-Tvergaard-Needleman model. The model discussed in this section is different from the void growth model described in Section 1.2.1 even though both of them start from the similar model, a unit element with a hole inside. The void growth model determines the evolution of the hole based on the Mises plasticity which is plastic incompressible and assumes crack formation occurs when two holes touch. The porous plasticity fracture model is based on the porous plasticity constitutive model, which is hydrostatic stress dependent and was developed by Gurson [25, 26] on the basis of void nucleation and growth using an upper bound approach. It was assumed that voids are embedded in a continuous media (matrix) and the matrix was treated as plastic incompressible. An important parameter, the void volume fraction f_v was introduced. It is assumed crack forms when f_v reaches a critical value.

The yield function for porous material developed by Gurson [25, 26] is

$$\Phi = \frac{\bar{\sigma}^2}{\sigma_M{}^2} + 2f_v \cosh(\frac{3}{2}\frac{\sigma_m}{\sigma_M}) - 1 - f_v{}^2 = 0 \qquad (1.2)$$

where $\bar{\sigma}$ is the macroscopic Mises equivalent stress, σ_m is the macroscopic mean stress or hydrostatic stress, σ_M is the equivalent flow stress of the matrix.

A modification to the Gurson yield function was made by Tvergaard [27, 28] who introduced two additional parameters q_1 and q_2. The yield function becomes

$$\Phi = \frac{\bar{\sigma}^2}{\sigma_M{}^2} + 2q_1 f_v \cosh(\frac{3q_2}{2}\frac{\sigma_m}{\sigma_M}) - 1 - (q_1 f_v)^2 = 0 \qquad (1.3)$$

According to this model, loss of material stress carrying capacity occurs when voids have grown so large that Eq. (1.3) has shrunk to zero, i.e. at $f_v = 1/q_1$, which is unrealistically large. A function $f_v^*(f_v)$ (Eq. (1.4)) replacing f_v in Eq. (1.3) was introduced by Tvergaard and Needleman [29] to model the complete loss of material stress carrying capacity at a realistic volume fraction.

$$f_v^*(f_v) = \begin{cases} f_{v0}, & \text{before any loading} \\ f_v, & \text{for } f_v \le f_{vc} \\ f_{vc} + \dfrac{\dfrac{1}{q_1} - f_{vc}}{f_{vF} - f_{vc}}(f_v - f_{vc}), & \text{for } f_v > f_{vc} \end{cases} \tag{1.4}$$

where f_{v0} is initial void volume fracture, f_{vc} is a critical value of void volume fraction at which the material stress carrying capacity starts to decay rapidly and f_{vF} is the actual void volume fraction associated with the complete loss of the stress carrying capacity. However, this function is quite complicated. To avoid the difficulty of dealing with Eq. (1.4), the onset of failure is often determined when the void volume fraction f reaches f_{fE} which is usually taken as an intermediate value of f_{vc} and f_{vF} [30].

Clearly, the void volume fraction f_v is a critical variable. Gurson [26] assumed that the increment of the void volume fraction came from void nucleation and growth, i.e.

$$df_v = df_{v\,nucleation} + df_{v\,growth} \tag{1.5}$$

Gurson [26] postulated that the rate of void volume fraction change due to void growth is closely related to the volumetric strain and can be written as

$$df_{v\,growth} = (1 - f_v)d\varepsilon_{kk}{}^p \tag{1.6}$$

where $d\varepsilon_{kk}{}^p$ is the rate of macroscopic plastic volumetric strain.

He also presented a model for the rate of void volume fraction change due to void nucleation based on the research performed on the micromechanics (eg. Argon et al. [31] and Gurland [32]).

$$df_{v\,growth} = M_1 d\varepsilon_M + M_2 d\left(\frac{\sigma_m}{1 - f_v}\right) \tag{1.7}$$

where ε_M is the equivalent strain of the matrix. M_1 and M_2 are two free parameters to be determined.

It was also assumed that the rate of plastic work in the matrix material equals to the macroscopic rate of plastic work, i.e.

$$\sigma_{ij}\dot{\varepsilon}_{ij}^{\ p} = (1-f_v)\sigma_M\dot{\varepsilon}_M \tag{1.8}$$

where σ_{ij} and $\varepsilon_{ij}^{\ p}$ are stress and plastic strain tensors, respectively.

and the matrix material follows a certain hardening law.

$$\sigma_M = \mathrm{F_h}(\varepsilon_M) \tag{1.9}$$

The rate of volume fraction change due to void nucleation in the form of Eq. (1.7) is relatively difficult to work out. Needleman and Rice [33] proposed another model

$$df_{v\,nucleation} = M_1 d\varepsilon_M + M_2 d(\sigma_M - \sigma_m) \tag{1.10}$$

Normal distributions of the parameters M_1 and M_2 were proposed by Chu and Needleman [34]. For strain controlled nucleation,

$$M_1 = \frac{f_{vN}^{\ n}}{s_N^n\sqrt{2\pi}}\exp[-\frac{1}{2}(\frac{\varepsilon_M-\varepsilon_N}{s_N^n})^2],\quad M_2 = 0 \tag{1.11}$$

and for stress controlled nucleation,

$$M_1 = \frac{f_{vN}^{\ s}}{s_N^s\sqrt{2\pi}}\exp[-\frac{1}{2}(\frac{(\sigma_M+\sigma_m)-\sigma_N}{s_N^s})^2],\quad M_2 = 0 \tag{1.12}$$

where, $f_{vN}^{\ n}$ and $f_{vN}^{\ s}$ are the void volume fraction of void nucleating particles, s_N^n and s_N^s are the standard deviations. The superscript n and s stand for the strain and stress controlled nucleation, respectively, while ε_N and σ_N are the nucleating strain and stress, respectively.

The major difficulty for applying the model in practical examples is a large number of coefficients to be determined. Clearly, there are two unknown parameters q_1, q_2 in the yield function (Eq. (1.3)), three parameters f_{v0}, f_{vc}, f_{vF} in the void volume fraction function $f_v^{\ *}$ (Eq. (1.4)) or two parameters f_{v0}, f_{vE} for the void volume fraction f_v, $f_{vN}^{\ n}, s_N^n, \varepsilon_N$ or $f_{vN}^{\ s}, s_N^s, \sigma_N$ for the increment of the void volume fraction f_v and

coefficients for the stress-strain law of the matrix (eg. two or three parameters for a power law material). Totally over ten parameters need to be determined for a single material. Moreover, those parameters are strongly coupled. Those factors make the model extremely difficult to apply in practical problems. That is the reason why there have been few successful industrial applications.

In the existing applications of this model published in the literature (eg. [34-39]), fixed values of certain parameters were taken (eg. $q_1 = 1.5, q_2 = 1, f_{vE} = 0.2$) and the initial void volume fracture f_{v0} was determined from metallography. Other parameters were found by fitting numerical simulation and experiments. However, the calibration procedure was not clearly defined and presented.

Faleskog and Gao [40, 41] made an attempt to calibrate q_1, q_2, f_{v0} and f_{vE} by using a cell model and by fitting of experiment and numerical simulations. The parameters for the hardening law of the matrix were chosen to fit the stress-strain curve of the actual material obtained from experiment. However, the parameters of the evolution law of the void volume fraction f_v were not considered in their methods. As mentioned earlier, most of ten parameters are strong coupled. This calibration procedure is a good start but clearly is far from a standard clean procedure. The calibration of G-T-N model still remains open. It strongly limits the model in industrial applications.

1.2.3 Damage Mechanics

The damage variable D_1 was firstly presented by Kachanov [42] to represent the loss of stiffness and integrity attributed to microcracks in terms of the effective surface density of microdefects. Based on this concept, Rabotnov [43] introduced an effective stress $\tilde{\sigma}$ related to the damage variable, namely,

$$\tilde{\sigma} = \frac{\sigma}{1 - D_1} \tag{1.13}$$

The strain behavior was assumed to be modified only through the effective stress by Lemaitre [44]. For example, the linear elastic strain ε_e becomes

$$\varepsilon_e = \frac{\tilde{\sigma}}{E} = \frac{\sigma}{(1 - D_1)E} \tag{1.14}$$

With those assumptions, the elastic law of damage mechanics, which are different from the continuum mechanics, can be expressed as

$$\sigma_{ij} = (1 - D_1)(\lambda \delta_{ij} \varepsilon^e_{kk} + 2\mu \varepsilon^e_{ij}) \tag{1.15}$$

where, λ, μ are Lame constants, δ_{ij} is the Kronecker symbol and ε^e_{ij} is the elastic strain. and the yield function is generalized to

$$F = \bar{\sigma} - (1 - D_1)(\sigma_y + R_a) \tag{1.16}$$

where $\bar{\sigma}$ is the equivalent stress, σ_y is the initial yield stress and R_a is the isotropic hardening scalar variable [44].

Thermodynamic potential and dissipation potential were introduced (eg. Lemaitre [45] and Wang [46]) to obtain the relation of damage strain energy release rate y and stress and strain state and finally the damage evolution law, which is the key point for the damage mechanics. It was assumed that there are two uncoupled part i.e. elastic and plastic part in thermodynamic potential and the elastic is quadratic in ε^e_{ij} and linear in $(1 - D_1)$ in almost all the literature. The damage strain energy release rate y then can be described as

$$y = -\frac{\bar{\sigma}}{2E}\left[\frac{2}{3}(1+\nu) + 3(1-2\nu)\left(\frac{\sigma_m}{\bar{\sigma}}\right)^2\right]^{\frac{1}{2}} \tag{1.17}$$

where, E is the Young's modulus, ν is the Poisson's ratio and σ_m is the mean stress.

The damage evolution was given by the normality property of the potential of dissipation, i.e.

$$\dot{D}_1 = -\frac{\partial \varphi}{\partial y} \tag{1.18}$$

where φ is the potential of dissipation.

However, the potential of dissipation has not been well established. Lemaitre [45] postulated a potential of dissipation φ as a power function of damage strain energy release rate y and linear in equivalent plastic strain rate $\dot{\bar{\varepsilon}}$,

$$\varphi = \frac{S_0}{(s_0+1)}\left(\frac{-y}{S_0}\right)^{s_0+1}\dot{\bar{\varepsilon}} \tag{1.19}$$

where s_{D0} and S_{D0} are material and temperature dependent.

This potential of dissipation and the Eqs. (1.17) and (1.18) finally leads to

$$\dot{D}_1 = \frac{D_{1c}}{\varepsilon_c - \varepsilon_0}\left[\frac{2}{3}(1+\nu) + 3(1-2\nu)\left(\frac{\sigma_m}{\bar{\sigma}}\right)^2\right]\bar{\varepsilon}^{2n}\dot{\bar{\varepsilon}} \tag{1.20}$$

for the material which follows the Ramberg-Osgood hardening law coupled with damage

$$\bar{\sigma} = (1-D_1)K\bar{\varepsilon}^n \tag{1.21}$$

where, K, n are material constants, D_{1c} is the damage failure at failure and $\varepsilon_0, \varepsilon_c$ are the one-dimensional strain at damage threshold and at failure.

Wang [46] assumed the dissipation potential in the form of

$$\varphi = \frac{S_D}{2(1-D)}\left(\frac{-y}{S_D}\right)^2 \frac{(\bar{\varepsilon}_c - \bar{\varepsilon})^{\alpha-1}}{\bar{\varepsilon}^{2n}} \tag{1.22}$$

where $\bar{\varepsilon}_c$ is the critical value of $\bar{\varepsilon}$ at failure and α_D is a damage coefficient.

A damage evolution law given in Eq. (1.23) was obtained based on the above dissipation potential (Eq.(1.25))

$$\dot{D}_1 = \frac{\alpha(D_{1c} - D_{10})}{(\varepsilon_c - \varepsilon_0)^{\alpha}}\left[\frac{2}{3}(1+\nu) + 3(1-2\nu)\left(\frac{\sigma_m}{\bar{\sigma}}\right)^2\right](\bar{\varepsilon}_c - \bar{\varepsilon})^{\alpha-1}\dot{\bar{\varepsilon}} \tag{1.23}$$

where D_{10} is the initial value of D_1.

Other damage evolution laws appeared in the literature were directly assumed instead of being derived from Eq. (1.18). For example, Dhar et al. [47] proposed the following damage evolution law

$$\dot{D}_1 = c_D\dot{\bar{\varepsilon}} + (a_1 + a_2 D_1)\frac{K^2}{2E}\bar{\varepsilon}^{2n}[\frac{2}{3}(1+\nu) + 3(1-2\nu)(\frac{\sigma_m}{\bar{\sigma}})^2]\dot{\bar{\varepsilon}} \qquad (1.24)$$

where, c_D, a_1, a_2 are material constants.

The damage mechanics and the porous plasticity fracture model look similar. The volume fraction f_v is one type of damage variable D_1. However, the porous plasticity fracture mode has a strong basis of physical mechanisms, while unfortunately, the damage mechanics does not have a solid foundation on the crack formation and growth mechanisms. Those damage laws were found on the basis of empirical assumptions. Also, the coupling of the damage variable and constitutive relation makes calibration of material constants in material models and damage laws very difficult to carry out. For example, obtaining the material constants in the Ramberg-Osgood hardening law from tensile tests becomes a hard task since it involves the damage variable which is generally unknown in the direct output of the test. Another drawback of the damage evolution model is the assumption that fracture occurs in a monotonic way to the point that a critical state is reached. In reality, the fracture process manifests itself only at the terminal phase of the monotonic loading process with little or no evidence of any macro-mechanical changes prior to the final stage. Those drawbacks lead to the fact that the damage mechanics is not widely used in industry.

1.2.4 Decohering Zone Models

The decohering zone model following early concepts of Barenblatt [48] and Hillerborg et al. [49] now becomes a popular method in fracture prediction especially in plane stress. Main idea of the decohering zone model is to simulate the fracture process zone using

special interface elements. Therefore, mechanical properties and formulations of the special interface elements are two key factors for this method.

The mechanical property of the special interface elements is often called the traction-separation relation which is described by stress σ and displacement δ normal to crack planes. However, shape of the traction-separation law has not been well developed and no universal function has been established. Needleman [50] proposed an exponential traction–separation relation.

$$\sigma = \sigma_c e z \frac{\delta}{l_{c0}} \exp(-z\frac{\delta}{l_{c0}}) \tag{1.25}$$

where, $z = 16e/9$, l_{c0} is the characteristic length of the decohering zone model.

Roychowdhury et al. [51] derived a traction–separation relation from an exponential free energy potential. The traction–separation relation has the following form

$$\sigma = \sigma_c e \frac{\delta}{\delta_c} \exp(-\frac{\delta}{\delta_c}) \tag{1.26}$$

where δ_c is the value of δ at $\sigma = \sigma_c$.

Eq. (1.25) and Eq. (1.26) are essentially the same since one can obtain $\delta_c = z/l_0$ from these two equations. Tvergaard and Hutchinson [52, 53] proposed a piecewise linear traction–separation relation as shown in Fig.1.3. These traction–separation laws experience a hardening behavior at beginning of the separation.

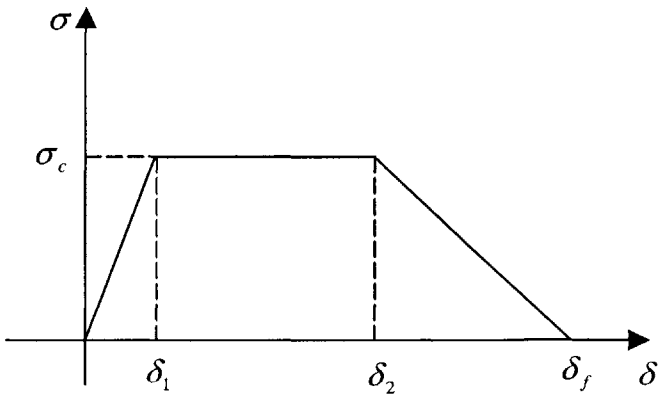

Fig. 1.3 Traction-separation relation proposed by Tvergaard and Hutchinson

However, Elices et al. [54] pointed out that a decohering zone in a homogeneous body could not have a hardening branch (actually it could have in a boundary layer depleted of precipitate with grain boundary cracking [55]) and the hardening part should be incorporated into the behavior of the continuum outside the decohering zone since the initial width of the decohering crack is zero and the corresponding elastic displacement is also zero. The traction-separation relation then becomes a softening function. Elices et al. [54] presented an inverse procedure to determine parameters of a bilinear softening function which is often introduced in concrete and other cementitious materials. An optimization based numerical approach was developed by Que and Tin-Loi [56] to determine key parameters of shape known softening functions with experimental data. The inverse problem was formulated as a mathematical program with equilibrium constraints (MPEC) and then converted to a nonlinear program. A bilinear softening function, three-branch piecewise linear softening law, power softening relation and a power-exponential softening law were introduced in their study. It was found that the piecewise linear laws were computationally more tractable and the three-branch law provided the best predictions of a wedge splitting test.

Moreover, Siegmund and Brocks [57] demonstrated that the separation work per unit area Γ_0 and the peak stress required for separation σ_c are not constant for different stress triaxialities by studying a center cracked panel using the modified Gurson model, where the separation work per unit area Γ_0 is defined as

$$\Gamma_0 = \int_0^\infty \sigma d\delta \tag{1.27}$$

A number of studies on formulations of the special interface elements have also been performed. Needleman [58] presented an early thought of the decohering zone methodology for finite element analysis in a study of void nucleation by inclusion debonding. The basic idea is to model the deformation by conventional continuum elements and to model fracture by special interface elements. The application of this concept is mainly in 2-D frameworks of plane strain and plane stress (eg. [53, 59-62]). The interface elements contain two surfaces attached to the surrounding continuum

elements. The displacements of the edge of the interface element are required to be compatible with displacements on the edge of the adjacent continuum element. A relatively small number of studies went to three dimensions. Several different 3-D decohering elements were introduced recently. Lin et al. [63] incorporated the decohering surface as a loading contribution in the formulation of a mixed boundary-value problem. De-Andres et al. [64] introduced a 3-D interface element which consists of two quadrilateral patches to predict fatigue crack growth in aluminum shafts. Very recently, Roychowdhury et al. [51] adopted a large displacement formulation for a 3-D decohering element to predict ductile tearing in thin aluminum panels. Finally Repetto et al. [65] described the calibration procedure from two dynamic tests and showed interesting examples of 2-D crack growth.

Further studies on mechanical properties and formulations of the special interface elements apparently are necessary for the decohering zone model. Besides, there are two fundamental limitations. The available decohering zone model can only deal with normal separation (eg. mode I crack) since the traction-separation law appeared in the literature is in terms of stress and displacement normal to the crack surface. Consequently, this model is not sufficient to predict shear failure and combined normal and shear separations. Also, since one has to introduce special interface elements along crack path, it is very difficult to predict crack formation and also crack growth for structures without obvious potential crack path. As pointed out by Scheider [66] who tried to simulate the cup-cone fracture in round bars using the decohering zone model, those two difficulties have to be overcome to make the decohering zone model applicable.

1.2.5 Empirical Models

A number of relatively simple crack formation criteria have been proposed in the past by the bulk-forming community. Those criteria lack a solid foundation and are based on observation, experience, and math simplicity. Those empirical criteria were verified over a restricted range of stress states.

It is postulated that fracture occurs at a material point in a body when the following scalar function reaches a critical value C.

$$\int_0^{\bar{\varepsilon}_f} g(\sigma_{ij})\mathrm{d}\bar{\varepsilon} = C \tag{1.28}$$

where g is a weighting function, which is generally a function of the components of the stress tensor σ_{ij}, $\bar{\varepsilon}$ is the equivalent strain, $\bar{\varepsilon}_f$ is the equivalent strain to fracture and C is a calibration constant. Often the above function is referred to as a "damage indicator" [67].

The simplest case is the equivalent strain criterion

$$\bar{\varepsilon} = \bar{\varepsilon}_f \tag{1.29}$$

which is essentially a limiting case of Eq.(1.28) when $g = 1$. Although it is well know that the equivalent strain to fracture is different for different stress states, this criterion is still being used in many leading nonlinear commercial codes such as ABAQUS, LS-DYNA and PAM-CRASH.

Cockcroft and Latham [68] postulated that facture is controlled by the maximum principal tensile stress integrated over the plastic strain path, i.e.

$$\int_0^{\bar{\varepsilon}_f} \frac{\sigma_1}{\bar{\sigma}} d\bar{\varepsilon} = C_{CL} \tag{1.30}$$

where C_{CL} is a material constant.

Based on this criterion, fracture crack may form due to shear stresses or tensile stresses but not compressive stresses. It was shown to be in reasonable agreement with observation of workability-the maximum deformation before crack formation during rolling, extrusion etc.

Brozzo et al. [69] proposed a modification to include an explicit dependence on hydrostatic stress for the prediction of formability limits in metal sheets.

$$\int_0^{\bar{\varepsilon}_f} \frac{2\sigma_1}{3(\sigma_1 - \sigma_m)} \mathrm{d}\bar{\varepsilon} = C_B \tag{1.31}$$

where C_B is a material constant.

Clift et al. [70] introduced equivalent stress into the function instead of maximum principal tensile stress and suggested a criterion of generalized plastic work per unit volume.

$$\int_0^{\bar{\varepsilon}_f} \sigma_1 d\bar{\varepsilon} = C_{Clift} \tag{1.32}$$

where C_{clift} is a material constant.

It was found that this criterion successfully predicted the site of crack formation but not the level of deformation at which crack formation should occur in three types of metal forming operation, simple upsetting, axisymmetric extrusion and strip compression and tension.

A simple version of McClintock's model (Eq. (1.1)) can be integrated over the strain path to fall in the form of Eq. (1.28).

$$\int_0^{\bar{\varepsilon}_f} [\frac{\sqrt{3}}{2(1-n)} \sinh(\frac{\sqrt{3}}{2(1-n)} \frac{\sigma_1+\sigma_2}{\bar{\sigma}}) + \frac{3}{4} \frac{\sigma_1-\sigma_2}{\bar{\sigma}}] d\bar{\varepsilon} = C_M \tag{1.33}$$

where C_M is a material constant.

Rice and Tracey [17]'s result was represented in the literature by taking the void enlargement as a damage measure.

$$\int_0^{\bar{\varepsilon}_f} \exp(\frac{3}{2} \frac{\sigma_m}{\bar{\sigma}}) d\bar{\varepsilon} = C_{RT} \tag{1.34}$$

where C_{RT} is a material constant.

Based on the qualitative result of LeRoy et al [19], a simple criterion also appeared in the literature.

$$\int_0^{\bar{\varepsilon}_f} (\sigma_1 - \sigma_m) d\bar{\varepsilon} = C_L \tag{1.35}$$

where C_L is a material constant.

Another simple criterion based on the fact that stress triaxiality plays a key role in ductile crack formation appeared in the literature.

$$\int_0^{\bar{\varepsilon}_f} \frac{\sigma_m}{\bar{\sigma}} d\bar{\varepsilon} = C_H \tag{1.36}$$

where C_H is a material constant.

Above criteria have only one material constant, which makes calibration straightforward. Criteria involving two material constants were also proposed (eg. Norris et al. [71] (Eq. (1.37)), Oyane et al. [72] (Eq. (1.38)), Atkins [73]) (Eq. (1.39)), Johnson and Cook [74] (Eq. (1.40), Wilkins et al. [75] (Eq. (1.41))).

$$\int_0^{\bar{\varepsilon}_f} \frac{1}{(1 - C_{N1}\sigma_m)} d\bar{\varepsilon} = C_{N2} \tag{1.37}$$

$$\int_0^{\bar{\varepsilon}_f} (1 + \frac{\sigma_m}{C_{O1}\bar{\sigma}}) d\bar{\varepsilon} = C_{N2} \tag{1.38}$$

$$\int_0^{\bar{\varepsilon}_f} \frac{(1 + \frac{d\varepsilon_2}{2d\varepsilon_1})}{(1 - C_{A1}\sigma_m)} d\bar{\varepsilon} = C_{A2} \tag{1.39}$$

$$\int_0^{\bar{\varepsilon}_f} \frac{1}{(C_{JC2} + C_{JC2} \exp(C_{JC3} \frac{\sigma_m}{\bar{\sigma}})} d\bar{\varepsilon} = 1 \tag{1.40}$$

$$\int_0^{\bar{\varepsilon}_f} (\frac{1}{1 - C_{W1}\sigma_m})^{C_{W2}} (2 - Max(\frac{S_2}{S_3}, \frac{S_2}{S_1}))^{C_{W3}} d\bar{\varepsilon} = C_{W4} \tag{1.41}$$

where C_{N1}, C_{N2}, $C_{O1}, C_{O2}, C_{A1}, C_{A2}, C_{JC1}$, C_{JC2}, C_{JC3}, C_{W1}, C_{W2}, C_{W3} and C_{W4} are material constants, $\varepsilon_1, \varepsilon_2$ are maximum and medium principal strains, S_1, S_2 and S_3 are the principal stress deviators.

The coupling of the material constants with the integrand and the existence of two or more material constants make the calibration procedure of those criteria difficult.

1.3 Objective

It has to be admitted, maybe reluctantly for some researchers, that although ductile crack formation has been studied for several decades, the mission has not been successfully accomplished. The main difficulty is explained on one hand by a complex mechanism of crack formation and the need of a simple and universal criterion and the corresponding standard calibration procedure on the other. The objective of the present research is to find a balance between the complexity of the physical mechanism of ductile crack formation and the simplicity needed for applications and to develop a relatively simple general criterion and a clean well-defined calibration procedure for the determination of ductile crack formation in a crack-free body. Crack formation is understood here as an appearance of a macroscopic crack with an order of 0.1 mm inside or on the surface of the body.

Several new findings are reported in this study.

- A ductile crack formation mechanism, "shear fracture" different from classical void nucleation, growth, and linkage is found in upsetting tests.
- An extensive study of various criteria is carried out. The applicability and effectiveness of those criteria are evaluated.
- A unique locus of crack formation in the equivalent strain and the stress triaxiality space is determined over the entire range of stress triaxiality encountered in practical situations for Al2024-T351. This is accomplished using conventional upsetting tests, tensile tests and also newly developed shear and combined loading tests. The locus clearly shows three different regions, which consists of two clear crack formation mechanisms: void nucleation, growth and linkage, the "shear fracture" in upsetting tests and a transition mode in between.
- A new criterion of crack formation prediction under monotonic loadings for industrial applications is developed based on the information of two crack formation mechanisms, one transition mode and the entire fracture locus. Preliminary component validation is presented.

- A cut-off value of stress triaxiality of -1/3 is revealed from upsetting tests.
- Effects of other factors such as specimen size, anisotropy, stress and strain ratio are discussed and quantified.
- A design of a specimen and experiment setup for studying crack formation under compression-tension reverse loadings is developed. A modification to the criterion is introduced to consider the effect of pre-compression in crack formation.

1.4 Structure of the Thesis

The present thesis consists of nine chapters. The motivation, objective and overview of the thesis are presented in *Chapter 1*. This chapter also includes a substantial literature review on prior approaches to ductile crack formation.

In *Chapter 2*, physical mechanisms of ductile crack formation are studied. Different processes of the classical void nucleation, growth, and linkage are reviewed and described. Fractography is performed on upsetting and notched round tensile specimens, which represent negative stress triaxiality and high stress triaxiality, respectively. A "shear fracture" mechanism different from the classical void nucleation, growth and linkage is observed in the upsetting specimen.

Performing numerical simulations is good a way to acquire individual components of stress and strain tensors at the locations of crack formation. The stress-strain curve is one of the most important inputs in numerical simulations. Approximate methods of determining stress-strain curves from upsetting and tensile tests are presented in *Chaper3*. The stress-strain curve for Al2024-T351 is obtained.

An extensive comparative study of a class of existing crack formation criteria is performed in *Chapter 4*. A series of upsetting and tensile tests, which give different stress sates, are carried out. Limitations of the criteria are presented.

In *Chapter 5,* the relationship of the two most important factors governing ductile crack formation, i.e. the equivalent strain and the stress triaxiality, is determined in a relatively wide range of stress triaxiality (-0.33~1.0) for Al2024-T351. New specimen configurations are developed to cover the relatively wide range of stress triaxiality together with the conventional upsetting and tensile tests. A clear mode transition is shown in the fracture locus. This chapter provides a new methodology of prediction of ductile crack formation under monotonic loadings. An analytical solution is derived for crack formation in upsetting tests for the negative stress triaxiality range.

Numerous other factors such as stress and strain ratio, specimen size, and anisotropy are studied in *Chapter 6* using suitable tests and parallel numerical simulations.

In reality, the loading path of a material element is often complex. Structures could experience unloading and even reverse loading. A preliminary study on crack formation under a compression-tension loading is carried out in *Chapter 7.* The design of a specimen and experiment setup is developed and a modification to the criterion is proposed to consider the effect of pre-compression in crack formation.

In *Chapter 8*, various problems with different materials, structures and loading conditions are conducted to validate the approach developed in *Chapter 5* for ductile crack formation by the present author and other colleagues.

Finally, main results are presented and discussed in *Chapter 9.* Recommendations for future study are provided.

Chapter 2

Physical Mechanisms of Ductile Crack Formation

The stress triaxiality is the most important parameter governing crack formation besides the equivalent strain. This conclusion has been arrived independently from void growth studies (eg. [3, 17]), from empirical routines (eg. [69, 71, 72, 76, 77]) and from other experimental and numerical studies (eg. [4, 5, 78, 79]). In this chapter, the physical mechanisms of ductile crack formation are described in different ranges of stress triaxiality.

Numerous studies on micro mechanisms of ductile fracture have been performed in the past. However, the majority focus on the high stress triaxiality range. Studies of the negative stress triaxiality range are very limited. In this chapter, the mechanisms reported in the literature are reviewed. Fractography is carried out on specimens that failed in the high stress triaxiality range and the negative stress triaxiality range. Besides the well-

known void nucleation, growth, and linkage mechanism, which occurs in the high stress triaxiality, a different mechanism is revealed in the negative stress triaxiality range.

2.1 Mechanisms dominating at High Stress Triaxialities

It is well known that void nucleation, growth, and linkage is the fundamental cause of dimple fracture in high stress triaxialities. This type of fracture mechanism has been extensively studied. Notched round bars under tensile loadings are classical examples exhibiting this mechanism. The common features of this fracture mode are rough fracture surfaces and dimples observed in SEM pictures. However, the way in which micro voids nucleate, grow and link is quite different depending on the microstructures and the history of stress, strain, and rotation.

Void nucleation is the first step for the crack formation in the high stress triaxiality range. As reviewed by Gurson [26], a number of studies [15, 31, 32, 80-85] in the literature have shown that a void can be nucleated either by matrix-particle decohesion illustrated in Fig. 2.1 (a) or by particle cracking displayed in Fig. 2.1 (b). It is generally observed that voids nucleate preferably in larger particles due to the local stress fields generated by the presence of larger rigid inclusions when matrix under plastic deformation and due to the more and larger flaws in larger particles leading to easier crack in the particles. Void nucleation could also occur in shear bands as shown in Fig. 2.2.

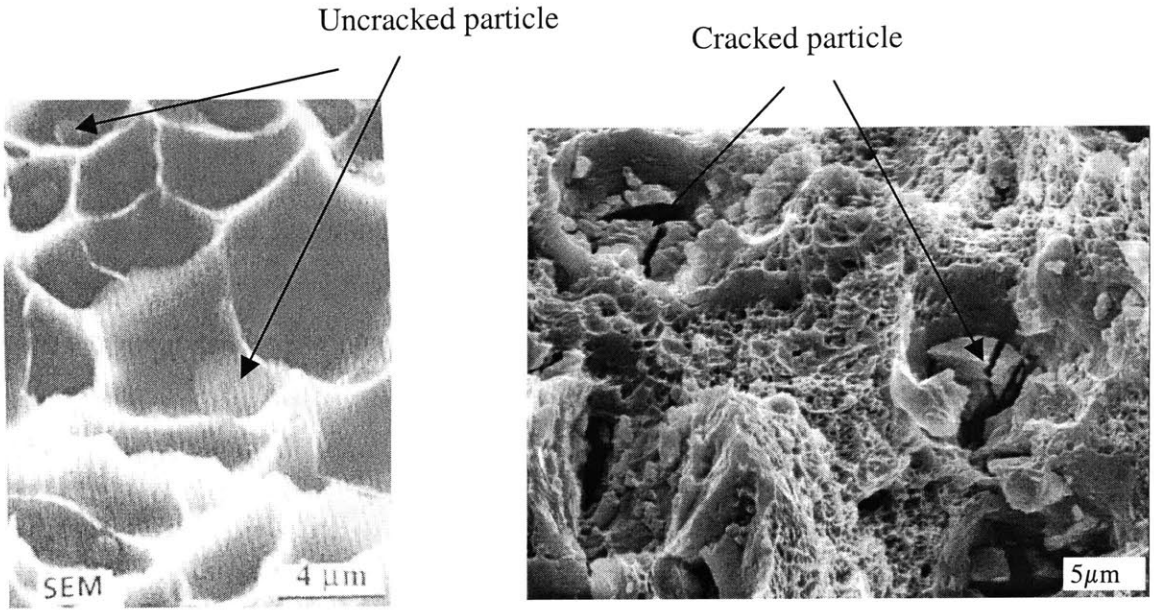

(a) matrix-particle decohesion in carbon steel (after Engel and Klingele [86])

(b) particle cracking and decohesion in Al 2024-T351

Fig. 2.1 Void nucleation due to matrix-particle decohesion and particle cracking

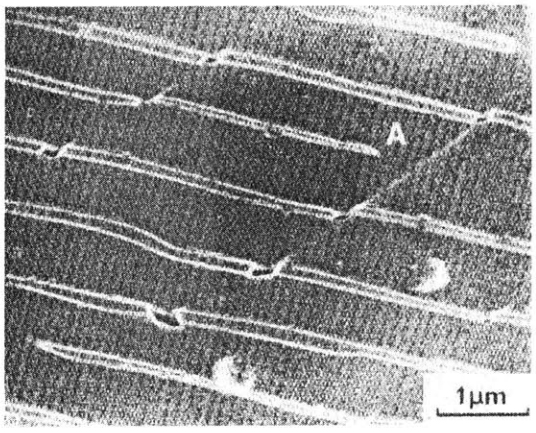

Fig. 2.2 Void nucleation in shear bands
(after Porter et al. [1])

Once voids nucleate, they will grow and finally link. McClintock [3] emphasized that changes in size, shape and spacing of the holes depend on the entire history of stress and strain. The processes of void growth and final linkage are also quite different for different microstructures, deformations and loading conditions. Rice and Tracey [17] pointed out that when a material is under very large mean stress, i.e. the stress triaxiality is very high, the volume changing contribution to void growth overtakes the shape changing part. McClintock et al. [18] noticed that there is a rotation and shape change of voids for materials under shear deformation (See Fig. 2.3). Thomason [87] also pointed out that ductile fracture in relative "low" stress triaxiality cases is due to relatively large "deviatoric" or shape changing void growth and relatively small "dilatational" or volume changing growth.

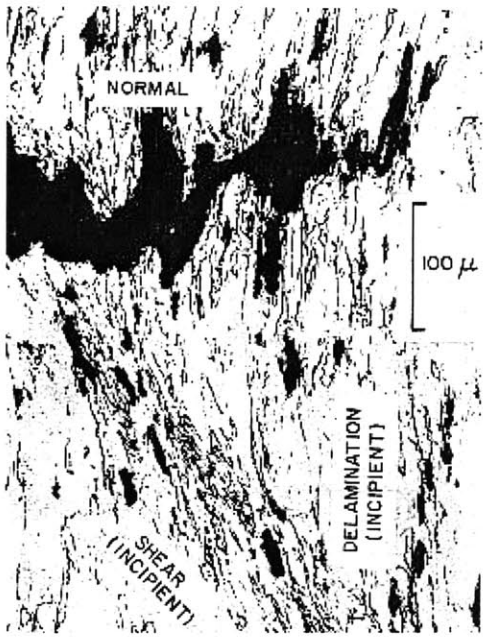

Fig. 2.3 Void growth and linkage in copper
(after Bluhm and Morrisey [2], McClintock [3])

Besides the different processes of void nucleation and growth, different processes of void linkage have been observed. As shown in Fig.2.4, void linkage could occur due to the internal necking of the matrix between two voids, simple touching of two voids and also could occur due to the so-called void sheet mechanism. Necking of the matrix, simple toughing of two voids and void sheet mechanism appears to be the three common ones. Schematic representations of the three processes are illustrated in Fig. 2.5-2.7, respectively. Those mechanisms are described in two-dimensions. Clearly, the real mechanisms in 3-D are more complicated. Thomason [87] assumed that the process of void linkage is due to the internal necking of the matrix between large voids in his study. McClintock [3] and Rice and Tracey [17] considered the simple touching of two voids as void linkage in their classical studies. Although the void sheet mechanism was found in a number of tests (eg. [4, 88, 89]), to the best of the author's knowledge, no good modeling has been developed. It should be noted that necking of the matrix and simple touching of two holes are similar and not easy to distinguish in real situations.

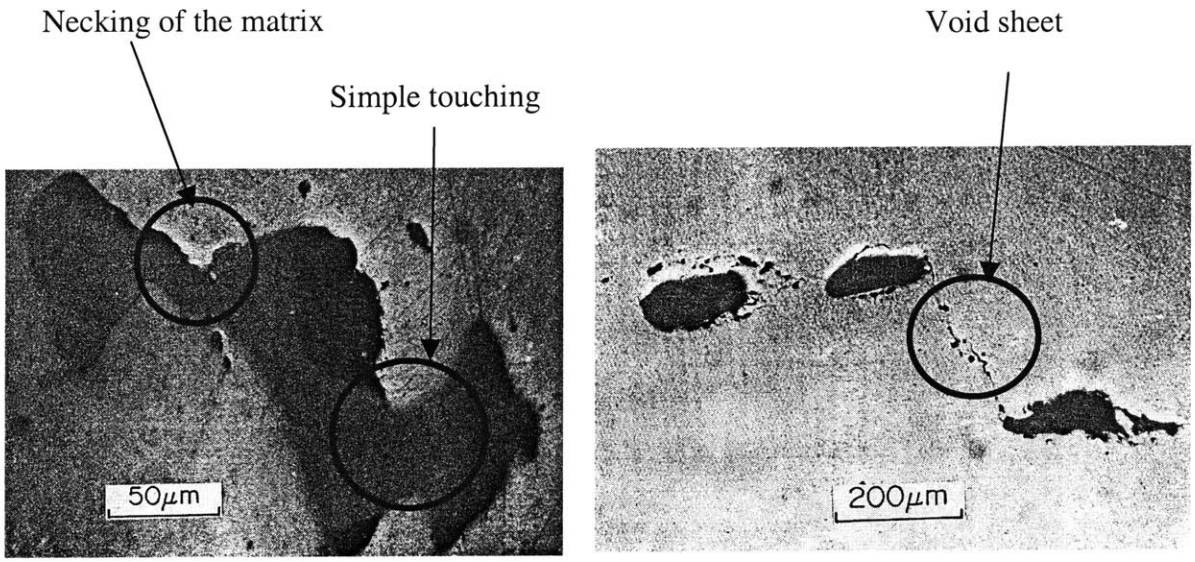

Fig. 2.4 Different modes of void linkage
(after Hancock and Mackenzie [4])

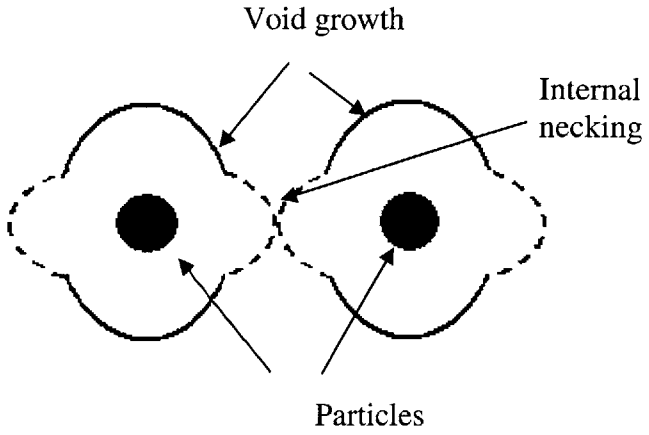

Fig. 2.5 Void linkage due to internal necking

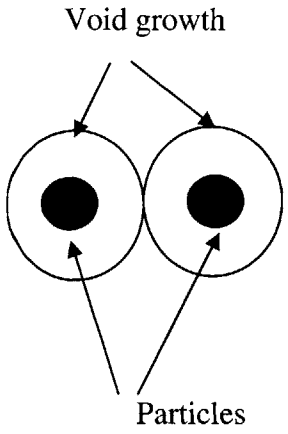

Fig. 2.6 Void linkage due to simple touching of two voids

Sometime, the sizes of voids, which link with one another, are very different. Especially, for alloys with different sizes of inclusions, voids nucleate first around large inclusions and then with the increase of plastic deformation voids may also nucleate and grow

around small inclusions as shown in Fig.2.1. This process usually leads to different sizes of dimples which have also been observed in a number of other studies (eg. Henry and Horstmann [90] and Brooks and Choudhury [91]) besides Fig. 2.1. Consequently, the linkage processes must be slightly different from those discussed above. As an example, the simple touching model of materials with different sizes of inclusions and voids becomes the one illustrated in Fig. 2.8. Likewise, the small changes should also be introduced to represent the other two linkage processes.

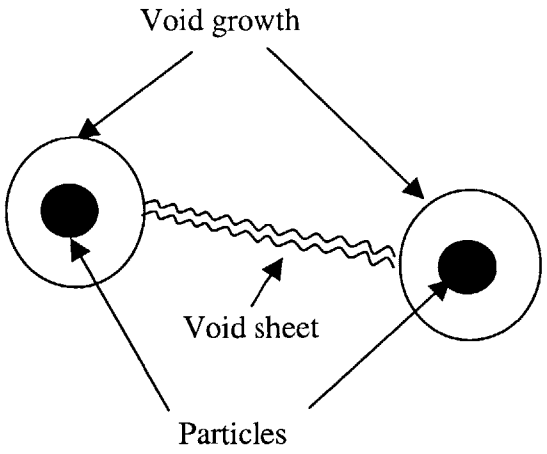

Fig. 2.7 Void linkage due to void sheet

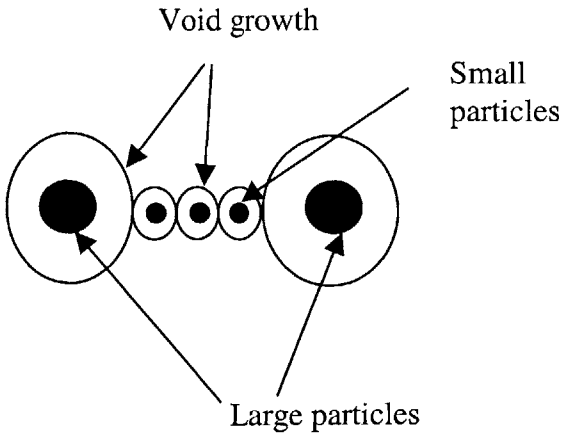

Fig. 2.8 Void growth and linkage in materials with large and small inclusions

The above representation does not involve rotation and shape change of voids. It is easy to imagine that the process of the void growth and linkage involving rotation and shape change of voids will be different from those without rotation and shape change. A criterion was developed to predict fracture involving rotation and shape change of voids by McClintock et al. [18]. It was assumed that large numbers of holes are scattered uniformly throughout a material and the solid is divided into a number of elements, each containing a single centrally-located hole and fracture occurs when the hole just touches the boundary of the deforming element in which it lies.

However, it is likely that void linkage does not occur even if a void touches the boundary of its element. This criterion can be improved in 3-D FEM modeling by checking the relative position of neighboring holes and calculating the minimum distance between two holes at every deformation increment until the distance reaches zero which is the condition of real void linkage. Figure 2.9 and 2.10 are schematic representations of simple touching model under relative "low" stress triaxiality for materials with only one type of inclusion and with two different inclusions, respectively. Again, similar changes should also be made to represent the other two linkage models.

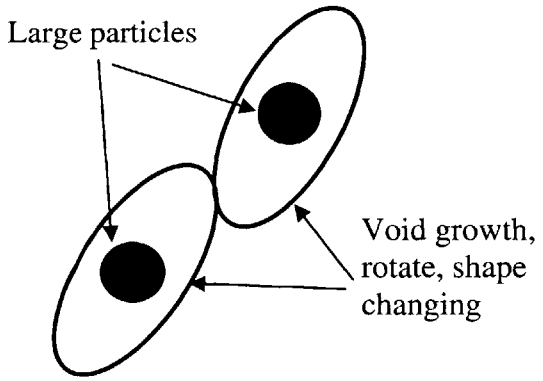

Fig. 2.9 Void linkage under relative "low" stress triaxiality

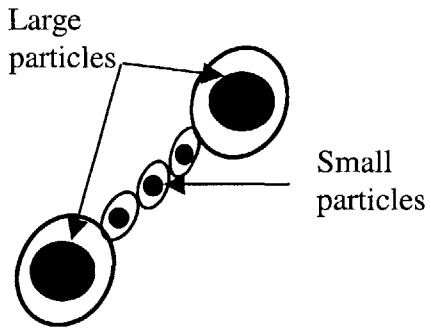

Fig. 2.10 Void linkage under relative low stress triaxiality in materials with large and small inclusions

Although, there are clear differences in the process of void nucleation, growth and linkage, the main characteristic is the same. This type of fracture mechanism generally occurs in the high stress triaxiality range and usually produces a rough surface.

In this thesis, all the specimens tested were cut from a same block of aluminum alloy 2024-T351. To study the mechanisms of crack formation of this material under high stress triaxiality, a fractured round tensile specimen with a circumferential notch (stress triaxiality =0.95, see Chapter 5) was examined.

Various components in Al 2024-T351 listed in Table 2.1 yield different inclusions. The largest inclusion or particle in Al2024-T351 is AlCuFeMn with a size of $10\,\mu$m. Other particles such as AlCuMg, AlMgSi, AlZnMg, AlZnMgCu, are less than $2\,\mu$m. The scanning electron microscope (SEM) pictures on fracture surfaces were taken for the notched round tensile specimen and are displayed in Fig. 2.11.

Table 2.1 Compsition of Al 2024-T351

Component	Weight %
Al	93.5
Cu	3.8-4.9
Mg	1.2-1.8
Mn	0.3-0.9
Fe	Max 0.5
Si	Max 0.5
Zn	Max 0.25
Ti	Max 0.15
Cr	Max 0.1

*Note: the value in the table only gives a range except for Al.

There is a difference between the center, which is the crack formation location and the edge of the section as shown in Fig. 2.11 (b) and Fig. 2.11 (c), respectively. In Fig. 2.11 (b), clearly voids nucleate first at the AlCuFeMn particles because of the particle cracking. Small voids also developed between the large voids nucleated at the AlCuFeMn particles with the increase of plastic deformation. This is a good example of the process schematically illustrated in Fig. 2.8. In Fig. 2.11 (c), besides the development of voids at large and small inclusions, one can also observe clear rotation and shape change of the voids. This process is much closer to the schematic mechanism displayed in Fig. 2.10. It is known that the stress triaxiality at the center is higher than at the edge for the round bars with a circumferential notch. That is the reason for the difference between those two fracture processes.

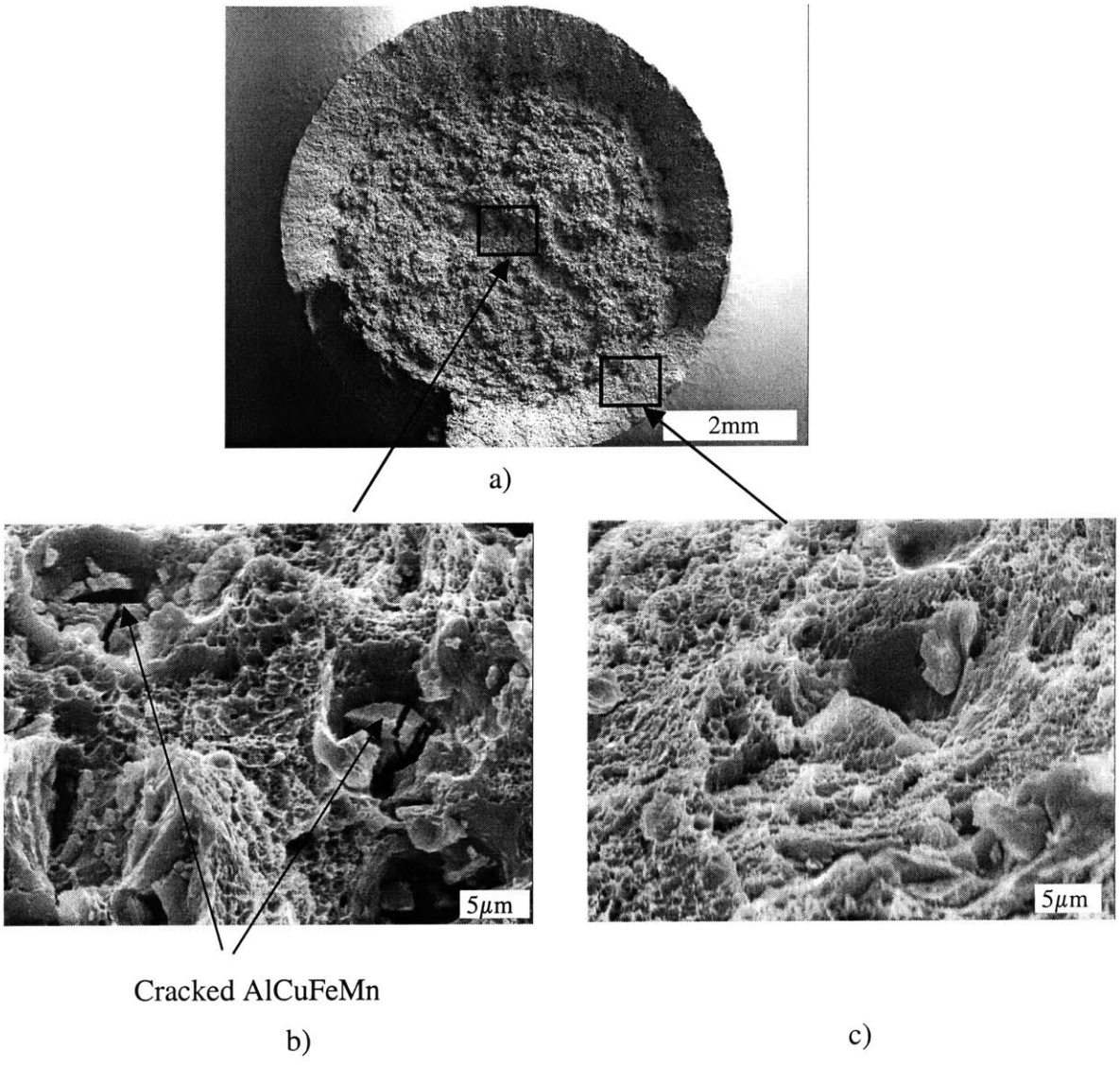

Fig. 2.11 Fractograph showing dimples in the notched tensile specimen

The broken specimen was also sectioned and polished. During the polishing process, the crack formation location, i.e. center of the specimen was carefully protected to avoid damage. A microscopic picture was taken on the polished sample and is shown in Fig. 2.12. It confirms that voids nucleated due to the crack of AlCuFeMn particles. Void linkage was likely due to simple touching or necking of the matrix in this case and the typical rough crack surface can also been clearly seen from the picture.

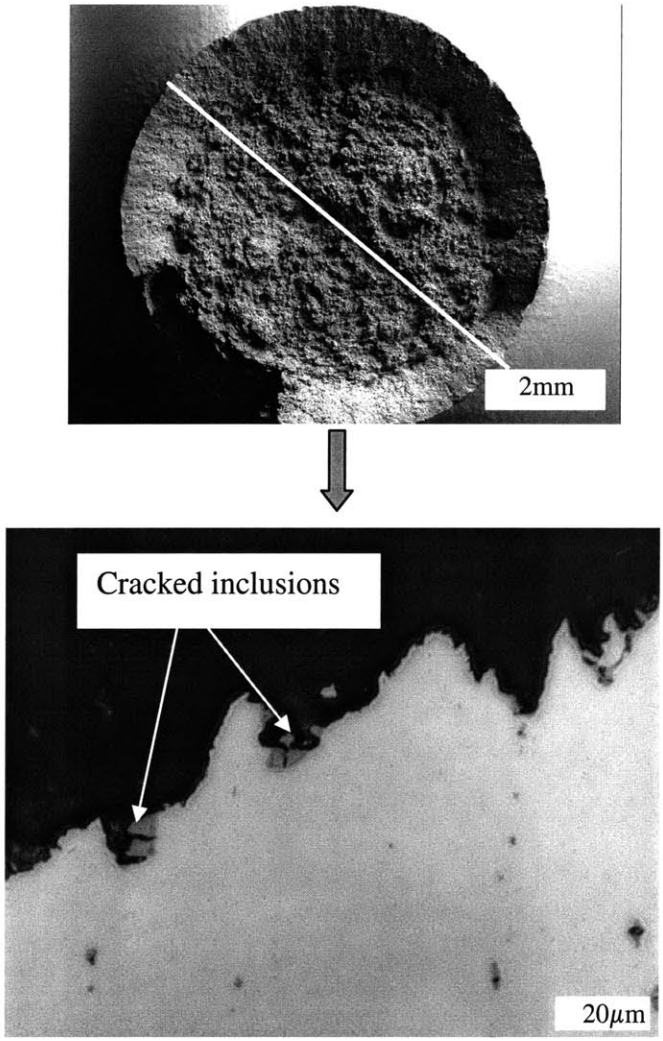

Fig. 2.12 Dimple fracture in the notched tensile specimen

2.2 Mechanisms dominating at Negative Stress Triaxialities

The knowledge of crack formation mechanisms in the negative stress triaxiality range is very limited. No well-established mechanism in this range can be found in the open literature. In order to uncover this "mystery", a preliminary microscopic study was

performed. Upsetting tests are good examples for ductile crack formation in the negative stress triaxiality range. It will be shown in Chapter 5 that the stress triaxiality is negative (-0.33 ~ -0.05) for this case. The SEM pictures on fracture surfaces were taken for a fractured upsetting specimen of Al2024-T351 with initial diameter of 12.5 mm and initial height of 12.5 mm and are presented in Fig. 2.13. The fracture surface is relatively flat and no clear dimples can be observed at the location of crack formation, which is the equatorial area. Crack formation clearly was due to a different failure mechanism from the void nucleation, growth, and linkage observed in the high stress triaxiality range.

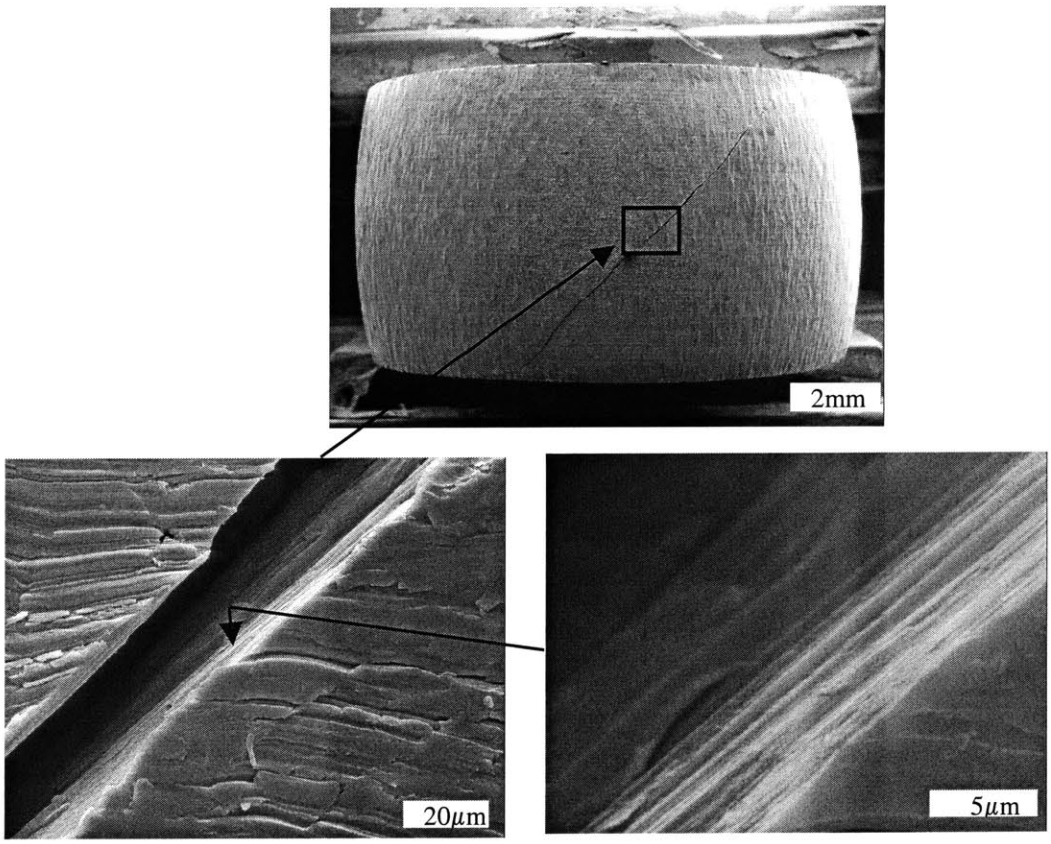

Fig. 2.13 Fractograph showing flat fracture surface in the upsetting specimen

This mechanism was further examined by sectioning the broken specimen. The equatorial area was protected to avoid damage during the polishing process. As illustrated in Fig. 2.14, crack is relatively smooth and goes through the matrix instead of the inclusion or

the connection of inclusions and matrix. There was no evidence showing cracked particle and nucleated voids. A possible reason for this type of failure is that the cylinder failed along the closest packed sliding planes [92]. A further study on this "shear fracture" mechanism is needed to get a deep understanding. However, it is beyond the scope of this study. It should be noted that "shear fracture" is just the name for this type of mechanism and it does not mean that this type of fracture is exclusively due to shear.

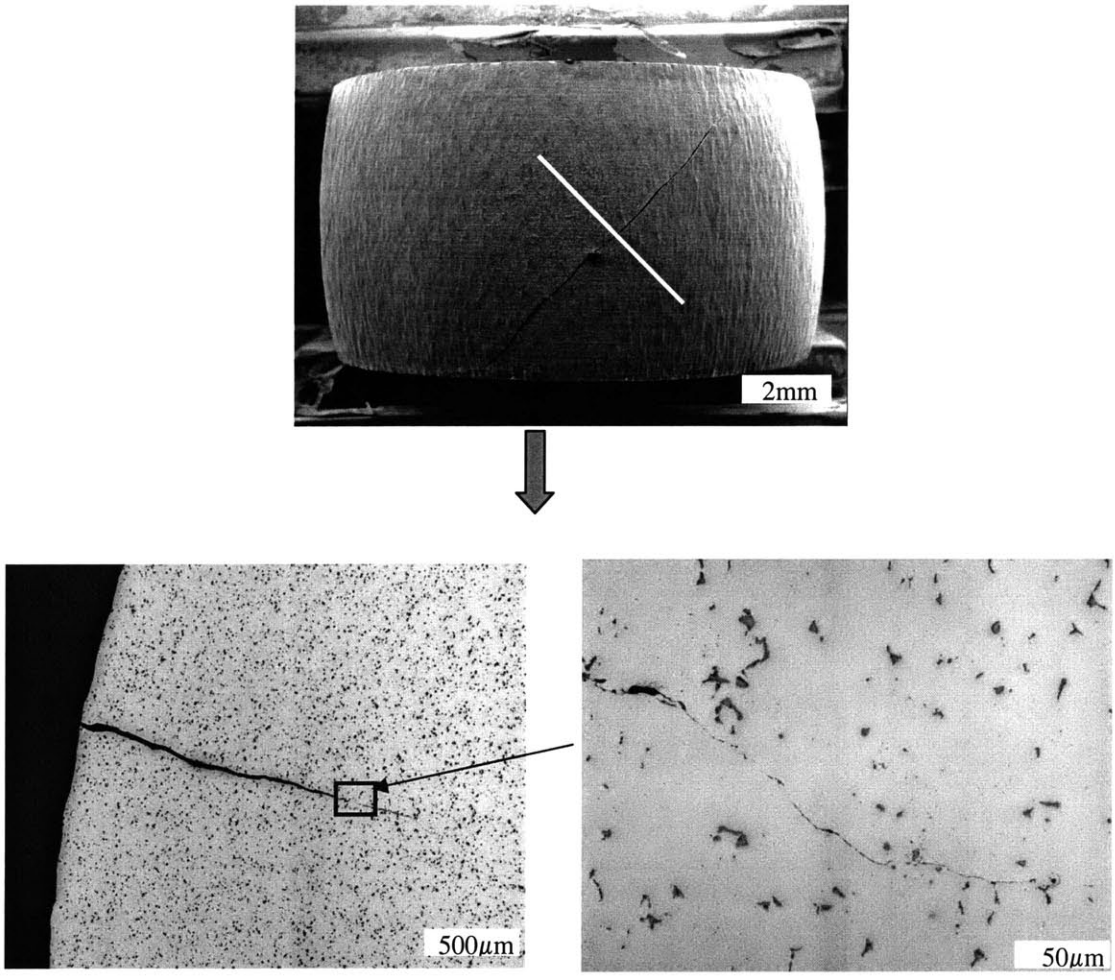

Fig. 2.14 "Shear fracture" through the matrix in the upsetting specimen

2.3 Mixtures of Mechanisms at Intermediate Stress Triaxialities

French and Weinrich [5] studied the influence of pressure on the tensile fracture of a very ductile copper with 233 MPa tensile strength. Classical void nucleation, growth and linkage were found in the fracture surface from the SEM examination in the case with no pressure. As the pressure increased, the relative area of the rough portion due to void nucleation, growth and linkage decreased. As displayed in Fig. 2.15, a limited number of voids can be observed for the case with 300 MPa pressure. Very few voids can be found in the fracture surface at a pressure of 500 MPa shown in Fig. 2.16. This mechanism is very similar to the "shear fracture" observed in the upsetting tests. Similar tests on steels have been carried out in an earlier study by Bridgman [93]. It was also observed by naked eye that roughness of fracture surface decreases with increase of the pressure.

As shown above, cracks form in two different ways in the high stress triaxiality and the negative stress triaxiality range, respectively. There are two competing fracture modes. "Shear fracture" favors the negative stress triaxiality while dimple fracture dominates in the high stress triaxiality range. Therefore, with the studies of French and Weinrich [5] and Bridgman [93] it is reasonable to conclude that crack formation in the intermediate stress triaxiality could due to the combination of those two mechanisms Although it is difficult to know the stress triaxiality of those two cases (Fig. 2.15 and Fig. 2.16) since significant necking was found during the deformation and the true stress was not given in the paper, it is likely that the case with 500 MPa is in the negative stress triaxiality range and it is clear that the stress triaxiality in the case with 500 MPa pressure is less than the one with 300 MPa pressure and the stress triaxiality in the case with 300 MPa pressure is less than the one with no pressure. Therefore, this study provided clear evidence supporting the above conclusion of the competition of "shear fracture" mode and void nucleation, growth and linkage mode.

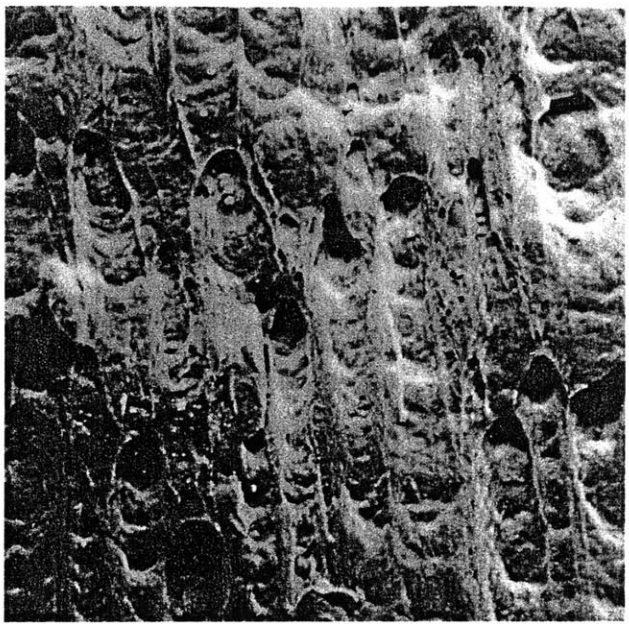

Fig. 2.15 Fracture surface of specimen fracture at pressure of 300 MPa, tensile strength of this copper is 235 MPa
(after French and Weinrich [5])

Fig. 2.16 Fracture surface of specimen fracture at pressure of 500 MPa, tensile strength of this copper is 235 MPa
(after French and Weinrich [5])

2.4 Discussion

It is clear that there are two different ductile crack formation mechanisms, namely "shear fracture" occurring in the negative stress triaxiality range and void nucleation, growth and linkage occurring in the high stress triaxiality range. A combination of those two mechanisms happens between those two ranges. In other words, the intermediate stress triaxiality range is a transition range. It should be mentioned that the definition of the three stress triaxiality ranges here is qualitative and not quantified. The boundary of the stress triaxiality ranges depends on materials. For Al2024-T351, a more precise definition can be found in Chapter 5.

As shown above, the crack formation mechanisms are very complex. No well-developed modeling has been proposed even for the whole process of the void nucleation, growth and linkage, which has been observed for decades. McClintock's cylindrical hole model [3], Rice-Tracey's spherical hole model [17] and Gurson's model [25, 26] developed in 1960-1970s are still the best in the area of modeling void growth and linkage. However, they did not consider void interaction and rotation. Also they assumed regular void shapes (elliptical cylinders or spheres), a homogenous distribution of voids and the simple touching as the process of void linkage. Clearly, the actual process is far more complicated than those models. With these facts, it is very hard to see the possibility of developing a much better model based on these complicated crack formation mechanisms in the near future. Apparently, approaches with a totally different point of view are needed in order to meet the urgent demand of the industry. Those approaches should avoid dealing with the details of the complex mechanisms.

Chapter 3

Determination of Stress-Strain Curve

It is clear that crack formation is governed by local stress and strain. It is almost impossible to measure individual components of stress and strain tensors directly from experiments. Performing numerical simulations is an alternative way to acquire individual components of stress and strain tensors at the potential locations of crack formation. The stress-strain curve is one of the most important inputs in numerical simulations.

Uniaxial tensile and compression tests are the most common ones to obtain the stress-strain curve. However, in compression tests, homogeneous compression is difficult to achieve because of the effect of friction between the ends of the specimen and the flat platens, and the associated "barreling" of specimens. In tensile tests, necking often occurs in ductile metals, which brings difficulties in determining stress-strain curve since stress and strain is not uniform in the neck and the gauge area.

Several approximate methods are discussed in this chapter to reduce the effect of friction in compression and to extrapolate the material property after necking in tension. The

stress-strain curve of Al2024-T351 is determined from compression and tension tests, respectively.

3.1 Determination of Stress-Strain Curve in Compression Tests

3.1.1 Specimen under "Cone-Shaped" Platens

The idea of compressing the specimen between cones to avoid barrel effect was first suggested by Siebel and Pomp [94] in 1927. Unfortunately, the uniform stress distribution can not be obtained even if the barrel effect is eliminated by choosing the certain angle of the cone for a certain friction condition because of the difference of the initial height between the center and the edge as shown in Fig.3.1. The barrel effect is clearly eliminated, but the stress distribution is not uniform.

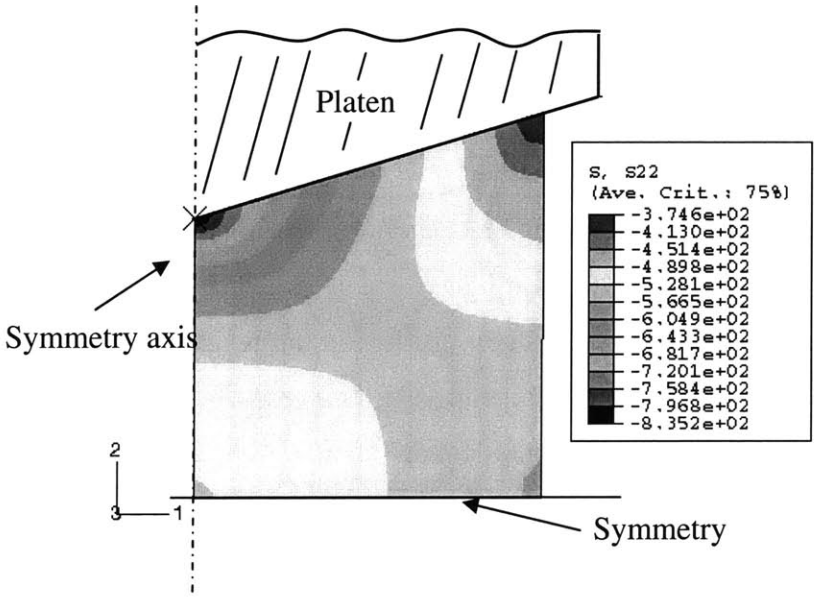

Fig. 3.1 Stress distribution for a specimen under "cone-shaped" platens

A relatively homogenous stress distribution can be achieved by making the height from the center to the edge of the specimen same and replacing one of the platen with a different shape to fit the specimen as shown in Fig. 3.2.

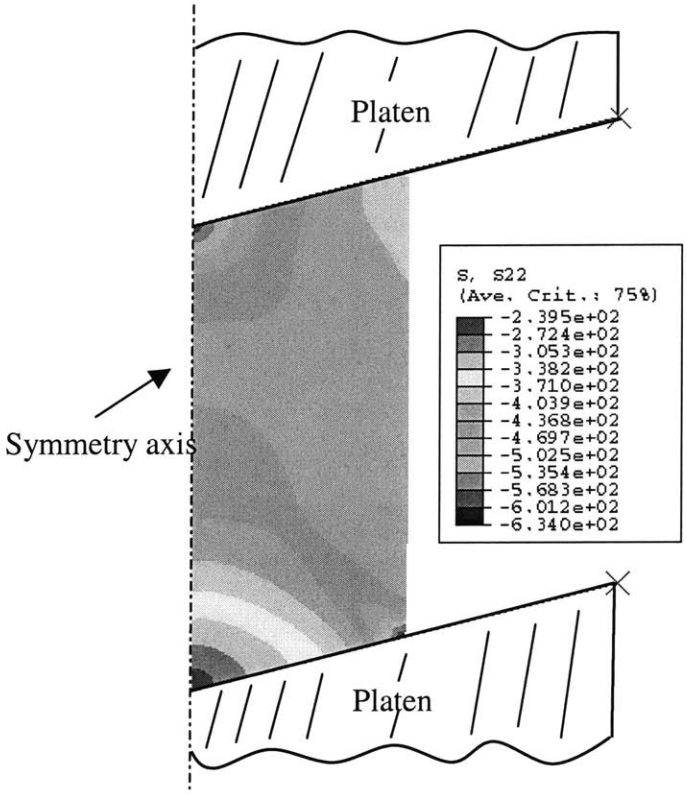

Fig. 3.2 Stress distribution for an improved specimen under "cone-shaped" platens

Even more uniform stress and strain distribution in the gage area can be obtained as shown in Fig. 3.3 and Fig. 3.4 by replacing the solid cylinder with a ring specimen. However, there are some limitations for this method. One limitation of this method is that the specimen with an optimum shape at the ends of the specimen is only effective for a certain range of friction. Another limitation is that it is not good for low ductility material because of high strain and high stress at some locations though the areas are small (shown in Fig. 3.3 and Fig. 3.4). Fracture might develop very early at those areas.

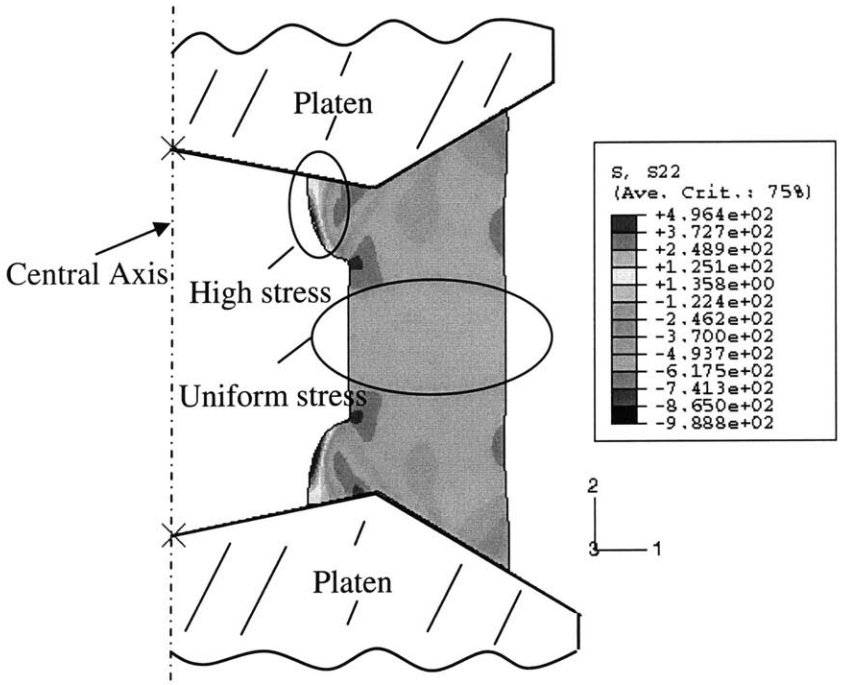

Fig. 3.3 Stress distribution for a ring specimen

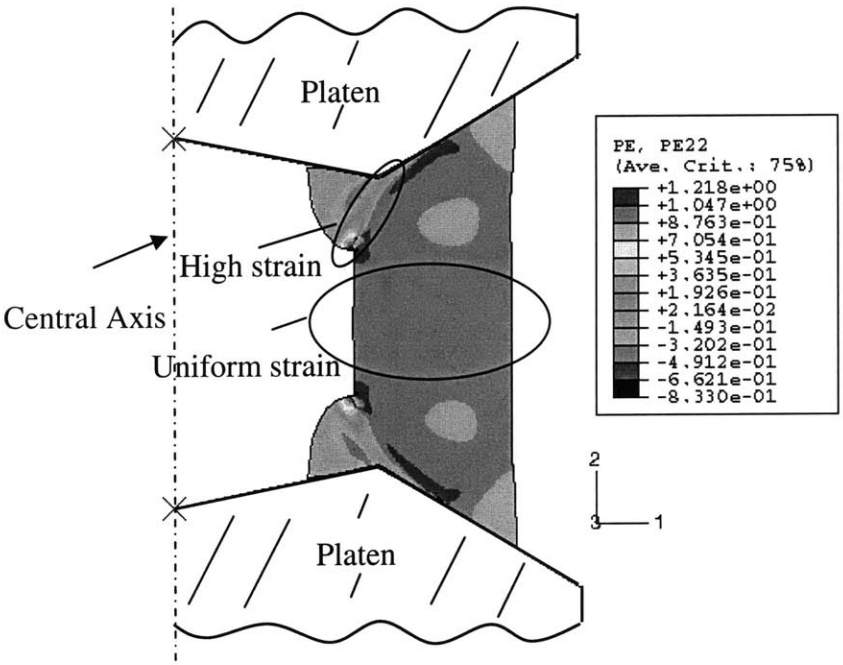

Fig. 3.4 Strain distribution for a ring specimen

3.1.2 Grooved Specimen

Another approximation to homogeneous compression may be obtained by introducing lubrication by means of oil, which is entrapped in concentric grooves machined on each end of the specimen. Loizou and Sims [95] successfully acquired approximate homogeneous compression (shown in Fig. 3.5) using this idea. Johnson [96, 97] obtained approximate stress-strain curves using a similar approach. This technique was also tried by the present author for Al 2024-T351 with the same grooves suggested by Loizou and Sims [95], but the barrel effect was not effectively eliminated.

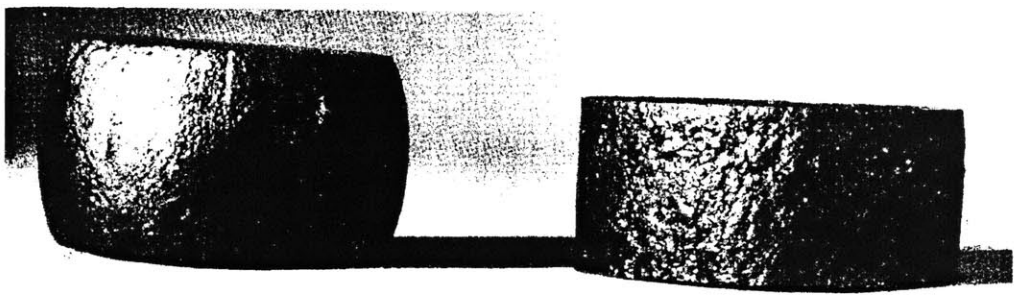

(a) Barreling on lubricated specimens without (left) and with grooves (right)

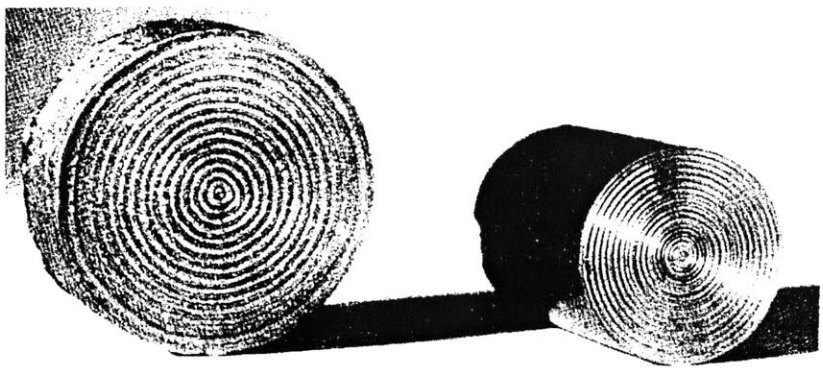

(b) Grooving of specimens after and before compression

Fig. 3.5 Simple compression of grooved specimens

(after Loizou N. and Sims R.B. [9])

The drawback of this method is that a lot of tests needed to determine the depth, shape and number of the grooves suitable to the particular material and friction condition. And it is not certain that good results can be obtained.

3.1.3 Extrapolation Method

The idea of extrapolation method is based on the fact that if cylindrical specimens with equal diameters but different heights are compressed, the degree of barreling effect depends on the original height of the specimen and is least for the highest one. Theoretically, there would be no barreling effect for a cylinder with an infinite height and then the mean compressive pressure could be taken as the flow stress in uniaxial compression. However, long cylinders will buckle before yielding.

According to Johnson and Mellor [98], the extrapolation method appears to be the most satisfactory approach for determining the stress-strain curves in uniaxial compression in general. The advantage of this method is that only a few tests needed to get satisfactory results.

Cook and Larke [99] used four cylinders with the ratios of initial diameter to initial height 0.5, 1.0, 2.0, 3.0 to obtain the stress-strain curve for copper. Graphs of compressive pressure at the different stage of the compression against the initial aspect ratio were plotted and then were extrapolated to the initial ratio of zero, which is the condition for no barreling to get the stress-strain curve.

Shey, Venner and Takomana [100] obtained the true flow stress of Aluminum 6061-T6 by plotting the pressure against instantaneous aspect ratio of current diameter to current height and extrapolating it to the instantaneous ratio of 0.5. It was found that once an

instantaneous aspect ratio of 0.5 is reached, the cylinder deforms virtually homogeneously [100].

In this thesis, the extrapolation method is used to obtain the stress-strain curve in compression for Al2024-T351. Cylinders with the ratios of initial diameter to initial height 0.5, 0.8, 1.0, 1.5 were compressed in a screw driven 200 kN MTS machine (See Fig. 3.6). The initial diameter of the specimens was 12.5 mm.

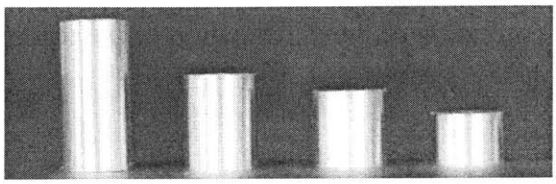

a) Initial

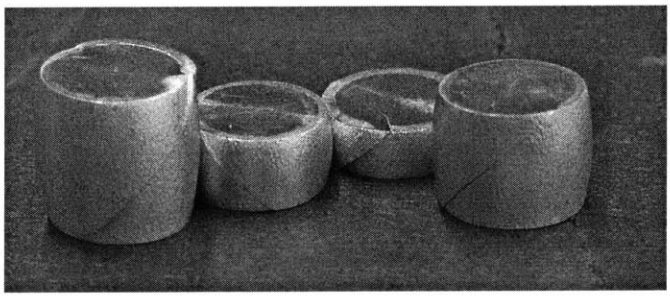

b) Deformed

Fig. 3.6 Compression specimens with different aspect ratios

Since the force level in the tests almost reached the capacity of the test machine which is 200 kN, the effect of the deformation of the system of the test machine may not be negligible. Stiffness of the test machine is assumed to be constant during the test. The total stiffness K_t can be expressed as

$$\frac{1}{K_t} = \frac{1}{K_s} + \frac{1}{K_m} \tag{3.1}$$

where, $K_s = \frac{EA}{h_0}$ is the elastic stiffness of the sample and K_m is the stiffness of the test machine, E is the Young's modulus, A is the cross section area and h_0 is the initial height of the specimen.

The total stiffness can be measured directly from the output of the test for the different samples. For same material EA is same. Then the stiffness of the machine can be obtained from Eq. (3.1), which is 250 kN/mm for this MTS machine. The displacement – force response with the correction of the deformation of the test machine is shown in Fig. 3.7.

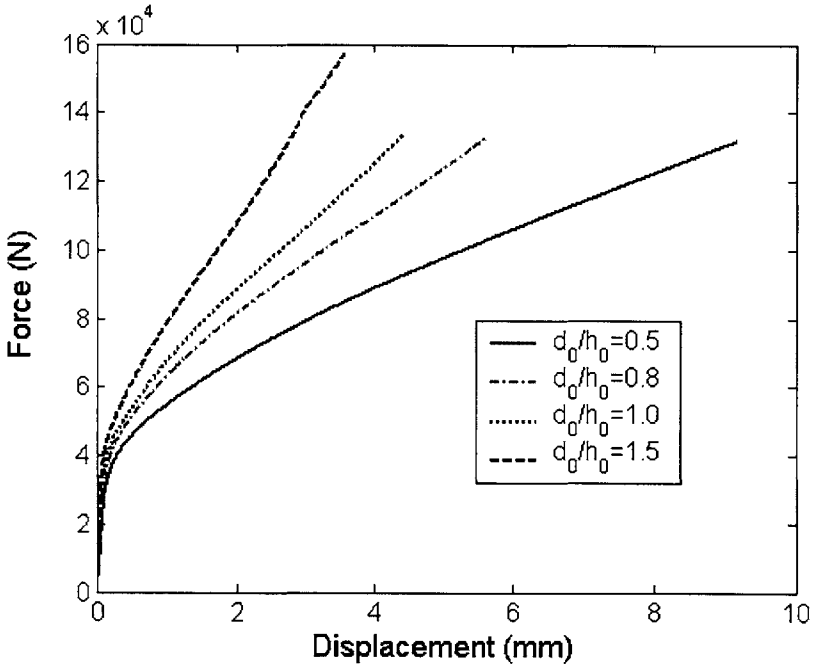

Fig. 3.7 Load-displacement response of upsetting tests

With the assumption of volume conservation i.e.

$$d^2 h = d_0^2 h_0 \tag{3.2}$$

where d_0 and d are the initial diameter and current diameter, respectively; h_0 and h are the initial height and current height, respectively.

The approximate stress-strain curves shown in Fig. 3.8 can be obtained from the force-displacement in Fig. 3.6 for four different types of specimens using the following definition

$$\bar{\sigma} = \frac{4P}{\pi d^2} = \frac{4Ph}{\pi {d_0}^2 h_0} \tag{3.3}$$

$$\bar{\varepsilon} = \ln(\frac{h_0}{h}) \tag{3.4}$$

where P is the load.

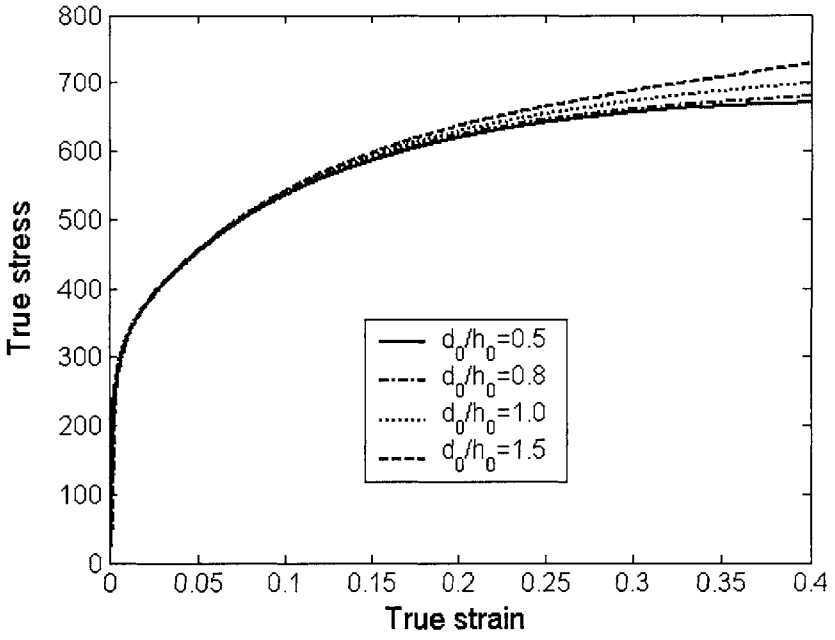

Fig. 3.8 Approximate stress-strain curves directly obtained from the force-displacement responses of different upsetting specimens

Clearly, the result obtained directly from Eq. (3.3) and (3.4) is good only when barreling is small. It can be seen that due to different degree of barreling the stress-strain curve obtained from the different specimens is different at large deformation while the curve is the same at small deformation. Therefore, the real true stress and strain curve for $\bar{\varepsilon} < 0.1$ of this material can be obtained directly from Fig. 3.8, while a correction should be introduced for $\bar{\varepsilon} \geq 0.1$. The real true stress and strain curve for $\bar{\varepsilon} \geq 0.1$ is determined

using the extrapolation method as follows. Seven data points are used to represent the curve for $\bar{\varepsilon} \geq 0.1$.

The seven points have the strain of 0.1, 0.15, 0.2, 0.25, 0.3, 0.35 and 0.4, respectively. The goal of the extrapolation method is clearly to obtain the corresponding stresses of those strains. Eq. (3.4) can be rewritten as

$$h = h_0 e^{-\bar{\varepsilon}} \tag{3.5}$$

Together with Eq. (3.2), the ratio of current diameter to current height for different specimen can be expressed as

$$\frac{d}{h} = \frac{d_0}{h_0} e^{\frac{3}{2}\bar{\varepsilon}} \tag{3.6}$$

The ratio of current diameter to current height for different specimens at the same strain level is different. For each strain, four corresponding stresses and ratios of current diameter to current height are obtained for the four different specimens based on Fig. 3.8 and Eq. (3.6). The relationship of the stress and the ratio of current diameter to current height for each strain was obtained and is illustrated in Fig.3.9. For each strain, there are four points, which represent the four different samples. By extrapolating the stress to $d/h = 0$, which is the idea case without barreling effect, the corresponding stress for each strain can be acquired. The stress-strain curve for $\bar{\varepsilon} \geq 0.1$ is then determined. By combining the curve for $\bar{\varepsilon} < 0.1$, the complete stress-strain curve for Al 2024-T351 was obtained and is shown in Fig. 3.10.

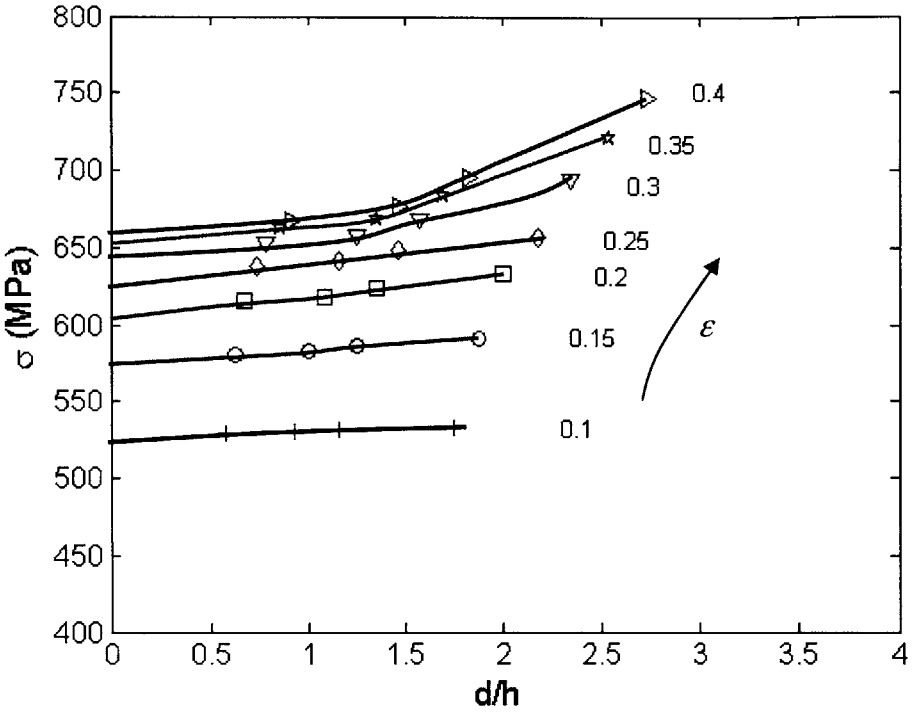

Fig.3.9 Flow stress against the current ratio for different plastic strains

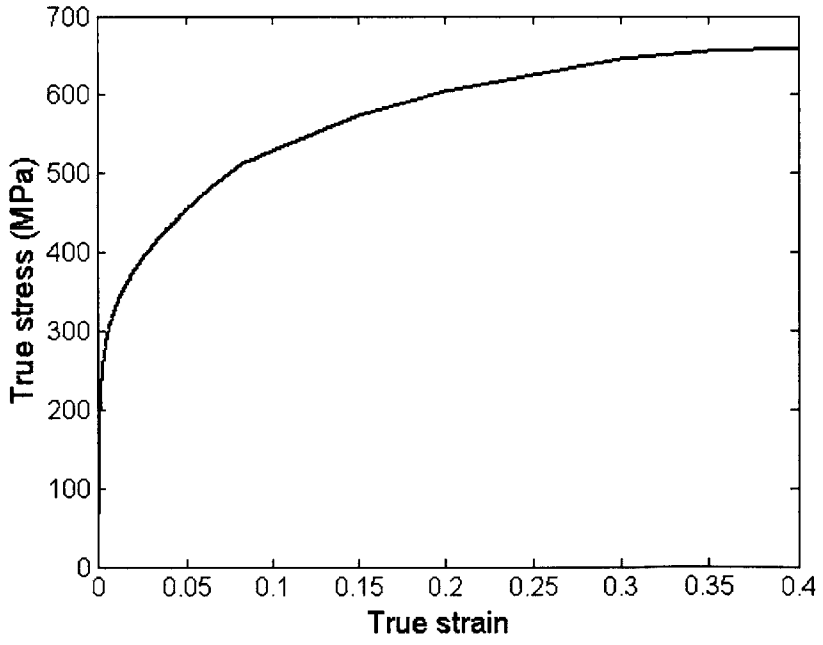

Fig.3.10 True compressive stress-strain curve for aluminum 2024-T351

3.2 Determination of Stress-Strain Curve in Tension Tests

3.2.1 Bridgman Correction

Round bars are most often used in tensile tests to get the stress-strain relation. The stress and strain are homogenous in the gauge area before necking occurs. The stress and strain curve up to necking can be determined as follows

$$\bar{\sigma} = \frac{P}{\pi a^2} \tag{3.7}$$

$$\bar{\varepsilon} = \ln(\frac{l}{l_0}) \tag{3.8}$$

where P is the load ; a is the current radius of the gauge section; l_0 and l are the initial and current gauge length, respectively.

After necking occurs, Eq. (3.7) and Eq. (3.8) are no longer valid. In order to obtain the local stress and strain in a necked round bar, Bridgman's [93] developed a semiempirical analysis in terms of the radius of curvature of the neck and the radius of the minimum cross section. The main feature of Bridgman's analysis is that the equivalent strain is constant across the minimum cross section, but the radial, hoop and axial stresses ($\sigma_{rr}, \sigma_{\theta\theta}$ and σ_{zz}, respectively) vary. The stress and strain are determined as follows referring the geometry given in Fig.3.11.

$$\bar{\varepsilon} = 2\ln(\frac{a_0}{a}) \tag{3.9}$$

$$\sigma_{zz} = \bar{\sigma}[1 + \ln(\frac{a^2 + 2aR - r^2}{2aR})] \tag{3.10}$$

$$\sigma_{rr} = \sigma_{\theta\theta} = \bar{\sigma}\ln(\frac{a^2 + 2aR - r^2}{2aR}) \tag{3.11}$$

$$\frac{\sigma_m}{\bar{\sigma}} = \frac{1}{3} + \ln\left(\frac{a^2 + 2aR - r^2}{2aR}\right) \tag{3.12}$$

where, $\sigma_{zz}, \sigma_{rr}, \sigma_{\theta\theta}, \bar{\sigma}$ and σ_m are axial, radial, hoop, equivalent and mean normal stress, respectively, $\bar{\varepsilon}$ is the equivalent strain, a and R are the radius of the minimum cross-section and the radius of the circumferential notch, a_0 is the initial value of a.

The stress sate at the neck essentially corresponds to a constant uniaxial tension with a superimposed hydrostatic tension building up toward the center. Therefore, the load carried by the hydrostatic stress must be subtracted from the total load carried by the minimum cross section to find the equivalent stress. This correction is called the Bridgman correction and is given as the ratio of equivalent strain to average axial stress based on the Bridgman analysis

$$\frac{\bar{\sigma}}{P/(\pi a^2)} = \frac{1}{(1 + 2R/a)\ln(1 + a/2R)} \tag{3.13}$$

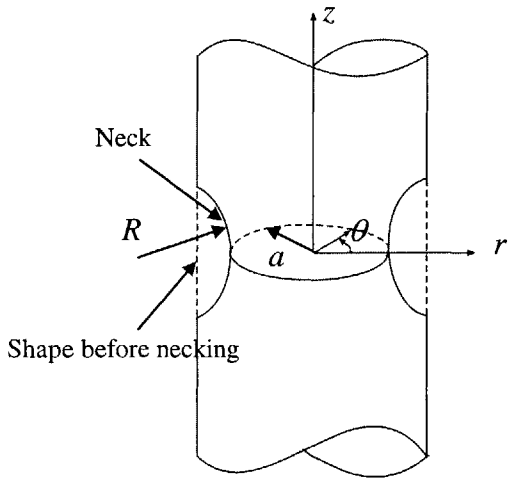

Fig. 3.11 Tensile necking in a round bar

Determination of the radius of the neck R is inconvenient. Bridgman [78] found that it could be avoided by using an empirical relation

$$\frac{a}{R} = \bar{\varepsilon} - \varepsilon_n \tag{3.14}$$

where ε_n is the uniaxial strain at tensile strength.

This method clearly depends on the measurement of the radius of the minimum cross section a and accuracy of the Bridgman solution and Eq. (3.15). Even if the difficulty of determining R can be avoided by using Eq. (3.14), still a should be measured during the test, which is also difficult because 1) the position of the neck is not known before the test; 2) it needs a series of tests with different loadings or pausing the test several times to obtain the evolution of a. In addition, the stress state in the neck given by the Bridgman solution essentially has not been verified. As reviewed by McClintock and Argon [101], "Marshall and Shaw [102] ran tensile tests on specimens which were machined to arbitrary values of longitudinal curvature at different stages. The found that the results they obtained could be correlated into a smooth curve by applying Bridgman correction. On the other hand, Parker et al. [103] determined the stress distribution in the neck of a tensile specimen by unloading a necked specimen, calculating the stress change on unloading from elasticity theory and then boring out the specimen to determine the residual stress. They disagreed with Bridgman's results". Recently, Alves and Jones [104] performed a finite element analysis for notched round bars under tensile loading. Stress triaxiality and equivalent strain were compared between numerical simulations and Bridgman solution and large difference was found. It should be noted that in their study, change of the radius of curvature due to the deformation was not considered in calculating stress and strain using the Bridgman solution. A more complete comparison is conducted in this study. Consider a round bar with initial radius of the minimum cross section $a_0 = 4$ mm and initial radius of the notch $R_0 = 4$ mm as shown in Fig. 3.12 and focus on one deformation stage ($a = 3.46$ mm, $R = 4.54$ mm). Comparisons of Bridgman solution and numerical simulation are displayed in Fig. 3.13 and Fig. 3.14 for equivalent strain and stresses, respectively. The difference of equivalent strain is relatively small (15%), while the difference of stresses is large (30%-50%).

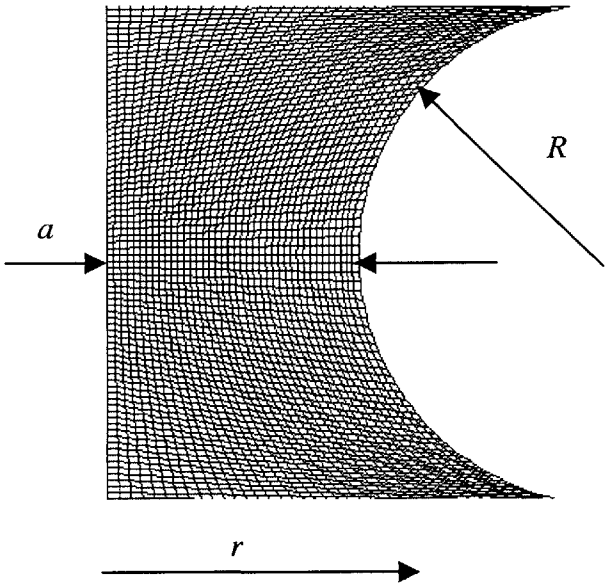

Fig. 3.12 Finite element mesh of the notch region

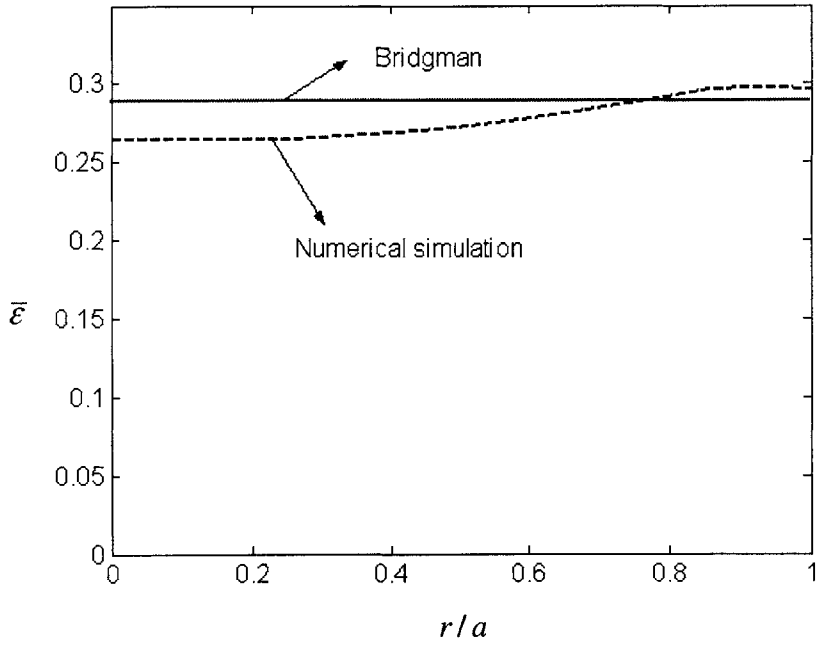

Fig. 3.13 Comparison of equivalent strain between Bridgman and numerical simulation

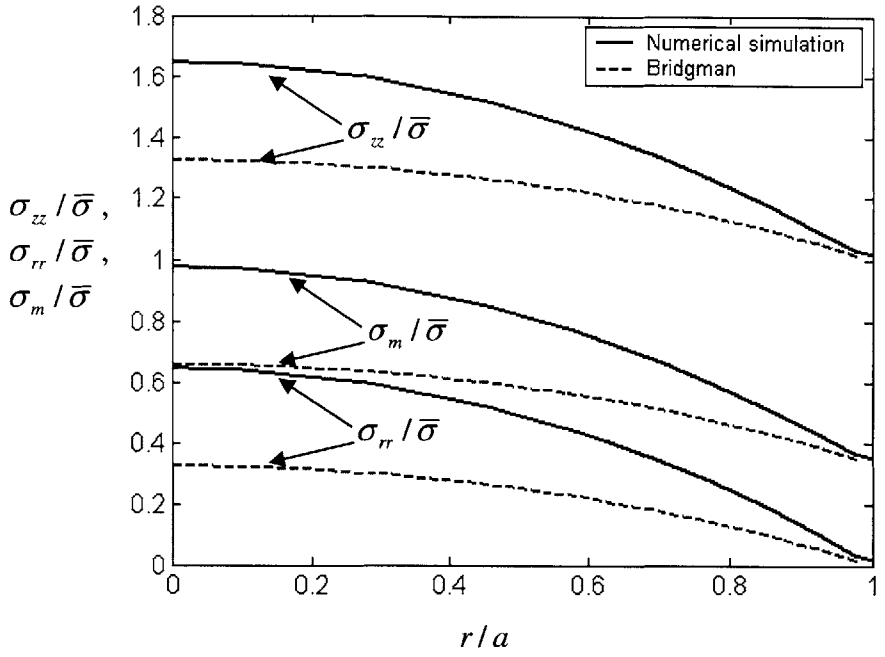

Fig. 3.14 Comparison of stresses between Bridgman and numerical simulation

3.2.2 Trial-and-Error Method

The stress-strain calculated by Eq. (3.7) and (3.8) is good before necking. In this thesis a trial-and-error method is used for searching an accurate stress-strain curve after necking occurs. The main idea is to iterate the stress-strain curve by comparing the load-elongation response of experiments and numerical simulations. The procedure is summarized as follows.

(1) Perform a tensile test on a round bar. Make sure that necking occurs inside the gauge area. Record the load-elongation response.

(2) Calculate the initial stress-strain curve using Eq. (3.7) and (3.8).

(3) Perform numerical simulation with the initial stress-strain obtained in Step (2) and compare the load-elongation response with experiment. Calculate the relative error of the force.

(4) Adjust the stress-strain curve based on the relative error obtained in Step (3) and replace the stress-strain curve with the new one in Step (3).

(5) Repeat Step (3) and (4) until the relative error becomes small.

By following this procedure, the stress-strain for Al2024-T351 was determined. Two round bars with a 9 mm diameter gauge section and 25.4 mm gauge length were tested. As shown in Fig. 3.15, necking occurred inside the gauge section. The two samples gave almost exactly the same result as illustrated in Fig. 3.16. Numerical simulations were performed using 4-node axisymmetrical elements. A finite velocity was applied to one end of the model while the other end was fixed. In order to study the possible mesh size sensitivity, a coarse and a fine mesh were developed. Initial and deformed model of coarse mesh and fine mesh are displayed in Fig. 3.17 and Fig. 3.18, respectively. Both coarse and fine models successfully captured the necking. No difference of the results was found between the coarse and fine mesh. A large number of runs were needed to get the correct points after necking. The stress-strain curve used in the simulations of tensile tests is shown in Fig.3.19. Comparison of the force-elongation between experiments and numerical simulations are illustrated in Fig. 3.20 which shows excellent correlation.

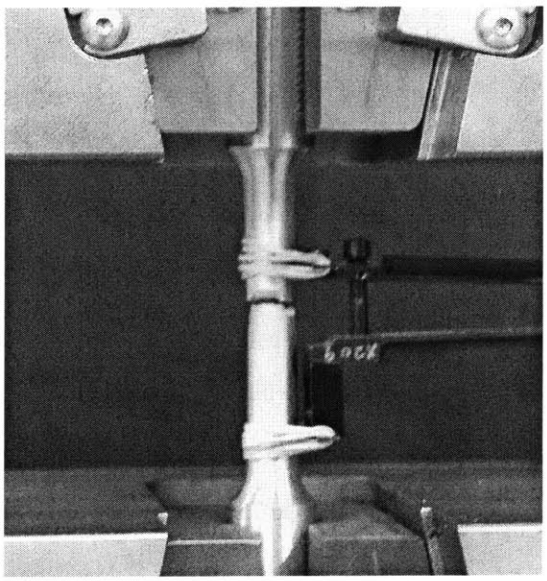

Fig. 3.15 Final stage of tensile test on a standard round bar

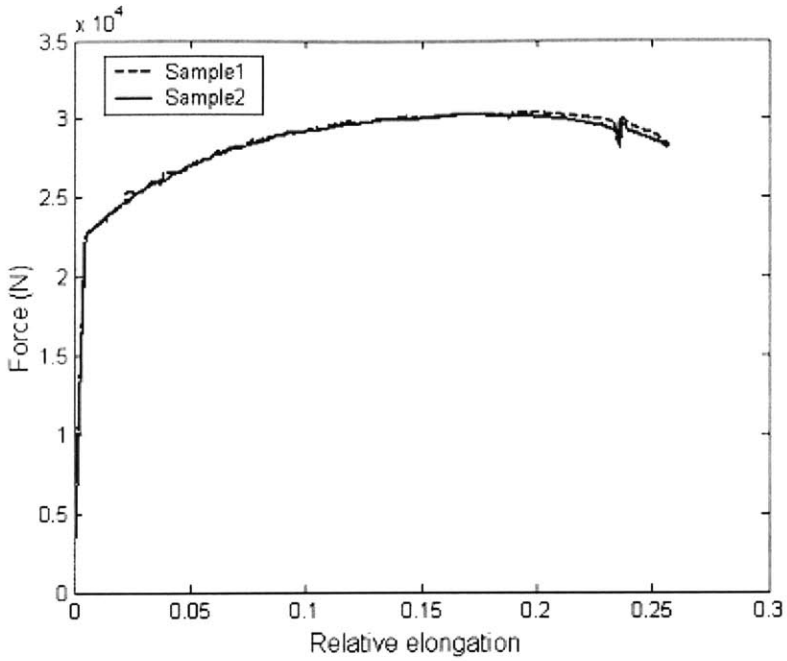

Fig. 3.16 Experimental force-relative elongation response of tensile tests on round bars

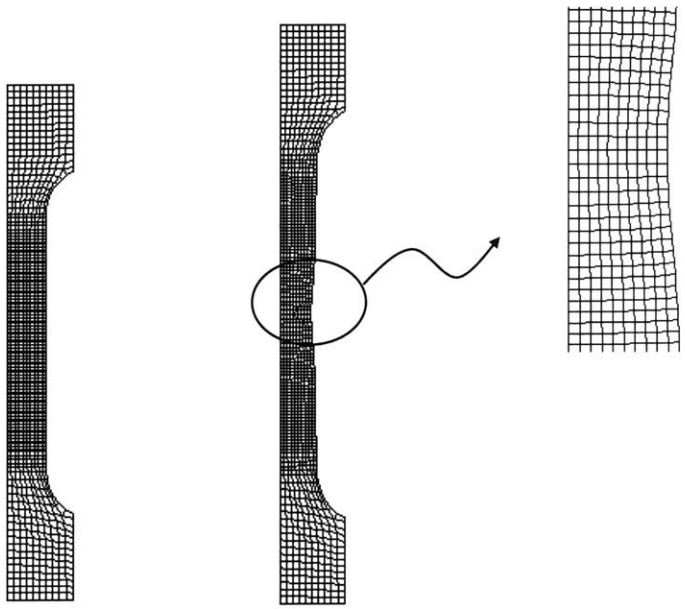

undeformed deformed

Fig. 3.17 Coarse mesh of round bars under tensile loading

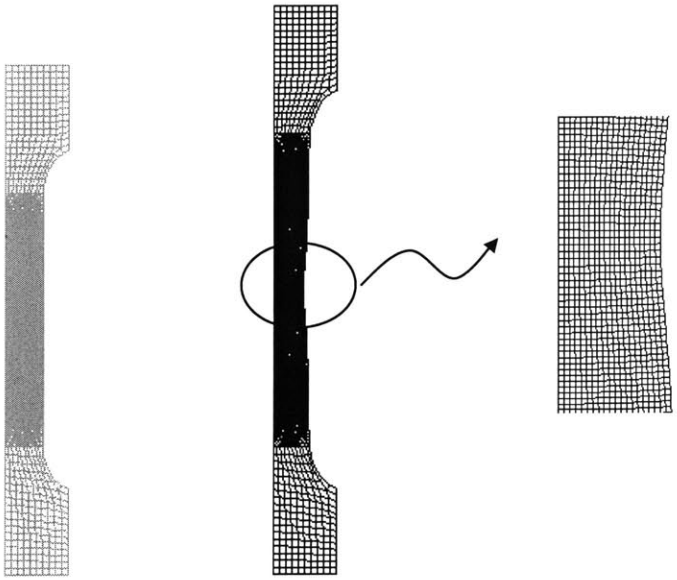

Fig.3.18 Fine mesh of round bars under tensile loading

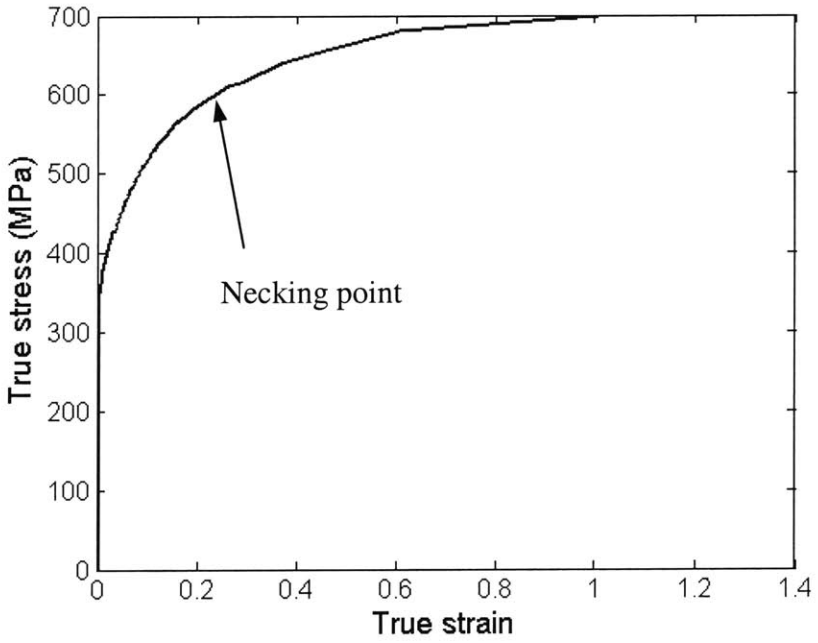

Fig.3.19 Stress-strain curve obtained using a trial-and- error method from tensile tests

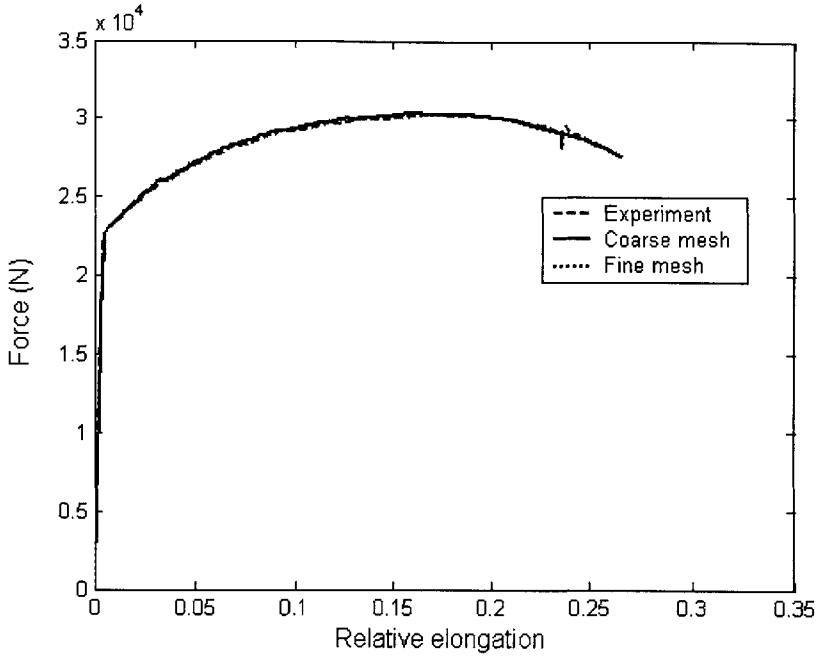

Fig. 3.20 Comparison of the force-elongation between experiments and numerical simulations (tensile tests on round bars)

3.3 Summary

Due to the inhomogeneous deformation in conventional compression and tension test, the stress-strain relation for materials can only be obtained approximately. Several approximate engineering methods were presented. The stress-strain curve for Al2024-T351 was obtained from both compression tests and tensile tests using one of the approximate methods each. It will be shown in the following chapters that the stress-strain determined in this chapter gives good correlation.

By putting the two curves together as shown in Fig. 3.21, it is found that those two curves are not exactly the same although the specimens were cut from a same block. This phenomenon has also been found in the literature (eg. White et al. [105]) and industrial applications. This material inhomogeneity is likely caused by the rolling process.

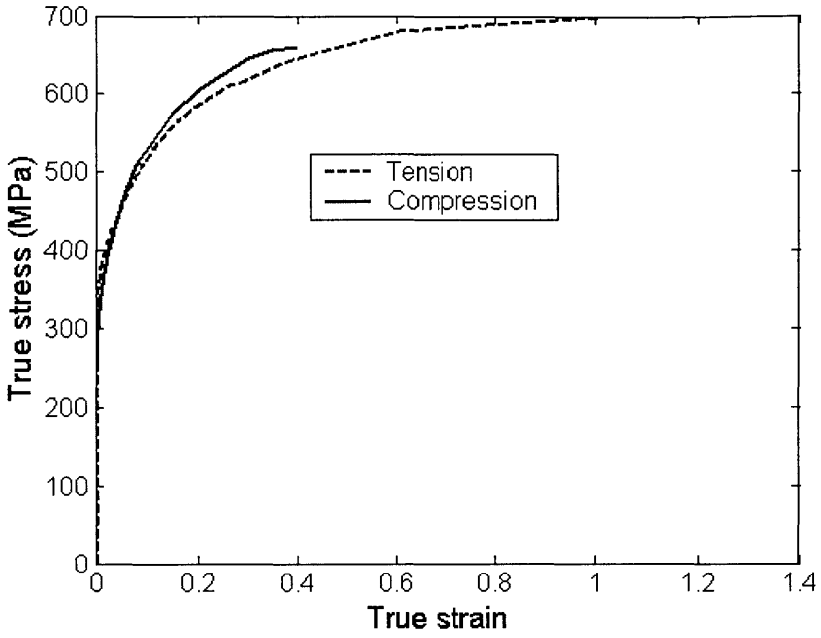

Fig. 3.21 Comparison of stress-strain curve obtained from tensile tests and compression tests

Chapter 4

Comparative Study of Various Fracture Models

Although various models based on different assumptions and different mechanical models have been proposed in the past to predict ductile crack formation, many of them such as porous plasticity fracture models, damage mechanics, decohering zone models, have not gone beyond the walls of academic institutions and found applications in industry. The crack formation criteria currently used in industry mostly are of an empirical nature or are based on models derived from the concepts of void nucleation, growth, and linkage. However, those criteria have not been critically evaluated and studied. In view of the complexity of crack formation mechanisms described in Chapter 2, it is difficult to expect a universal criterion capturing all the crack formation and clearly evaluation of those criteria is necessary. The objective of this chapter is to apply those crack formation models to some common tests to evaluate the range of their applicability.

4.1 Selection of Models

Since no universal crack formation criteria have been developed, engineers have been using different criteria. The crack formation criteria being used in industry mostly are the empirical models and the models derived from void nucleation, growth, and linkage. They are relative simple and easy to calibrate. Those criteria are postulated that fracture occurs at a point in a body when the scalar function reaches a critical value (Eq. (1.28)). Different weighting functions were proposed in different criteria.

Among those crack formation criteria, the criteria listed in Table 4.1 appear to be the more often cited in the literature.

Table 4.1 Functional forms of fracture criteria

Criterion	Formula
Equivalent strain	$\bar{\varepsilon} = \bar{\varepsilon}_f$
Cockcroft – Latham [68]	$\int_0^{\bar{\varepsilon}_f} \frac{\sigma_1}{\bar{\sigma}} d\bar{\varepsilon} = C_{CL}$
Hydrostatic stress	$\int_0^{\bar{\varepsilon}_f} \frac{\sigma_m}{\bar{\sigma}} \mathrm{d}\bar{\varepsilon} = C_H$
Clift [70]	$\int_0^{\bar{\varepsilon}_f} \bar{\sigma} d\bar{\varepsilon} = C_{Clift}$
Brozzo [69]	$\int_0^{\bar{\varepsilon}_f} \frac{2\sigma_1}{3(\sigma_1 - \sigma_m)} d\bar{\varepsilon} = C_B$
Rice-Tracey [17]	$\int_0^{\bar{\varepsilon}_f} \exp(\frac{3}{2}\frac{\sigma_m}{\bar{\sigma}}) d\bar{\varepsilon} = C_{RT}$
LeRoy [19]	$\int_0^{\bar{\varepsilon}_f} (\sigma_1 - \sigma_m) d\bar{\varepsilon} = C_L$
McClintock [3]	$\int_0^{\bar{\varepsilon}_f} [\frac{\sqrt{3}}{2(1-n)} \sinh(\frac{\sqrt{3}}{2(1-n)} \frac{\sigma_1 + \sigma_2}{\bar{\sigma}}) + \frac{3}{4} \frac{\sigma_1 - \sigma_2}{\bar{\sigma}}] d\bar{\varepsilon} = C_M$

* Note: A short description of the listed criteria is given in Chapter 1.

4.2 Selection of Tests

Ductile crack formation occurs in many tests such as upsetting, tension, shear, bending, torsion and deep drawing tests. As shown in Chapter 2, the crack formation mechanisms in upsetting tests and tensile tests are different. Also, upsetting tests and tensile tests have been studied by a number of engineers and are well defined (eg. [4, 6, 93, 106-108]). Those tests can be easily conducted in a standard universal testing machine. Therefore, those two types of tests are clearly good candidates to assess effectiveness and accuracy of existing crack formation criteria. A series of tests including upsetting tests on short cylinders with different aspect ratios and tensile tests on smooth and notched round bars were carried out. All the specimens were cut from a same block of Al2024-T351. The specimens prior to testing are shown in Fig.4.1. Parallel numerical simulations were also performed to obtain local individual components of stress and strain tensors, which are necessary for the evaluation.

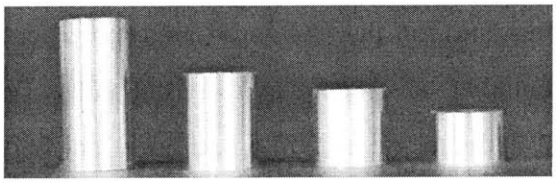

a) Upsetting specimens

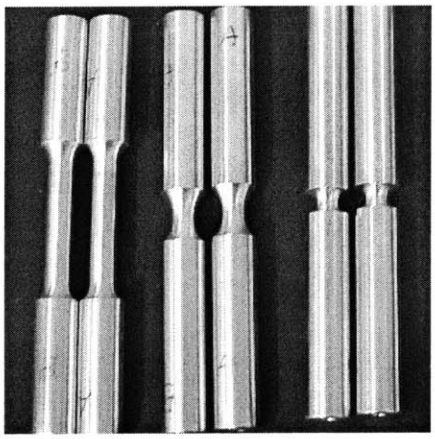

b) Tensile specimens

Fig. 4.1. Undeformed upsetting and tensile specimens

4.3 Upsetting

One of commonly used tests for studying crack formation is the uniaxial compression of short cylindrical specimens between flat platens (the so-called upsetting test). Because of the friction between specimens and flat platens, a barreling near the equator of specimens occurs. The resulting tensile circumferential stresses are developed causing specimens to fracture.

4.3.1 Experiments

Four types of cylindrical specimens with different aspect ratio were compressed between two flat compression platens in a 200kN MTS machine. Those cylinders had a same diameter of 12.5 mm but different heights. The initial aspect ratios d_0 / h_0 were 0.5, 0.8, 1.0 and 1.5, respectively. Six specimens each were compressed to different stages in order to capture crack formation at the equatorial area more accurately. As an example, Fig. 4.2 shows representative specimens at different stages of compression for the specimen with an initial diameter of 12.5 mm and an initial height of 12.5 mm. Force-displacement responses with the correction of test machine stiffness are shown in Fig. 3.7.

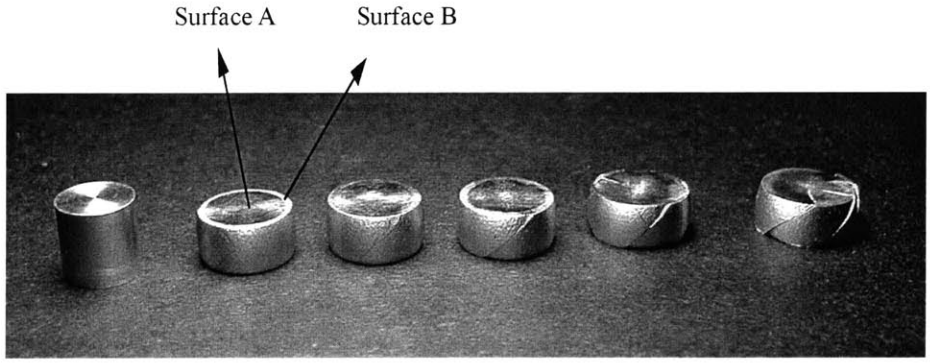

Fig. 4.2. Upsetting specimens at different stages of compression

4.3.2 Numerical Simulations

It is almost impossible to obtain individual components of stress and strain tensors, which are key factors in crack formation, directly from experiments. Performing numerical simulations is an alternative way to acquire individual components of stress and strain tensors at the locations of crack formation.

Parallel numerical simulations of the upsetting tests for crack formation were carried out using the finite element code ABAQUS. In finite element models, cylindrical specimens were modeled as 4-node axisymmetrical elements. The compression platens were modeled as two rigid surfaces. A surface-to-surface contact with friction was introduced to model the interaction between the platen and the specimen. A boundary condition was applied at the top platen while the bottom platen was fixed. The stress-strain curve shown in Fig. 3.10 was used as material input. Three different meshes were developed to study mesh sensitivity for each specimen. As an example, an evolution of equivalent plastic strain in the equatorial area from the three meshes shown in Fig. 4.3 for the specimen with initial diameter of 12.5 mm and initial height of 12.5 mm is illustrated in Fig. 4.4. The difference of the three meshes in stress and strain calculations was less than 2%.

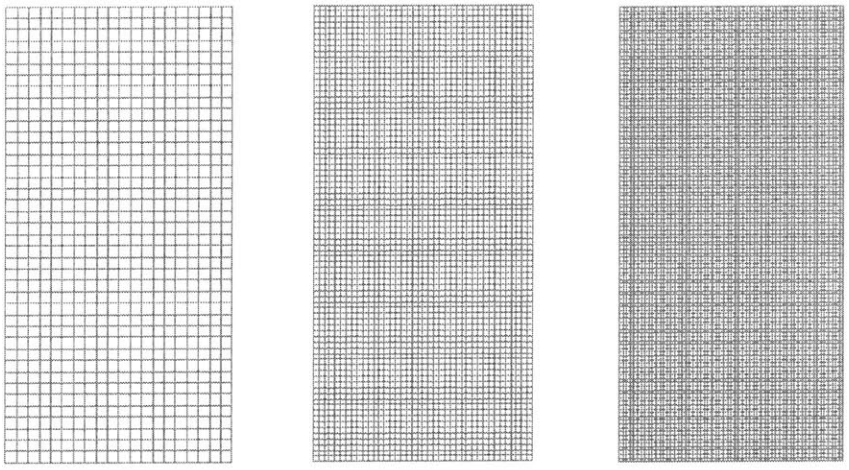

Coarse mesh (20*40) Medium mesh (40*80) Fine mesh1 (60*120)

Fig. 4.3 Three different meshes for upsetting tests (d_0 / h_0=1)

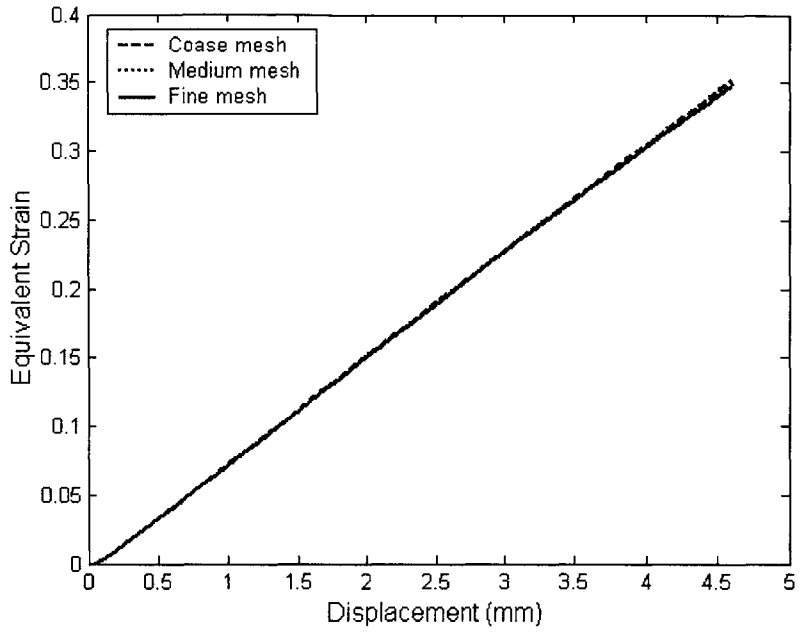

Fig. 4.4. Evolution of the equivalent plastic strain at the equatorial area (upsetting)

Friction coefficients between the platen and the specimen were determined by fitting the experimental and numerical results. From the deformed upsetting specimens depicted in Fig. 4.2, it can be found that the friction on surface A and surface B (outer ring), which originally is part of the circumferential surface, is different. Therefore, different friction coefficients were used to model the friction between platen and surface A and the friction between platen and surface B in numerical simulations. Numerical simulations with different combinations of friction coefficients of platen-surface A and platen-surface B were performed. The one with friction coefficient $\mu = 0.15$ for platen-surface A and $\mu = 0.5$ for platen-surface B gave best results. As an example, for the specimen with initial diameter of 12.5 mm and initial height of 12.5 mm at the onset of fracture ($\delta = 4.4$ mm, where δ is the displacement of top platen), the diameter of the equator was 15.67 mm and the diameter of the end of the specimen was 15.1mm in this numerical simulation, which were close to 15.75 mm and 15.1mm measured in the experiment, respectively. Correlation of the force-displacement responses as presented in Fig. 4.5 was also good. The deformation shape of those four specimens is shown in Fig. 4.6.

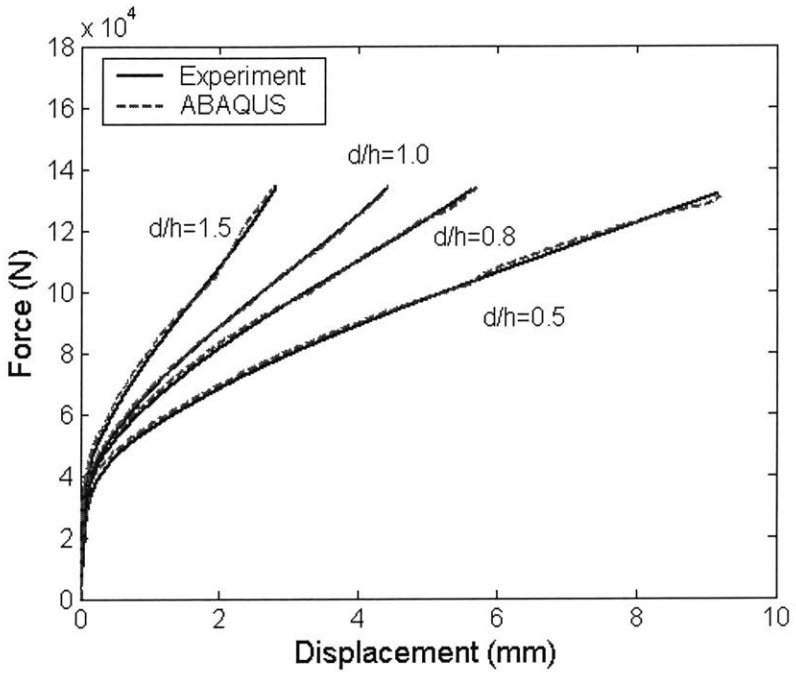

Fig. 4.5 Comparison of load-displacement response (upsetting tests)

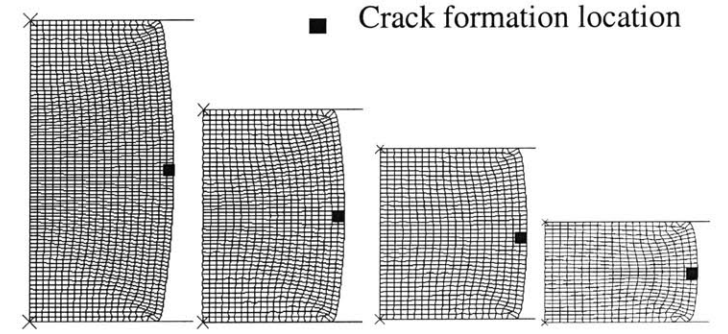

d_0 / h_0=0.5 d_0 / h_0=0.8 d_0 / h_0=1.0 d_0 / h_0=1.5

Fig. 4.6 Deformed shapes of upsetting specimens

4.4 Tension

4.4.1 Experiments

As shown in Fig. 4.1, besides standard smooth round specimens, tensile tests were also carried out on two different types of notched specimens. Round classical specimens with a 9 mm diameter gauge section and 25.4 mm gauge length and two different types of notched specimens with a same 8 mm minimum cross section and different notch radius 12 mm and 4 mm, were tested to get the information of crack formation in different stress states. As an example, the final stage of the test on the specimen with a 12 mm radius of notch is shown in Fig. 4.7. An extensometer was attached to measure the elongation of the gauge area during the experiment. Clearly, fracture occurred inside the gauge area. From the fractured specimens displayed in Fig. 4.8, it can be seen that fracture was due to void nucleation, growth and, linkage. Two samples of each case were tested and the results were repeatable. As an example, the force-displacement responses of two samples of the bar with 12 mm radius of notch are illustrated in Fig. 4.9. Not only the force level but also the crack formation point is the same.

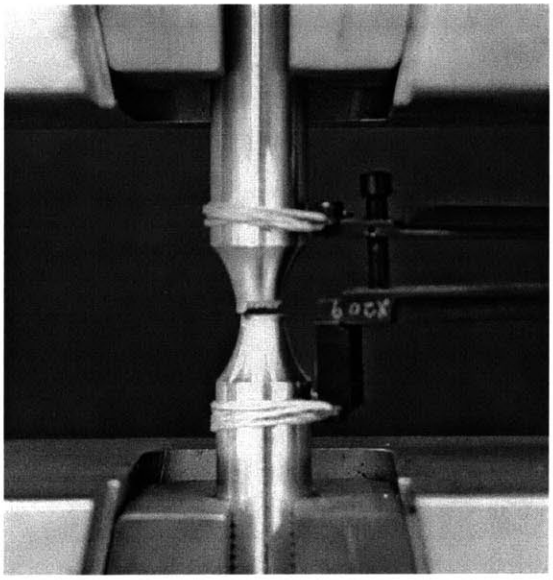

Fig. 4.7 Final stage of the test on the round bar with a 12 mm radius of notch

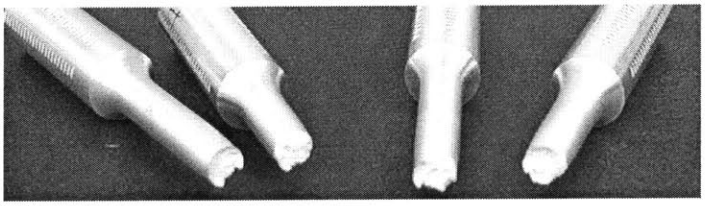

a) smooth standard round bar

b) notched bar (R =12 mm)

c) notched bar (R =4 mm)

Fig.4.8 Fractured tensile specimens showing dimple fracture

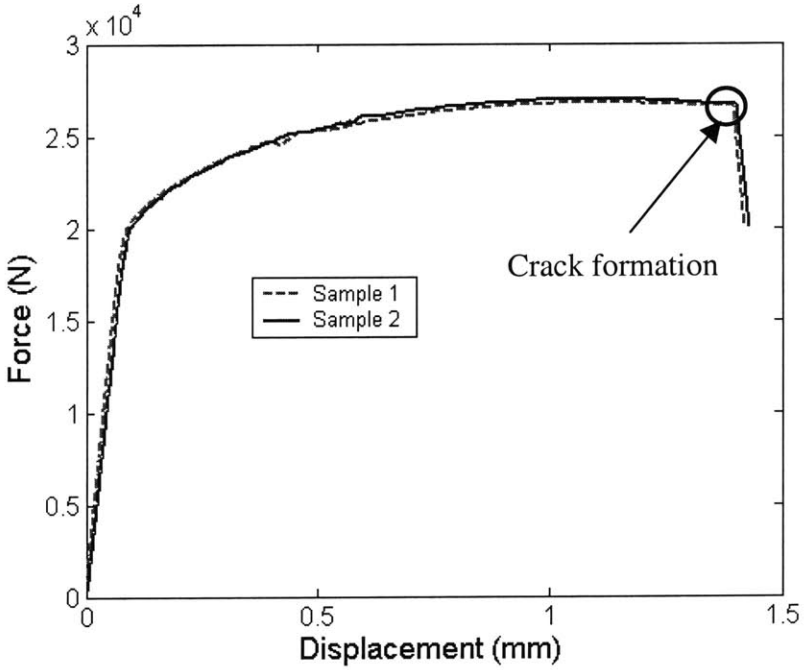

Fig.4.9 Responses of notched specimens (R =12mm)

4.4.2 Numerical Simulations

Detailed finite element modeling on the standard smooth round bar is given in Chapter 3. Finite element modeling on the two notched round bars was the same as the standard smooth round bar. The stress-strain curve shown in Fig.3.19 was also the material input for the two notched bars. In addition, two different meshes were developed for each specimen. Comparisons of equivalent plastic strain at center of the neck are illustrated in Fig.4.10-4.12, for smooth and two notched round bars, respectively. It clearly shows that the result presented here is not mesh dependent. Force-displacement responses of experiments and numerical simulations correlated almost perfectly as displayed in Fig. 3.20, Fig. 4.13 and Fig. 4.14. Only the responses up to the crack formation point are shown in the pictures since the present study focuses on crack formation. Determination of crack formation is given in Section 4.5. Final diameters of the minimum cross-section obtained from numerical simulations were 7.17mm, 6.9 mm and 7.2 mm for smooth and two notched round bars, respectively, which were very close to 7.2 mm, 6.8 mm and 7.15 mm measured from experiments. The deformed shape of the three tensile specimens is shown in Fig. 4.15.

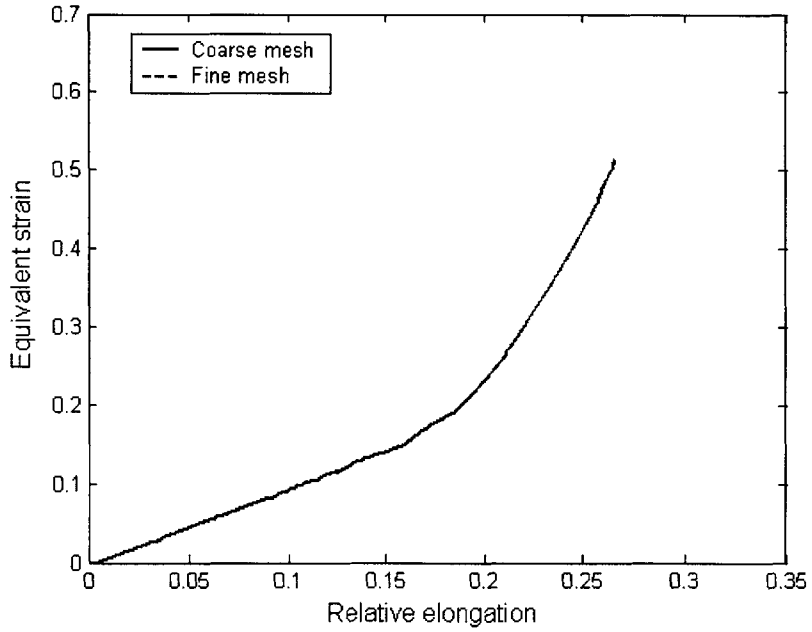

Fig. 4.10. Evolution of the equivalent plastic strain at the center of the neck (smooth)

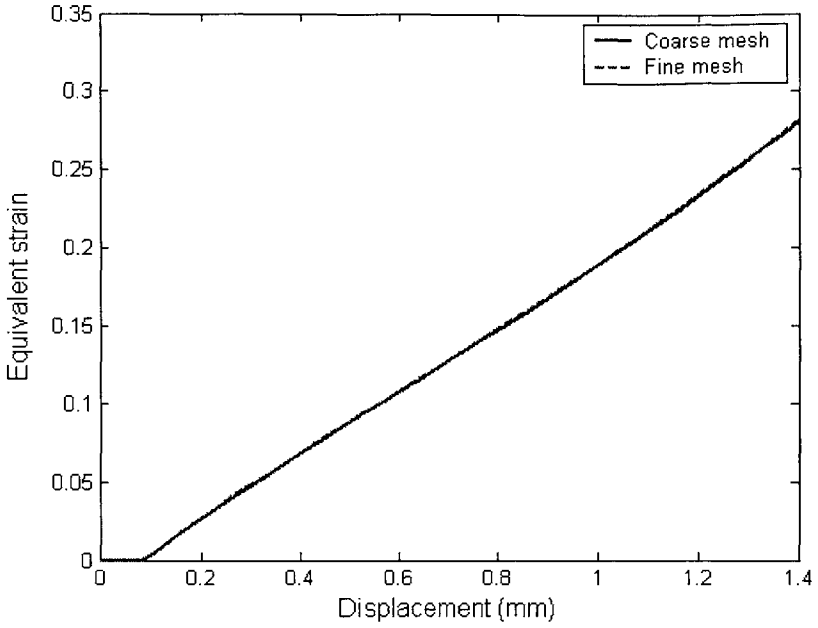

Fig.4.11 Evolution of the equivalent plastic strain at the center of the neck (R =12mm)

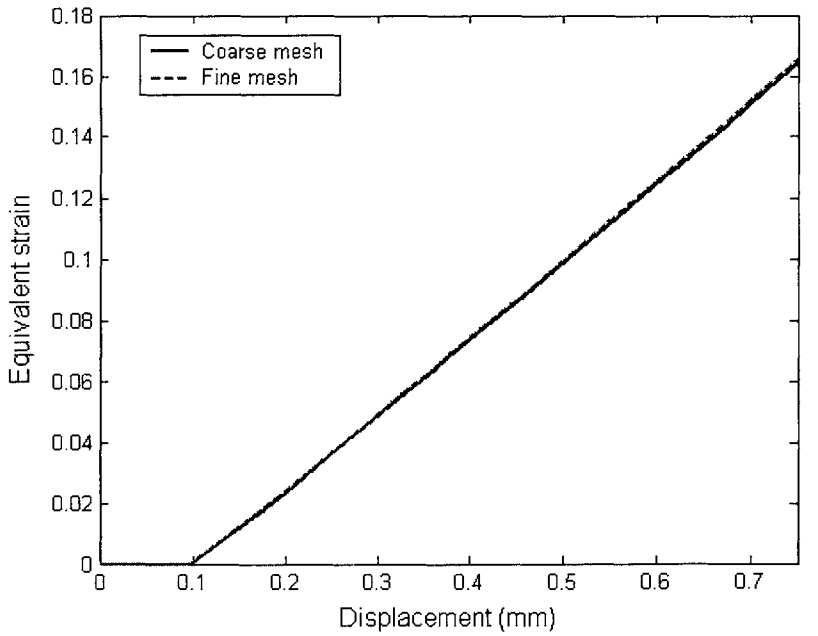

Fig.4.12 Evolution of the equivalent plastic strain at the center of the neck (R =4mm)

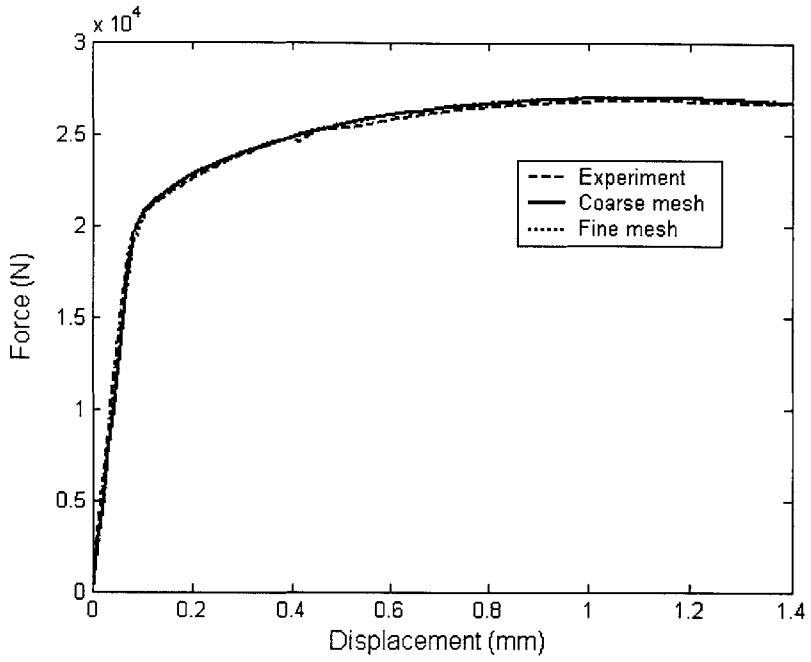

Fig.4.13 Response comparison of experiment and numerical simulations (R =12mm)

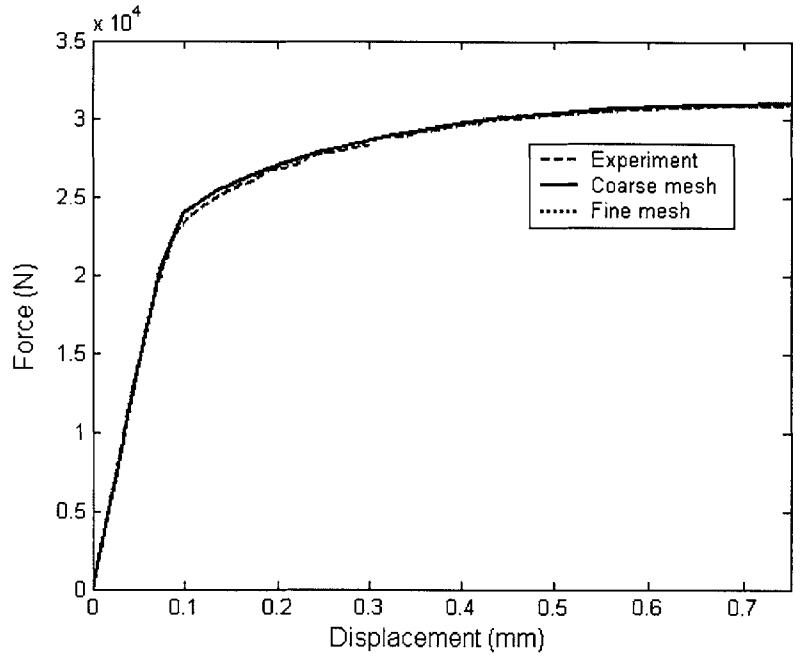

Fig.4.14 Response comparison of experiment and numerical simulations (R =4mm)

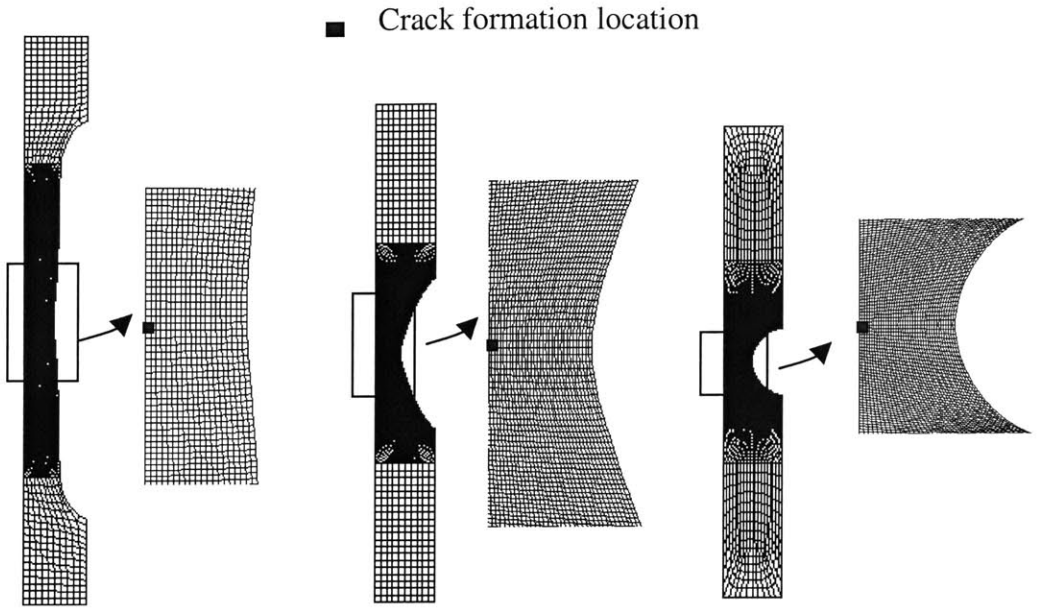

Fig. 4.15 Deformed shapes of tensile test specimens

4.5 Discussion

Since the correlation of the experimental and numerical results was almost perfect for all the cases considered in this study, it is reasonable to study the crack formation criteria based on the individual components of stress and strain tensors at locations of crack formation obtained from numerical simulations.

From tests, crack formation is indicated at the critical locations by the displacement to crack formation δ_f. It can be determined from both experimental observation and

numerical simulations. In the upsetting tests and tensile tests, the locations of crack formation are the equatorial area and the center of round bars, respectively. This observation was also reported by a number of other studies [4, 6, 13, 106]. There was a sudden load drop in the force-displacement responses in tensile tests (See Fig. 4.9)). This drop is taken as the point of crack formation in this study. However, this type of sudden drop in force level did not occur in some of the upsetting tests. Therefore, crack formation in upsetting tests is determined by observing the crack on the external surface of the equatorial area during the experiment. To do this, short cylinders were compressed to different stages and then were examined.

The criteria listed in Table 4.1 have the same form (Eq. (1.28)) which involves one material dependent constant for each criterion. The value of the left hand side of each criterion obtained from different tests at crack formation is taken as an indictor to assess the effectiveness of the various criteria. This value is determined by evaluating the integral of the fracture criteria at the locations of crack formation based on the results of numerical simulations and is summarized in Fig.4.16. Since the specimens tested in this thesis were cut from a same block of Al 2024-T351, the value of the left-hand side of each criterion obtained from different tests at crack formation should be the same if the criterion works well for all the tests. For example, the equivalent strain criterion indicates that crack formation is controlled only by the equivalent strain. When the equivalent strain $\bar{\varepsilon}$ reaches a critical value $\bar{\varepsilon}_f$ which is only dependent on material, crack formation occurs. If the equivalent strain criterion is a universal crack formation criterion, the equivalent strain at crack formation obtained from different tests on the same material should be the same.

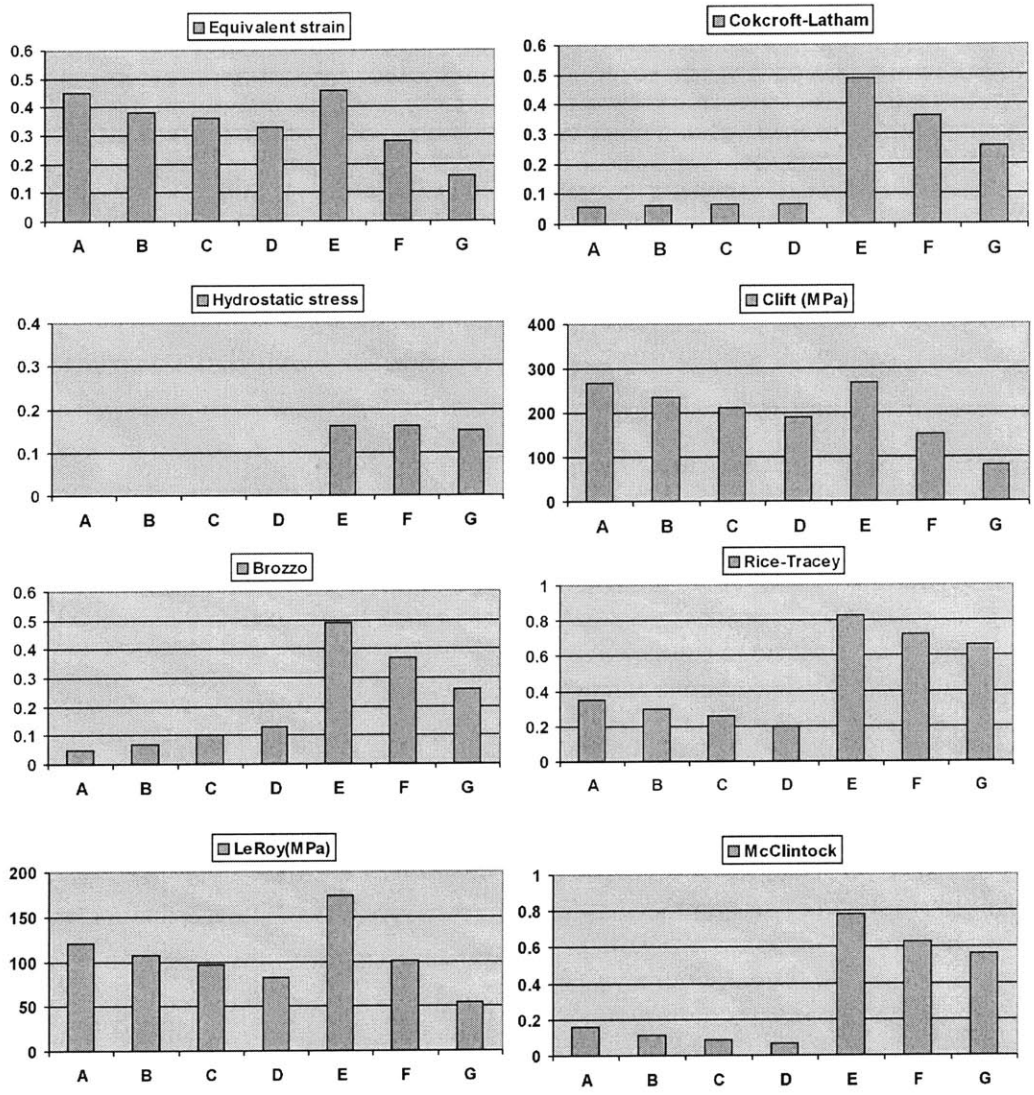

A: upsetting ($d_0 / h_0 = 0.5$), B: upsetting ($d_0 / h_0 = 0.8$), C: upsetting ($d_0 / h_0 = 1$), D: upsetting ($d_0 / h_0 = 1.5$), E: standard round, F: notched round (R=12 mm), G: notched round (R=4 mm)

Fig. 4.16 Material constants of fracture criteria for Al2024-T351

For all those crack formation criteria, the value of the left hand side of a single criterion obtained from the tests is not unique. The values are very different from case to case. The values of the Cockcroft-Latham and Brozzo criterion obtained from tensile tests on smooth specimens are 4-5 times larger than the corresponding ones from upsetting tests.

The values of the McClintock and Rice-Tracey criterion achieved from tensile tests on smooth specimens are 3-4 times larger than the ones from upsetting tests. The values of the equivalent strain criterion, Clift criterion and LeRoy criterion from tensile tests on smooth specimens are about 3 times larger than the corresponding values obtained from tensile tests on the specimens with 4 mm radius of circumferential notch. The hydrostatic stress criterion fails to predict fracture in upsetting tests since hydrostatic stress is negative at the crack formation location all the time in upsetting tests in this study. However, the values of the hydrostatic stress criterion from the tensile tests on smooth and two notched specimens are close, which means the hydrostatic stress criterion works well for the three tensile tests. The Cockcroft-Latham criterion is suitable for upsetting tests. Actually the Cockcroft-Latham criterion is equivalent to the experimental fracture locus of upsetting tests first reported in the literature by Kudo and Aki [6]. This will be shown analytically in Chapter 5. The McClintock and Rice-Tracey criterion give fairly good result for the two notched round bars. It is understandable since on one hand those two models were developed based on void nucleation, growth, and linkage which is the mechanism of crack formation occurred in these tensile tests, on the other hand those two models involve a lot of assumptions (See Chapter 2) which is hard to achieve in reality.

The strain to crack formation is to a large extent controlled by the stress triaxiality. In this chapter, the tests considered falls into a relatively wide range of the stress triaxiality. For the upsetting test, the stress triaxiality is –0.33 at the beginning (uniaxial compression state) and increases to near zero at the crack formation. The stress triaxiality is a constant of 0.33 before the necking (uniaxial tension state) for the tensile test on smooth specimens and increases to 0.5 at the crack formation. In the tensile tests on the two notched specimens, the stress triaxiality is approximately constant and is 0.65 and 0.95 for R =12 mm and R =4 mm, respectively.

It is recognized that crack formation could also be described in terms of other damage indicators as a different combination of stresses and strains. However, in view of the present results, the two different fracture mechanisms described in Chapter 2 and also the

results of others (eg. [70, 108-110]) it would appear that no single damage indicator could be devised covering the entire spectrum of the stress triaxiality.

As shown in the previous section, although none of the criteria studied in this paper gives consistent results for the wide range of the stress triaxiality, certain crack formation criteria work well for a more narrow range of the stress triaxiality. The hydrostatic stress criterion works quite well for the three tensile tests, which are in the range of high stress triaxiality. The Cockcroft and Latham criterion gives a good prediction of crack formation in upsetting tests, which are in the range of negative stress triaxiality. It should be noted that those two criteria are the same except the weighting functions. Therefore, different forms of weighting functions in Eq. (1.28) seem necessary and effective for a wide range of problems. They can be determined from different tests, which cover the entire range of the stress triaxiality. Clearly, the function for the range of negative stress triaxiality can be obtained by upsetting tests or the tests under hydrostatic pressures, while the function for the range of high stress triaxiality can be developed by tensile tests on notched specimens. The function for the range of intermediate stress triaxiality can be determined by suitable shear tests or tests under combined loadings. This is the main task of Chapter 5.

Chapter 5

A New Criterion for Ductile Crack Formation

5.1 Introduction

The mechanisms of ductile crack formation, as described in Chapter 2 are complex. Yet, there is an urgent need of relatively simple criteria for prediction of ductile crack formation in engineering applications. It has been shown in Chapter 4 that various empirical criteria and criteria based on void nucleation, growth, and linkage have a narrow range of applicability. It is the objective of this thesis to develop a relatively simple and general criterion with an acceptable degree of accuracy and a well defined calibration procedure.

All the tests reported in this study were performed under quasi-static loading and room temperature. The effect of strain rate and temperature is not considered. However, recent work by Hopperstad et al [111] and Teng and Wierzbicki [10] indicate that the strain rate dependence and temperature effects on crack formation are small in a steel and aluminum alloy, respectively.

In all cases considered in this chapter the loading was monotonic. It is recognized that in reality, the loading path of a material element might not be monotonic. Structures could experience unloading and even reverse loading. It is well known that Bauschinger effect, which is characterized by a reduced yield stress upon load reversal after plastic deformation has occurred during the initial loading, occurs during reverse loading. However, little work on the effect of reverse loading on ductile crack formation is reported in the literature. A pilot study on the effect of pre compression on ductile crack formation under tensile loading is carried out in Chapter 7.

5.2 A New Ductile Crack Formation Criterion

Ductile crack formation is a localized behavior. It is reasonable to postulate that crack formation occurs when damage accumulation, which is measured in terms of stresses and strains, reaches a critical value at a critical location. A general and widely accepted expression for ductile crack formation is presented in Eq. (1.28). Different integrands in Eq. (1.28) (called weighting functions) have been proposed in the past. Due to the different complex mechanisms described in Chapter 2 leading to ductile crack formation, functional dependence of the ductile crack formation criterion on the stress state can not be the same for all possible types of tests. However, by narrowing the range of applicability, good predictions have been obtained by introducing a suitable weighting function as shown in Chapter 4. Therefore, it is necessary and also effective to introduce different weighting functions for different stress and strain states. This is the main idea of the present chapter. Rather than working with individual components of the stress and strain tensor, crack formation is formulated in terms of the corresponding first and second invariants in this study. Thus, the number of parameters responsible for crack formation is reduced to three $(\sigma_m, \bar{\sigma}$ and $\bar{\varepsilon})$, i.e. the mean stress σ_m, the equivalent stress $\bar{\sigma}$ and the equivalent strain $\bar{\varepsilon}$ (Note that because of plastic incompressibility, the mean strain vanishes, $\varepsilon_m = 0$). There is overwhelming evidence that ductile crack formation strongly

depends on the stress triaxiality as mentioned in Chapter 2 from void growth studies (eg. [3, 17]), from empirical routines (eg. [69, 71, 72, 76, 77]) and from other experimental and numerical studies (eg. [4, 5, 78, 79]).

The general criterion (Eq. (1.28)) now reduces to

$$\int_0^{\bar{\varepsilon}_f} g(\frac{\sigma_m}{\bar{\sigma}})d\bar{\varepsilon} = C \tag{5.1}$$

By dividing both sides with the constant C, we can get

$$\int_0^{\bar{\varepsilon}_f} f(\frac{\sigma_m}{\bar{\sigma}})d\bar{\varepsilon} = 1 \tag{5.2}$$

In this thesis the integral is called damage indicator D. When it reaches unit, then crack formation occurs. It should be noted that this damage indicator D is different from the damage variable D_1 in damage mechanics described in Chapter 1. A good representation of the weighting function f clearly is

$$f(\frac{\sigma_m}{\bar{\sigma}}) = \frac{1}{\bar{\varepsilon}_f(\frac{\sigma_m}{\bar{\sigma}})} \tag{5.3}$$

Then Eq. (5.2) becomes

$$D = \int_0^{\bar{\varepsilon}_f} \frac{1}{\bar{\varepsilon}_f(\frac{\sigma_m}{\bar{\sigma}})} d\bar{\varepsilon} = 1 \tag{5.4}$$

The key point now is to find appropriate stress triaxiality dependence f of the damage increment or a fracture locus in the equivalent strain to fracture and the stress triaxiality space.

Studies of effect of stress triaxiality on equivalent strain to crack formation for metals performed in the past were mainly using pre-notched round tensile specimens. For example, Hancock and Mackenzie [4] carried out a series of tensile tests on pre-notched steel specimens. It was found that the ductility depends markedly on the triaxiality of the stress state. In their study, the stress triaxiality was calculated using the Bridgman's [78] formula (Eqs. (3.3) and (3.4)). The experimental results were correlated with the Rice-Tracey exponential function. Wierzbicki et al. [108] found that the following equation

$$\bar{\varepsilon}_f = \left(\frac{\sigma_m}{\bar{\sigma}}\right)^{\frac{5}{3}} \tag{5.5}$$

gives a better correlation with Hancock's experimental data than the Rice-Tracey criterion. However, those results should be revisited since the Bridgman formula does not give an accurate calculation of stress triaxiality and equivalent strain as shown in Chapter 3 and others (eg. [104, 109, 112]). Recently, Mirza et al. [79] performed an experimental and numerical study on three different materials (pure iron, mild steel and aluminum alloy BS1474) over a wide range of strain-rates (10^{-3}-10^{4} s^{-1}). The equivalent strain to crack formation for all three materials was found to be strongly dependent on the level of stress triaxiality. No significant effect of strain-rate could be ascertained from the experimental results provided fracture remains fully ductile. However, for mild steel, a transition to a brittle fracture mode was observed as the strain-rate was increased.

For lower stress triaxialities, Bridgman [78] performed a set of experiments on standard round bars under hydrostatic pressure for different steels. The stress triaxiality and equivalent strain were calculated from the approximate Bridgman formula. It was found that for some steels (eg. stainless steels and high carbon steels), the equivalent strain to crack formation increases with the hydrostatic pressure (decrease of the mean stress or the stress triaxiality) while for some steels (eg. SAE 1045) equivalent strain to crack formation decreases with the increase of hydrostatic pressure. Similar tests on a very ductile copper was carried out by French and Weinrich [5] in their study. The equivalent strain to crack formation calculated using the Bridgman formula was found increasing with the hydrostatic pressure. However, this type of tests cannot be done in a universe tensile machine and clearly needs a much more sophisticated facility with a pressure chamber.

Clearly, the community still lacks an effective and simple way to establish the relation of the equivalent strain to crack formation and the stress triaxiality. No such relation has been found for a single material in a wide range of the stress triaxiality.

5.2.1 Experimental Determination of Fracture locus

In this study, suitable configurations of specimens for the intermediate stress range are designed. Together with upsetting and tensile tests, totally 11 tests described in Fig. 5.1 on 2024-T351 aluminum alloy were performed in a universal test machine to find the relation of the equivalent strain to crack formation and the stress triaxiality in a relatively wide range of the stress triaxiality (-0.33~1.0). All the specimens were cut from a 6' long, 6" wide and 3" thick block of 2024-T351 aluminum alloy. The procedure is briefly described as follows.

1) Perform a series of tests and obtain force-displacement responses.
2) Perform parallel numerical simulations.
3) Determine from tests the location of crack formation and displacement to crack formation δ_f for each case.
4) Calculate evolution of the equivalent strain and the stress triaxiality at the crack formation location ($\bar{\varepsilon}$ vs. δ and $\sigma_m / \bar{\sigma}$ vs. δ) for each case.
5) Determine the equivalent strain to crack formation, the stress triaxiality and the average stress triaxiality for each case.
6) Plot the results from Step 5 in $\bar{\varepsilon}_f$-$(\sigma_m / \bar{\sigma})_{av}$ space and construct the limiting failure curve.

In all parallel numerical simulations, two or three different meshes with different mesh size were developed. It was found that the results including stress and strain obtained from different finite element models are the same (within 4%).

Test Number	Specimen description	Range of Stress triaxiality $\sigma_m / \bar{\sigma}$
1	Cylinder ($d_0 / h_0 = 0.5$)	-0.33 ~ -0.12
2	Cylinder ($d_0 / h_0 = 0.8$)	-0.32 ~ -0.05
3	Cylinder ($d_0 / h_0 = 1.0$)	-0.32 ~ -0.05
4	Cylinder ($d_0 / h_0 = 1.5$)	-0.32 ~ -0.05
5	Asymmetric	-0.4 ~ -0.09
6	Flat	0 ~ 0.02
7	Flat	0.04 ~ 0.15
8	Plate with a circular hole	0.33
9	Round, smooth	0.33 ~ 0.5
10	Round, large notch	0.6 ~ 0.7
11	Round, small notch	0.9 ~ 1

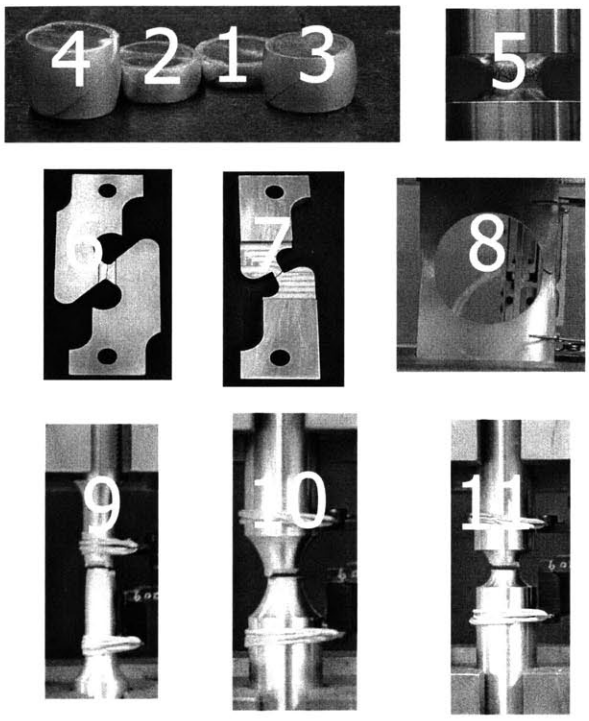

Fig. 5.1 A photograph of specimens used to calibrate Al2024-T351 for failure locus and ranges of triaxiality calculated in these tests.

5.2.1.1 Negative Stress Triaxiality

Axial compression of short cylinders (so-called upsetting tests) provides clues of ductile crack formation in the range of negative stress triaxiality. The barreling of the cylindrical surface furnishes considerable flexibility since barrel severity changes by altering the die contact friction conditions and cylinder aspect ratio d_0 / h_0. This leads to a variation of the tensile hoop stress at the bulge surface. Therefore, the upsetting tests can be utilized to provide a broad range of stress and strain sates in the equatorial area.

a) Conventional upsetting test

Compression of four short cylinders with different aspect ratios has been performed in Chapter 4. The stress triaxiality vs. equivalent strain at equatorial area, which is the crack formation location, is illustrated in Fig. 5.2. It can be seen that the stress triaxiality was negative all the time during the deformation.

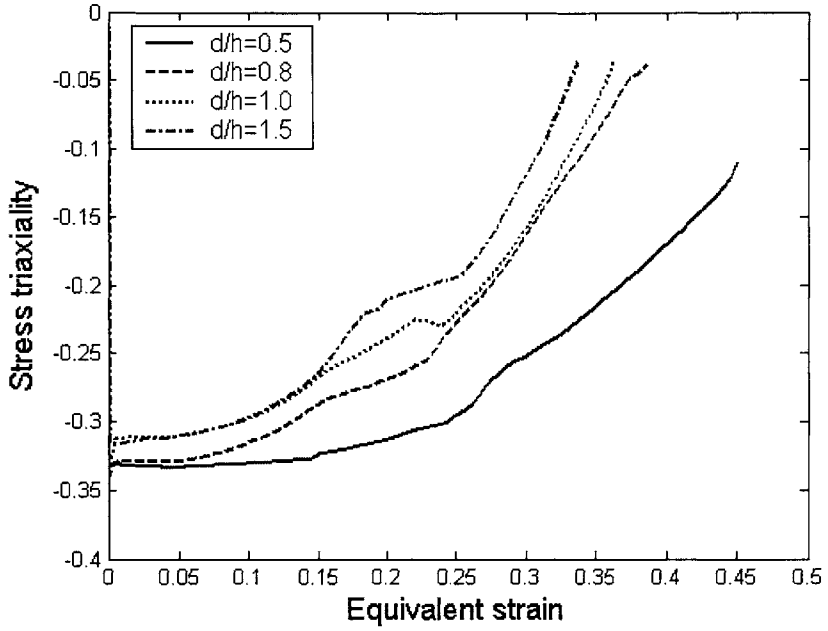

Fig. 5.2 The evolution of the stress triaxiality at equatorial area of upsetting tests

b) New compression test

Conventional upsetting tests involve a certain amount of friction between specimens and die platens. The presence of friction is responsible for the barrel effect and fracture, but it also brings difficulties and extra efforts in performing numerical simulations (See the numerical simulation in Chapter 4 for upsetting tests). A new promising type of compression specimen shown in Fig. 5.3 was designed and tested, which removed the undesirable effect of friction and still provided crack formation at the surface (Fig. 5.4).

The specimen was machined as round bars with a notched small gauge section in the middle. Crack formation also occurred at the equatorial area (Fig. 5.4). There was no deformation in the shoulders and hence there was no horizontal force acting on the ends of the specimen due to friction. In order words, friction did not play a role in the test with this particular design. Same as the upsetting tests, six specimens were tested to different stages to capture the crack formation point.

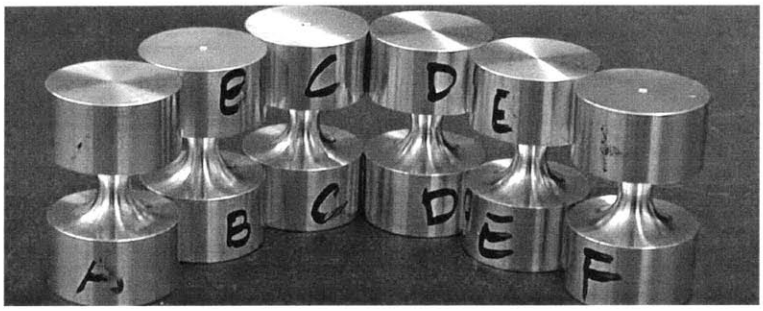

Fig. 5.3 A new configuration of compression test

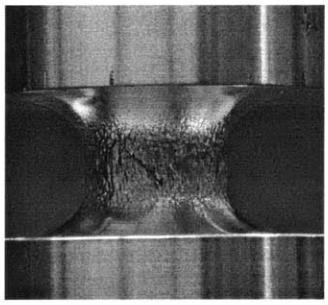

Fig. 5.4 A deformed new compression specimens showing crack formation at the surface

The finite element modeling for the new compression test was similar to the conventional upsetting tests. The specimen for the new compression test was also modeled as 4-node axisymmetrical elements. The compression platens were modeled as two rigid surfaces. Also, a surface-to surface contact was introduced to model the interaction between the platen and the specimen. A downward velocity boundary condition was applied at the top platen while the bottom platen was fixed. The deformed mesh is shown in Fig. 5.5. Three friction coefficients 0, 0.2 and 0.5 were introduced. Comparison of force-displacement response is displayed in Fig. 5.6. The stress triaxiality vs. equivalent strain at the crack

formation location is shown in Fig. 5.7. The correlation between experiment and numerical simulations were perfect. It clearly shows that finite element models with different friction coefficients gave the same result. This test was independent of the friction condition.

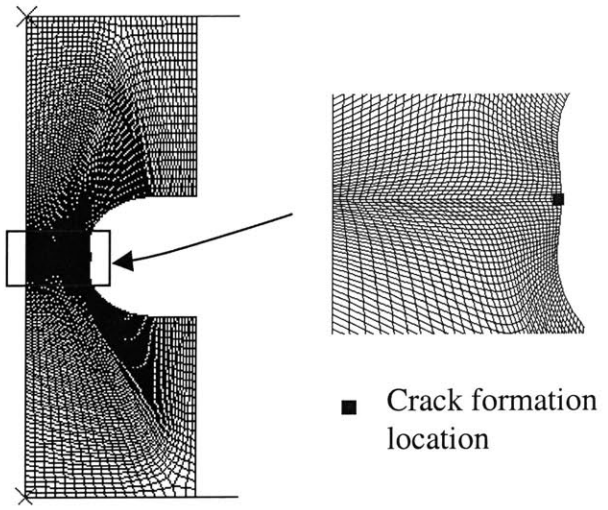

Fig. 5.5 Deformed shape of the new compression test

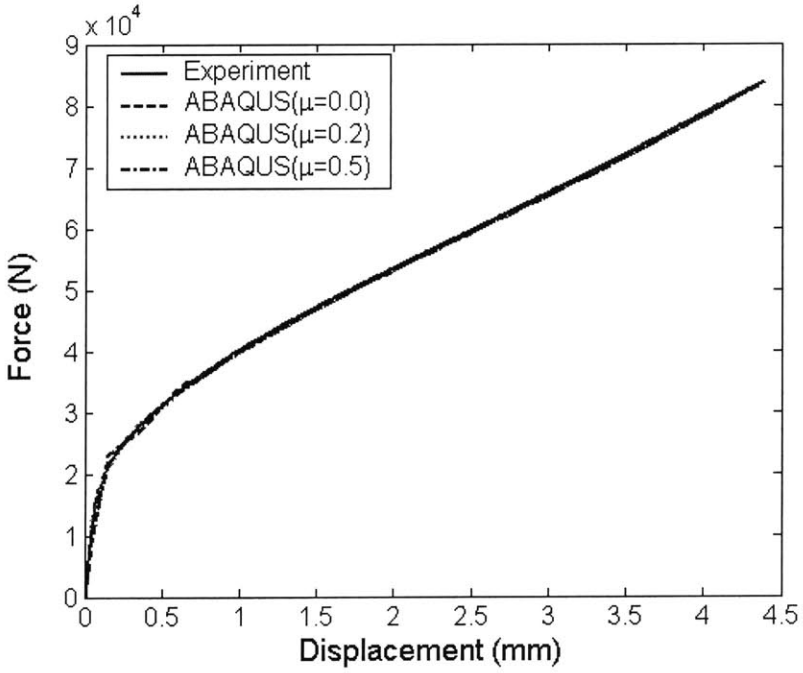

Fig. 5.6 Comparison of force-displacement (new compression test)

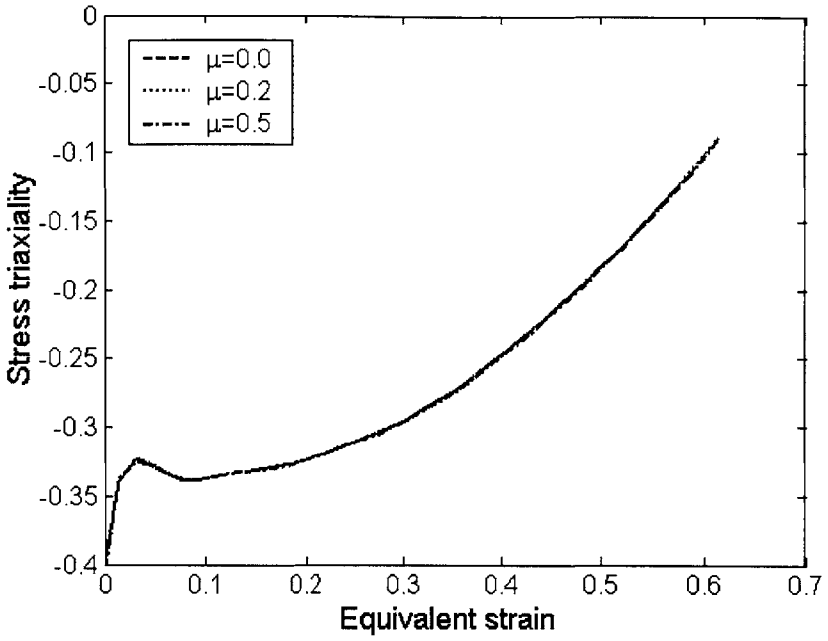

Fig. 5.7 The stress triaxiality vs. equivalent strain at the critical location of the new compression tests

5.2.1.2 Intermediate Stress Triaxiality

Acquiring reliable data in the range of intermediate triaxiality has been a challenging task. The responses of the specimen and in particular the magnitudes of local stresses and strains depend to a large extent on the shape of the free boundary. Thus, the first and substantial task is to design the shape of the specimens so that fracture will start inside rather than at the free edge of the test piece.

a) Pure shear test

A pure shear test is understood as the one in which the mean stress is zero or very small compared to the equivalent stress at locations of crack formation. In a search for the "best" shear test, a new specimen configuration illustrated in Fig. 5.8(a) was proposed

based on the concept of a "butterfly" gauge section. The specimen was pulled through two pins. Fractured specimen is displayed in Fig. 5.8(b), from which it can be seen that fracture occurred due to "shear". It was observed that crack formation occurs at point A shown in Fig. 5.8(b).

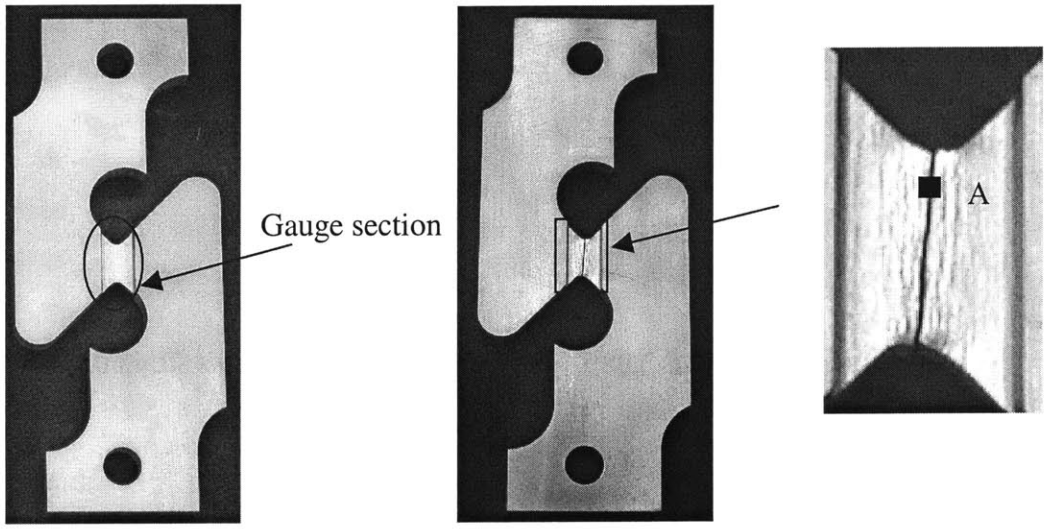

a) undeformed specimen b) fractured specimen

Fig. 5.8 A new specimen configuration of pure shear tests

Shell elements were used to model the pure shear test specimen. Two pins were model as rigid surfaces. A node-surface contact was introduced to model the interaction between the pin and the specimen. An upward velocity boundary condition was applied at one pin while another one was fixed. The deformation shape is shown in Fig. 5.9, from which it can be seen that plastic deformation was localized in the "butterfly" section. Comparison of the force-displacement response is displayed in Fig. 5.10. The correlation was almost perfect. The stress-triaxiality was less than 2% at the crack formation location during the plastic deformation (See Fig. 5.11). Therefore, this test can be taken as a pure shear test.

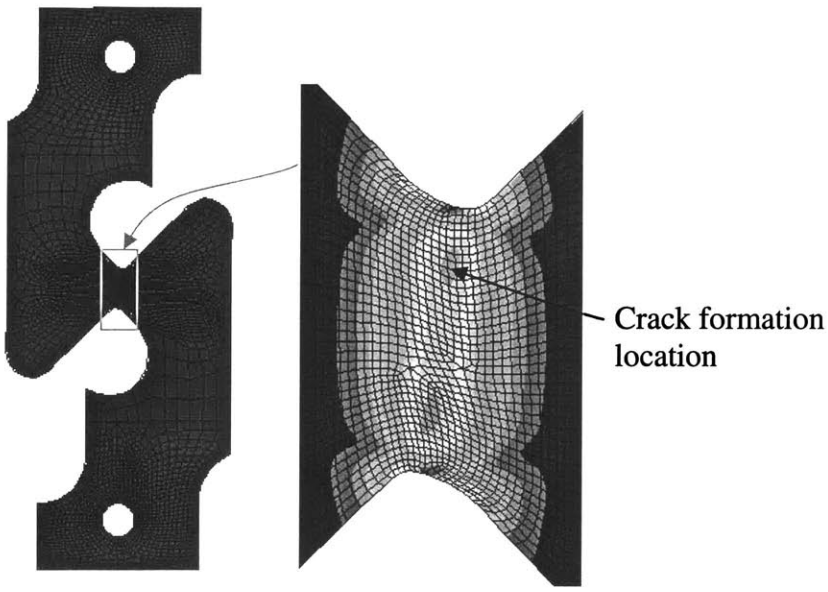

Fig. 5.9 Deformation shape of pure shear test (Equivalents strain distribution)

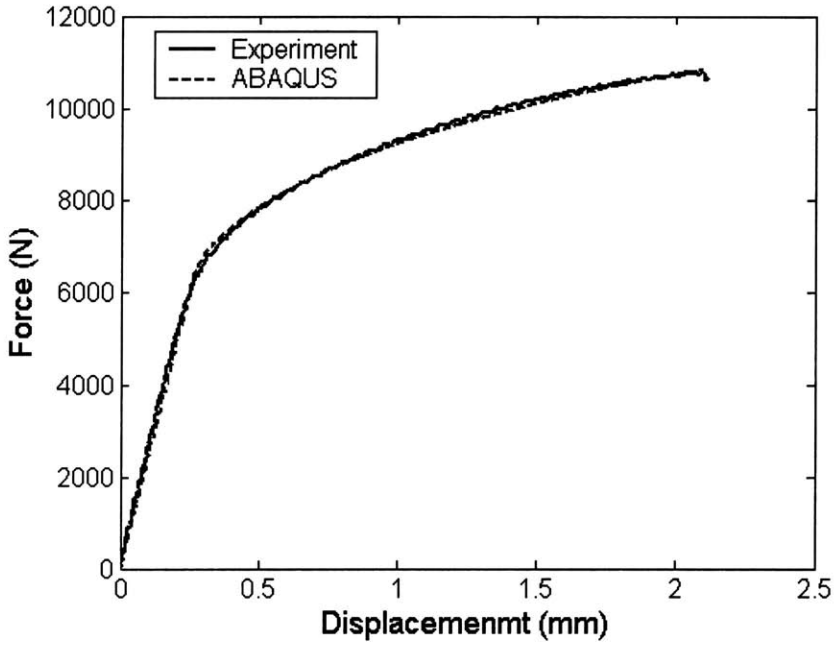

Fig. 5.10 Comparison of force-displacement response (pure shear test)

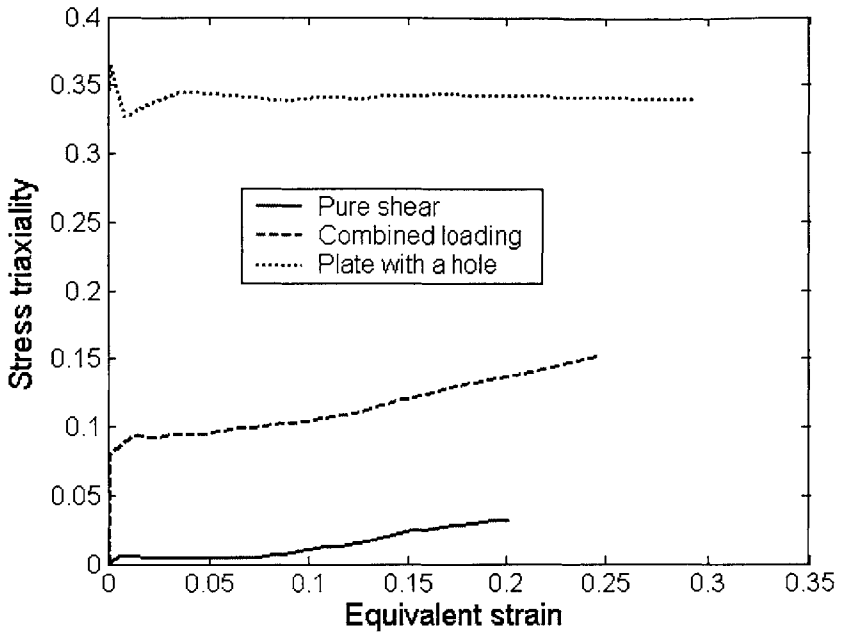

Fig. 5. 11 The stress triaxiality vs. equivalent strain of the tests in the intermediate stress triaxiality range

b) Test under combined loading

A specimen configuration for combined shear and tension loading shown in Fig.5.12 (a) was developed such that it provides information on crack formation in the range between pure shear tests and tensile tests. Similarly in the case of the pure shear test, the specimen was pulled through two pins. The gauge section was obviously under a combined shear and tension loading. It was observed that crack formation occurs at point B shown in Fig. 5.12(b). The finite element modeling was the same as the pure shear test. The deformation shape is shown in Fig. 5.13. Plastic deformation was localized in the small gauge area. Comparison of the force-displacement response is displayed in Fig. 5.14. The correlation was also quite good. The stress-triaxiality was between 0.1 and 0.15 at the crack formation location during the plastic deformation (See Fig. 5.11).

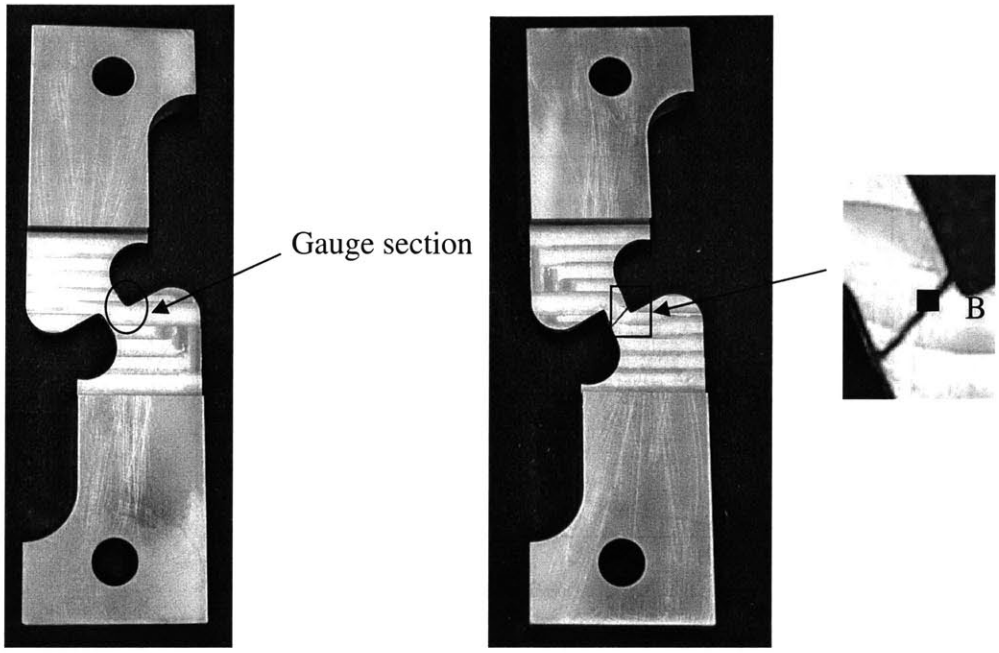

a) undeformed specimen b) fractured specimen

Fig. 5. 12 A new specimen configuration of tests under combined loading

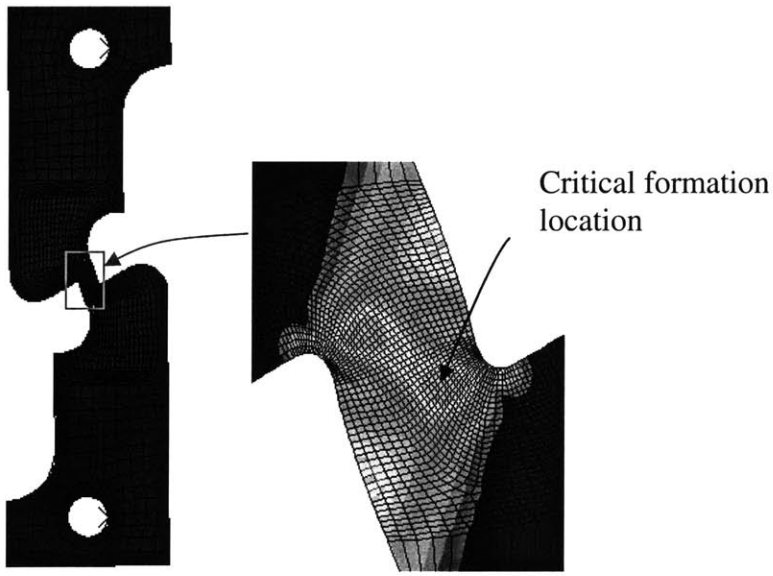

Fig. 5.13 Deformed shape of the combined loading test (Equivalent strain distribution)

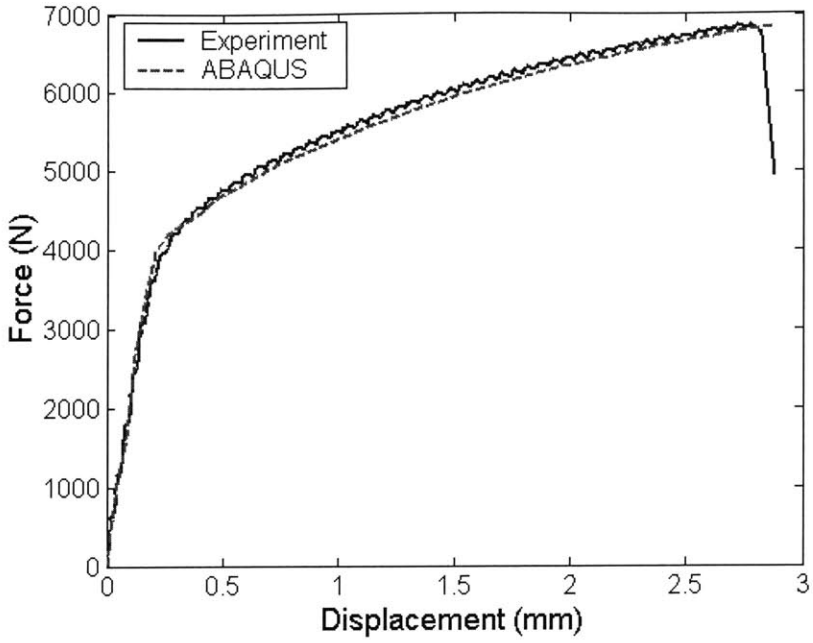

Fig. 5.14 Comparison of force-displacement response (combined loading test)

c) Test on plates with a circular hole under tensile loading

A plate with 4 mm thick, 50 mm wide and 20 mm radius of the hole in the middle subjected to tensile load as displayed in Fig. 5.15 was carried out experimentally and numerically. Crack formation occurred at the middle of the circumferential surface of holes perpendicular to the load.

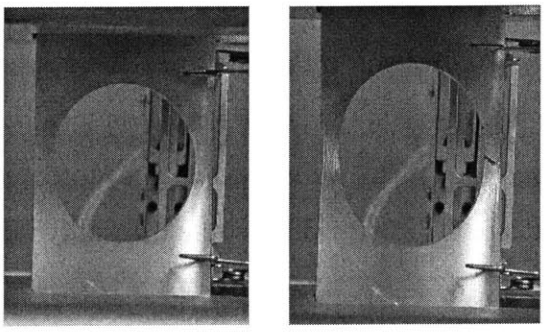

Fig. 5.15 Initial and final deformed shapes of tensile tests on a plate with a circular hole under tensile loading

The specimen was modeled as 8-node solid elements. A finite velocity was applied to one end of the model while the other end was fixed. Deformed configuration from the experiments and the numerical simulation is displayed in Fig. 5.16. Comparison of the force-displacement is shown in Fig. 5.17. Correlations of the experiment and the numerical simulation are almost perfect. The point of crack formation experienced a constant stress-triaxiality of 0.33 during the entire plastic deformation (See Fig. 5.11).

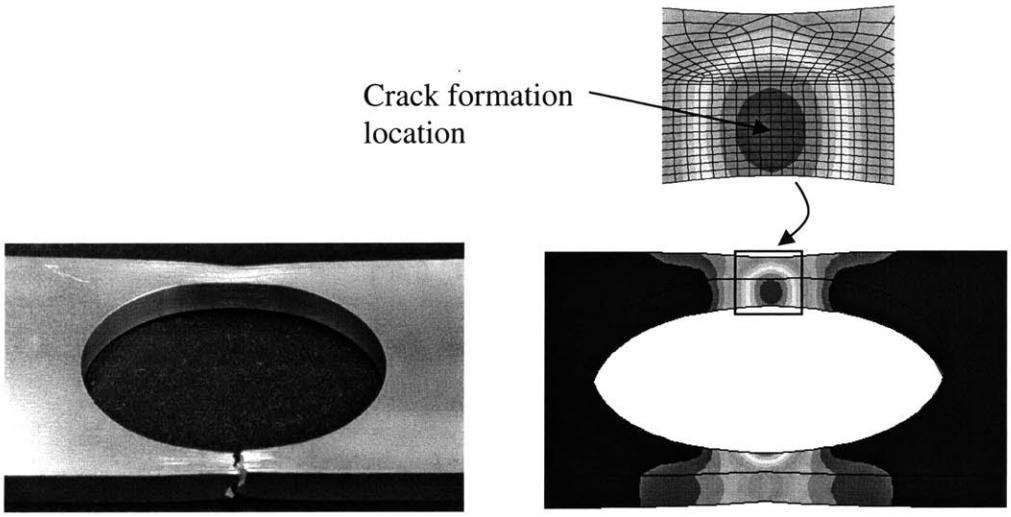

a) experiment b) solid element (Equivalent strain distribution)

Fig. 5.16 Comparison of deformed shapes from experiments and numerical simulations (tensile tests on a plate with a circular hole under tensile loading)

The three different types of tests for the intermediate stress triaxiality range gave relatively constant stress triaxiality at the crack formation location (Fig. 5.11). Cleary the configurations of the three specimens were good choices to determine the fracture locus and the weighting function in the intermediate stress triaxiality range.

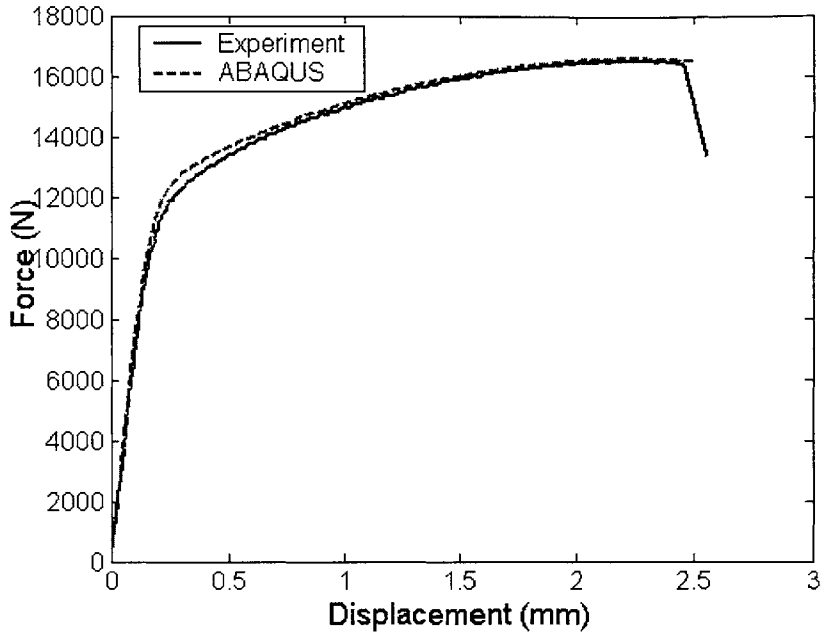

Fig. 5.17 Comparison of load-displacement response
(tensile test on plates with a circular hole)

5.2.1.3 High Stress Triaxiality

Finally, tensile tests on three different specimens were performed for the determination of the limiting curve. Detailed results of experiments and numerical simulation of those three tests have been described in Chapter 4. The stress triaxiality vs. equivalent strain at the crack formation locations is illustrated in Fig. 5.18.

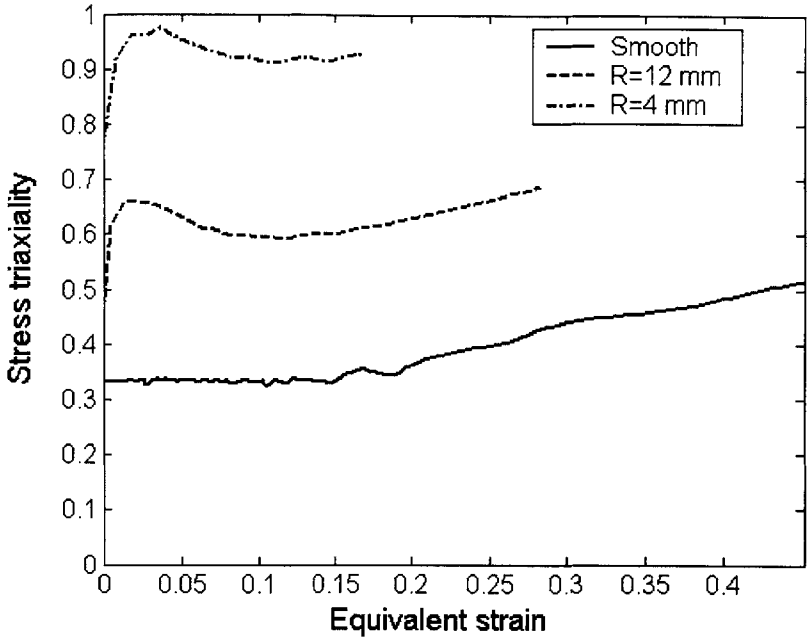

Fig. 5.18 The stress triaxiality vs. equivalent strain at the crack formation locations in tensile tests

5.2.1.4 Fracture Locus

Since the correlation of the experimental and numerical results was almost perfect for all the 11 cases for determination of fracture locus, it is reasonable to establish the fracture locus based on the individual components of stress and strain tensors at crack formation locations obtained from numerical simulations.

Crack formation is fully described by critical locations and the displacement to crack formation δ_f. Same as the Chapter 4, in the tensile tests and the tests for intermediate

stress triaxialities, the displacement to crack formation δ_f is determined as the displacement corresponding to the sudden drop, while the displacement to crack formation δ_f is determined by observation in the upsetting and the new compression tests. The numerical simulations provide stress and strain components and also load-displacement response. The relationship of displacement and equivalent strain at the critical location can also be obtained from the numerical simulations for each case. Then, the equivalent strain to crack formation is determined as the equivalent strain which corresponds to the displacement to crack formation δ_f as shown in Fig. 5.19 for the pure shear test as an example.

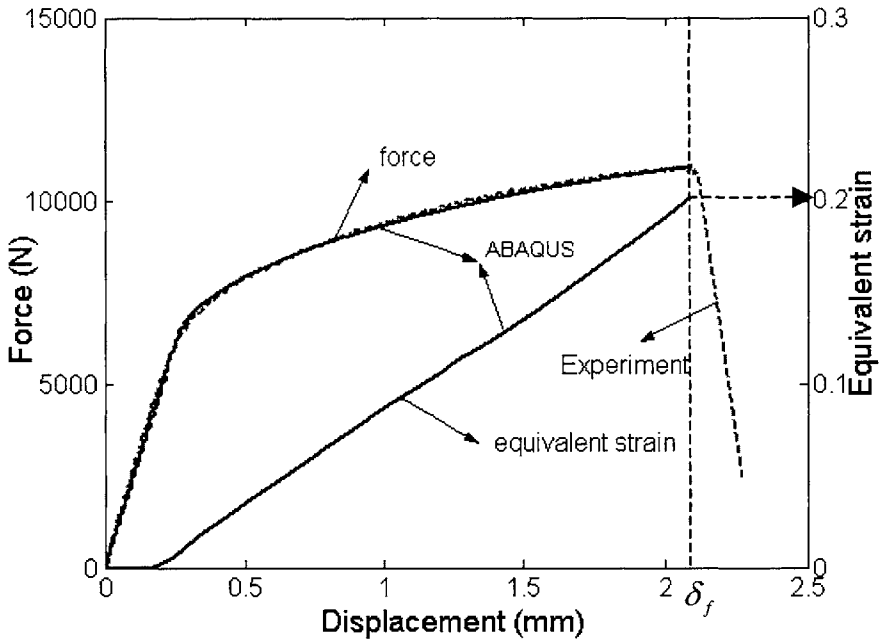

Fig.5.19 Comparison of the experimental and numerical load-displacement response and growth of the equivalent strain at the crack formation location (shear test)

The stress triaxiality at the critical location during the deformation is not strictly constant. An average value $(\frac{\sigma_m}{\bar{\sigma}})_{av} = \frac{1}{\bar{\varepsilon}_f}\int_0^{\bar{\varepsilon}_f} \frac{\sigma_m}{\bar{\sigma}} d\bar{\varepsilon}$ is taken as a first approximation. The coordinate of the relative point on the fracture locus of the pure shear test is then (0.0,

0.2). A similar procedure is then repeated for the remaining ten points on the failure diagram, shown in Fig. 5.20. It can be clearly seen that equivalent strain to crack formation differs significantly for specimens under different stress triaxialities. In the range of negative stress triaxiality, the equivalent strain to crack formation decreases with the stress triaxiality and reaches a minimum of 0.2 at the stress triaxiality $(\sigma_m / \bar{\sigma})_{av} = 0$, which corresponds to the pure shear test. Then it increases in the intermediate stress triaxiality range with the stress triaxiality and reaches a peak of 0.45 at the stress triaxiality $(\sigma_m / \bar{\sigma})_{av} = 0.4$ which corresponds to the tensile test on smooth specimen. Finally, it decreases again with the stress triaxiality in the range of high stress triaxiality. There are a sufficient number of points on Fig. 5.20 to be able to develop an analytical representation of the fracture locus. It clearly shows that one function is not enough to cover the whole range.

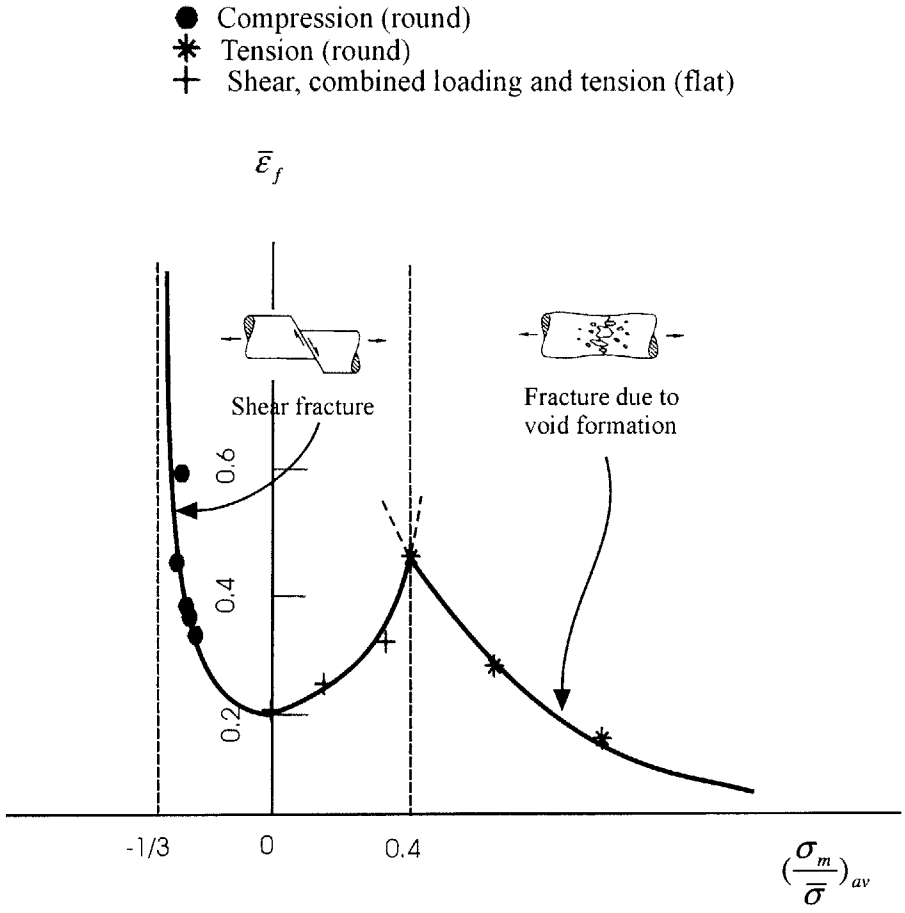

Fig. 5.20 Dependence of the equivalent strain to crack formation on the stress triaxiality

The existence of the three ranges of stress triaxiality has so far been qualitative. From Fig. 5.20, the boundary of the stress triaxiality ranges for Al 2024-T351 can be found. Clearly the negative stress triaxiality range is defined as $(\sigma_m / \bar{\sigma})_{av} < 0$ and the intermediate stress triaxiality range is defined as $(\sigma_m / \bar{\sigma})_{av} = 0 \sim 0.4$ while the high stress triaxiality range is defined as $(\sigma_m / \bar{\sigma})_{av} > 0.4$. It should be noted that the above boundaries for stress triaxiality range is only for Al2024-T351. The boundary of the stress triaxiality ranges would depend on materials.

5.2.2 Theoretical Determination of Fracture Locus from Upsetting

Ductile crack formation in upsetting tests was studied experimentally first by Kudo and Aoi [6]. The results were later confirmed and extended by a number of others (eg. Kuhn and Dieter [106], Thomason [113, 114], Ganser et al. [115]). Local strains were determined in the tests by means of small grid markings at the mid-height of the cylindrical surface shown in Fig. 5.21. A short summary of the experiment is given as follows.

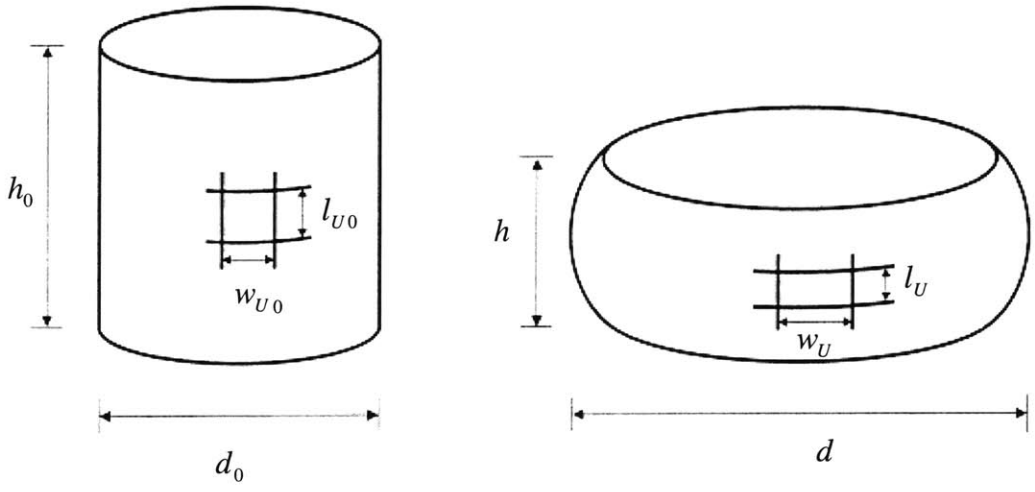

Fig.5.21 Small grid markings to measure strains in upsetting tests

Measurements of the grid dimensions at various stages of the test permitted calculation of the principal strains, strain increments, and strain histories. The logarithmic surface strains in the cylindrical coordinate system (r, θ, z) shown in Fig. 5.22 were

$$\varepsilon_{\theta\theta} = \ln \frac{w_U}{w_{U_0}} \tag{5.6}$$

$$\varepsilon_{zz} = \ln \frac{l_U}{l_{U_0}} \tag{5.7}$$

where l_{U0} and l_U are initial and current vertical grid spacing, w_{U0} and w_U are initial and current circumferential grid spacing.

The incompressibility condition gives the radial strain ε_{rr}

$$\varepsilon_{rr} = -(\varepsilon_{\theta\theta} + \varepsilon_{zz}) \tag{5.8}$$

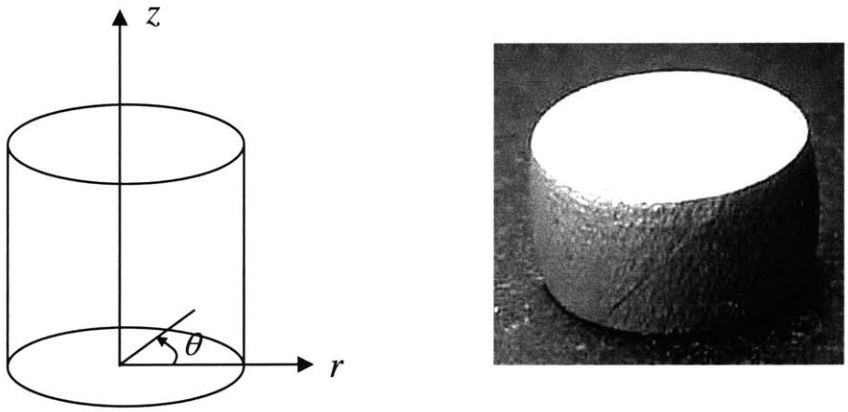

Fig.5.22 A cylindrical coordinate system and a photograph of a crack produced by the secondary hoop tension in the equatorial region of the specimen

The point of crack formation was determined by observing crack formation near equator. Note that crack formation in upsetting tests occurred in the equatorial region on the outer

surface of the specimens. It is interesting that the failure locus determined by many authors was always represented as a straight line (Eq. (5.9)) in the space of $\{\varepsilon_{\theta\theta}, \varepsilon_{zz}\}$ independent of the material, friction coefficient, and the height to diameter ratio of the cylinders.

$$\tilde{\varepsilon}_{\theta\theta} + \frac{1}{2}\tilde{\varepsilon}_{zz} = C_U \tag{5.9}$$

where $\tilde{\varepsilon}_{\theta\theta}$ and $\tilde{\varepsilon}_{zz}$ are components of the strain tensor at the point of crack formation in the hoop and axial direction, respectively, C_U is a constant depending on materials

However, the loading trajectory in the strain space depended on the friction condition and the aspect ratio of specimens as illustrated in Fig. 5.23 from Kudo and Aoi's study [6] on a steel. Short cylinders of Al 2024-T351 with different aspect ratio in this study were also compressed, which was extensively reported in Chapter 4. As shown in Fig. 5.24, the failure locus of Al2024-T351 also falls into Eq. (5.9). It clearly indicates that the failure locus is independent of materials.

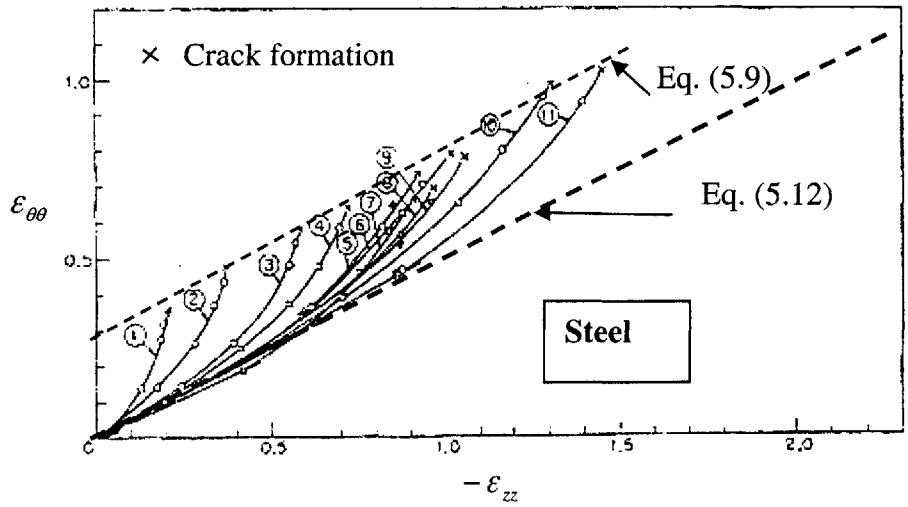

Fig. 5.23 Strain path in the region of potential crack formation for various aspect ratios and friction coefficient and a limiting straight line failure locus
(after Kudo and Aoi [6])

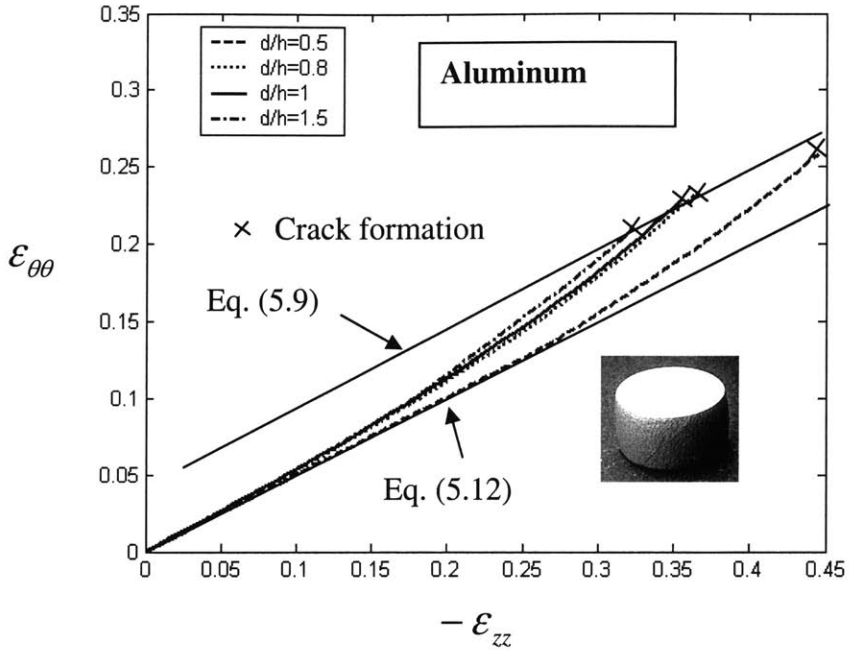

Fig. 5.24 Strain path in the region of potential crack formation for various aspect ratios and a limiting straight line failure locus in Al 2024-T351

When there is no friction between die surfaces and cylinders, no barreling will develop and the compression will be homogenous. The strains at the lateral surface of cylinders are then uniform. The relation between the hoop and axial strain can be found from volume conservation (See Eq. (3.2)).

Thus,

$$\frac{h_0}{h} = (\frac{d}{d_0})^2 \tag{5.10}$$

Taking the logarithm of both sides of Eq. (5.10), we have

$$\ln\frac{h_0}{h} = 2\ln(\frac{d}{d_0}) \tag{5.11}$$

This gives,

$$\varepsilon_{\theta\theta} + \frac{1}{2}\varepsilon_{zz} = 0 \tag{5.12}$$

By comparing Eq. (5.9) for the compression with barreling and Eq. (5.12) for the compression without barreling, one can find that the barreling effect is essentially responsible for a departure of strain trajectories from the straight line given by Eq. (5.12).

It should be noted that $\tilde{\varepsilon}_{\theta\theta}$ and $\tilde{\varepsilon}_{zz}$ in Eq. (5.9) are the "ultimate" values of strain at crack formation. They should be distinguished from the current values $\varepsilon_{\theta\theta}$ and ε_{zz} so that the final accumulated strains are

$$\tilde{\varepsilon}_{\theta\theta} = \int d\varepsilon_{\theta\theta}$$
$$\tilde{\varepsilon}_{zz} = \int d\varepsilon_{zz} \tag{5.13}$$

Clearly, the radial stress σ_{rr} is zero at the outer surface of cylinders because of zero surface traction. The shear stress σ_{rz} vanishes due to symmetry. Also, the radial gradient $\frac{\partial}{\partial r}$ of all quantities is negligible in the equatorial region, so the stress state is essentially plane stress in the equatorial region. Also, shear components of the stress and strain tensors and their rate tensors vanish because of rotational symmetry.

With the approximate plane stress and the absence of shear components, the yield condition becomes

$$\sigma_{\theta\theta}^2 - \sigma_{\theta\theta}\sigma_{zz} + \sigma_{zz}^2 = \bar{\sigma}^2 \tag{5.14}$$

Inverting the Levy-Mises flow rule and neglecting the elastic deformation one can show that all the remaining components of the stress tensor can be expressed in terms of the strain rate ratio α.

$$\sigma_{\theta\theta} = -\frac{2}{\sqrt{3}}\bar{\sigma}\frac{\alpha+\frac{1}{2}}{\sqrt{1+\alpha+\alpha^2}} \tag{5.15}$$

$$\sigma_{zz} = -\frac{2}{\sqrt{3}}\bar{\sigma}\frac{1+\frac{\alpha}{2}}{\sqrt{1+\alpha+\alpha^2}} \tag{5.16}$$

$$\sigma_m = -\frac{1}{\sqrt{3}}\bar{\sigma}\frac{1+\alpha}{\sqrt{1+\alpha+\alpha^2}} \tag{5.17}$$

and

$$d\bar{\varepsilon} = \frac{2}{\sqrt{3}}\sqrt{1+\alpha+\alpha^2}\,d\varepsilon_{zz} \tag{5.18}$$

where

$$\alpha = \frac{d\varepsilon_{\theta\theta}}{d\varepsilon_{zz}} \tag{5.19}$$

Introducing now Eq. (5.13) and (5.19) into the failure locus (Eq. (5.9)), Eq. (5.9) is then transformed to

$$\int(\alpha+\frac{1}{2})d\varepsilon_{zz} = C_U \tag{5.20}$$

Note that the strain increment ratio α does not need to be constant. The present derivation is therefore valid for non-proportional as well as proportional loading. The crucial step in the derivation is to divide and multiply the integrand of Eq. (5.20) by $\frac{2}{\sqrt{3}}\sqrt{1+\alpha+\alpha^2}$,

$$\int\frac{\alpha+\frac{1}{2}}{\frac{2}{\sqrt{3}}\sqrt{1+\alpha+\alpha^2}}\frac{2}{\sqrt{3}}\sqrt{1+\alpha+\alpha^2}\,d\varepsilon_{zz} = C_U \tag{5.21}$$

From Eq. (5.17), $\frac{\sigma_m}{\bar{\sigma}}$ depends on the parameter α. Replacing α with $\frac{\sigma_m}{\bar{\sigma}}$, Eq. (5.21) becomes

$$\int_0^{\bar{\varepsilon}_f}\frac{3}{2}\frac{1+\frac{\sigma_m}{\bar{\sigma}}\sqrt{12-27\left(\frac{\sigma_m}{\bar{\sigma}}\right)^2}}{3\frac{\sigma_m}{\bar{\sigma}}+\sqrt{12-27\left(\frac{\sigma_m}{\bar{\sigma}}\right)^2}}d\bar{\varepsilon} = C_U \tag{5.22}$$

By diving both sides by C_U then, we have

$$\int_0^{\bar{\varepsilon}_f}\frac{3}{2C_U}\frac{1+\frac{\sigma_m}{\bar{\sigma}}\sqrt{12-27\left(\frac{\sigma_m}{\bar{\sigma}}\right)^2}}{3\frac{\sigma_m}{\bar{\sigma}}+\sqrt{12-27\left(\frac{\sigma_m}{\bar{\sigma}}\right)^2}}d\bar{\varepsilon} = 1 \tag{5.23}$$

It is worth to mention that the first term in Eq. (5.21) is recognized as proportional to the normalized hoop stress $\frac{3}{4}\frac{\sigma_{\theta\theta}}{\bar{\sigma}}$ (see Eq. (5.15)). According to Eq. (5.18) the second term is simply the increment of the equivalent strain $d\bar{\varepsilon}$. Thus, Eq. (5.21) can be put in the equivalent form

$$\int_0^{\bar{\varepsilon}_f} \frac{\sigma_{\theta\theta}}{\bar{\sigma}} d\bar{\varepsilon} = \frac{4}{3} C_U = C_{CL} \tag{5.24}$$

Because $\sigma_{\theta\theta}$ is the maximum (tensile) principal stress σ_1 as shown in Fig. 5.25 from numerical simulations, Eq. (5.24) is similar to the well-known Cockcroft and Latham [68] crack formation criterion which was postulated rather than empirically derived. This conclusion is also confirmed by numerical simulations. As shown in Fig. 5.26, the following equation is valid at the equatorial area all the time during upsetting tests.

$$\varepsilon_{\theta\theta} + \frac{1}{2}\varepsilon_{zz} = \frac{3}{4}\frac{\sigma_{\theta\theta}}{\bar{\sigma}} \tag{5.25}$$

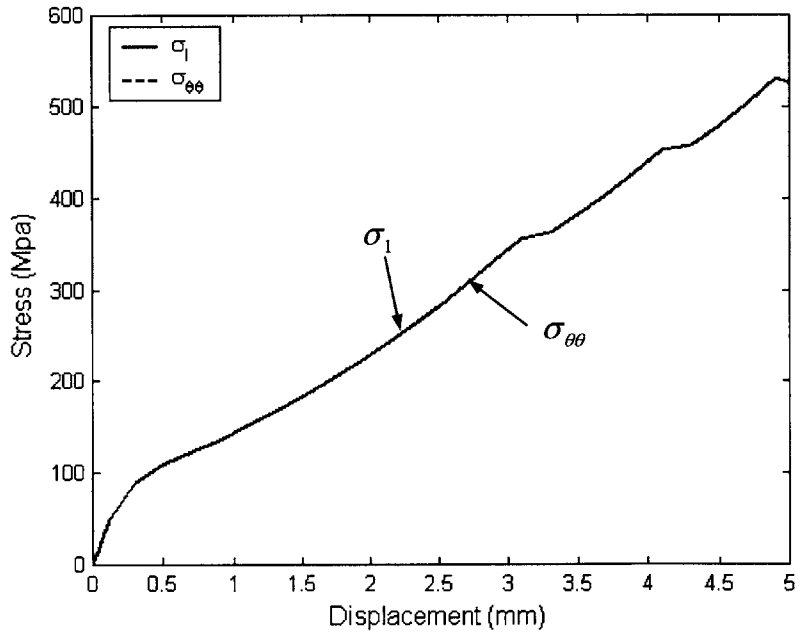

Fig. 5.25 Stresses at the equatorial area of upsetting specimens

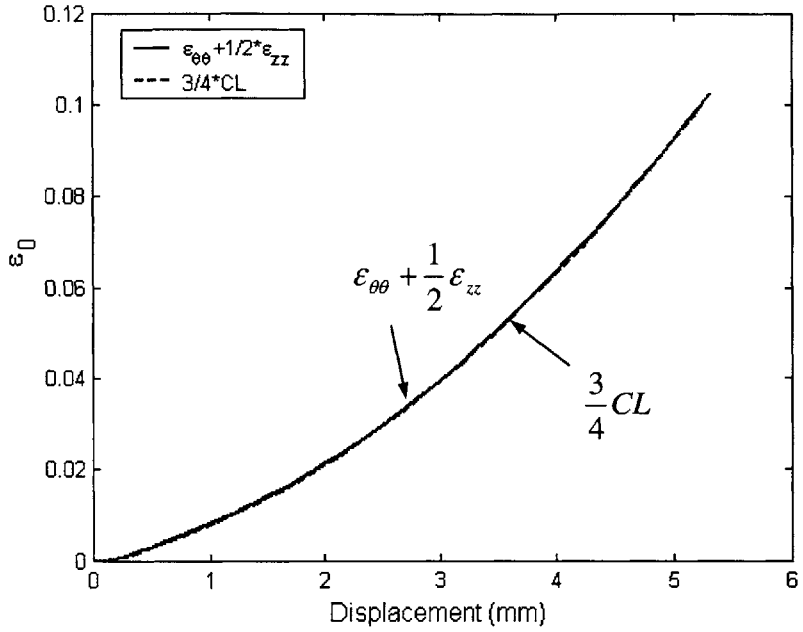

Fig.5.26 Comparison of the integrand of Eq. (5.20) and Eq. (5.24)

By comparing Eq. (5.23) with Eq. (5.4) and determining the constant C_U from Fig. 5.24, we can get the fracture locus in the negative stress triaxiality range.

$$\bar{\varepsilon}_f(\frac{\sigma_m}{\bar{\sigma}}) = 0.07 * \frac{3\frac{\sigma_m}{\bar{\sigma}} + \sqrt{12 - 27(\frac{\sigma_m}{\bar{\sigma}})^2}}{2(1 + \frac{\sigma_m}{\bar{\sigma}}\sqrt{12 - 27(\frac{\sigma_m}{\bar{\sigma}})^2})} \tag{5.26}$$

In addition, it has been shown in Chapter 4 that the hydrostatic stress criterion (Eq. (1.36)) works well for the high stress triaxiality range. Similarly, by diving both sides with the constant C_H which can be determined from the test, the fracture locus in the high stress triaxiality range can be described as

$$\bar{\varepsilon}_f(\frac{\sigma_m}{\bar{\sigma}}) = \frac{0.16}{\frac{\sigma_m}{\bar{\sigma}}} \tag{5.27}$$

A good correlation of Eq. (5.26) and Eq. (5.27) with the experimentally determined fracture locus (Fig. 5.20) is found as shown in Fig. 5.27. It indicates that the experimental

obtained fracture locus by taking average stress triaxiality as an approximation is satisfactory.

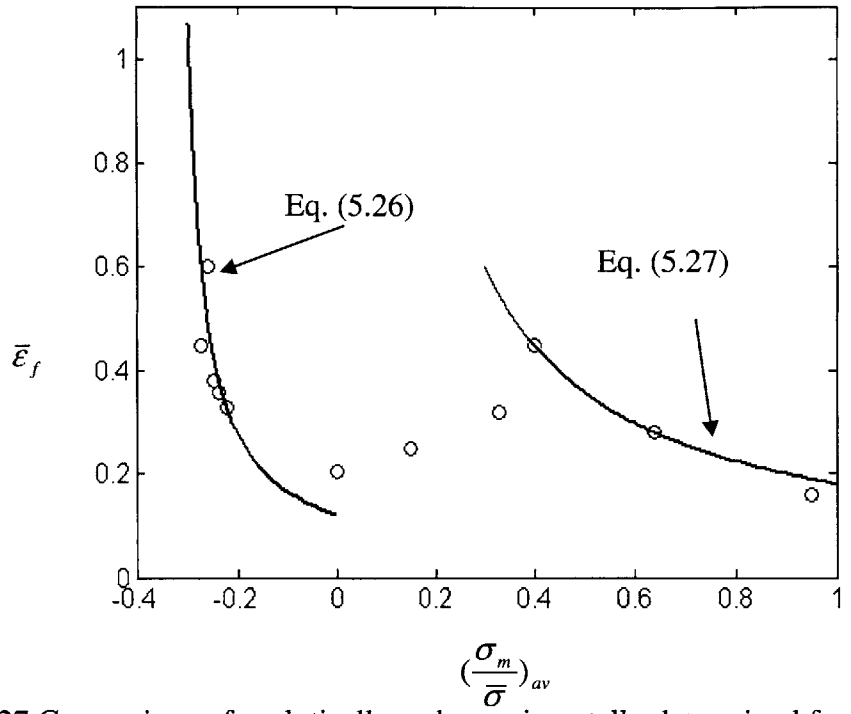

Fig. 5.27 Comparison of analytically and experimentally determined fracture locus

5.3 Cut-Off Value of Stress Triaxiality

One of the most important findings of the present thesis is determination of limiting value of the stress triaxiality below which fracture could never occur. The existence of a such cut-off value comes from the analysis of the results of the upsetting tests performed by the many authors in the past including Kudo and Aoi's [6], Kuhn and Dieter [106], Thomason [113, 114], Ganser et al. [115] and the present author. Compression test pieces in the above papers were manufactured from different types of steels and various aluminum alloys. In all cases, it was found that fracture initiates at the equatorial area of the short cylinders whenever the strain trajectory in the space of principal strains reaches the straight line limiting curve given by Eq. (5.9). From Figs 5.23 and 5.24, it is clear that

the line corresponding to $\sigma_m / \bar{\sigma} = -1/3$ never intersects the fracture locus, Eq. (5.9). Another proof for the existence of the cut-off value for fracture comes from the consideration of the Cockcroft-Latham criterion for fracture initiation, Eq. (5.24). It was shown earlier in the thesis that this equation is an alternative representation of our empirical fracture criterion (5.9). It should be noted that according to Eq. (5.24), fracture can initiate only under the presence of tensile secondary hoop stress, $\sigma_{\theta\theta} / \bar{\sigma} > 0$. This is equivalent to the requirement of $\sigma_m / \bar{\sigma} > -1/3$.

Perhaps the most straightforward proof of the existence of the cut-off value of stress triaxiality comes from the analysis of Eq. (5.26), which again is a restatement of the empirical fracture locus, Eq. (5.9) transformed into the space of the stress triaxiality and the equivalent strain. It is easy to see that in the limiting case, $\sigma_m / \bar{\sigma} \to -1/3$ the numerator of the equation (5.26) tends to zero. This means that the equivalent strain to fracture $\bar{\varepsilon}_f$ must be infinite.

Even though the above conclusion seems to be straightforward, no one has pointed out on this property.

It is interesting to see if the existence of the limiting value of stress triaxiality is consistent with earlier tensile tests on round bars conducted under different hydrostatic pressures. The most comprehensive experimental program in the above test configuration was performed by Bridgman and described in his famous book [93]. A more recent follow up was described in a series of papers by French and Weinrich [5, 116, 117]. We shall analyze first the results of that Australian team and then go into the interpretation of a large volume of experiment data by Bridgman.

For illustration, let us consider a commercial copper tensile specimen subjected to the tensile deformation with a superimposed hydrostatic pressure. French and Weinrich [5] presented a graph showing the histories of mean stress as a function of the tensile strain (which is almost identical to equivalent strain, see Fig. 3.13), Fig. 5.28. In each test, the

hydrostatic pressure was held constant while the axial strain was gradually increasing all the way to fracture in the universal testing machine.

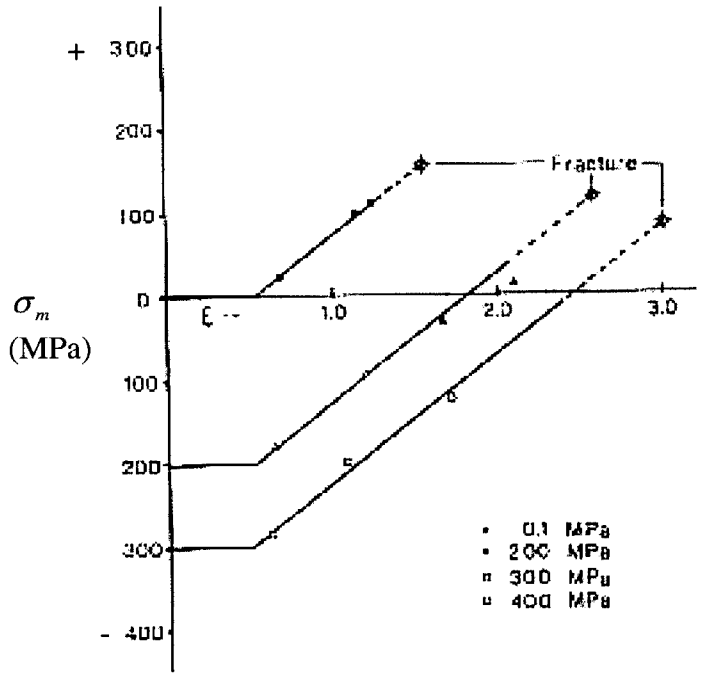

Fig. 5.28 Evolution of mean stress in tensile tests with hydrostatic stress on a copper (after French and Weinrich [5])

Therefore, the hydrostatic stress which is the sum of the pressure and stress components due to the tensile loading was monotonically increasing as shown in Fig. 5.28. In order to transform the above data to our coordinate system $[(\sigma_m/\bar{\sigma})_{av}, \bar{\varepsilon}_f]$, the time history of the equivalent stress $\bar{\sigma}$ should be known. This information was not given by the authors. In the absence of any additional information, we have normalized the mean stress σ_m (which is known) by the ultimate tensile strength of the copper, converted into the true value $\bar{\sigma} \approx 270$ MPa. The plot shown in Fig. 5.28 was made by the authors using the Bridgman formula for stress triaxiality, Eq. (3.12). We have shown earlier that Eq. (3.12) are inaccurate for deep necks. A more exact numerical analysis on the necking problem summarized in Fig. 3.14 points out on the need of increasing the stress triaxiality by a

factor of 1.4. Because of the linearity of the function shown in Fig. 5.28, the average stress triaxiality is equal to one half of the sum of the initial and final values.

$$(\frac{\sigma_m}{\bar{\sigma}})_{av} = \frac{1}{2}[(\frac{\sigma_m}{\bar{\sigma}})_{inital} + (\frac{\sigma_m}{\bar{\sigma}})_{final}] \tag{5.28}$$

The expression for the initial stress triaxiality at the beginning of tensile tests is

$$(\frac{\sigma_m}{\bar{\sigma}})_{initial} = -\frac{p}{\bar{\sigma}} + \frac{1}{3} \tag{5.29}$$

where, p is the magnitude of the hydrostatic pressure. The expression for the final stress triaxiality of tensile tests, using the Bridgman correction is

$$(\frac{\sigma_m}{\bar{\sigma}})_{final} = -\frac{p}{\bar{\sigma}} + 1.4\,[\frac{1}{3} + \ln(1 + \frac{a}{2R})] \tag{5.30}$$

The results of calculation for four cases considered by the authors are summarized in Table 5.1.

In conclusion, the average stress triaxiality corresponding to the two highest hydrostatic pressures were respectively 0.18 and 0.06. Both these values are above the cut-off value of -1/3. At the same time, one can see from the above table that the initial stress triaxiality was in some cases smaller than -1/3. However, fracture is an incremental process in which the history of stress triaxiality rather than the initial value counts. In the deformation process, the triaxiality actually changed to large positive values, so that in all cases the average stress triaxiality agreed with newly introduced concept of a cut-off value.

Table 5.1. Summary of the tests by French and Weinrich [5]

Pressure (MPa)	Initial stress triaxiality	Final stress triaxiality	Average stress triaxiality	Strain to fracture	Comments
0.1	0.33	0.8	0.57	1.6	
200	-0.47	0.82	0.18	2.5	
300	-0.78	0.86	0.06	3	
400	-1.15	N.A.	N.A.	N.A.	Incomplete data on final stage.

Bridgman in his famous book [93] presented a wealth of experiment data regarding the hydrostatic pressure tests of metals. In fact, he studied twenty different types of steels and with each type several different heat treatments. For each particular steel and heat treatment, tensile tests were performed under several constant levels of hydrostatic pressure ranging from 0 to 2700 MPa. All together over 350 tests were fully or partially documented in his book. For the purpose of the present proof of the correctness of our concept of limited triaxiality parameter, we have analyzed only 46 most representative cases and constructed an interesting plot shown in Fig. 5.29. The vertical axis denotes the estimated average stress triaxiality while on the horizontal axis is the number of sample cases. Tests in which fracture was observed are indicated by the empty circles while those results in which no fracture occurred are denoted by the stars. Typical data presented by Bridgman include the following information from which points shown in Fig. 5.29 were evaluated. We show an example of raw data in case of a stainless steel

Specimen number 17-0-2,

Hydrostatic pressure $p = 1550$ MPa

Logarithmic strain to fracture $\varepsilon_f = 2.29$

Fracture/No fracture: fracture

Average stress at maximum load (engineering) $S_U = 1764$ MPa

Neck profile $a/R = 1.29$

Substituting the above values into the equations 5.28-5.30, the resulting triaxiality parameter $(\frac{\sigma_m}{\bar{\sigma}})_{av} \approx 0.3$ (point labeled with an arrow in Fig. 5.29)

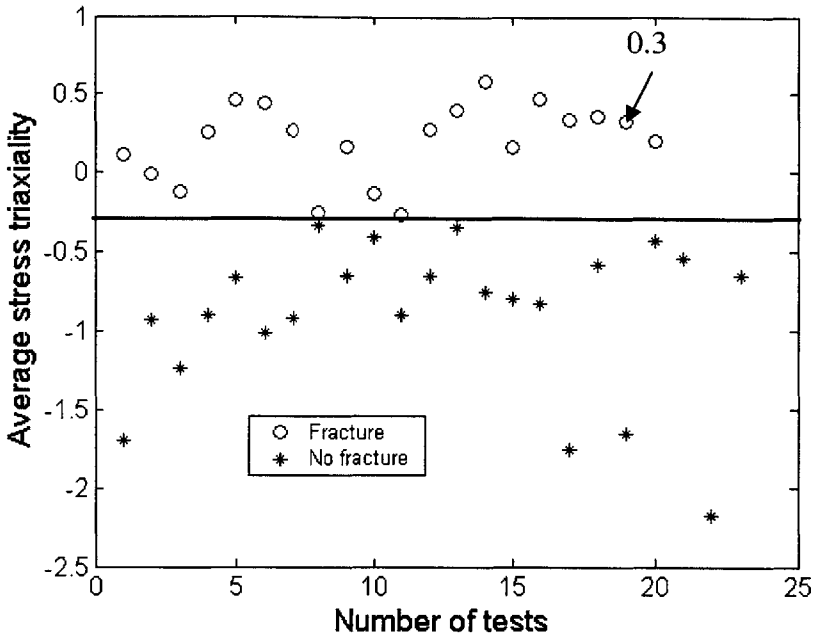

Fig. 5.29 Average stress triaxiality in Bridgman tensile tests with superimposed hydrostatic pressure

One can see that two sets of points (empty circles represent fractured, stars represent no fractured) are separated by a line with an ordinate -1/3. In another words, the existence of cut-off value of the average stress triaxiality for fracture has been independently confirmed through a "statistical" evaluation of representative tests out of a pool of four hundreds tests performed by Bridgman.

Here at MIT, we do not have a specialized equipment to perform a combined tensile test with hydrostatic pressure. Instead, we have performed a "virtual" test in which 2024-T351 aluminum alloy round specimens were subjected to tension under a constant hydrostatic pressure. In particular, we wanted to see if indeed the constant hydrostatic pressure increase the ductility (equivalent strain to fracture) of the specimen, so that a much deeper necks are observed. Another advantage of the "virtual" test is a precise determination of the stress and strain states at the point of crack formation.

The dimensions were identical to the round tensile specimen described in Chapter 3. Several runs were made with increasing magnitudes of hydrostatic pressure which were held constant in each "virtual" test. A series of deformed meshes of the specimens at the point of crack formation (center of the neck) is shown in Fig. 5.30. It is seen that the depth of the neck increases with the hydrostatic pressure while the neck radius R is decreasing. The above results were obtained using the fracture locus for 2024-T351 aluminum alloy defined early in this Chapter.

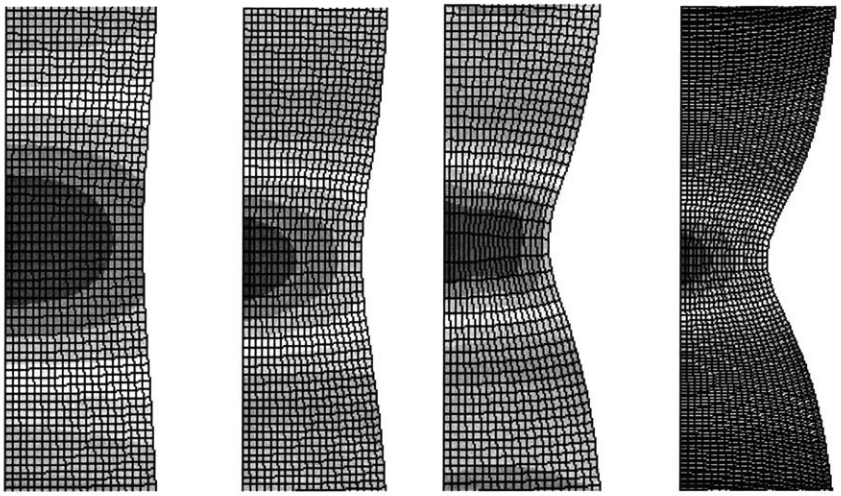

$p = 0$ MPa $p = 400$ MPa $p = 600$ MPa $p = 1000$MPa

Fig. 5.30 Deformed meshes of the specimens at the point of crack formation under combined tension and hydrostatic pressure

It is interesting to determine the accuracy of Bridgman correction for stress triaxiality, for tensile tests with a hydrostatic stress as compared to the more exact ABAQUS calculation.

$$\frac{\sigma_m}{\bar{\sigma}} = -\frac{p}{\bar{\sigma}} + \frac{1}{3} + \ln\left(\frac{a^2 + 2aR - r^2}{2aR}\right) \tag{5.31}$$

The plot of the stress triaxiality parameter as a function of radial coordinate in the symmetry plane of the neck is shown in Fig. 5.31. It can be seen that Bridgman formula underestimates the true stress triaxiality at the center of the specimen by approximately a

factor of 2. Such large error is observed for deep necks where the Bridgman's formula becomes increasingly inaccurate. In order to construct Fig. 5.29 we were using the 1.4 correction factor. If the correction factor further increases, this will move all the empty points in Fig. 5.29 somewhat higher.

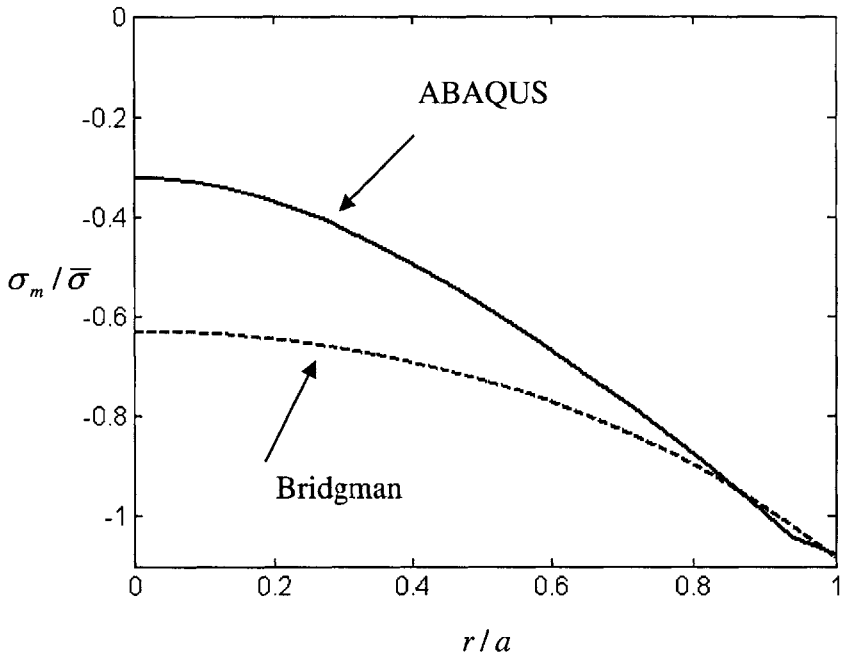

Fig. 5.31 Comparison of Bridgman and ABAQUS prediction of stress triaxiality for a deep neck

It can be observed that the ductility of 2024-T351 aluminum alloy is relatively low compared to the material tested by Bridgman [93] and French and Weinrich [5]. The diffuse neck corresponding to zero pressure is very shallow (See Fig. 30). In order to produce deep necks, we have artificially double the ductility of 2024-T351 aluminum alloy and made additional computer runs. The resulting shapes of the neck at the point of fracture are shown in Fig. 5.32. Now, the calculated "virtual" deep neck for 2024-T351 aluminum alloy with double ductility under 1000 MPa and the deep neck for a copper under 500 MPa reported by French and Weinrich [5] is shown Fig. 5.33.

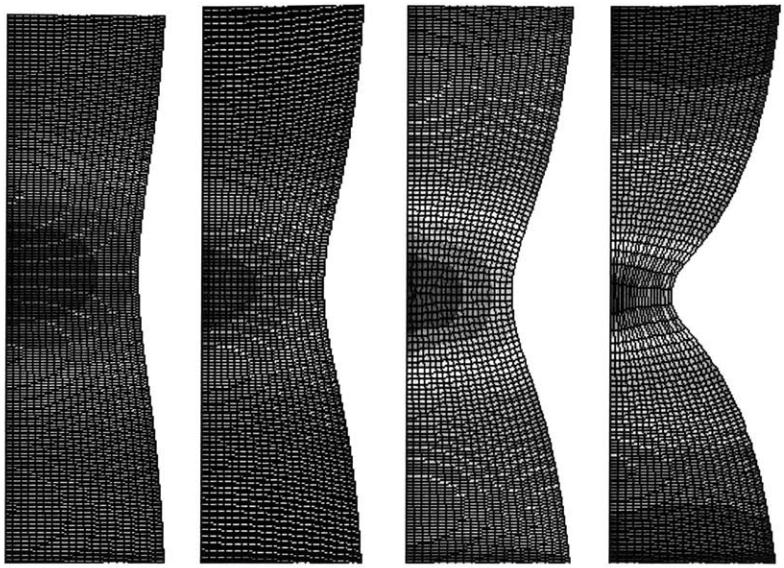

$p = 0$ MPa $p = 400$ MPa $p = 600$ MPa $p = 1000$MPa

Fig. 5.32 Deformed meshes of the specimens at the point of crack formation under combined tension and hydrostatic pressure with artificially doubled ductility of Al 2024-T351

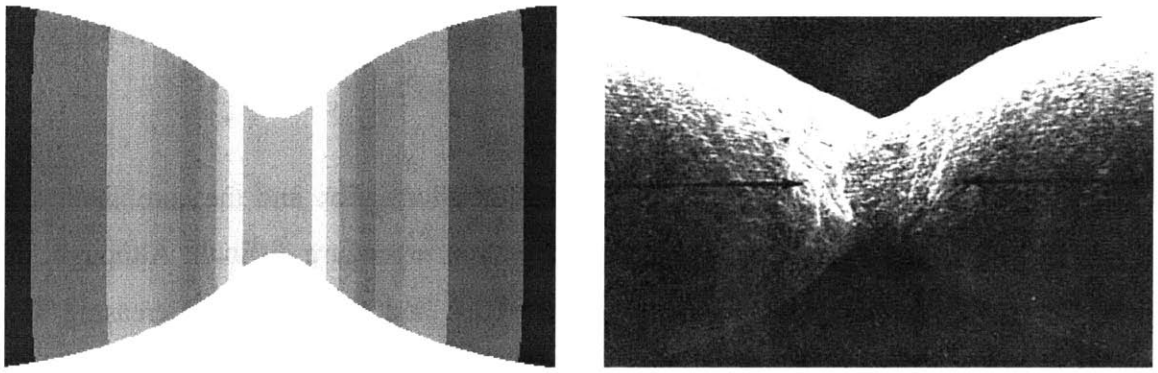

(after French and Weinrich [5])

Fig. 5.33 Calculated "virtual" and reported deep neck

It can be concluded that the present fracture criterion with the triaxiality function taking an infinite asymptotic value for stress triaxiality approaching -1/3 captures most of the features reported in the present and earlier experiments with high negative hydrostatic stress.

5.4 Mode Transition

The question of mode transition was raised for the first time by Wierzbicki and Muragishi [108] who showed that the weighting function was not smooth and, at least for steels, must be composed of two branches. Subsequently, a qualitative explanation of this behavior was given by Hooputra et al [110] who suggested that there are two different crack formation mechanisms depending on the range of a triaxiality parameter.

It is clear from the study of the physical mechanisms of ductile crack formation in Chapter 2 that there are two different mechanisms, i.e. "shear fracture" dominating at negative stress triaxialities and void nucleation, growth, and linkage dominating at negative stress triaxialities. Also, there is a clear transition from "shear fracture to void nucleation, growth, and linkage in the intermediate stress triaxiality range. The two different mechanisms and the transition can also be confirmed from the fracture locus shown in Fig. 5.20 where two monotonic decreasing curves in the negative stress triaxiality range and the high stress triaxiality range, respectively, are connected by an increasing curve in the intermediate stress triaxiality range.

The appearance of two mechanisms of ductile crack formation and the combination of those two in the transition zone makes the calibration procedure difficult. Although, the transition zone for Al2024-T351 is $0 < \sigma_m / \bar{\sigma} < 0.4$ and the curve is increasing as a parabolic from 0.2 to 0.45, the transition region can be narrow or wide and the jump between could be (positive or negative) large or small as shown in Fig. 5.34 for different materials. For example, for the SAE 1045 steel tested by Bridgman [78] and Al 2024-T351, the equivalent strain to crack formation increases with the stress triaxiality in the transition region, while for the stainless steels and high carbon steels tested by Bridgman [78] and the copper tested by French and Weinrich [5], the equivalent strain to crack formation decrease with increasing of the stress triaxiality in the transition region. Still it

is not quite clear how does transition occur from the "shear" dominating crack formation to crack formation due to void nucleation, growth, and linkage.

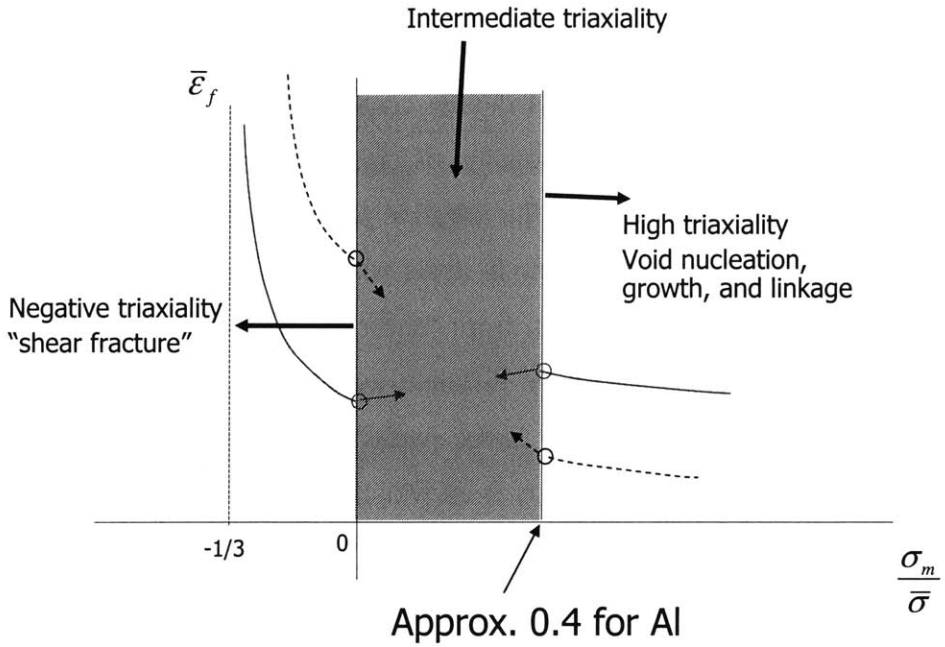

Fig. 5.34 A possible mode transition between the void growth dominated mode and "shear fracture" dominated mode

However, in the main stream of research it was postulated that $\bar{\varepsilon}_f(\sigma_m/\bar{\sigma})$ is a monotonically decreasing function of its argument (eg. Rice and Tracey [17], Johnson and Cook [74, 118], Borvik et al. [119, 120]). Furthermore, most of the calibration data reported in the literature was obtained from tensile tests on un-notched and notched specimens (eg. Alves and Jones [104], Johnson and Cook [74]). These correspond to moderate or large stress triaxialities, i.e. $\sigma_m/\bar{\sigma} > 1/3$. Extrapolating the function $\bar{\varepsilon}_f(\sigma_m/\bar{\sigma})$ into small, zero or negative triaxialities, as it was done by Johnson and Cook [74] and Borvik et al [120] is a risky procedure that may lead to substantial errors. It was shown in Chapter 4 that crack formation in compression (upsetting) can not be correctly predicted from calibration performed in tension and vice versa. A need for constructing fracture envelope in the entire range of stress triaxiality is apparent.

5.5 Conclusion and Discussion

A new methodology of prediction of ductile crack formation for industrial applications was developed based on the mechanisms of crack formation described in Chapter 2. Since "shear fracture" dominates in the negative stress triaxiality range, void nucleation, growth, and linkage favors in the high stress triaxiality range and in between ductile crack formation is under a transition from "shear fracture" to void nucleation, growth, and linkage with the stress triaxiality, different weighting functions were introduced for different stress triaxiality ranges. Those weighting functions were determined by performing a number of different tests from which a relationship of the equivalent strain to crack formation and the stress triaxiality was found. An extensive experimental program to determine the above relationship in a relatively wide range of stress triaxialities was reported. Eleven different specimens were tested under compression, shear, tension and combined loading. It was found that the fracture envelope of Al2024-T351 constructed on the plane of the equivalent strain to crack formation and the stress triaxiality consists of three different branches. Two regimes correspond to "shear fracture" and void nucleation, growth, and linkage in the negative stress triaxiality range and the high stress triaxiality range, respectively. There must also be a transition area in the intermediate stress triaxiality. This is an entirely new finding because it was previously believed that the fracture locus is a monotonic function of the stress triaxiality parameter. Three new configurations of specimens for the intermediate stress triaxiality range, which give relatively constant stress triaxialities during deformation, were developed. It is recognized that the fracture locus is specific for a given material. The main contribution of the thesis is not necessarily the derivation of such a locus for a particular aluminum alloy but rather a development of a general methodology for constructing the fracture locus for any ductile material. In addition, an analytical solution of the fracture locus of the negative stress triaxiality range was derived from the reported failure locus of upsetting tests.

The new type of compression specimen was designed that successfully removes the friction effect. However, the equivalent strain to crack formation for the new compression test was higher than the conventional upsetting test on cylinders for the same amount of the stress triaxiality (See Fig. 5.27). The discrepancy of the results obtained from these two types of compression tests should be explained in the future study. It would appear though that in the new compression specimen, the gauge section developed considerable amount of orange skin deformation. Therefore it was very difficult to observe visually the true crack formation.

The expression for the weighting functions was formulated in this chapter in terms of invariants of the stress and strain tensors, $\bar{\varepsilon}$, σ_m, and $\bar{\sigma}$. The tests performed in this Chapter were restricted to plane stress and axial symmetry. It is recognized that other types of stress or strain conditions and other variables such as stress and strain ratio, rotation, surface/subsurface, strain and stress gradient, strain hardening, anisotropy of materials and specimen size were not included. The effects of some of those variables will be discussed and quantified in Chapter 6.

The preceding analysis and the calibration method applies strictly to a homogeneous and isotropic material that has not been subjected to any prior loading history. However, such raw materials hardly exist in practice. Steel mills and foundries and aluminum companies are supplying customers with semi-products such as sheets, hot or cold-formed profiles, extrusions, castings and components made by forging, stamping, etc. Each metal forming operation introduces a deformation-induced history. Hooputra et al. [110] recognized that plastic deformation introduced into a given part during forming or deep drawing will change the crashworthiness properties of that part. They also developed a practical method of tracking down the effect of the loading path on the forming-limit diagrams. The effect of prior loading history on fracture properties of semi-products or structural components has not been well understood. However, since the present approach to predict crack formation is based on the accumulation of damage, it is reasonable to superimpose the damage caused by manufacturing to the total damage as a first approximation to account for any possible pre-loading in industry applications.

Finally, it should be pointed out that since the test conducted did not include torsion tests and a different mechanism may appear in torsion tests [121], the application of the present approach for torsion tests remains open. Also, it is difficult to deal with crack formation with the effect of heat treatment, and for welded components the effect of the heat affected zone with the present approach. Clearly, determination of weldment strength and failure requires a much more detailed analysis and this topic falls outside the realm of the present study.

Chapter 6

Effect of Other Variables on Crack Formation

In Chapter 5, damage accumulation was measured in terms of invariants of the stress and strain tensors, $\bar{\varepsilon}$, $\bar{\sigma}$ and σ_m. It is recognized that other variables, ratio of stress and strain components, specimen size, anisotropy of materials, gradient, strain hardening, surface/subsurface, and rotation might also play a role in ductile crack formation. The effects of some of those variables are discussed and quantified in this Chapter.

Additional tensile tests on flat specimens, flat-grooved plates, thick-walled pipes and solid square bars were conducted to study the effect of stress and strain ratio together with the tensile tests on smooth and notched round bars. The effect of plate thickness and size was evaluated from 18 plates with different thickness and hole sizes. Finally short cylinders cut from different direction of the material were compressed to study the effect of anisotropy.

6.1 Effect of Strain and Stress Ratio

In this context, again, ductility is the ability of a material to accept large amount of deformation without crack formation. In many practical problems, equivalent strain to crack formation at the critical location in tensile specimens is taken as a measure of ductility [3, 4, 77, 122, 123]. Different types of tensile test pieces are often used such as flat, round specimens. However, equivalent strain to crack formation is dependent on the stress state, which is related to boundary and shape of specimens and clearly is not the same in tensile tests on specimens with different geometries. Consequently, different specimens do not necessarily have the same fracture ductility. Clausing [122] observed from the tests on flat-grooved plates (shown in Fig. 6.1) that tensile ductility of structural steels was substantially reduced when the stress and strain state was changed from axisymmetric (round specimen) to combined plane strain and stress (flat-grooved plate). The degree of difference was found dependent on hardness of steels.

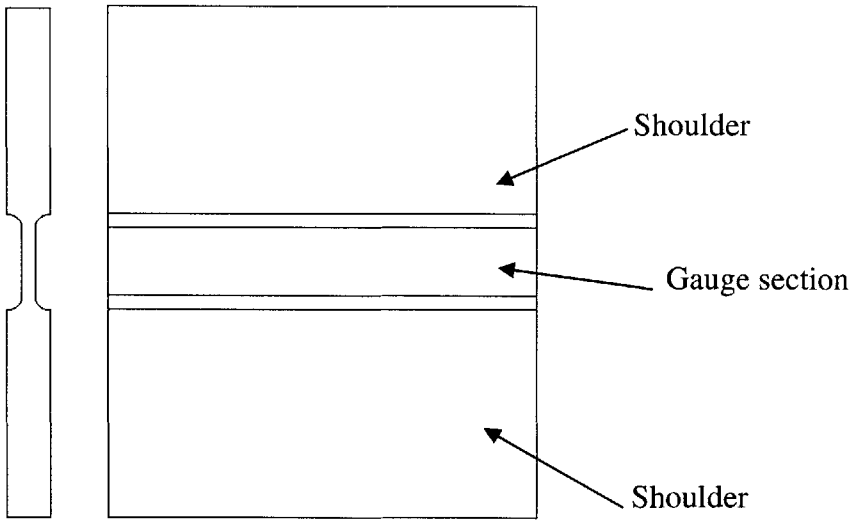

Fig. 6.1 Flat-grooved plate

The interpretation for the difference is qualitative and limited to the degree of physical constrain. Therefore, detailed study on fracture ductility of tensile specimens with different geometries for a same material will certainly contribute to a more complete picture. As shown in Chapter 5, crack formation depends not only on the equivalent strain alone but also on the stress triaxiality. In this section, additional tensile tests on flat specimens, flat-grooved plates, thick-walled pipes and solid square bars were conducted. Those tests together with the tensile tests on smooth and notched round bars give not only different stress triaxiality but also different stress and strain ratio. They certainly provide a good way to study the effect of stress and strain ratio on crack formation and also the effectiveness of the measurement of the damage accumulation in terms of the equivalent strain and the stress triaxiality.

6.1.1 Theoretical Considerations

6.1.1.1 Flat Specimen

For ductile metals, necking occurs usually before crack formation in a flat specimen under uniaxial tension. Obviously, necking is an important mechanism in flat specimens under tension for crack formation prediction. The deformation analysis of local stress for necking under plane stress was conducted by many authors such as Hill [124] and McClintock et al. [7]. The necking is spread over a length of the order of the width w shown in Fig. 6.2 while the rest of the structure remains rigid. This is called diffuse necking. The diffuse necking occurs in uniaxial stress states when the slope of the equivalent stress-strain curve reaches

$$\frac{d\bar{\sigma}}{d\bar{\varepsilon}} = \bar{\sigma} \tag{6.1}$$

For a power-law material which has the relation

$$\bar{\sigma} = \sigma_0 \bar{\varepsilon}^n \tag{6.2}$$

the corresponding equivalent strain is

$$\bar{\varepsilon} = n \tag{6.3}$$

where, σ_0 and n are two material constants for power law materials.

If diffuse necking continues, localized necking also shown in Fig 6.2 may occur over a length of the order of the sheet thickness. The localized necking occurs when the slope of the equivalent stress-strain curve reaches

$$\frac{d\bar{\sigma}}{d\bar{\varepsilon}} = \frac{\bar{\sigma}}{2} \tag{6.4}$$

For a power-law material, the corresponding equivalent strain is

$$\bar{\varepsilon} = 2n \tag{6.5}$$

The surroundings of the localized neck, the so-called shoulders remain rigid and the strain parallel to the localized neck vanishes. From Mohr's circle of strain the localized necking turns out to be inclined to the loading at an angle of

$$\phi = \frac{\pi}{4} + \frac{1}{2}\sin^{-1}(\frac{1}{3}) \approx 54.7^0 \tag{6.6}$$

The above analysis for necking is not sufficient for crack formation prediction since in most cases for ductile metals, crack formation occurs at a certain stage inside the neck after localized necking occurs.

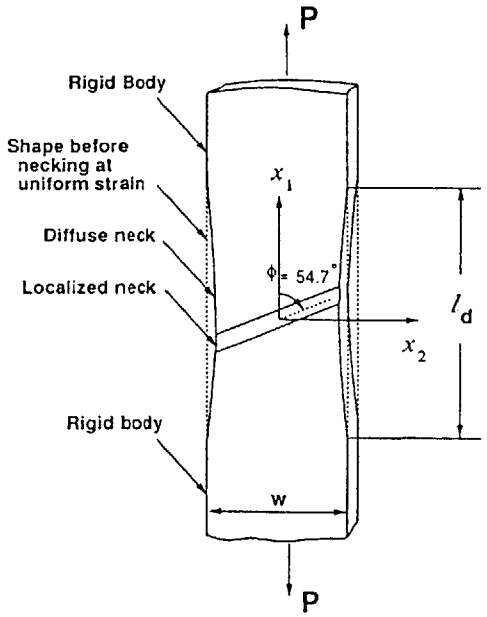

Fig. 6.2 Tensile necking in a flat specimen (after McClintock and Zheng [7])

6.1.1.2 Round Solid Bar

Round bars are most often used in tensile tests to get material properties including fracture properties. For ductile materials, necking also occurs in round bars before crack formation. The necking occurring in a round bar is similar as the diffuse necking in a flat specimen.

Obviously, neck is the most highly stressed and strained part and therefore is the critical area for this specimen. The most widely used approximately analysis of the stress state in the neck is the one carried out by Bridgman [78] (Eq. (3.9)-(3.12)) which however does not give an accurate calculation of stress triaxiality and equivalent strain [104, 109, 112] (See Chapter 3). In the present thesis, a more exact solution is used instead of Bridgman solution.

6.1.1.3 Flat-Grooved Plate

Compared to flat specimens and round bars, flat-grooved specimens are not widely used for fracture calibration. The specimen shown in Fig. 6.1 was introduced by Clausing [122] who investigated fracture ductility of steel experimentally. During his tests, the crosshead was stopped at frequent intervals after the specimen yields. The load and crosshead position just prior to the stopping of the crosshead were recorded. With the crosshead stopped, the thickness of the minimum section was measured. Then the strain was calculated each time from

$$\varepsilon = \ln(\frac{t_0}{t}) \tag{6.7}$$

where t_0 is the original thickness in the gauge section, and t is the current thickness of the minimum section. The strain was plotted against the crosshead displacement and the resulting curve was extrapolated to the known value of the crosshead displacement when

final fracture occurred. Finally, the corresponding strain at final fracture was read from the curve. However, the strain obtained from Eq. (6.7) is only good when the strain is uniform along the minimum section while this condition is difficult to achieve because of necking and possible end effects. In addition, unloading and reloading during the tests might also play a role in crack formation. Finally, this method also clearly depends on the accuracy of the extrapolation.

McClintock and Zheng [7] studied a similar specimen and found that the stress and strain were uniform across most of the width which is so called transverse plane strain (TPS) zone shown in Fig. 6.3. The specimen was modeled with two distinct zones: plane stress and TPS zones (Fig. 6.3). To correct for the uniaxial and transition effects (Fig. 6.3), it was proposed that a uniaxial stress σ_{ps} exists in transition zones near the edges (Fig.4) and that

$$\sigma_{ps} = \sigma_{pn}\sqrt{3}/2 \tag{6.8}$$

$$w_{ps} = \frac{L_0}{2}\tan 54.7^0 \tag{6.9}$$

where σ_{pn} is the stress of the TPS zone, w_{ps} is half of the total transition zone and l_0 is original length of the gauge section (Fig. 6.3).

The equivalent stress $\bar{\sigma}$ and strain $\bar{\varepsilon}$ in the TPS region were expressed by the following two equations.

$$\bar{\sigma} = \frac{\frac{\sqrt{3}}{2}P/wt}{1-(1-\frac{\sqrt{3}}{2})(\frac{l_0}{w_0})\tan 54.7^0} \tag{6.10}$$

$$\bar{\varepsilon} = \frac{2}{\sqrt{3}}\ln\frac{l-t_0}{l_0-t_0} \tag{6.11}$$

where, P is the load, w, t and l are the width, thickness and length, respectively, w_0, t_0 and l_0 are initial values of w, t and l, respectively.

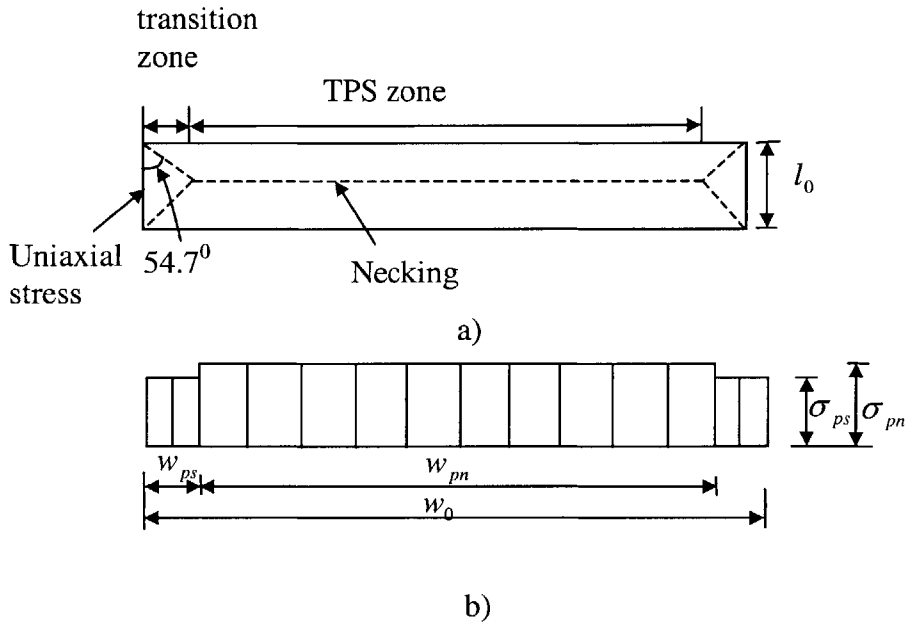

Fig. 6.3 McClintock's plane strain zone boundaries (a) and stress distribution (b) in gauge section of the flat-grooved specimen

As described above, the analytical models by Hill, Bridgman, Clausing and McClintock provide a clear picture of the plastic deformation of flat specimens, round bars and flat-grooved plates under uniaxial tension, respectively. However, those models involve assumptions, such as the uniform strain distribution along the minimum cross section, which may lead to errors in strain and stress calculations at the critical locations. In this study, the stress and strain at the location of crack formation were obtained by performing parallel numerical simulations.

6.1.2 Experiments

Additional tensile tests on flat specimens, flat-grooved specimens, solid bars with a square cross section and thick-walled pipes were carried out using a universal testing machine (Model 45G, MTS System Corporation, Eden Prairie, MN) with a 200 kN load cell at a loading rate of 0.2 mm/sec, as shown in Fig. 6.4. All those specimens were cut from the same block of 2024-T351 aluminum alloy. The dimensions of those specimens are listed in Table 6.1. During the test, an extensometer with 25.4 mm gauge length was used to measure the displacement. Load-displacement responses were recorded using TestWorks software (Sintech Division, MTS). Tests were stopped at system instability with a corner on the load trace. Crack formation occurred inside the gauge section for all the five cases. Fractured specimens are shown in Fig. 6.5. As expected, diffuse necking and later localized necking occurred in the flat specimen. Circumferential necking was observed in the thick-walled pipe, while the flat-grooved specimen experienced some diffuse necking. Diffuse necking in two transverse directions developed in the solid square bar and no clear localized necking was found in this specimen.

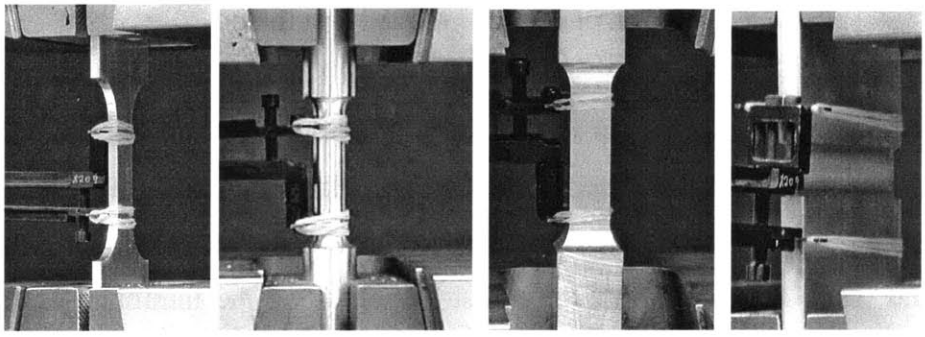

a) flat specimen b) round pipe c) solid bar d) flat-grooved

Fig. 6.4 Initial set up of tensile tests on different specimens

Table 6.1 Dimensions of tensile specimens (units: mm).

Specimen	Gauge length	Width	Thickness	Outer diameter	Inner diameter
Flat specimen	25.4	12.5	3	N/A	N/A
Thick-walled pipe	25.4	N/A	N/A	9	1.8
Solid square bar	25.4	9	9	N/A	N/A
Flat-grooved plate	8	50	1.6	N/A	N/A

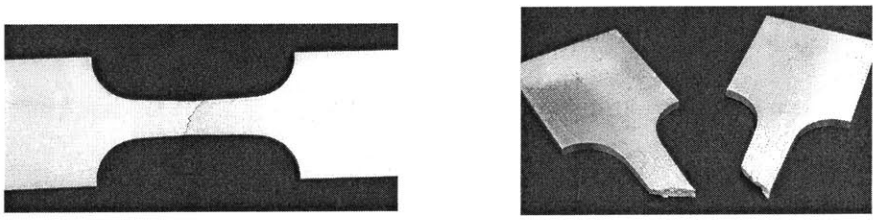

a) fractured flat specimen

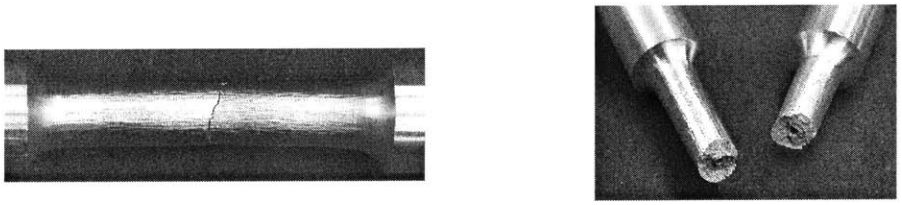

b) fractured thick-walled pipe

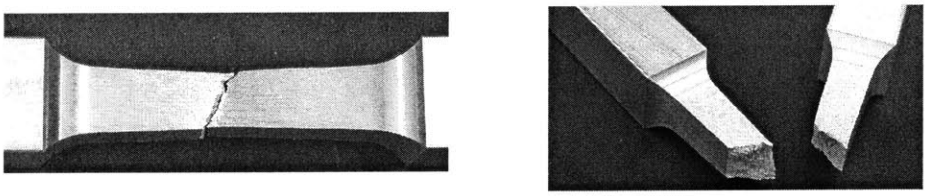

c) fractured solid bar

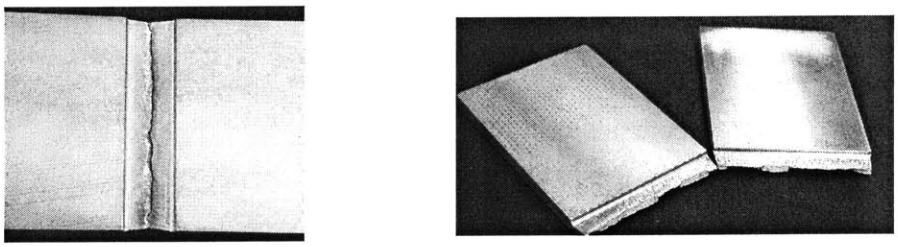

d) fractured flat-grooved specimen

Fig. 6.5 Fractured tensile specimens

6.1.3 Numerical Simulations

Numerical simulations of the additional tensile specimens under tensile loading were performed using ABAQUS STANDARD 6.2. In all simulations, a finite velocity was applied to one end of the model while the other end was fixed. Two or three different meshes for each case were developed to study mesh size sensitivity. As an example, the finite element meshes for the solid square bar are shown in Fig. 6.6. The difference between different meshes used in stress and strain calculation was found small (within 4%) for all four cases. An extensive numerical study on round bars has been presented in Chapter 4.

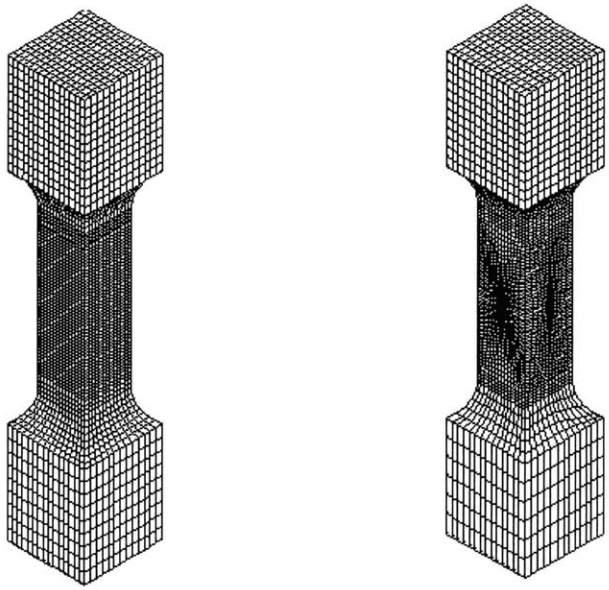

coarse mesh fine mesh

Fig. 6.6 Finite element models for the square solid bar

6.1.3.1 Flat Specimen

The specimen was molded by 4-node shell elements. As shown in Fig. 6.7, the numerical simulation successfully captured diffuse necking and localized necking, which are main features of tensile tests on flat specimens and are clearly displayed in the tested specimen. Final width of the minimum cross section obtained from the numerical simulation was 10.6 mm, which was close to 10.4 mm measured from the test. Amazingly, even the angle of the shear band from the test and the numerical simulation was found the same as the analytical result (Eq. (6.6)), which was 54.7^0 (Fig. 6.7). In addition, the correlation of the force-displacement response between the numerical simulation and test up to crack formation was almost perfect (Fig. 6.8). The stress triaxiality versus equivalent strain is presented in Fig. 6.9.

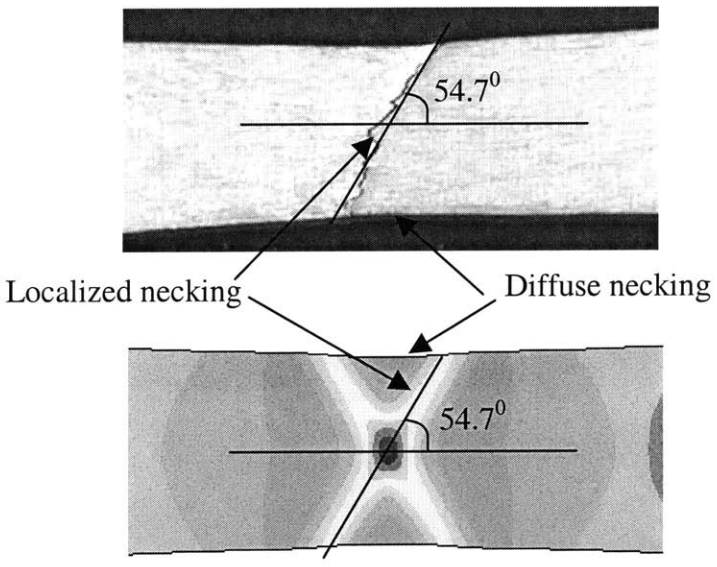

Fig. 6.7 Deformed flat specimen
(color-coded map is the equivalent strain distribution)

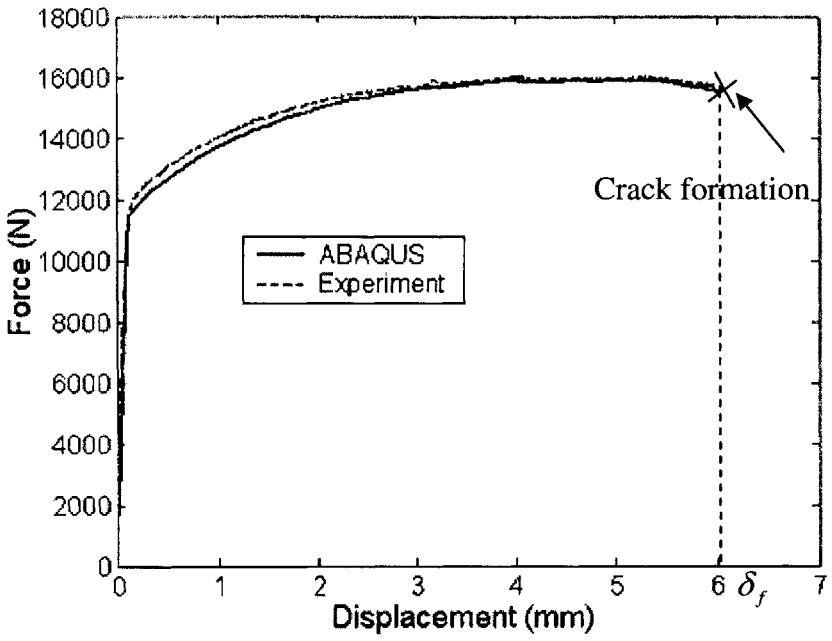

Fig. 6.8 Comparison of force-displacement response (flat specimen)

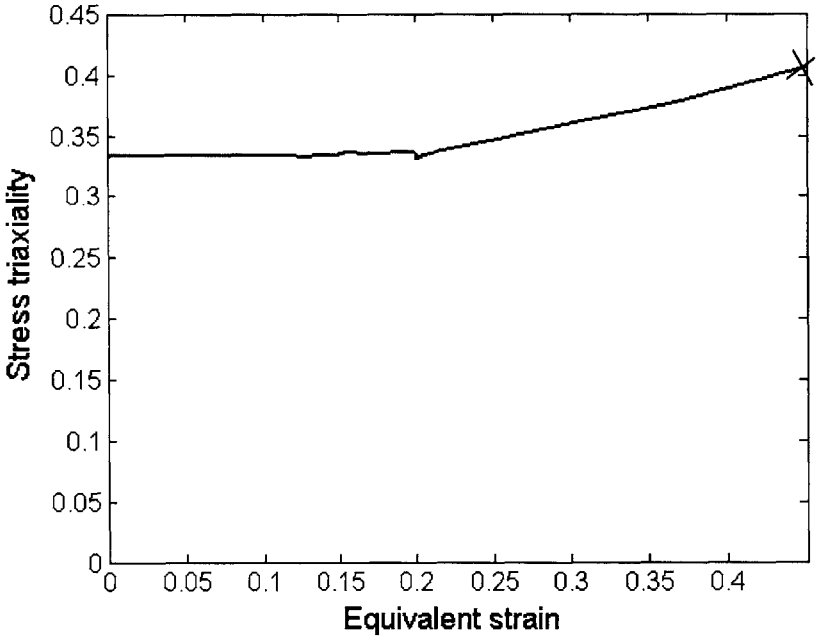

Fig. 6.9 The stress triaxiality versus the equivalent strain at crack formation location (flat specimen)

6.1.3.2 Thick-Walled Pipe

The thick-walled pipe was modeled by 4-node axisymmetrical elements. The material can flow inward during the deformation. The numerical simulation corrected well with the experiment both in the deformation shape and force-displacement response up to crack formation (Fig. 6.10, Fig. 6.11). Final diameter obtained from the numerical simulation was 7.6 mm while the value was 7.5 mm measured from the test. The stress triaxiality versus equivalent strain is illustrated in Fig. 6.12.

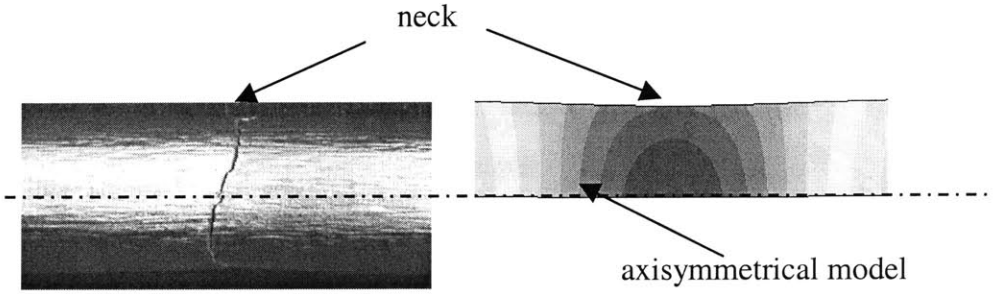

Fig. 6.10 Deformed thick-walled pipe
(color-coded map is the equivalent strain distribution)

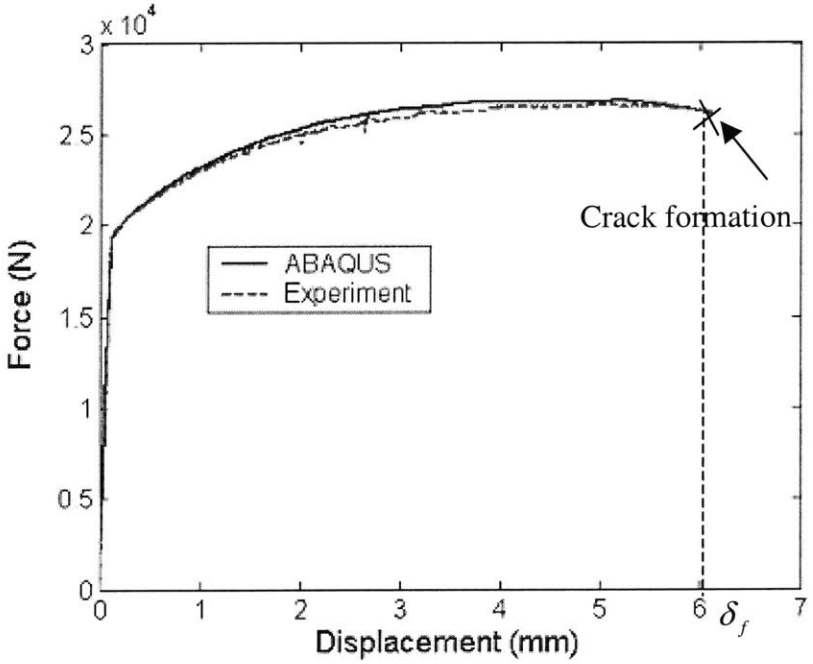

Fig. 6.11 Comparison of force-displacement response (thick-walled pipe)

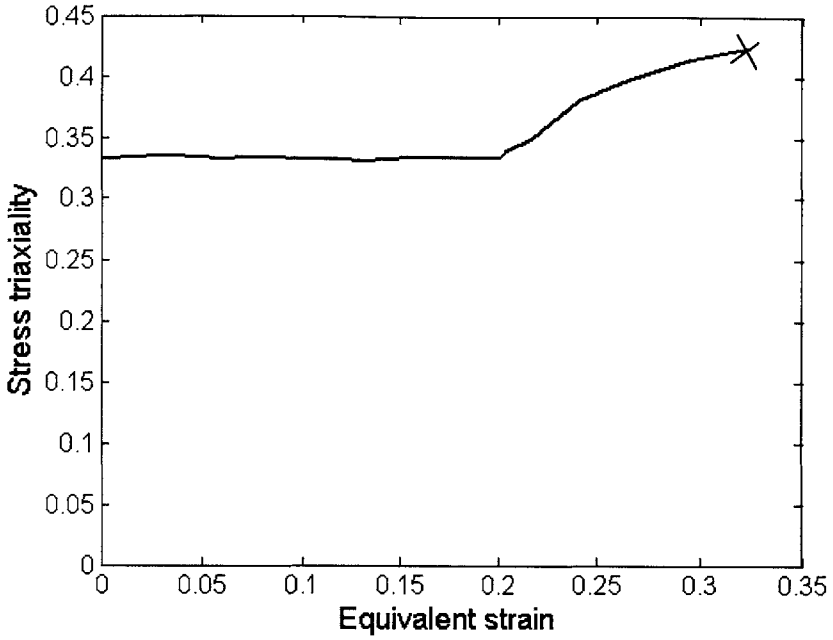

Fig. 6.12 The stress triaxiality versus the equivalent strain at crack formation location (thick-walled pipe)

6.1.3.3 Square Solid Bar

8-node solid elements were used in order to model the general 3-D stress state in the solid bar. The model developed successfully captured the diffuse necking in two directions (Fig.6.13), which is different from the flat specimen. Same deformation shape and force-displacement response up to crack formation as shown in Fig. 6.13 and Fig. 6.14, respectively, were obtained from experiments and numerical simulation. Final dimension of the minimum cross section was 7.6mm X 7.6 mm obtained from the numerical simulation, while the value was 7.5 mm X 8 mm measured from the test. The stress triaxiality versus equivalent strain is illustrated in Fig. 6.15.

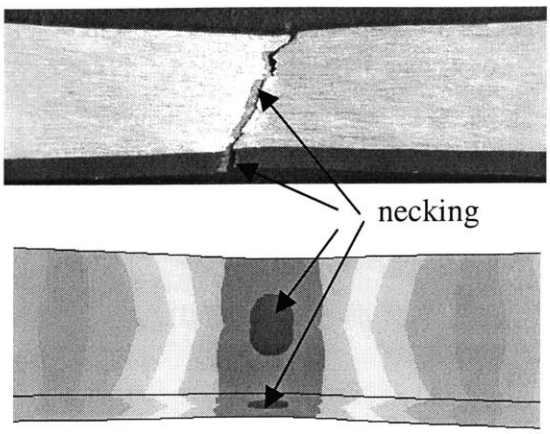

Fig. 6.13 Deformed square solid bar
(color-coded map is the equivalent strain distribution)

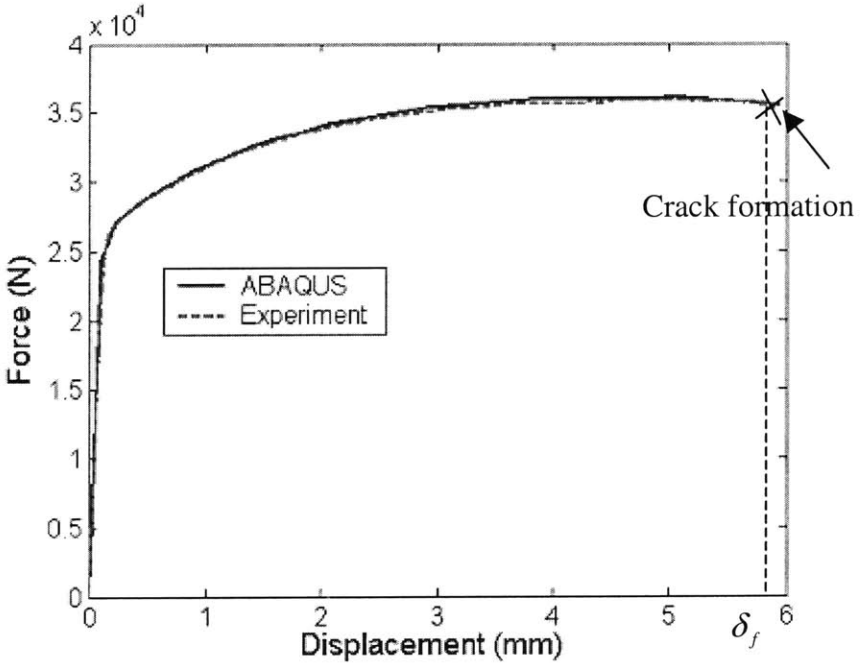

Fig. 6.14 Comparison of force-displacement response (square solid bar)

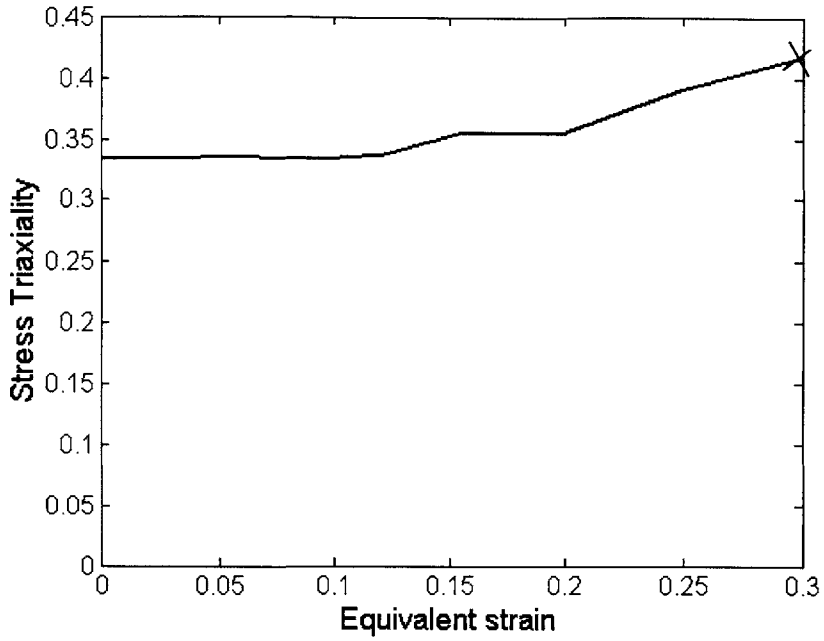

Fig. 6.15 The stress triaxiality versus the equivalent strain at crack formation location (square solid bar)

6.1.3.4 Flat-Grooved Specimen

Since the flat-grooved specimen and the loading condition was symmetric in all three directions, only 1/8 specimen was modeled by 8-node solid elements instead of plane strain elements. Diffuse necking occurring in the experiment was also observed in the numerical simulation (Fig.6.16). Final width of the minimum cross section was 48.6 mm both obtained from the numerical simulation and test. Correlation of the force-displacement response between numerical simulation and test up to crack formation was good (Fig.6.17). The stress triaxiality versus equivalent strain is illustrated in Fig. 6.18. It was found that a plane strain zone (Fig. 6.16) developed at the center region of the gauge section. This region was highly stressed and strained (Fig. 6.16). As shown in Fig. 6.19, the length of the plastic zone obtained from the simulation is 70% of the total width,

while the estimated value using McClintock and Zheng [7]'s formula (Eq. 6.9)) is 80% of the total width for this case based on Eq. (6.9) and Fig. 6.3.

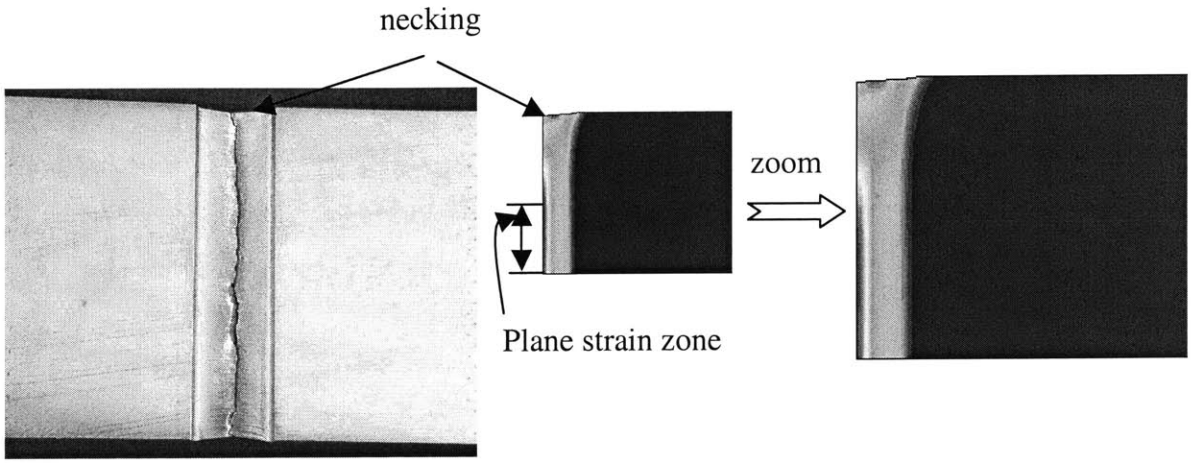

Fig. 6.16 Deformed flat-grooved specimen
(color-coded map is the equivalent strain distribution)

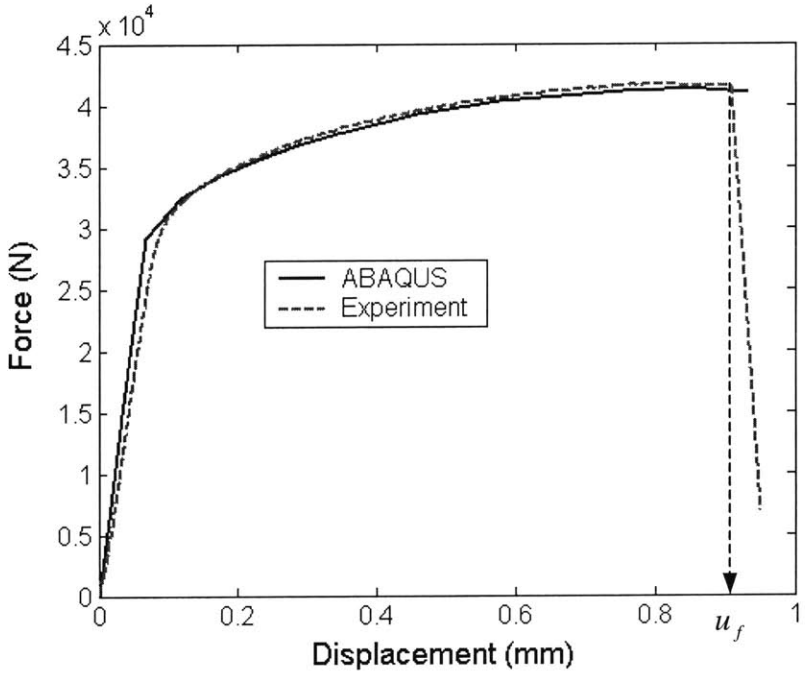

Fig. 6.17 Comparison of force-displacement response (flat-grooved specimen)

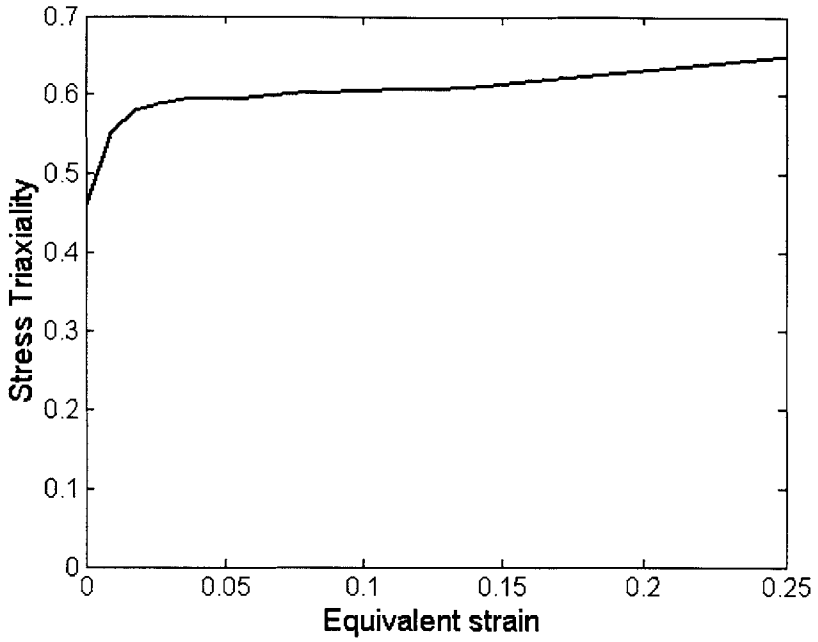

Fig. 6.18 The stress triaxiality versus the equivalent strain at crack formation location (flat-grooved specimen)

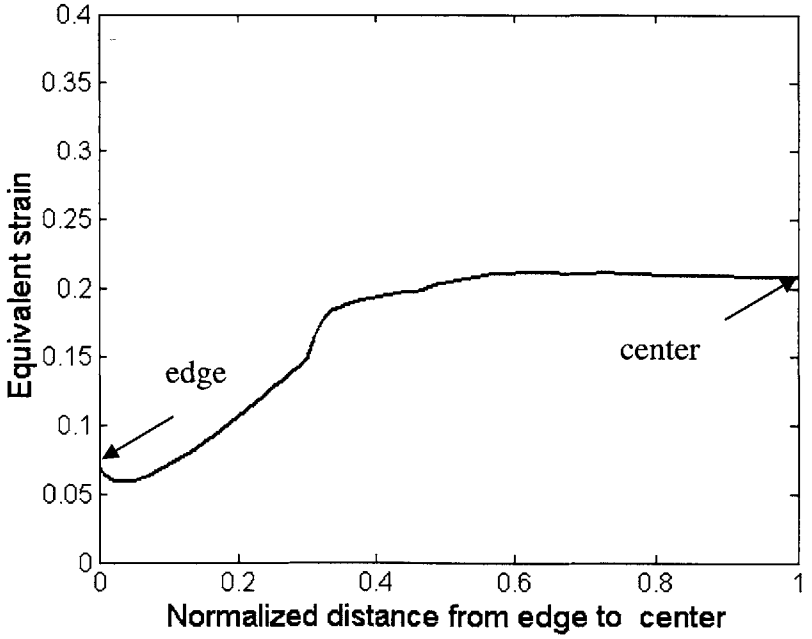

Fig.6.19 Strain distribution along the minimum cross section of the flat-grooved specimen

6.1.4 Result and Discussion

Critical Crack Location

Generally, it is not easy to see the location of crack formation because the crack propagates fast and mostly starts inside the specimens instead of on the surface. In the classical tests on flat specimens and round bars, the crack starts at the center of the neck, which is confirmed by sectioning. The critical location in this study is taken as the most possible one along the path of the final crack obtained from the test based on the fracture locus shown in Fig. 4.27. The crack formation location is at the center of the neck for the flat specimen and round bar. It agrees with the classical observation. The critical location is also at the center of the neck for the solid bar and flat-grooved specimen while it is at the inner free edge of the minimum cross section for this thick-walled pipe. In all the tests, there is a sudden load drop and system stability, which is taken as an indicator of crack formation.

Stress and Strain State

Although all the specimens are under tensile loading, the stress and strain states are quite different as summarized in Table 6.2. This is mainly due to the different geometry of the specimens and also the different necking formation. It is understandable that the equivalent strain to crack formation $\bar{\varepsilon}_f$, which is a measure of fracture ductility, is not the same for all the tensile specimens. The difference between the round bar and the flat-grooved specimen is very large. The equivalent strain to crack formation of the flat-grooved specimen is only about half of the round bar. The round smooth bar and two round notched bars have different stress triaxialities and different fracture ductility though they have same stress and strain ratios. In comparison, the flat specimen and round bar, the flat-grooved specimen and the round notched bar with $R = 12mm$ and

$a = 4mm$ have similar stress triaxialities and similar fracture ductility though they have different stress and strain ratios. Furthermore, as shown in Fig. 6.20, the result of the additional four types of tests falls fit in the fracture locus of Fig. 5.20 in the equivalent strain to crack formation and the stress triaxiality space. It seems that the equivalent strain and the mean stress triaxiality are the two most important parameters, while stress and strain ratios do not come in to the picture or are of only secondary importance.

Table 6.2 List of the parameters form FEA

Specimen	$\bar{\varepsilon}_f$	$(\frac{\sigma_m}{\bar{\sigma}})$	$\frac{(\sigma_2 - \sigma_3)}{(\sigma_1 - \sigma_3)}$	$\frac{(\varepsilon_2 - \varepsilon_3)}{(\varepsilon_1 - \varepsilon_3)}$
Flat specimen	0.44	0.38	0.1	0.33
Round bar	0.45	0.4	0	0
Thick-walled pipe	0.33	0.34	0.08	0.08
Square bar	0.32	0.36	0	0
Flat-grooved plate	0.26	0.62	0.45	0.5
Round notched bar ($R = 12mm, a = 4mm$)	0.28	0.65	0	0
Round notched bar ($R = 4mm, a = 4mm$)	0.16	0.95	0	0

* σ_1, σ_2 and σ_3 are maximum, medium and minimum principal stresses, respectively. $\varepsilon_1, \varepsilon_2$ and ε_3 are maximum, medium and minimum principal strains, respectively

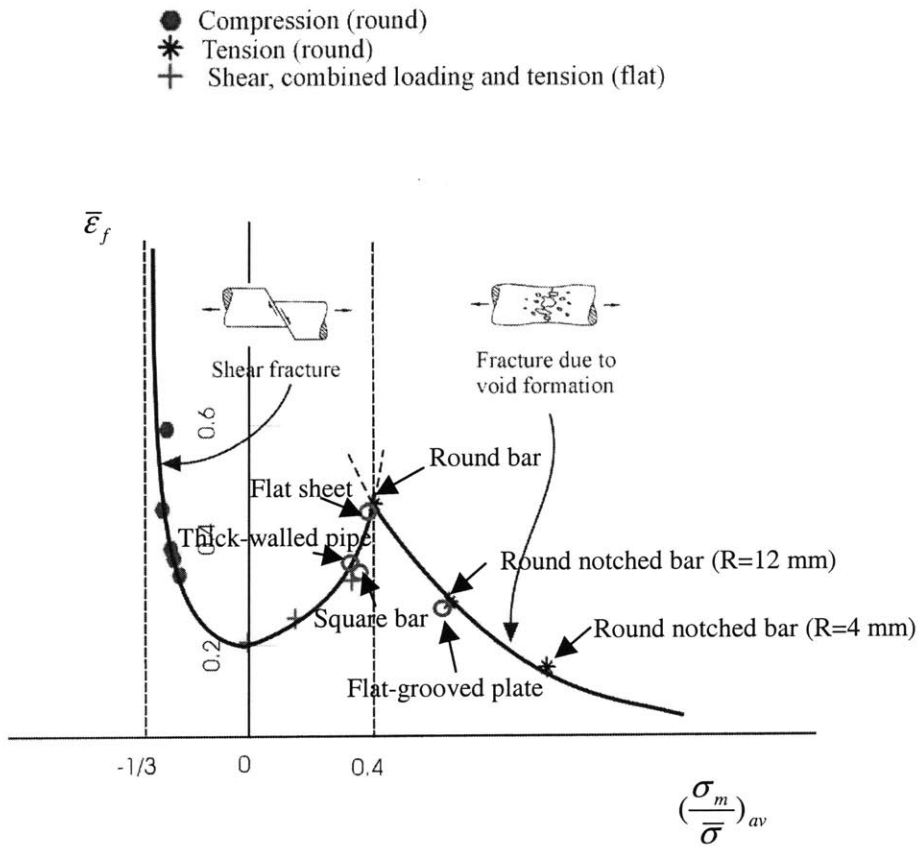

Fig. 6.20 Fracture locus in the equivalent strain and the stress triaxiality space of Al2024-T351. Open circles indicate the five points obtained in the present Chapter.

6.2 Effect of Specimen Size

The effect of specimen size on fracture has been studied in the literature. However, the focus of those studies was on fracture toughness in pre-cracked structures (eg. Bluhm [125], Taira and Tanaka [126], Chow and Nho [127], Pardoen et al. [128, 129], Minami et al. [130]). However, the literature still lacks studies of size effect on crack formation in uncracked bodies. Recently, Okazawa et al. [131] studied necking bifurcation in tensile steel specimens. The importance of the 3-D analysis for thick steel plates was emphasized in their work but the difference between 2-D analyses and 3-D analyses was not quantitatively assessed.

In this section, the dependence of specimen size on crack formation in uncracked bodies is investigated in the problem of rectangular plates with a circular hole at the center (Fig. 6.21) subjected to tensile loads. Eighteen specimens with different thicknesses (t_0=2mm-12mm) of the plate and different diameters of holes (d_{t0}=10mm-40 mm) were tested in order to get a wide range of the ratio of thickness to ligament and the ratio of diameter of hole to ligament. The ligament is defined as $l_{t0} = (w_0 - d_{t0})/2$ as shown in Fig. 6.21. A solid element finite element model as well as a shell element model for each case was developed to study effectiveness of shell element formulation on local stress and strain and then fracture ductility quantitatively.

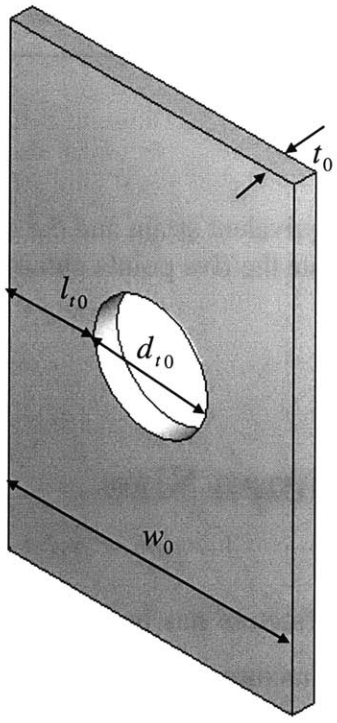

Fig.6.21 Geometrical parameters describing the specimen for size effect

6.2.1 Experiments

Tensile tests on 18 different specimens shown in Fig. 6.22 were carried out using a universal testing machine (Model 45G, MTS System Corporation, Eden Prairie, MN) with a 200 kN load cell at a loading rate of 0.2 mm/sec. As shown in Fig.6.21, the specimens are characterized by width w_0, thickness t_0, diameter of hole d_{t0} and ligament l_{to}. In this study, all plates had the same width of 50mm, but different thickness. Detailed dimensions of the specimens are listed in Table 6.3. All those specimens shown in Fig. 6.22 were cut from the same block of 2024-T351 aluminum alloy. During the test, an extensometer of 50 mm gage length was used to measure the displacement. Load-displacement responses were recorded using TestWorks software (Sintech Division, MTS). Tests were stopped as soon as either the crack formation was observed by naked eye or a sudden drop of the load starts to occur. Initial setup and final deformed and cracked specimens are illustrated in Fig. 6.23 and Fig. 6.24, respectively. As an example, the deformed shape for a thin plate (t_0=2mm, d_{t0}=20mm), a medium thick plate (t_0=5mm, d_{t_0}=40mm) and a very thick plate (t_0=12 mm, d_{t0}=40mm) together with a color-coded equivalent strain distribution (obtained from numerical simulation which will be discussed in the following section) are shown in Fig. 6.25, Fig. 6.26 and Fig.6.27, respectively. An important feature of the design of specimens was that crack started at the same location, which was middle of the circumferential surface of holes perpendicular to the load (See Fig. 6.24, 6.25(a), 6.26(a) and 6.27(a)). The presence of the hole prevented necking at the critical location thus avoiding complicated issues caused by necking during the entire plastic deformation. However, it should be noted that the location of crack formation would change to the center of the ligament for the holes with infinite radius. In the deformed specimens illustrated in Fig. 6.25 (a), Fig. 6.26 (a) and Fig. 6.27(a), there was a clear necking at the both edges of the plate, but not at the edges of the hole because of the inhomogeneous stress and strain fields caused by the hole.

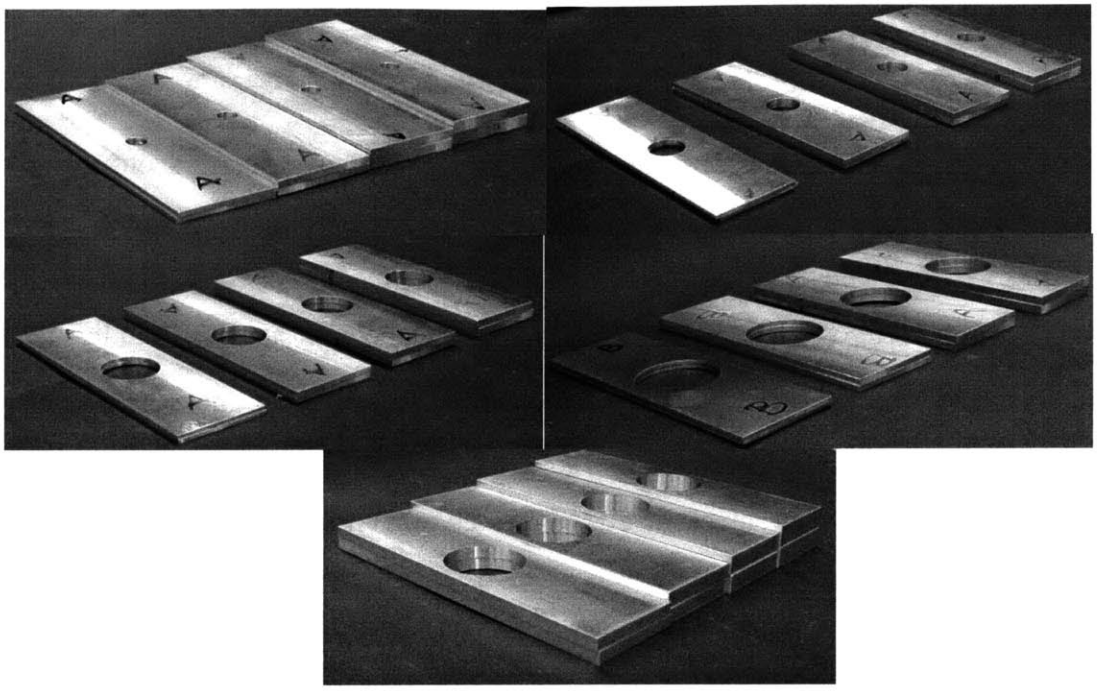

Fig. 6.22 Specimens with different thickness and size of holes

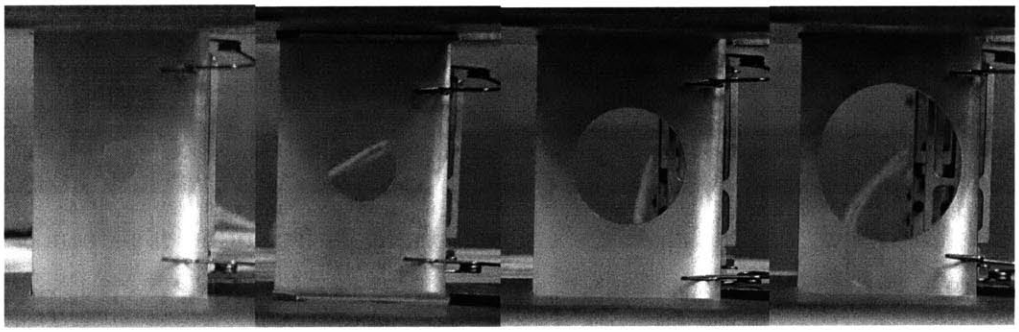

a) d_{t0}=10 mm b) d_{t0}=20 mm c) d_{t0}=30 mm d) d_{t0}=40mm

Fig. 6.23 Initial setups for specimens with different holes

Table 6.3. Geometry of specimens for studying thickness and size effect

Specimen	Width w_0 (mm)	Thickness t_0 (mm)	Diameter of hole d_{t0} (mm)	Ligament l_0 (mm)	$\bar{t} = \frac{t_0}{l_{t0}}$	$\bar{d} = \frac{d_{t0}}{l_{t0}}$
1	50	2	10	20	0.1	0.5
2	50	3	10	20	0.15	0.5
3	50	4	10	20	0.2	0.5
4	50	5	10	20	0.25	0.5
5	50	2	20	15	0.133	1.33
6	50	3	20	15	0.2	1.33
7	50	4	20	15	0.267	1.33
8	50	5	20	15	0.333	1.33
9	50	2	30	10	0.2	3
10	50	3	30	10	0.3	3
11	50	5	30	10	0.5	3
12	50	2	40	5	0.4	8
13	50	3	40	5	0.6	8
14	50	4	40	5	0.8	8
15	50	5	40	5	1	8
16	50	8	40	5	1.2	8
17	50	10	40	5	2	8
18	50	12	40	5	2.4	8

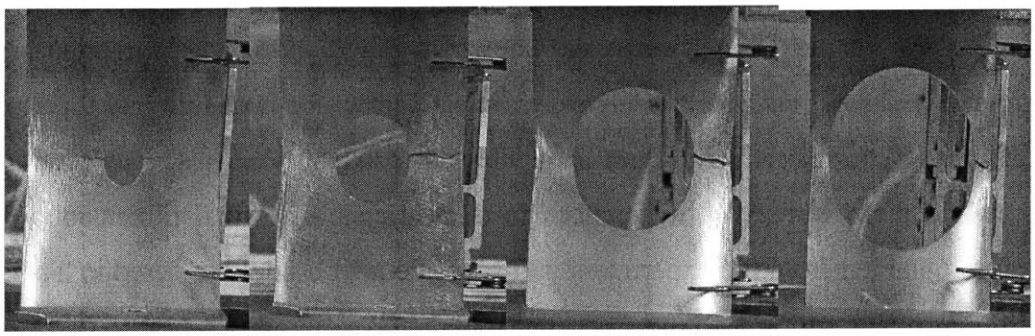

a) d_{t0}=10 mm b) d_{t0}=20 mm c) d_{t0}=30 mm d) d_{t0}=40mm

Fig. 6.24 Final deformed shapes of specimens with different holes ($t_0 = 2$ mm)

6.2.2 Numerical simulations

Parallel numerical simulations of all the 18 tests were performed using the commercial finite element code ABAQUS/STANDARD in order to obtain individual components of stress and strain tensors at the location of crack formation.

In the numerical simulations, all specimens were modeled as 8-node solid elements (eg. Fig. 6.28 (a)) as well as 4-node shell elements (eg. Fig. 6.28 (b)) to evaluate the effectiveness of shell element discretization. A finite velocity was applied to one end of the model while the other end was fixed. In all simulations, two or three different meshes for each case were developed to study mesh sensitivity. The difference of local strain and stress was small (within 4%)).

Comparisons of deformed configurations from experiments and numerical simulations for a thin plate (t_0=2mm, d_{t0}=20mm), a medium thick plate (t_0=5mm, d_{t0}=40mm) and a very thick plate (t_0=12mm, d_{t0}=40mm) are displayed in Fig. 6.25, Fig. 6.26 and Fig. 6.27, respectively. The solid element model successfully captured the necking and the thinning in both the thin and the thick plate. The shell element model was able to capture the necking in both the thin and thick plates, but failed to capture the thinning in the thick plate. Comparisons of force-displacement responses between tests and numerical simulations for all the 18 specimens are shown in Fig. 6.29-6.32. Correlations of the experiments and solid element models were almost perfect for both thin and thick plates. Correlations of the experiments and shell element models were also perfect for thin plates, while there were 10% differences in thick plates. The final dimensions of the specimens obtained from the experiment and solid element model are listed in Table 6.4. The difference was within 5%.

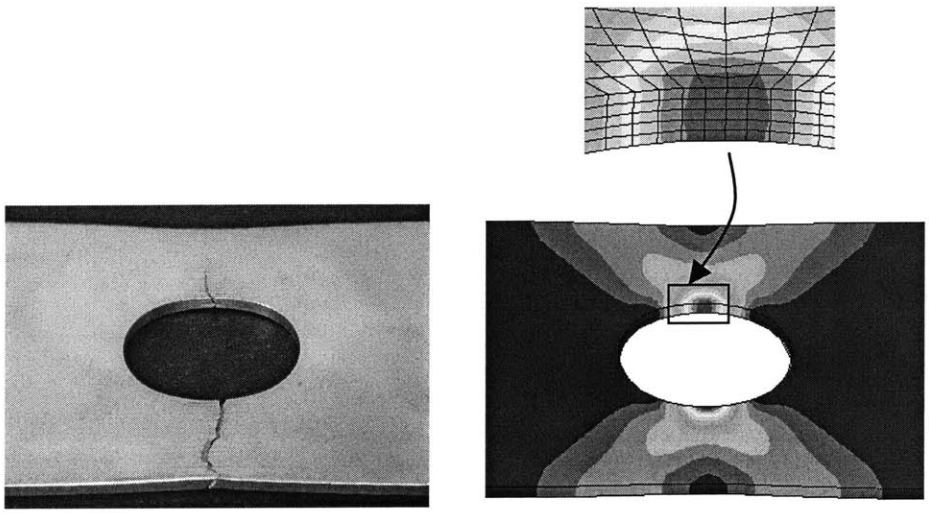

a) experiment b) solid element (equivalent strain distribution)

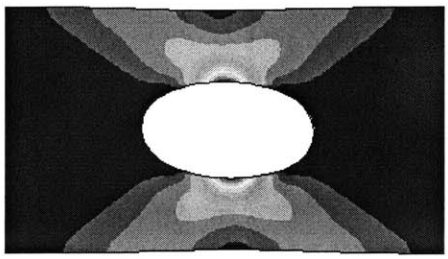

c) shell element (equivalent strain distribution)

Fig. 6.25 Comparison of deformed shape from experiments and numerical simulations

(t_0=2 mm, d_{t0}=20 mm, $\bar{t} = 0.1$, $\bar{d} = 0.5$)

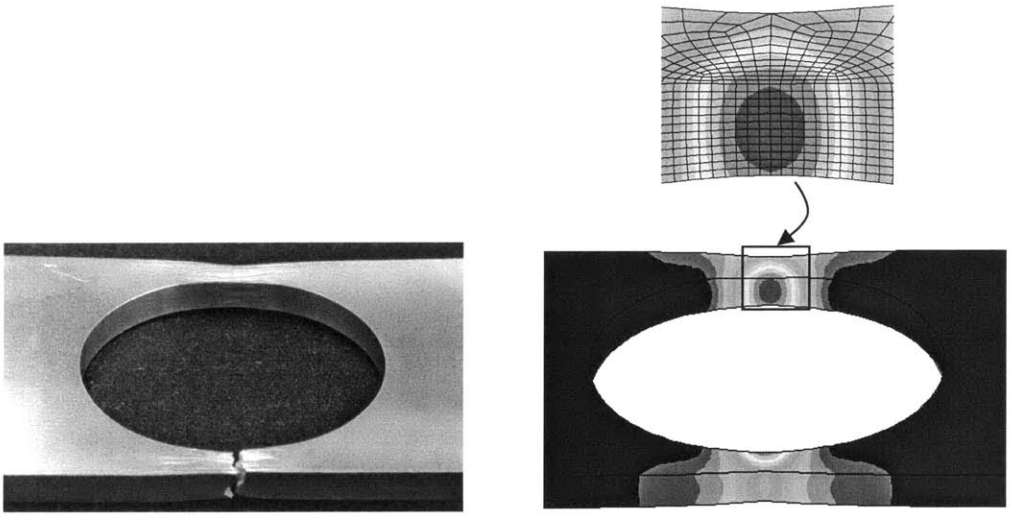

a) experiment b) solid element (equivalent strain distribution)

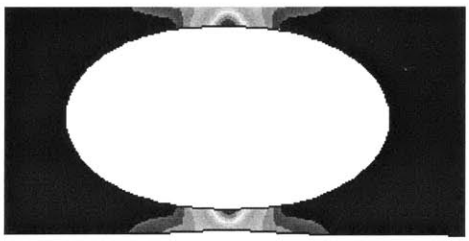

c) shell element (equivalent strain distribution)

Fig. 6.26 Comparison of deformed shape from experiments and numerical simulations

(t_0=5 mm, d_{t_0}=40 mm, $\bar{t}=1$, $\bar{d}=8$)

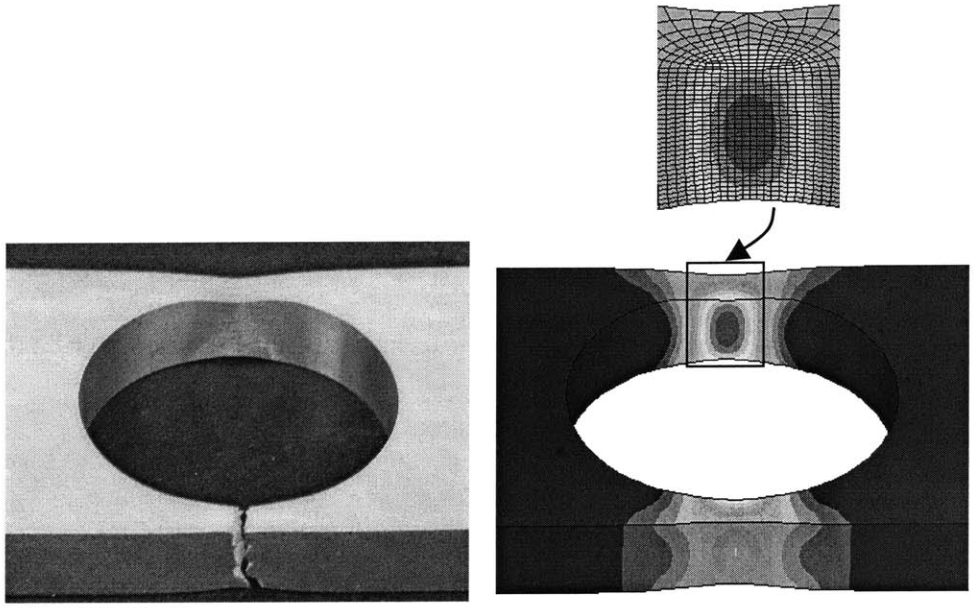

a) experiment b) solid element (equivalent strain distribution)

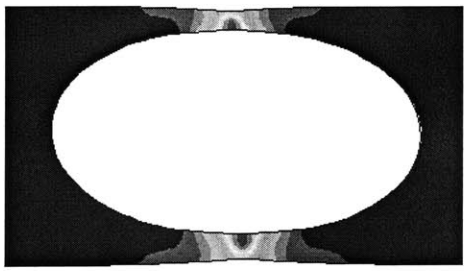

c) shell element (equivalent strain distribution)

Fig. 6.27 Comparison of deformed shape from experiments and numerical simulations

(t_0=12 mm, d_{t0}=40 mm, $\bar{t} = 2.4$, $\bar{d} = 8$)

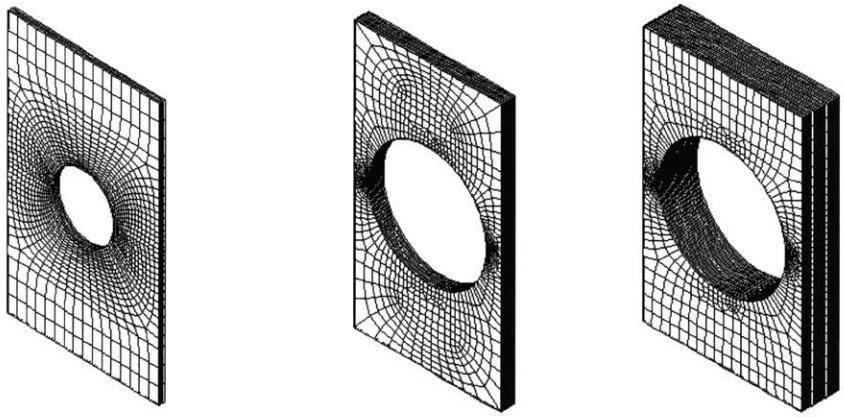

d_{t0}=20mm, t_0=2mm　　d_{t0}=40mm, t_0 =5 mm　　d_{t0}=40mm, t_0=12 mm

a) solid element models

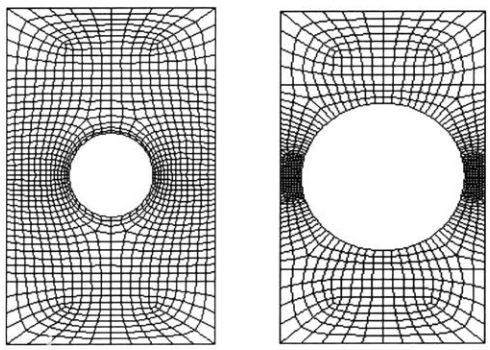

d_{t0}=20mm,　　d_{t0}=40mm

b) shell element models

Fig. 6.28 Finite element models of the specimens for size effect

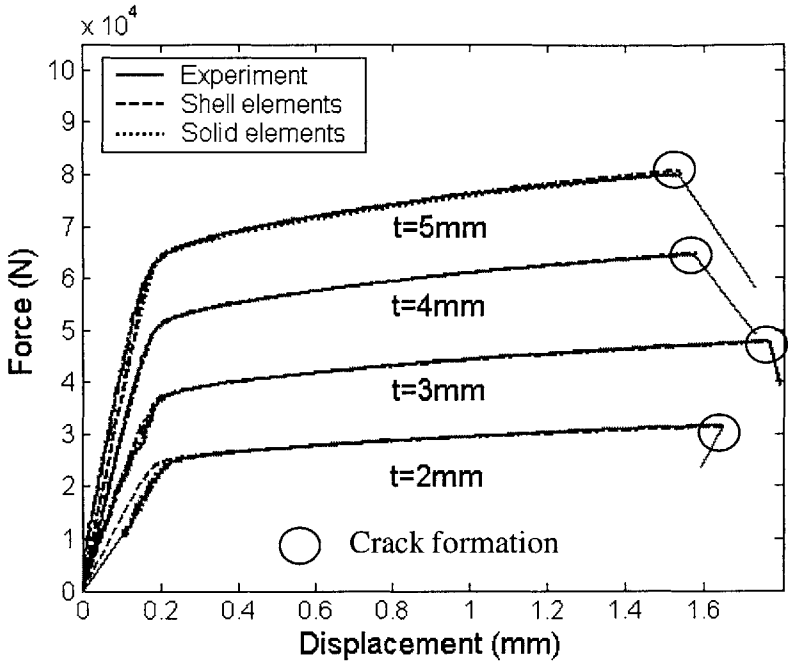

Fig. 6.29 Comparisons of force-displacement responses (d_{t0}=10mm)

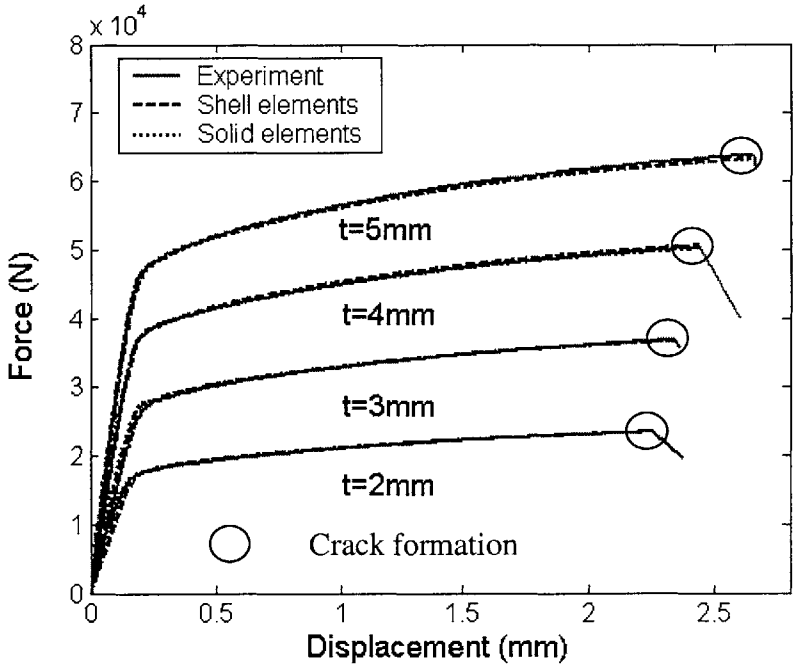

Fig. 6.30 Comparisons of force-displacement responses (d_{t0}=20mm)

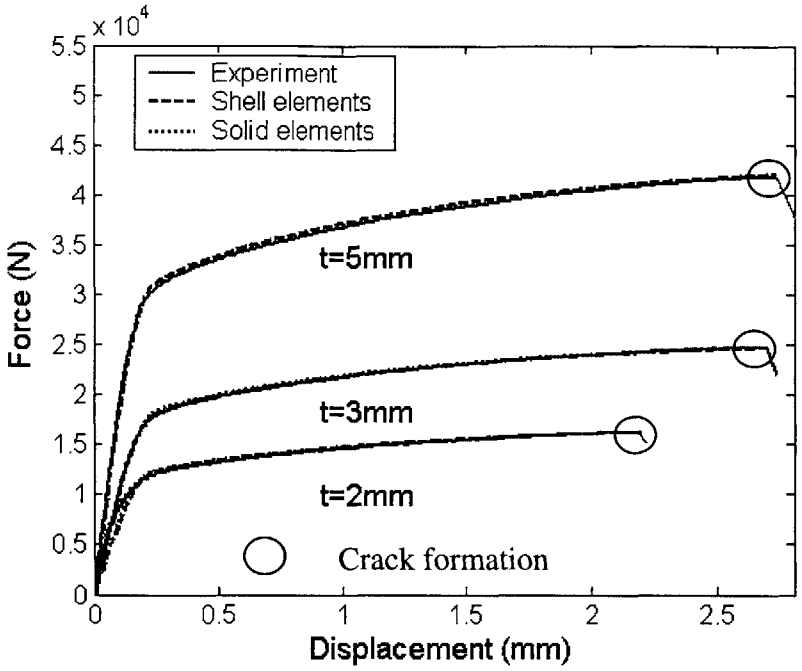

Fig. 6.31 Comparisons of force-displacement responses (d_{t0}=30mm)

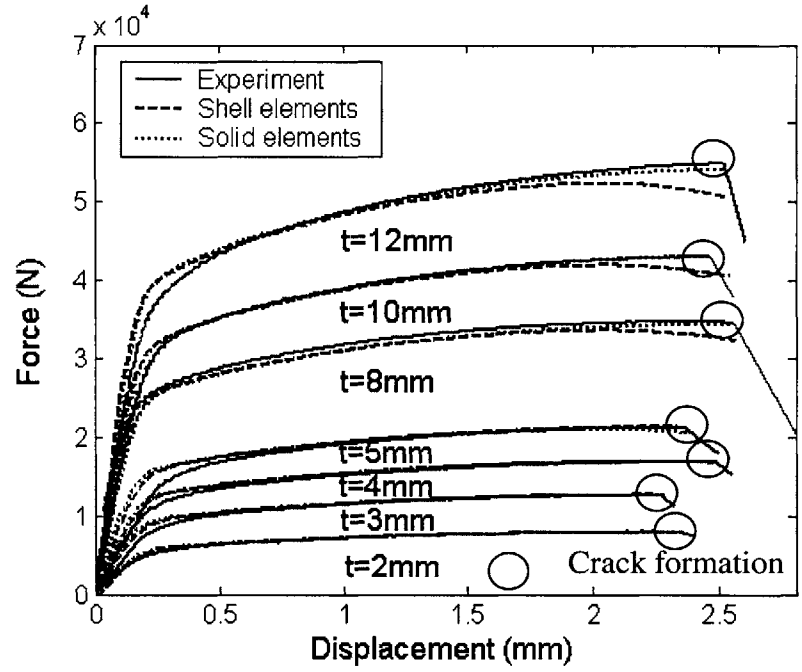

Fig. 6.32 Comparisons of force-displacement responses (d_{t0}=40mm)

Table 6.4. Final dimensions of specimens for studying thickness and size effect

Specimen	Thickness t_f (mm)		Ligament l_f (mm)	
	ABAQUS (Solid element model)	TEST	ABAQUS (Solid element model)	TEST
1	1.72	1.7	19.6	19.4
2	2.54	2.6	19.5	19.4
3	3.5	3.5	19.6	19.2
4	4.42	4.7	19.6	19.2
5	1.75	1.7	14.5	14.8
6	2.59	2.62	14.4	14.2
7	3.47	3.53	14.4	14.0
8	4.26	4.37	14.3	13.8
9	1.77	1.78	9.5	9.47
10	2.52	2.62	9.3	9.2
11	4.28	4.4	9.3	9.0
12	1.7	1.7	4.37	4.2
13	2.58	2.65	4.46	4.32
14	3.4	3.28	4.42	4.3
15	4.32	4.38	4.51	4.3
16	6.9	6.79	4.52	4.3
17	8.7	8.6	4.56	4.4
18	10.5	10.3	4.59	4.53

6.2.3 Results and Discussion

There was a sudden load drop in the force-displacement responses obtained from tests (Fig. 6.29-6.32). This drop is taken as crack formation in this study. The test for one of the specimens (d_{t0}=10 mm) was successfully stopped just after crack formation as shown

in Fig. 6.24 (a). The corresponding load-displacement response of this case still experienced a rapid drop, but not to zero. Therefore, it is reasonable to take the start of this drop as the displacement to crack formation.

As shown in Fig. 6.33-6.36 the stress triaxiality at the critical location is almost a constant during the deformation. Moreover, the magnitude of the mean stress triaxiality of all the cases is similar and is close to 1/3 which characterizes the uniaxial tension. Therefore, the integrand in Eq. (5.4) is the same and constant for all the 18 specimens under the present proportional loading. Then, Eq.(5.4) reduces to

$$\varepsilon_f = \text{Const} \tag{6.12}$$

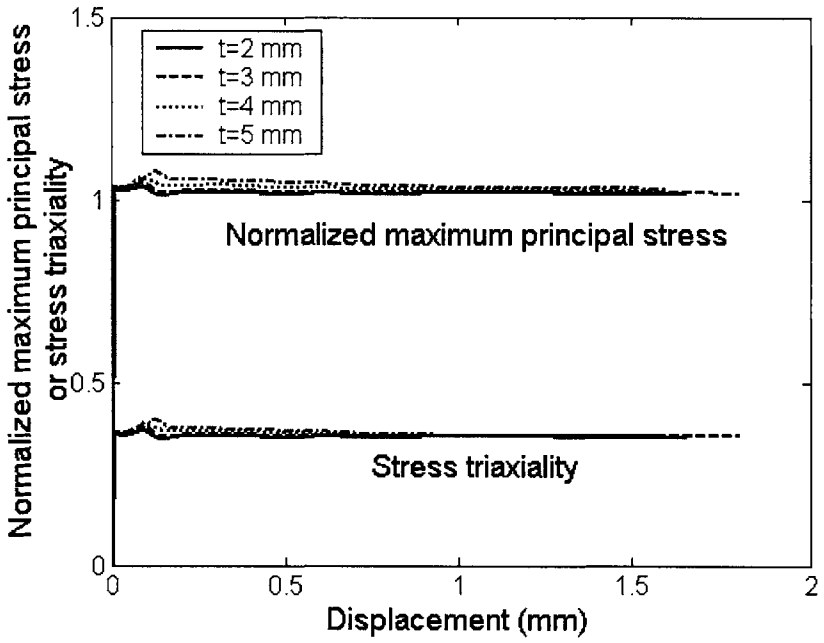

Fig. 6.33 Evolution of normalized maximum principal stress and stress triaxiality at the critical location (d_{t0}=10 mm)

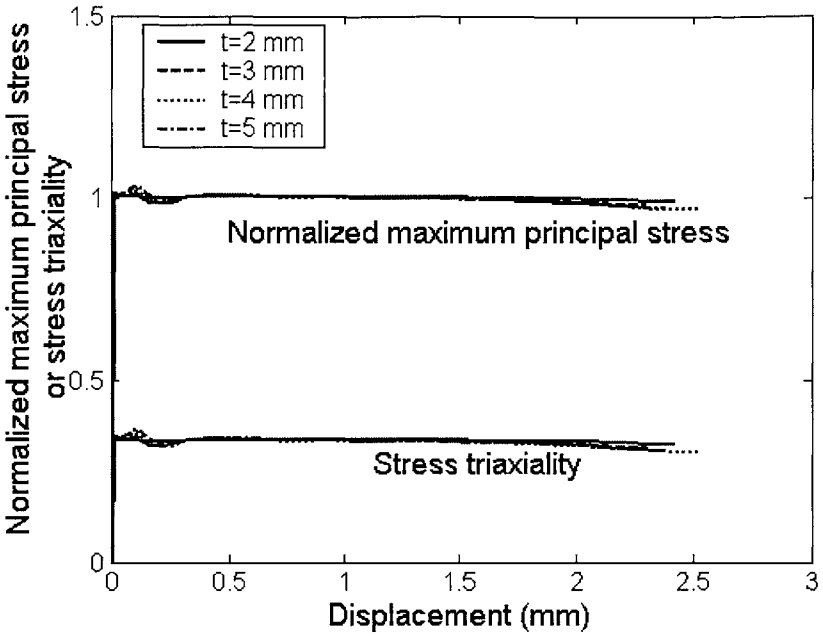

Fig. 6.34 Evolution of normalized maximum principal stress and stress triaxiality at the critical location (d_{t0}=20 mm)

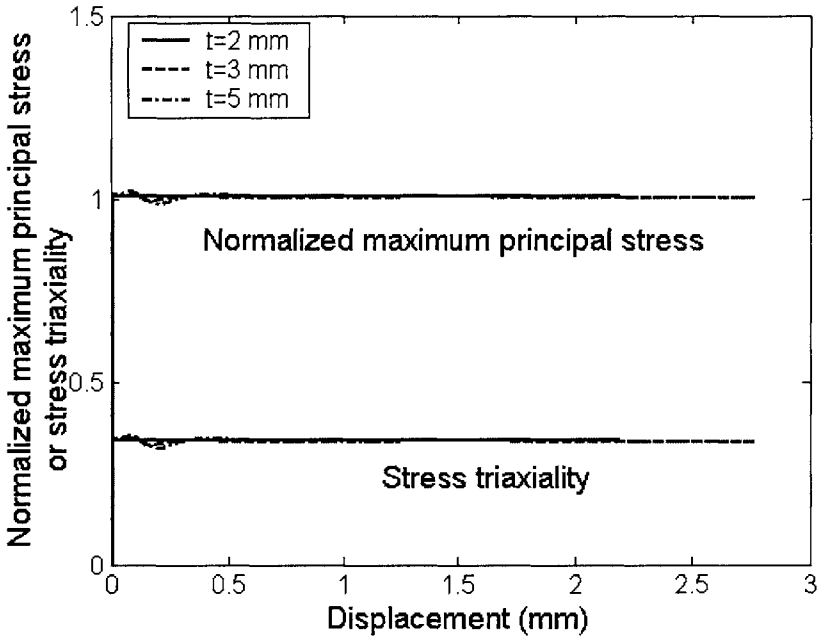

Fig. 6.35 Evolution of normalized maximum principal stress and stress triaxiality at the critical location (d_{t0}=30 mm)

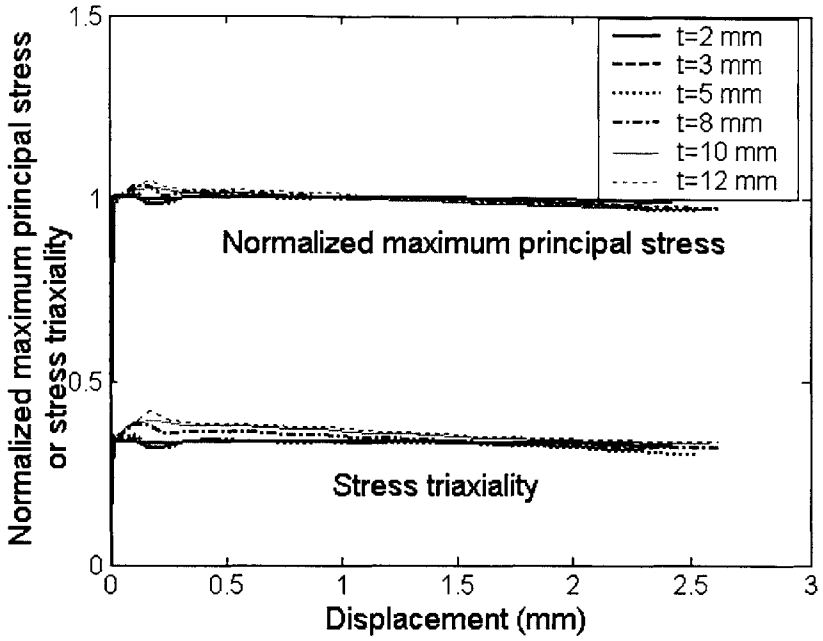

Fig. 6.36 Evolution of normalized maximum principal stress and stress triaxiality at the critical location (d_{t0}=40 mm)

The two non dimensional parameters $\bar{t}$, $\bar{d}$ defined in Table 5.3 are used to represent the specimens. The equivalent strains to crack formation is determined from numerical simulations of both solid element model and shell element model as the equivalent strains at the critical locations at the stage of crack formation which was obtained from the tests. Comparison of results obtained from the solid element model and shell element model is displayed in Fig.6.37. The difference is within 5% for $\bar{t} \leq 0.5$, while it becomes larger and is as high as 40% for the thickest plate. Note that the difference in the predicted load-displacement curves between solid and shell element model is much smaller. For thin plates ($\bar{t} \leq 0.5$), the strain distribution across the thickness is uniform and the plate can be approximately taken as in a plane stress condition (Fig. 6.25 (b)). The model using shell elements with 5 integration points is able to predict the correct strain at the critical location. However, for thick plates, the strain distribution across the thickness is not uniform as shown in Fig. 6.26 (b) and Fig. 6.27 (b). Cleary, the shell element model is insufficient to get the right strain at the critical location for thick plates ($\bar{t} > 0.5$).

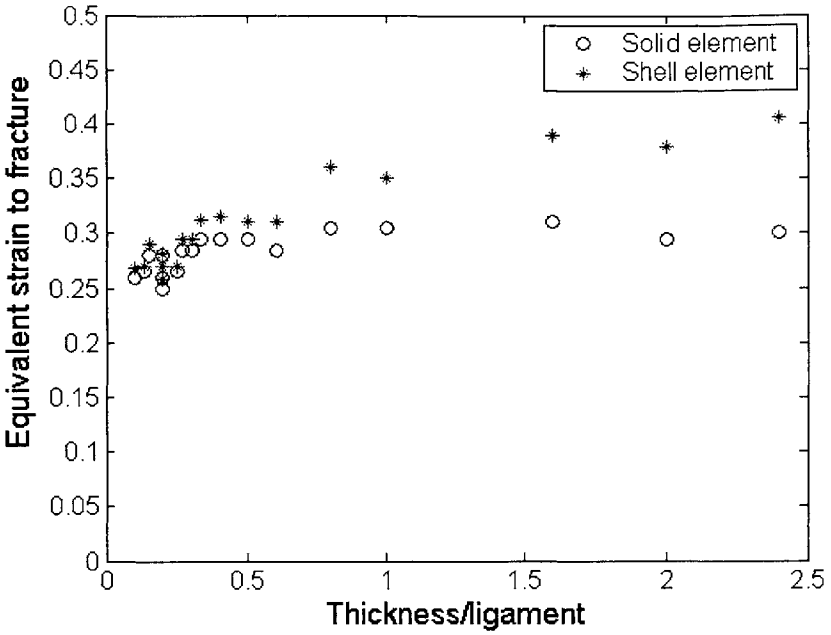

Fig. 6.37 Comparison of solid and shell element model in predicting crack formation

The dependence of the equivalent plastic strains to crack formation $\bar{\varepsilon}_f$ on the ratio of thickness to ligament $\bar{t}$ and the ratio of hole diameter to ligament $\bar{d}$ from the solid element models is shown independently in Fig. 6.38 and Fig. 6.39, respectively for all 18 data points. Eq. (6.12) gives quite good prediction (within 10 % difference) for different sizes of specimens ($0.1 \le \bar{t} \le 2.4, 0.5 \le \bar{d} \le 8$).

Size effect or stress and strain gradient effects were also expressed in statistical terms (eg. Weibull [132], McClintock [133], Minami [134]). Most of the specific ductility distribution proposed in the literature is either stress or strain based but not both of them. McClintock [133] used a strain based specific ductility distribution. An effective length for stress or strain gradient was obtained. It is clear that stress or strain only is not enough to characterize ductility. The application of statistical model with either stress or strain based specific ductility distribution must be limited to specific cases. A more general model should be related to both strain and stress. Following the concept of statistical

model, ductility is less for larger specimen. However, it is hard to find this trend in Fig. 6.38 and Fig. 6.39.

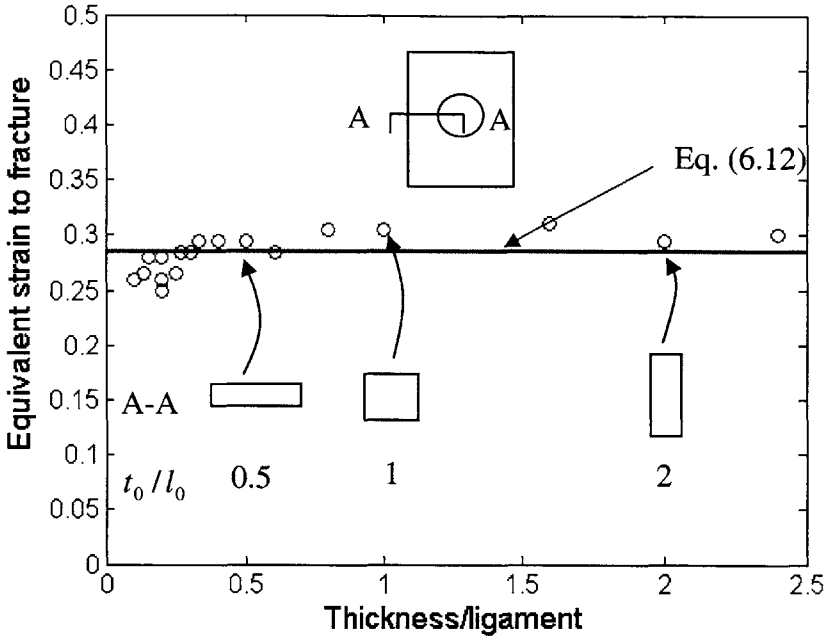

Fig. 6.38 Equivalent strain to fracture vs. normalized thickness (solid element model)

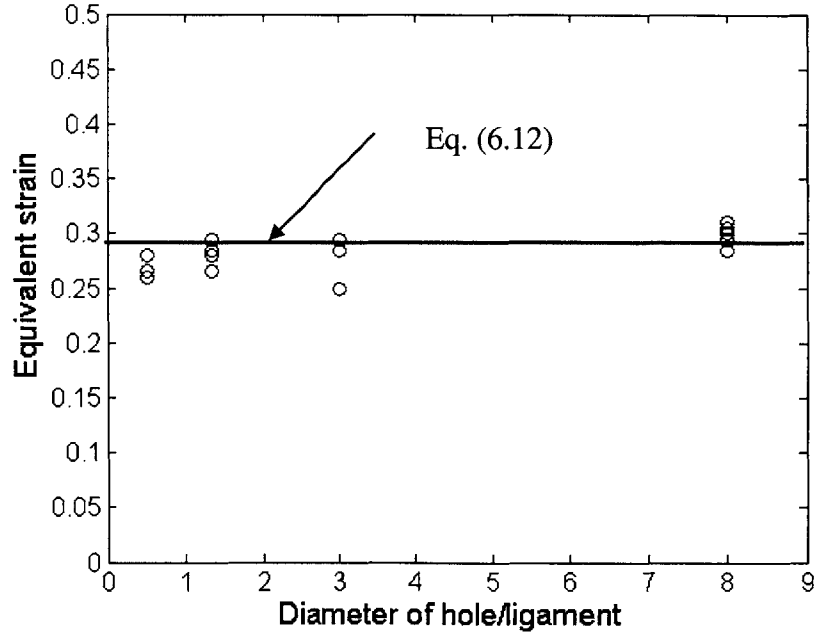

Fig. 6.39 Equivalent strain to fracture vs. normalized diameter (solid element model)

An interesting behavior is observed from the graph (Fig. 6.38). The equivalent strain to crack formation $\bar{\varepsilon}_f$ is seen to increase with the ratio of thickness to ligament $\bar{t}$ when $\bar{t} \leq 1.0$. It reaches maximum around $\bar{t} = 1.0$ and then decreases. This dependence of $\bar{\varepsilon}_f$ on $\bar{t}$ could be more precisely understood as the dependence of $\bar{\varepsilon}_f$ on the aspect ratio of the cross section of the rectangle (Fig. 6.38). Note that specimens with the same aspect ratio should have the same fracture ductility. For example, specimens with the ratio of thickness to ligament $\bar{t}$ of 0.5 and 2.0 essentially have the same aspect ratio of the cross section. And those two specimens have the same fracture ductility.

6.3 Anisotropy

Most of steels and aluminum alloys including Al 2024-T351 are often assumed isotropic in the literature and also in industry. However, due to the process of manufacturing the material may exhibit different behaviors in different directions. It should be mentioned that for FCC materials such as aluminum alloy, it is almost isotropic elastically and plastically. Here we consider possible anisotropy in crack formation. The specimens tested in the previous sections were machined from the rolling direction as shown in Fig. 6.40. The loading acting on the specimens during the test was in the rolling direction.

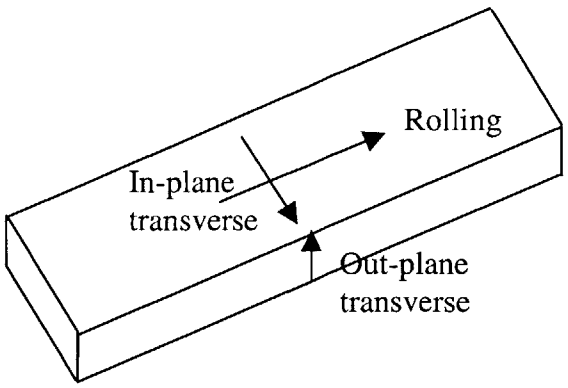

Fig. 6.40 Orientation in a material block

Hancock and Mackenzie [4] conducted a series of tensile tests on notched specimens cut from the two transverse directions on three different steels (Q1, HY130 and ESR) using the Bridgman formula. It was found that the difference of equivalent strain to crack formation with same stress triaxiality obtained from the specimens cut from the two different transverse directions was small (within 15%) in ESR, while the difference of equivalent strain to crack formation was large (more than 40%) in both Q1 and HY130. However it should be pointed out again the result needs revisited due to the inaccuracy of the Bridgman formula (See Chapter 3). Lesuer [135] performed an experiment study on Ti-6Al-4V titanium and 2024 –T3 aluminum in the three different directions for compression and in the two in-plane directions for tension. No difference of strain at crack formation in tensile specimens of Ti-6Al-4V cut in the two in-plane directions was found, while small difference (less than 15%) was observed in compression in the three different directions. The difference in ductility of 2024–T351 aluminum alloy was very small (less than 3%) in tension in the two in-plane directions (no data was given in compression).

To further study the possible anisotropy of Al 2024-T451, short cylinders with a height of 12.5 mm and diameter of 12.5 mm were cut from the current block of Al2024-T351 along the in-plane transverse direction shown in Fig. 6.40. Recall that cylinders machined along the rolling direction with the same geometry have been studied in Chapter 4. Comparison of the force-displacement response is displayed in Fig. 6.41. The difference of the maximum force before crack formation is within 3%. The difference of the displacement to crack formation gives a small difference in equivalent strain to crack formation. The equivalent strain to crack formation in compression in the rolling direction is 0.36 while it is 0.34 in the in-plane transverse direction. The difference is in consistent with the texture of this material illustrated in Fig. 6.42. The particle has an orientation along the rolling direction, which maybe responsible for the small difference of the force-displacement response and also the strain to crack formation. It should be mentioned that the difference of ductility between the rolling direction and the out-of-plane transverse direction may be larger.

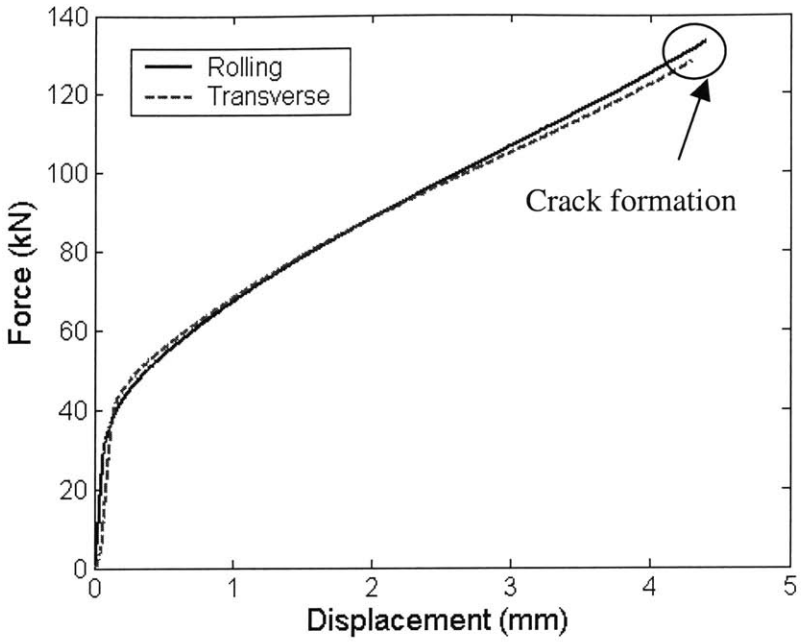

Fig. 6.41 Comparison of the force-displacement response of compression in two directions

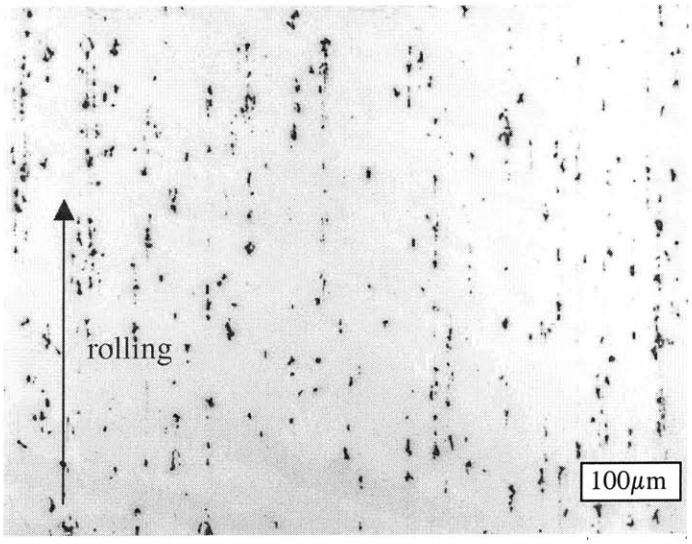

a) Polished specimen

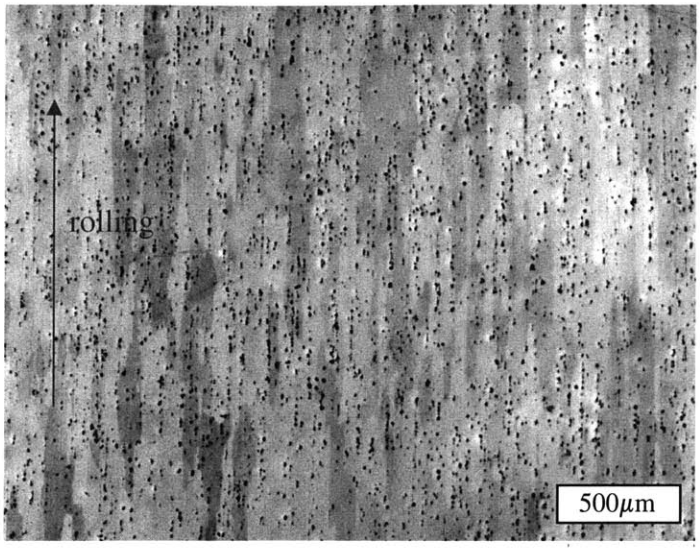

b) Etched specimen

Fig. 6.42 Texture of Al 2024-T351

Chapter 7

Ductile Crack Formation under a Single Reversal of Strain

7.1 Introduction

Previous chapters deal with crack formation under monotonic loading. However, in reality, the loading path of a material element can be complex. Structures can experience unloading and even reverse loading. For example, in the crushing of a square tube, material at the location of folds experiences a complex compression-tension loading path. The tube is under compression before any fold develops while when fold forms tensile stress and strain develop at the location of the fold. Through-thickness crack propagation in bending is another example. The material points which are originally on the compressive side go into tension as the bending axis of the beam moves with propagating crack. Also, offshore platforms and ships under wave loading, buildings under seismic loading and aircrafts under air current are good examples. Moreover, man-made

structures are usually preloaded during manufacturing. Dell et al. [136] pointed out that due to the geometrical complexity of some parts which result from functional requirements, there will be highly pre-strained regions resulting from the manufacturing process. In case of car crash the local strain history in certain members is a result of its forming process as well as subsequent deformation. The deformation of a member should be viewed as a two-stage process. It is suggested in Chapter 5 that as a first approximation, damage due to pre-loading caused by manufacturing can be superimposed to the total damage especially for the cases that two processes are in the same stress triaxiality range.

It is recognized that the effectiveness of the idea of linear superposition of damage accumulation determined in monotonic loadings strongly depends on the degree of coupling of those two stages. Probably this idea is good for processes that do not involve any reverse or cyclic loading. The effectiveness of this idea for the processes involving reversed loading is questionable since it is well known that Bauschinger effect, which is characterized by a reduced yield strength upon load reversal after plastic deformation has occurred during the initial loading, occurs during reverse loading. It is likely that similar phenomena may also exist in stress and strain to crack formation under reversed loadings.

McClintock [137] emphasized that surface roughening and the resulting strain concentration under cyclic loading can contribute to crack nucleation. Seok et al. [138] investigated effect of cyclic loading on fracture resistance curves in C(T) specimens and showed that the resistance curves decreased with decreasing minimum-to-maximum load ratio and decreasing incremental plastic displacement. Harvey [139] tested specimens of cold worked and annealed Nickel 270 in strain controlled cycling followed by monotonic tensile loading to fracture and examined the fracture surface using the scanning electron microscopy (SEM). He found that cyclic loading increased the total number of microvoids while the aspect ratio of microvoids was independent of precycling and was only a function of the monotonic tensile loading. Other studies were mostly focused on the effect of pre-loading on fracture toughness crack tip opening displacement (CTOD), J

integral and *J-R* resistance curve (eg. Cosham [140], Fields and Miller [141], El-Fadaly et al. [142], Miyata et al. [143] Homma et al. [144] and Hagiwara et al. [145])

The objective of this chapter is to evaluate the effect of reverse loading on crack formation quantitatively. In this study, crack formation occurs due to plastic overloading, which is different from high cycle fatigue which includes hundreds or thousands or even more cycles. 0-20% pre-compression followed by monotonic tension to fracture at strains of typically 20-30% are investigated. A modification to the criterion developed in Chapter 5 is presented.

7.2 Experiments

The conventional compression test and tensile test are not suitable for compression-tension reverse loadings. A special specimen and experimental step up were then designed. The specimen consists of long shoulders with screw threads and a smooth circumferential notch at the center. A fractured specimen showing the long screw thread is displayed in Fig. 7.1. The dimensions given in Fig. 7.2 were determined such that the specimen would not buckle in compression and both the stress triaxiality and equivalent strain are the largest at the center under tensile loading to make sure fracture starts at the center. A setup of the test is illustrated in Fig. 7.3. One adapter and two nuts at each end were used to connect the specimen to the testing machine and to make the specimen tight enough to provide a smooth transition from compression to tension. A light extensometer with 25.4 mm initial gage length was attached to the specimen to measure the displacement. Specimens were carefully tightened with adapters and nuts to avoid preloading.

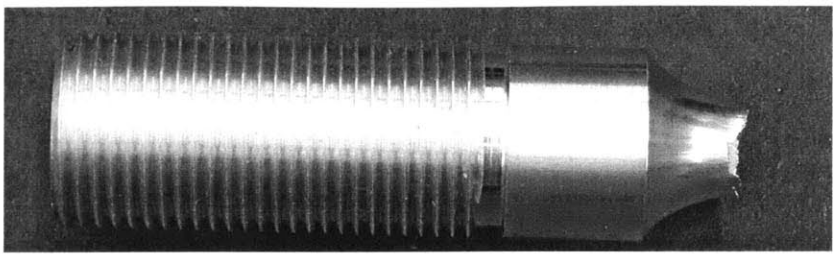

Fig. 7.1 Fractured compress-tension specimen

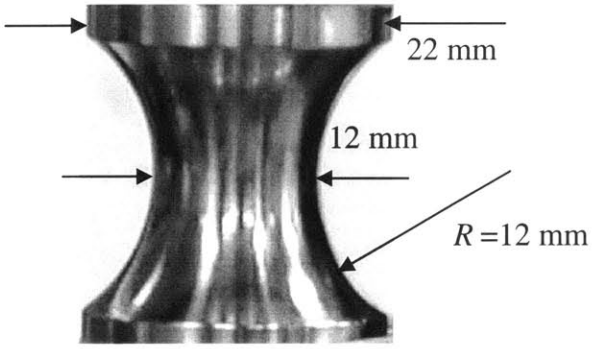

Fig. 7.2 Main dimensions of the compression-tension specimen

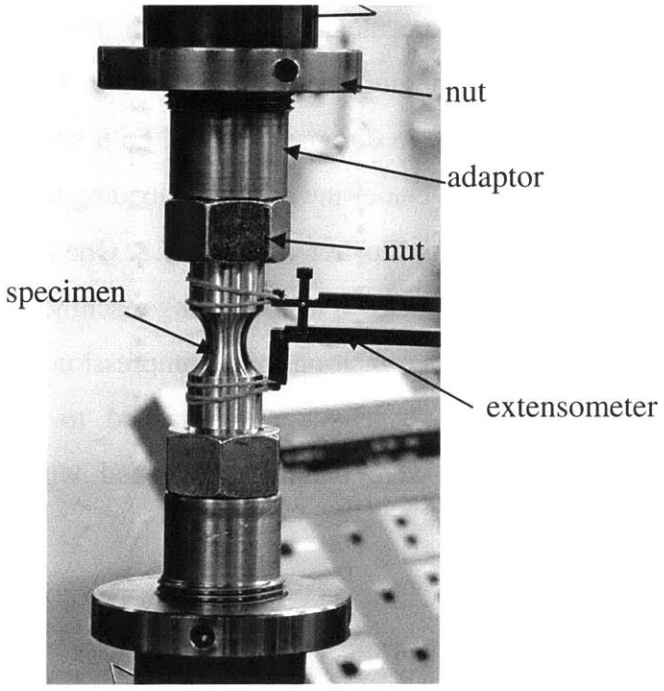

Fig. 7.3 Setup of the compression-tension test

Totally 8 specimens cut from the same block of Al2024-T351 were tested. Two specimens were pulled directly to fracture without any pre-compression. Two were compressed to 4% and then pulled to fracture. Although it does not have a practical meaning since the section inside the gauge length is different, for convenience the degree of compression η is defined as

$$\eta = \frac{l - l_0}{R/2} \tag{7.1}$$

where, l: current reading of the extensometer ; l_0: initial gage length of the extensometer = 25.4 mm.

Another pair of specimens were compressed to 8 % and then pulled to fracture. The last two specimens were compressed to 14 % and 20 %, respectively, and then pulled to fracture. Since repeatable results were obtained in loading case 1, 2 and 3, only one specimen each was tested for both loading case 4 and 5. A summary of the test is given in Table 7.1.

Table 7.1. A summary of the compression-tension test

Loading case	Compression degree η	Tension degree	Number of Samples
1	0	To fracture	2
2	4%	To fracture	2
3	8%	To fracture	2
4	14%	To fracture	1
5	20%	To fracture	1

The specimens fractured under 0% and 20% compression followed by monotonic tension to fracture are shown in Fig. 7.4. Similar rough fracture surfaces can be observed. Therefore it is reasonable to assume that the specimens failed in a same fracture mode, i.e. void nucleation, growth, and linkage. However, it can also be noticed that the final

diameter of the minimum cross section of the specimen under monotonic tension is much smaller than the one under tension with 20% pre-compression.

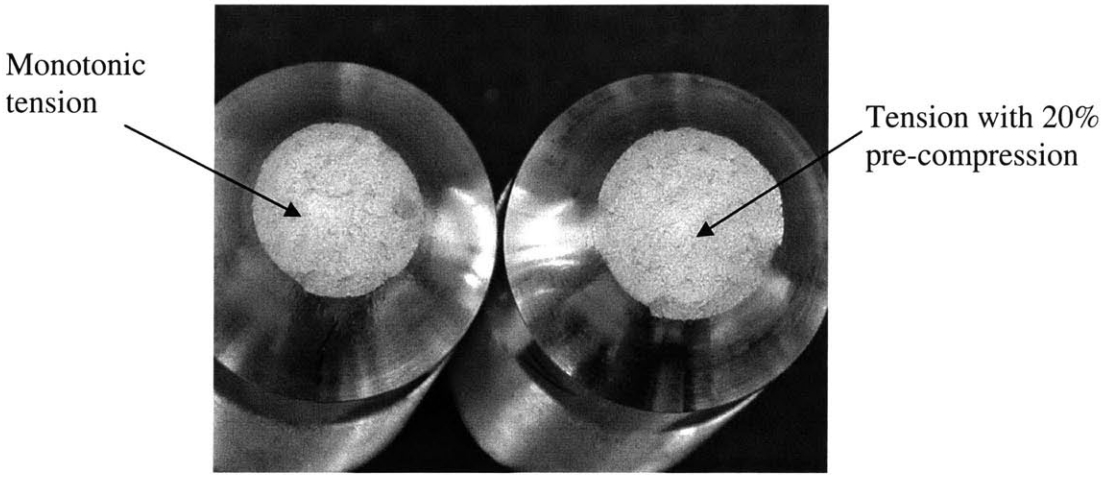

Fig. 7.4 Comparison of deformed specimens under monotonic tension and under tension with 20% pre-compression

Force-displacement responses during the tests were recorded and are displayed in Fig. 7.5. All the pre-compressed specimens went to the plastic range and followed a same path while the tensile part was quite different depending on the degree of compression η. A smooth transition from the compression to tension can be seen in the force-displacement responses. The specimen with larger η experienced a higher force level in tension but smaller final positive displacement. This result is understandable because of strain hardening of the material and different levels of plastic strain due to the pre-compression. The sudden drop of the force shown in Fig. 7.5 was due to fracture and is taken as the point of crack formation.

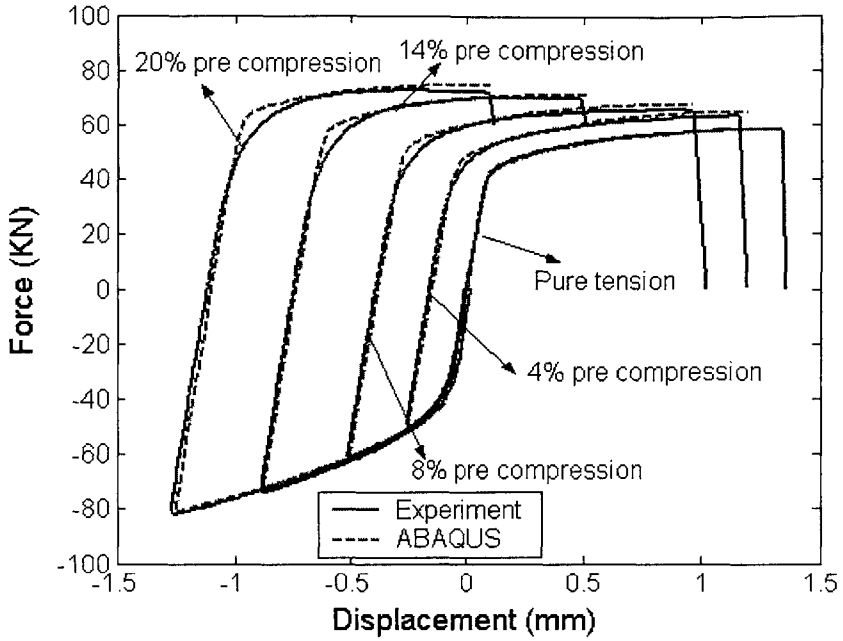

Fig. 7.5 Force-displacement responses of compression-tension tests

7.3 Numerical simulations

Parallel numerical simulations of all the tests were carried out using commercial finite element code ABAQUS. As shown in Fig. 7.6, 4-node axisymmetrical elements were used to model the specimens. A finite velocity was applied to one end of the model while the other end was fixed.

Bauschinger effect is a common phenomenon observed in cycle loading tests. This effect is characterized by a reduced yield stress upon load reversal after plastic deformation has occurred during the initial loading. A number of material models (eg. [105, 146-149]) have been proposed in the literature to predict the Bauschinger effect. Among those models, same yield function but different evolutions of kinematic hardening and the isotropic hardening behavior were introduced The model used in this study is the

nonlinear isotropic/kinematic model embedded in ABAQUS. The yield surface is defined by the function

Fig. 7.6 Finite element mesh of compression-tension tests

$$F = f(\boldsymbol{\sigma} - \boldsymbol{\alpha}) - \sigma^0 = 0 \tag{7.2}$$

where σ^0 is the yield stress, $\boldsymbol{\sigma}$ is the stress tensor and $f(\boldsymbol{\sigma} - \boldsymbol{\alpha})$ is the equivalent Mises stress with respect to the backstress tensor $\boldsymbol{\alpha}$ which is defined as

$$\mathrm{f}(\boldsymbol{\sigma} - \boldsymbol{\alpha}) = \sqrt{\frac{3}{2}(\boldsymbol{S} - \boldsymbol{\alpha}^{dev}):(\boldsymbol{S} - \boldsymbol{\alpha}^{dev})} \tag{7.3}$$

where $\boldsymbol{S}$ is the deviatoric stress tensor and $\boldsymbol{\alpha}^{dev}$ is the deviatoric part of the backstress tensor.

This model assumes associated plastic flow rule, which gives the relation

$$\dot{\boldsymbol{\varepsilon}} = \dot{\bar{\varepsilon}} \frac{\partial F}{\partial \boldsymbol{\sigma}} \tag{7.4}$$

where $\dot{\boldsymbol{\varepsilon}}$ is the rate of plastic flow and $\dot{\bar{\varepsilon}}$ is the equivalent plastic strain rate. The evolution of the equivalent plastic strain is obtained from the following equivalent plastic work expression,

$$\sigma^0 \dot{\bar{\varepsilon}} = \boldsymbol{\sigma} : \dot{\boldsymbol{\varepsilon}} \tag{7.5}$$

The evolution law of this nonlinear isotropic/kinematic material model consists of two components: a nonlinear kinematic hardening component, which describes the translation of the yield surface in terms of the backstress $\boldsymbol{\alpha}$, and an isotropic hardening component, which describes the change of the size of the yield surface defined by the equivalent stress σ^0 as a function of the equivalent plastic strain $\bar{\varepsilon}$. The evolutions of the kinematic hardening and the isotropic hardening behavior are given in Eq. (7.6) and Eq.(7.7), respectively.

$$\dot{\boldsymbol{\alpha}} = C_k \frac{1}{\sigma^0}(\boldsymbol{\sigma} - \boldsymbol{\alpha})\dot{\bar{\varepsilon}} - \gamma \boldsymbol{\alpha} \dot{\bar{\varepsilon}} \tag{7.6}$$

$$\sigma^0 = \sigma\big|_0 + Q_\infty (1 - e^{-b\bar{\varepsilon}}) \tag{7.7}$$

where, C_k, γ are material constants related to kinematic hardening; $\sigma\big|_0$ is the initial yield strength and Q_∞, b_i are material constants related to isotropic hardening.

A series of those material constants were introduced. The material properties listed in Table 7.2 gave the best correlation of force-displacement with the experiment.

In all simulations, besides the mesh illustrated in Fig. 7.6, a coarser mesh was also developed to study mesh sensitivity for each case. The numerical solutions (strain and stress) obtained from those two meshes were found within 2%. Force-displacement responses obtained from numerical simulations correlated quite well with experiments as shown in Fig. 7.5. Shape of the specimens at the point of crack formation of the specimen under monotonic tension and the specimen under tension with 20 % pre-compression is displayed in Fig. 7.7. As observed in the experiment, the final radius of the minimum cross section of the specimen under monotonic tension was much smaller than the specimen under tension with 20% pre-compression. The final diameters of the specimens obtained from the numerical simulation and the test were close as given in Table 7.3.

Table 7.2. Material properties of Al2024-T351

Young's modulus E (MPa)	Poisson's ration ν	C_k (MPa)	γ	$\sigma\|_0$ (MPa)	Q_∞ (MPa)	b_i
74633	0.3	750	10	300	220	14

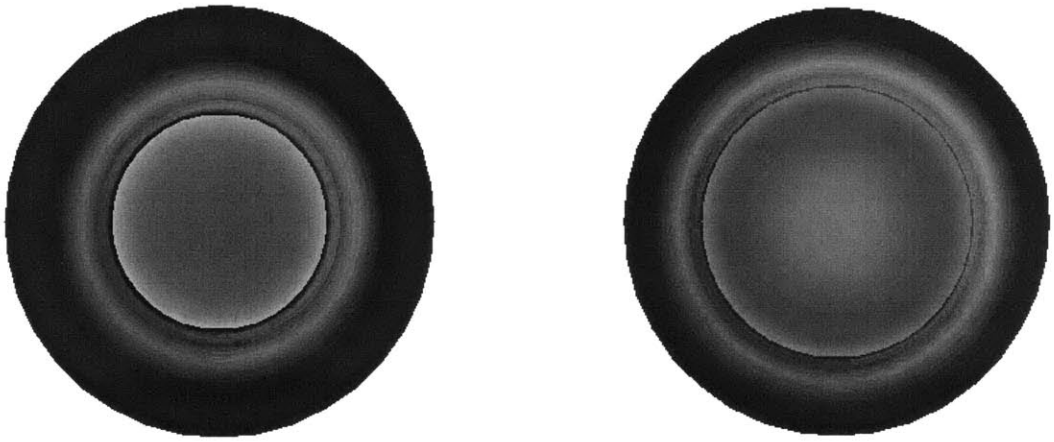

monotonic tension tension with 20% pre-compression

Fig. 7.7 Deformation at the point of crack formation of compression-tension specimen

Table 7.3 Final diameters of the specimens under compression-tension

Loading case	Test (mm)	ABAQUS (mm)
1	10.9	10.92
2	11.0	11.1
3	11.3	11.32
4	11.5	11.7
5	12.0	11.92

All points in the critical cross-section were totally under compression during the compression stage due to the relatively small degree of compression and the circumferential notch, which prevented the "barrel" effect often observed in conventional upsetting tests. No positive tensile stress was found during the entire compression process.

7.4 Fracture Criterion for Strain Reversal

The relation between the stress triaxiality and the equivalent strain at the center of the specimen is shown in Fig. 7.8. The transition point in the figure indicates the change from compression to tension. For the specimen under monotonic tension, the stress triaxiality is about 0.7 which is in the high stress triaxiality range for Al2024-T351, while for the specimens with pre-compression, the stress triaxiality is about –0.7 in the compression stage and then changes directly to a positive value in the range of the following monotonic tension.

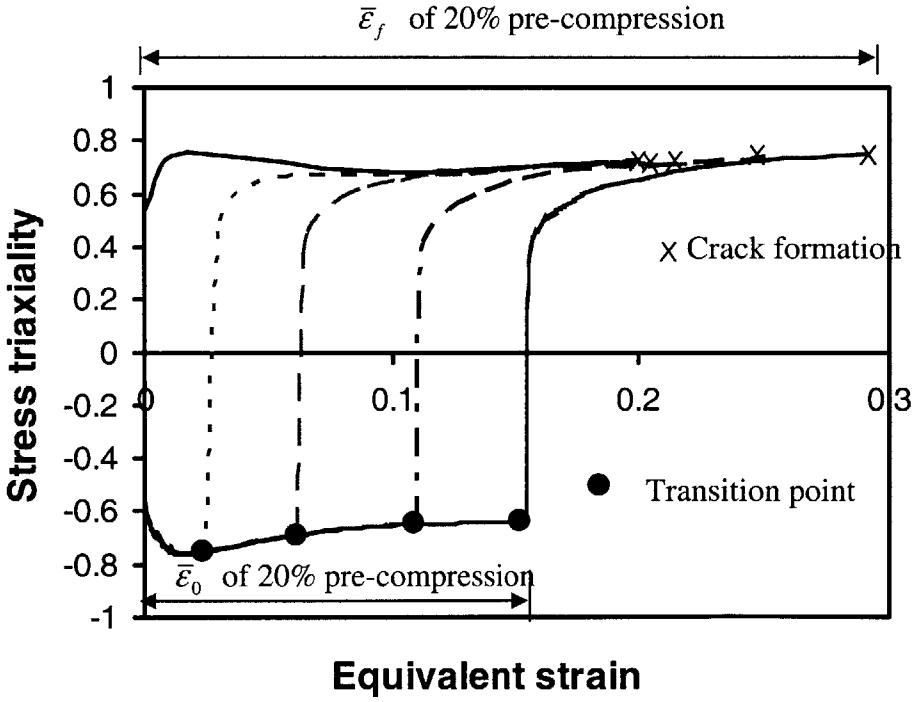

Fig. 7.8 Stress triaxiality vs. equivalent strain in compression-tension

7.4.1 Damage Superposition

The idea of damage superposition is to divide the whole process into several independent stages and calculate the individual damage and then sum them up. It is assumed that damage increments per strain and stress increment are independent of prior damage. In the problems considered here, there are two different stages for each case. The idea of superposition of damage accumulation gives

$$D = \int_0^{\bar{\varepsilon}_0} f_c(\frac{\sigma_m}{\bar{\sigma}})d\bar{\varepsilon} + \int_{\bar{\varepsilon}_0}^{\bar{\varepsilon}_f} f_t(\frac{\sigma_m}{\bar{\sigma}})d\bar{\varepsilon} \tag{7.8}$$

where, $\bar{\varepsilon}_0$ is the equivalent strain when tension starts, $f_c(\frac{\sigma_m}{\bar{\sigma}})$ and $f_t(\frac{\sigma_m}{\bar{\sigma}})$ are the weighting functions for the compression and tension, respectively.

In the compression stage, the stress triaxiality is about –0.7. As shown in Fig. 5.20, there is a cut off value at the stress triaxiality of –1/3. Thus the first term of Eq. (7.8) is zero. In the tension stage, the stress triaxiality is about 0.7 which falls in the high stress triaxiality range. Therefore Eq. (7.8) becomes

$$D = \int_{\bar{\varepsilon}_0}^{\bar{\varepsilon}_f} 6.7\frac{\sigma_m}{\bar{\sigma}}d\bar{\varepsilon} \tag{7.9}$$

It should be noted that the coefficient 6.7 was determined in Chapter 5 for Al2024-T351. Equivalent strains due to pre-compression and monotonic tension and the final accumulated damage D_c measured by Eq. (7.9) of the five cases are listed in Table 7.4. The accumulated damage under monotonic loading is unit which is the condition for crack formation. However, the final accumulated damage under monotonic tension is more than those under compression-tension. It indicates that superposition of damage accumulation defined in monotonic loadings is not proper for reverse loadings. The pre-compression plays an important role in crack formation.

Table 7.4 A summary of the damage of compression-tension tests

Loading case	$\bar{\varepsilon}_0$	$\bar{\varepsilon}_f$	$\bar{\varepsilon}_t = \bar{\varepsilon}_f - \bar{\varepsilon}_0$	D_c
1	0	0.2	0.2	1
2	0.03	0.21	0.18	0.87
3	0.06	0.23	0.17	0.73
4	0.11	0.25	0.14	0.62
5	0.155	0.29	0.13	0.53

7.4.2 A Modification to the New Criterion

From Table 7.4, it can also be seen that the equivalent strain due to pre-compression $\bar{\varepsilon}_0$, the total equivalent strain to fracture $\bar{\varepsilon}_f$ and the difference between those two values $\bar{\varepsilon}_t = \bar{\varepsilon}_f - \bar{\varepsilon}_0$ are not the same for different cases. The value of $\bar{\varepsilon}_t$ actually is the equivalent strain due to the tensile loading. This value is smaller for the cases with larger degrees of pre-compression. The relation of $\bar{\varepsilon}_t$ and $\bar{\varepsilon}_0$ is displayed in Fig. 7.9. It approximately follows a linear relation

$$\bar{\varepsilon}_t = \beta_1 - \beta_2 \bar{\varepsilon}_0 \tag{7.10}$$

where, $\beta_1 = 0.2, \beta_2 = 0.53$.

However, it should be noted that this relation is obtained from the present cases with about 0.7 stress triaxiality under the tensile loadings. Equivalent strain to fracture is strongly dependent on the stress triaxiality. Therefore, the numerical values of the two coefficients in Eq. (7.10) depend on the stress triaxiality. This relation cannot be used in the cases with different stress triaxialities.

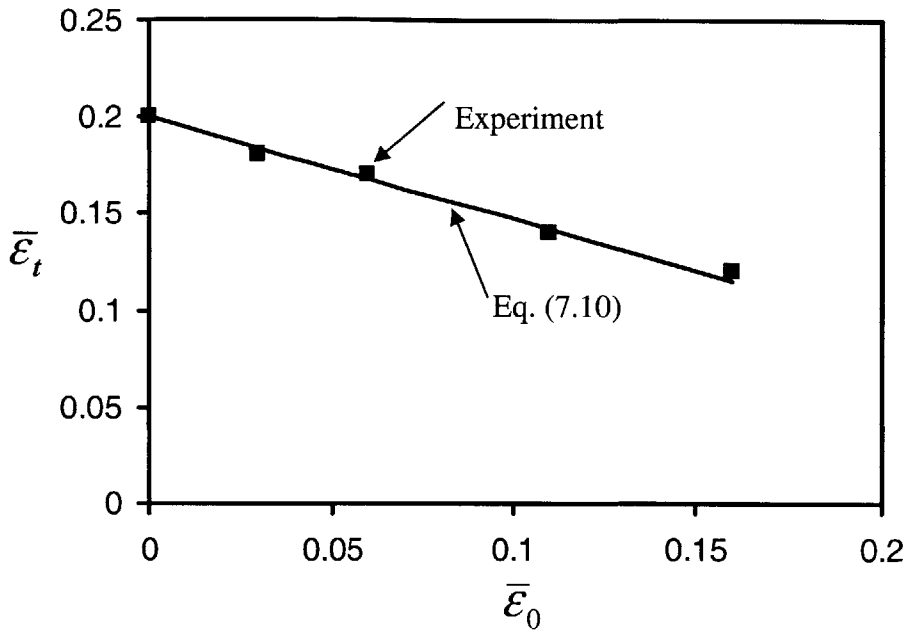

Fig.7.9. The relation of $\bar{\varepsilon}_t$ and $\bar{\varepsilon}_0$ in compression-tension tests

A more general criterion can be developed based on the fracture locus (Fig. 5.20) obtained in Chapter 5 for monotonic loadings. After a given pre-compression, the microstructure is different from the original one. We can treat that for each $\bar{\varepsilon}_0$ there is a new material. Thus Eq. (5.1) becomes

$$D = \int_{\bar{\varepsilon}_0}^{\bar{\varepsilon}_f} \frac{1}{C(\bar{\varepsilon}_0)} f(\frac{\sigma_m}{\bar{\sigma}}) d\bar{\varepsilon} = 1 \tag{7.11}$$

In our test program the tensile loading is in the range of high stress triaxiality and $f(\frac{\sigma_m}{\bar{\sigma}}) = \frac{\sigma_m}{\bar{\sigma}}$ for this range. Then we have

$$D = \int_{\bar{\varepsilon}_0}^{\bar{\varepsilon}_f} \frac{1}{C(\bar{\varepsilon}_0)} \frac{\sigma_m}{\bar{\sigma}} d\bar{\varepsilon} = 1 \tag{7.12}$$

Only one test is needed to find the critical value and we have that one test. Actually, the critical value $C(\bar{\varepsilon}_0)$ actually is the same as D_c listed in Table 7.4. The relation between the critical value $C(\bar{\varepsilon}_0)$ and pre-compression strain $\bar{\varepsilon}_0$ is shown in Fig.7.10 and approximately follows

$$C(\bar{\varepsilon}_0) = C(0) - 0.5\bar{\varepsilon}_0 \tag{7.13}$$

It is seen that pre-compression is reducining the ductility of the material. As shown in Fig. 7.11, the pre-compression actually moves the fracture locus down. The magnitude of the shift depends on the degree of pre-compression.

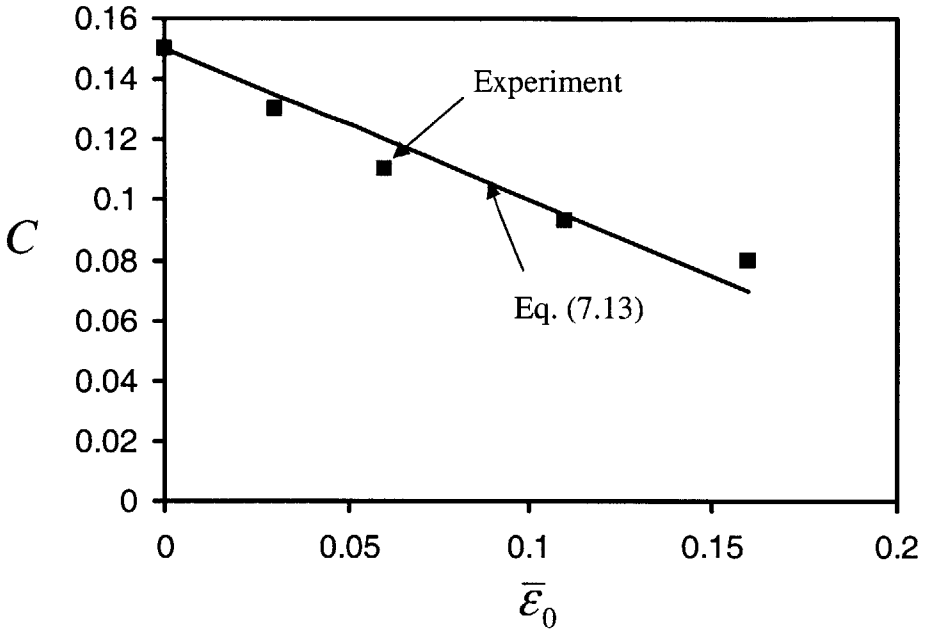

Fig.7.10. The relation of $\bar{\varepsilon}_t$ and $\bar{\varepsilon}_0$ in compression-tension tests

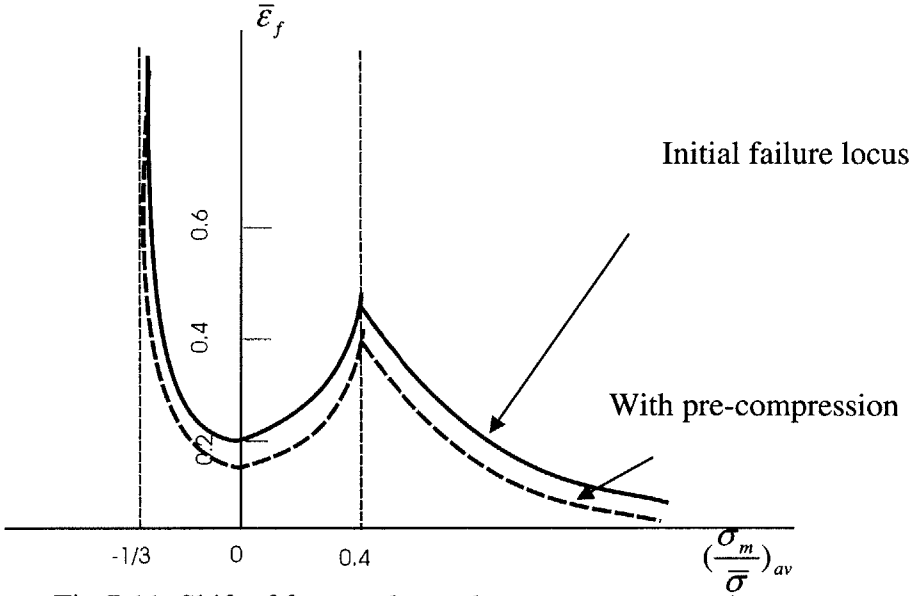

Fig.7.11. Shift of fracture locus due to pre-compression

7.5 Conclusion and Discussion

A special design of a specimen and experiment setup for studying crack formation under compression-tension reverse loadings was developed. Repeatable experimental results were obtained with this specimen and experimental setup. Totally five different loading cases including monotonic tension to crack formation, 4%, 8%, 14%, and 20% pre-compression followed by monotonic tension to crack formation were carried out. A simple criterion was developed to predict crack formation in this type of reverse loadings. The pre-compression played a very important role in crack formation. Pre-compression indeed reduces the ductility of the material. If we would not know about prior history of loading we would get the right-hand picture instead of the left one illustrated in Fig. 7.12.

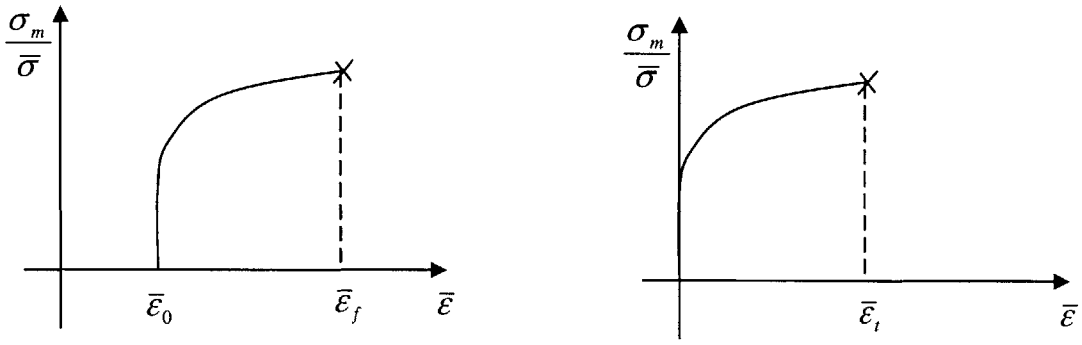

Fig. 7.12 Stress triaxiality vs. equivalent strain in the tension stage

It was shown that the idea of linear superposition of damage accumulation is not good for compression followed by monotonic tension. This is understandable since the pure compression plays a role in the later void nucleation, growth, and linkage although it does not cause any direct damage accumulation as indicated in Chapter 5. The strain due to

pre-compression certainly makes voids easy to nucleate in the following tensile stage. Also, it might have a contribution to final linkage of voids.

In the new damage measurement proposed in this study (Eq. (7.11)), the equivalent strain of the compression is taken as the low limit of the integral of the second term. The idea of non-zero lower limit was first proposed by Atkins [76]. He pointed out that the question of a threshold below which damage does not accumulate is very important. However, although the lower limit has been taken as zero in literature that is unlikely in practical microstructures when debonding around inclusions or inclusion cracking must first occur to form voids. The lower limit should depend not only on materials but also on the stress triaxiality. Unfortunately, this idea is still an unconfirmed thought. Although the importance of the threshold remains open in monotonic loading, it is likely that a low limit should be introduced in the reverse loadings since contributions to crack formation due to the tensile loading and the compressive loading are different.

The pre-strain was imposed before void nucleate in this test. In those cases, pre-tensile strain and pre-compression strain might have similar effect on final crack formation. It certainly becomes another story for the cases when pre-strain is applied after void nucleate or for materials with initial porosity. The effect of pre-compression strain on later void growth and linkage clearly is different from pre-tensile strain.

A qualitative representation of void growth and linkage under tension with pre-compression and pre-tension is illustrated in Fig. 7.13 considering an element with two holes. For holes under compression in y direction, the space between the holes and the dimension of holes in x direction becomes larger, while the space between the holes and the dimension of holes in y direction becomes smaller. It is totally opposite for holes under tension. So the shape of the holes and the space between the holes are different before the following monotonic tension. Void growth occurs along x direction under following tension in y direction. The space between the holes and the size of the holes become smaller in x direction and finally two holes link together because of necking of the ligament or simple touching of the two holes. It is likely the final shape of the element

and also the holes are different for those two cases. It should be pointed out that the contribution of pre-compression and pre-tension to crack formation depends also on the mechanisms of void linkage, which is related to materials.

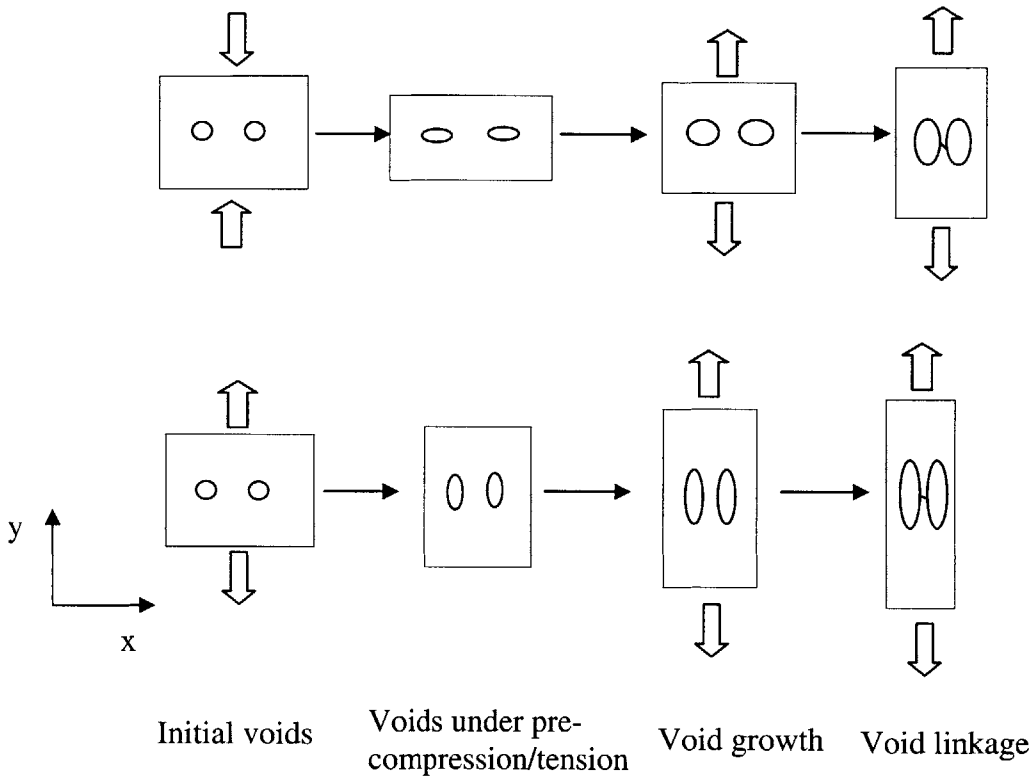

Fig. 7.13 Void growth and linkage under tension with pre-compression/tension

However, this is only a qualitative explanation since in reality the shape and distribution of holes and loading cases are more complicated, not to mention crack formation involving more than one cycle. In the latter case, the stress that the structure experiences changes back and forth from one stress triaxiality range to another stress triaxiality. The damage not only involves void nucleation, growth, and linkage but also "shear fracture." Due to the complicated processes occurs in reverse loading, detailed study on physical mechanisms is needed to have a clearer picture on damage accumulation.

Chapter 8

Applications

The objective of the present thesis is to formulate the condition for ductile crack formation. Many people would question the correctness of the present approach until evidence on component validation is presented. The author conducted one component test, a solid aluminum 2024-T351 beam with a smooth round notch under 3-point bending. Besides, other colleagues in the Impact and Crashworthiness Lab took the present formulation further and presented an extensive component validation, which includes an aluminum sandwich panel under 4-point bending, a thin steel plate under hemispherical punch, a steel double hull structure under static conical punch loading and the penetration of a ductile aluminum beam by a rigid projectile. Those results will be included in respective PhD theses of my colleagues. With a permission of my thesis advisor, a short overview of the application of my crack formation condition is presented here.

8.1 3-point Bending of a Round-Notched Solid Beam

A 260 mm long solid beam with a 20mm by 20 mm cross section and a 10 mm radius of notch at the tensile side was tested under 3-point bending as shown in Fig. 8.1. The diameter of the two supporting rollers was 45 mm while the diameter of the punch was 50 mm. The specimens were cut from the same block of Al2024-T351 along the rolling direction. Quite repeatable results displayed in Fig. 8.2 were obtained from two samples.

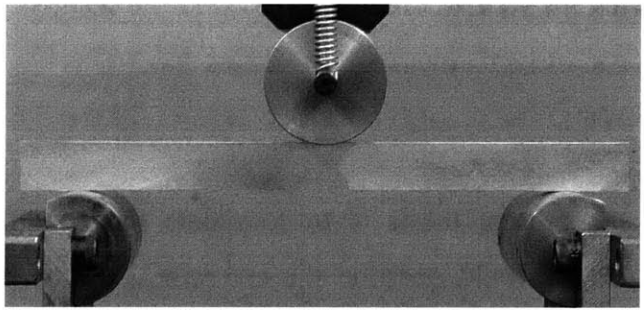

a) Initial set up

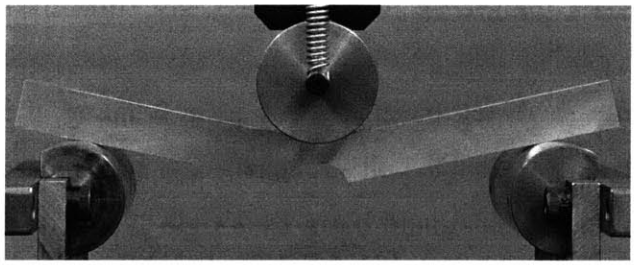

b) Final stage

Fig. 8.1 Initial setup and final stage of 3-point bending test

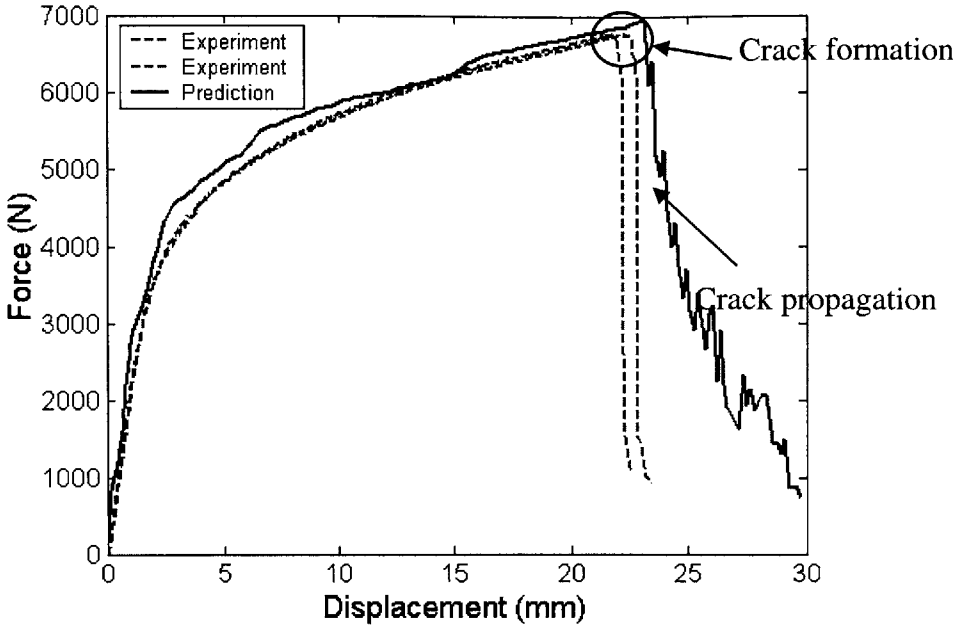

Fig. 8.2 Force–displacement response of 3-point bending

In the numerical simulation, rigid surfaces were used to model the punch and the two rollers. The solid beam was modeled by 8-node solid elements. As illustrated in Fig. 8.3, the mesh close to the notch was much finer than other parts. A "tied" condition in ABAQUS was defined to connect the fine part and the coarse part as shown in Fig. 8.3. The whole finite element model of the three-point bending and the deformation shape at the final stage is displayed in Fig. 8.4. A fracture model in ABAQUS corresponding to Eq. (5.4) was used. The fracture locus displayed in Fig. 5.20 was introduced as an input to the fracture model. During the numerical simulation, all the solid elements modeling the beam were checked automatically at every time step for possible fracture. As illustrated in Fig. 8.2, the numerical prediction with the present approach and the fracture locus given in Fig. 8.27 gives almost the same value of displacement to crack formation as the value found in the experiment. Also, the numerical simulation predicts the same crack formation location, which is at the root of the smooth notch, as displayed in Fig. 8.5.

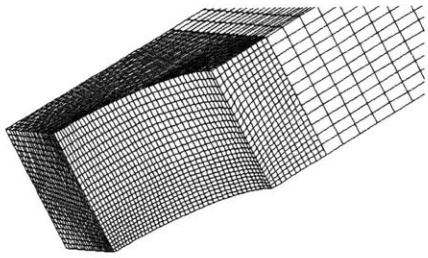

Fig. 8.3 Finite element mesh of the solid beam
(only showing the area close to the notch)

Initial stage

Final stage

Fig. 8.4 Numerical simulation of 3-point bending

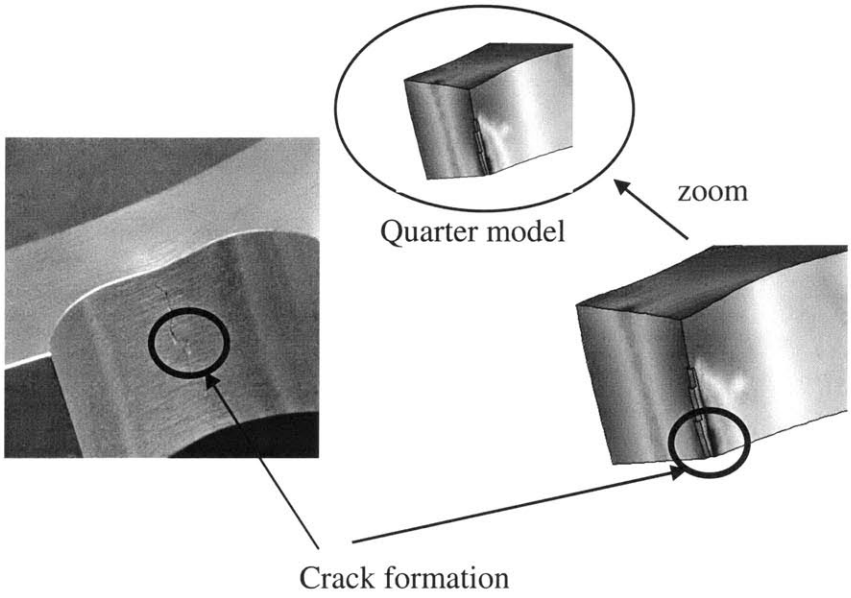

Fig. 8.5 Crack formation in 3-point bending

A first attempt to capture crack propagation is made in this example using the present approach. Crack propagation is understood as a sequence of crack formation. During the numerical simulation, when the damage accumulation reaches the critical value at an integration point, the stress is set to zero at the integration point. However, the present approach does not predict correctly the response after crack formation (crack propagation) shown in Fig. 8.2 though the crack propagation pattern depicted in Fig. 8.6 seems quite realistic. The experiment shows a more rapid force drop than the numerical simulation.

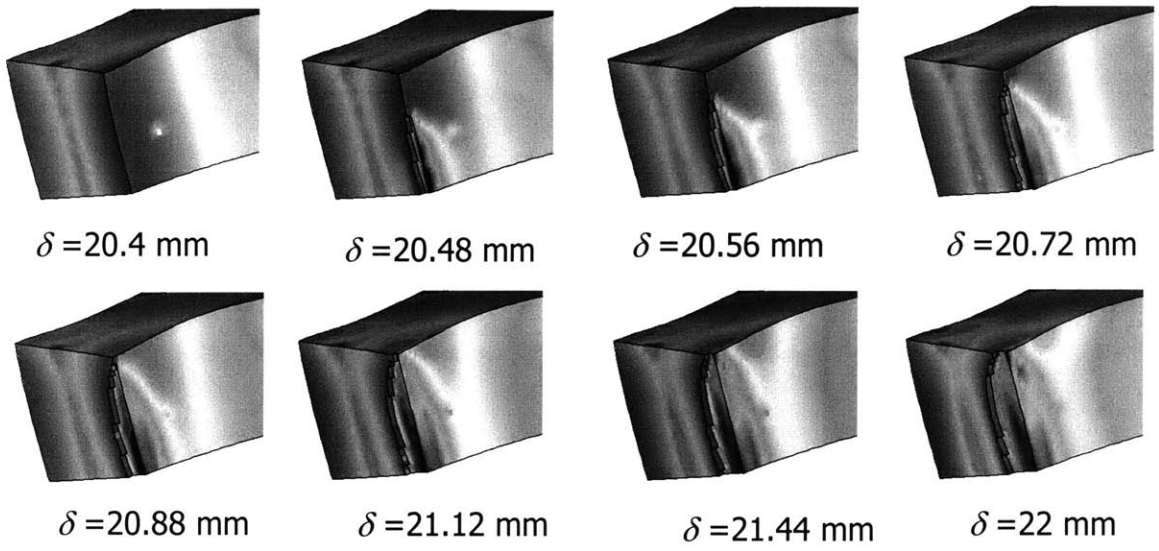

* δ : Displacement of the punch

Fig. 8.6 Predicted crack propagation pattern in 3-point bending

One important reason for the difference is the strain reversal. The material points, which were originally on the compressive side, went into tension as the bending axis of the beam moves with propagating crack. As illustrated in Fig. 8.7, three points A, B, C located was originally located in tensile side, neutral axis and compression side, respectively. The evolutions of strain for the three points are different because of the moving of the axis during crack propagation. Point C clearly experiences a compression-tension reversal. It has been shown in Chapter 7 that the critical damage accumulation D_c is different for the material with different degree of pre compression. The critical damage accumulation D_c with higher degree of pre compression has lower value. In the present simulation the fracture locus obtained in monotonic loading (Fig. 5.20) was introduced and the critical damage accumulation was set to unit for all the material points as the one without pre compression. This artificially increased the resistance of the beam. Therefore, the present simulation could not correctly predict the fracture of the element which was originally in compression side.

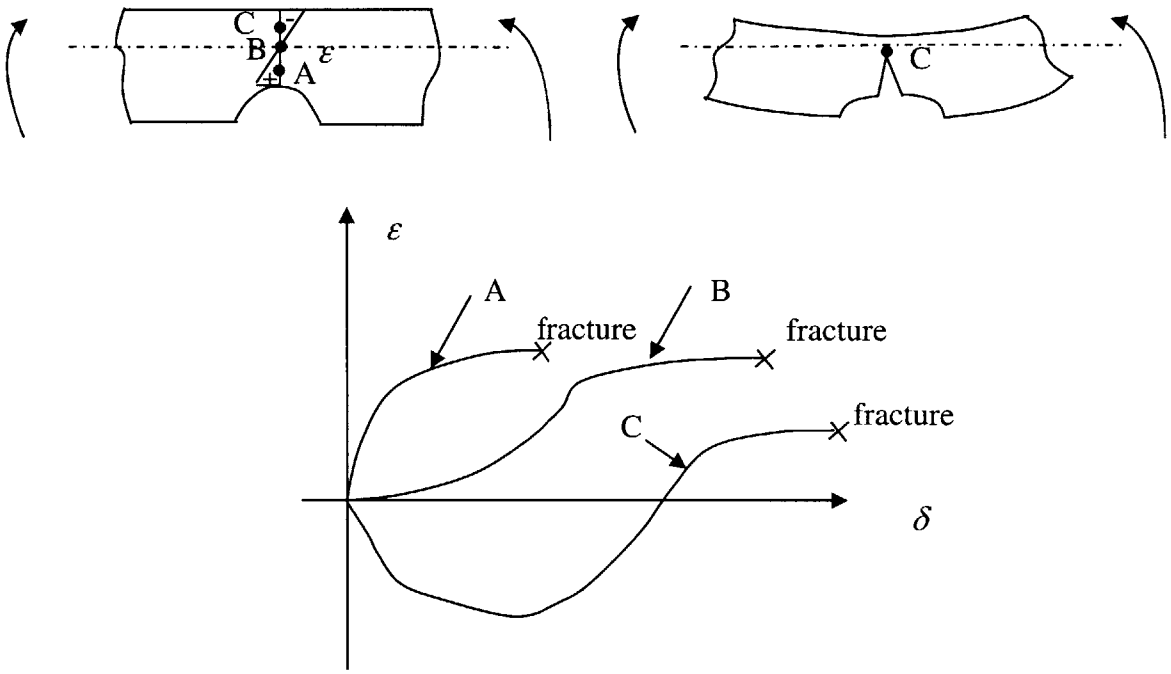

Fig. 8.7 Evolution of strain along the thickness

It should be noted that the effect of strain reversal did not occur until Point B failed. The difference in the earlier stages may be due to the following two reasons.

- The present approach developed is based on the crack formation in uncracked bodies. Once crack forms the stress and strain field changes to the crack tip fields extensively studied in fracture mechanics (See Appendix).
- In the experiment, the crack actually is the material decohering and there is no loss of material, while in the numerical simulation, crack is described by removal of a series of elements.

Clearly, further studies on crack propagation are needed. However, it is not the focus of the present thesis. The approach developed in this thesis was also applied by my colleagues to other aluminum and steel structures under various loadings. A short overview is presented in the following sections.

8.2 4-Point Bending of a Sandwich Panel

The present approach of prediction of crack formation was also applied to a sandwich aluminum panel under 4-point bending (Fig. 8.8) by Zheng and Wierzbicki [8]. The deformation was concentrated in the central part of the panel (Fig.8.9). As shown in Fig.8.10, after the peak load is reached, the magnitude of the reaction force drops mainly due to load plate buckling and the gradual lose of stiffness and strength of the compression flange. A sudden drop in the experimentally measured reaction force occurring at the punch displacement $\delta = 66mm$ was due to crack formation in the panel. Separate calibration of the material used in the panels was performed. At each step the condition for crack formation was checked. The predicted displacement to crack formation $\delta_f = 67mm$ agrees with the measured crack formation point. The prediction also gives the same location as obtained in the experiment (Fig.8.8).

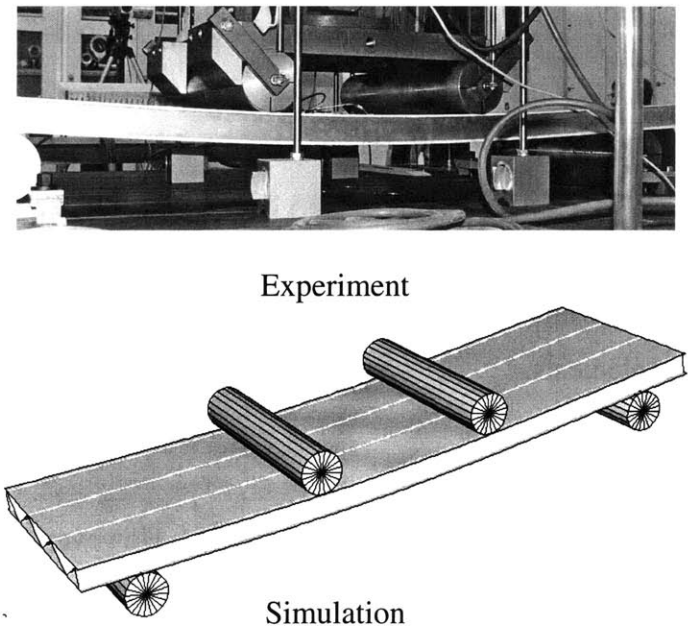

Fig. 8.8 Experiment and numerical simulation of 4-point bending
(after Zheng and Wierzbicki [8])

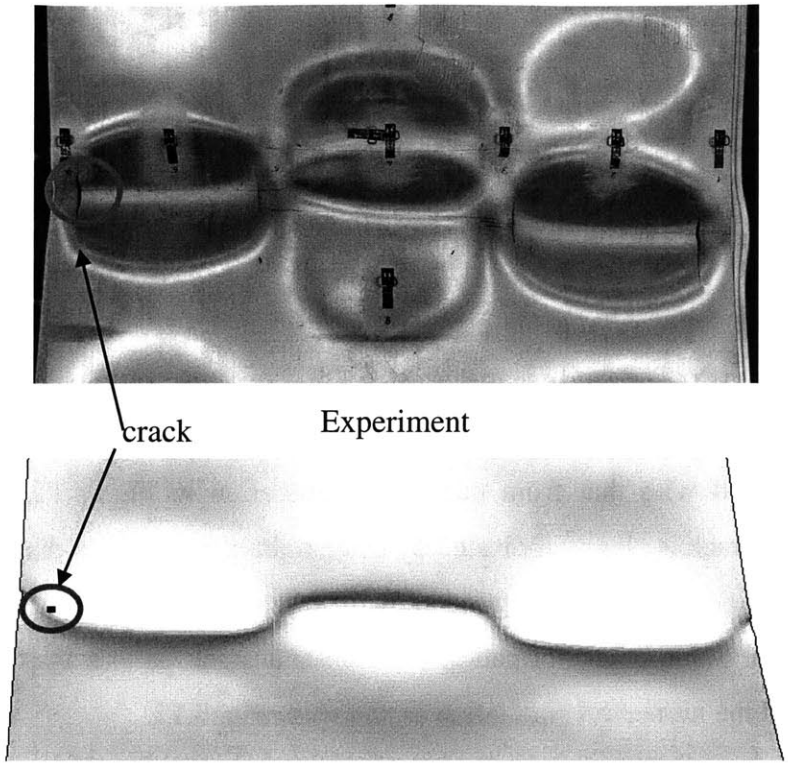

Fig. 8.9 Crack location from experiment and prediction in 4-point bending (after Zheng and Wierzbicki [8])

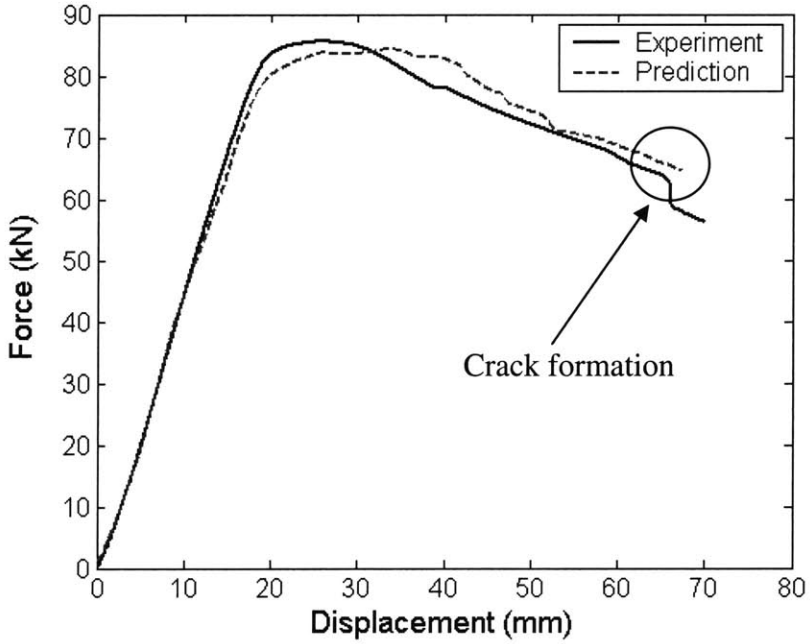

Fig. 8.10 Force–displacement response of 4-point bending (after Zheng and Wierzbicki [8])

8.3 Thin Plate under Hemispherical Punch Indentation

Another example for verifying the present approach is a steel thin plate indented by a hemispherical punch. The study was performed by Lee et al. [9]. Separate calibration of the material of the thin plate was performed. The experimental punch force-displacement curve is compared with that from numerical simulation in Fig. 8.11. Formation of a circumferential crack is clearly indicated by sudden drop in the force-displacement curve. It is seen that the prediction is in a good agreement with the experiment up to the point of crack formation. Same crack formation location and crack pattern was observed in the experiment and the numerical simulation as shown in Fig. 8.12.

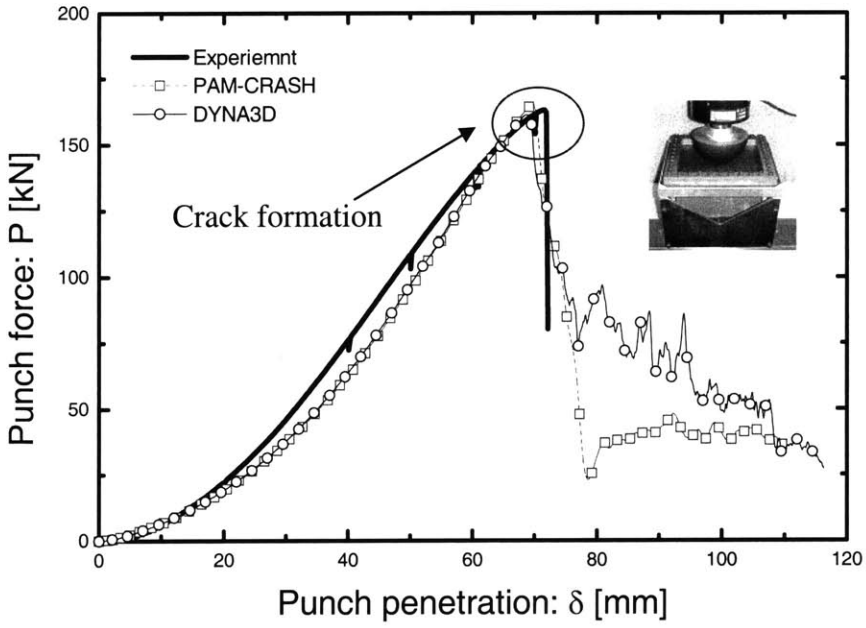

Fig.8.11 Comparison of experimental and numerical force-penetration curves (After Lee et al. [9])

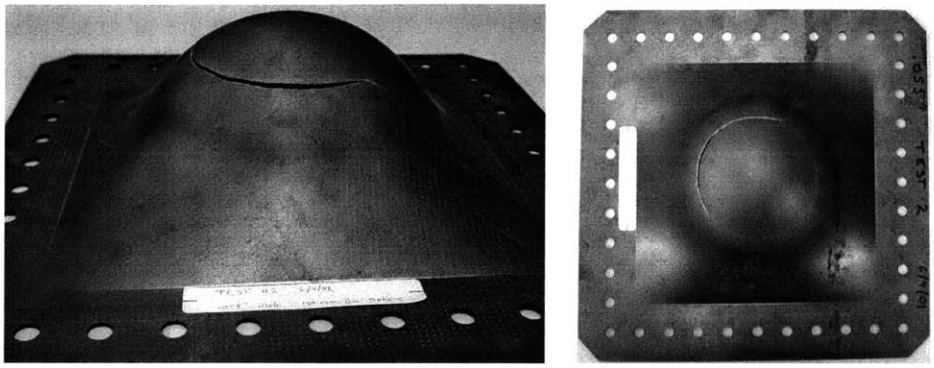

(a) Experiment

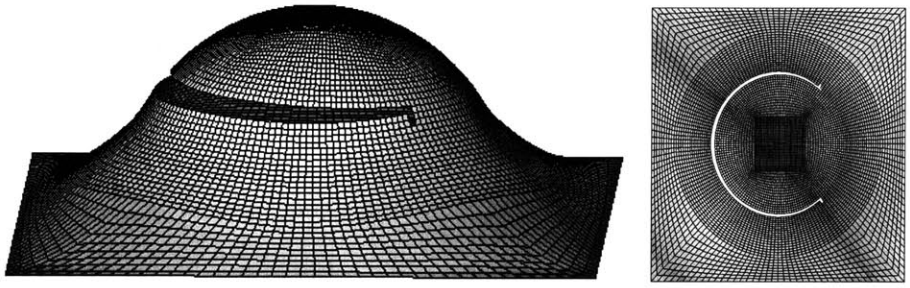

(b) Simulation

Fig. 8.12 Comparison of experimentally and numerically obtained circumferential crack (After Lee et al. [9])

8.4 Double Hull under Static Conical Punch Loading

A more complex structure with clamped conditions under conical punch loading was studied numerical by Lee and Wierzbicki [150] and experimentally by Yahiaoui et al. [151]. The structure consisted of two plates and stiffeners in between. Separate

calibration of the material used was also performed. Amazingly, the numerical simulation with the present crack formation approach accurately predicts not only crack formation but also crack propagation which is also understood as a sequence of crack formation in both fracture pattern and force-displacement response shown in Fig. 8.13 and Fig. 8.14, respectively.

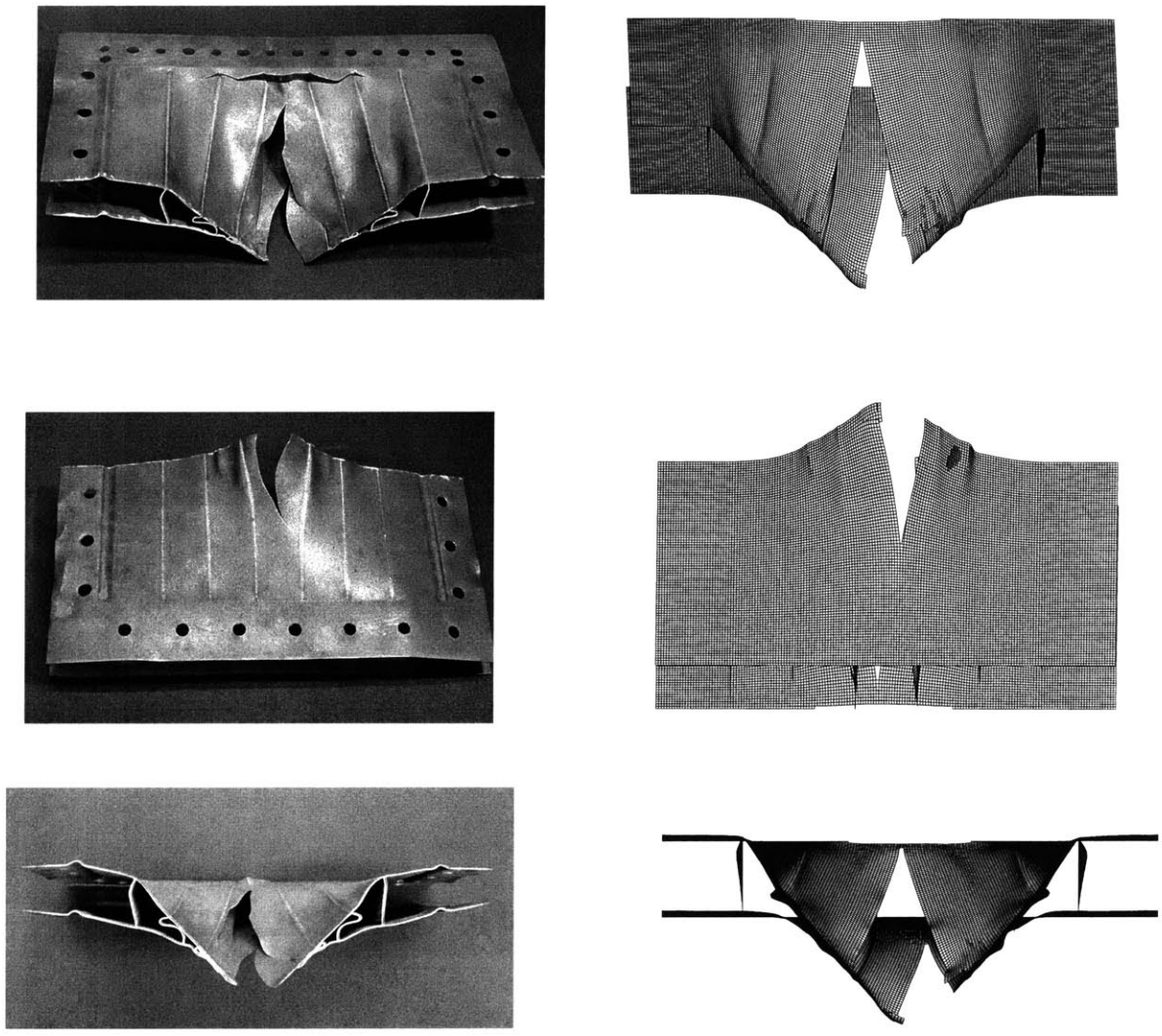

Fig. 8.13 Comparison of experimentally and numerically obtained crack pattern (After Lee et al.[150])

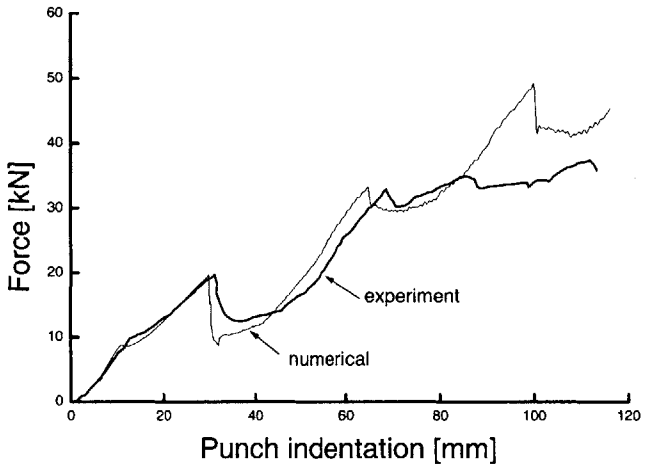

Fig.8.14 Comparison of experimental and numerical force-penetration curves (After Lee et al.[150])

8.5 Penetration of a Ductile Beam by a Rigid Projectile

Besides static studies, the present approach was also applied in a dynamic study by Teng and Wierzbicki [10] on high velocity perforation of a thin beam by a flat rigid projectile. Unrealistic failure mode illustrated in Fig. 8.15 was obtained using the constant equivalent strain criterion independent of stress triaxiality, which is commonly used in commercial codes. Immediately after impact large compressive stresses were developed under the flat nose projectile. It can be seen from the failure mode that elements under the flat punch due to this large compressive stress are fractured and the material was eroded layer by layer, which is clearly not realistic. By introducing the present ductile crack formation criterion, the artificial erosion of elements was removed. A more realistic

sequence of failure pattern shown in Fig. 8.16 was obtained. A shear crack mode along the edge of the punch was developed. Again, crack propagation is understood as a sequence of crack formation.

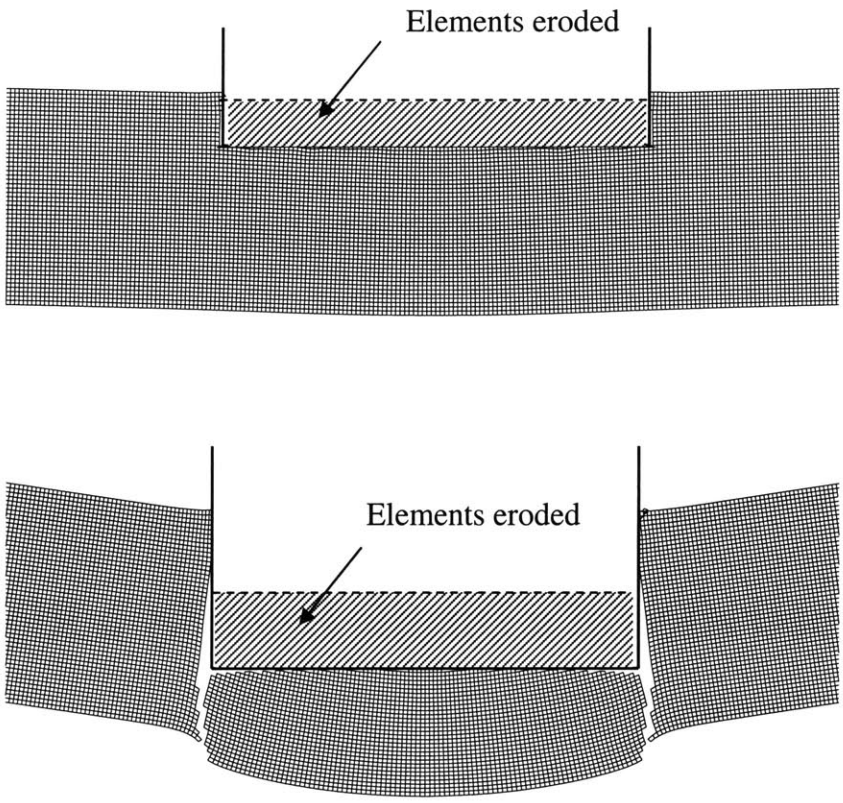

Fig. 8.15 Progressive formation of a shear crack in a beam struck by a flat-nose rigid projectile with the constant equivalent strain criterion
(after Teng and Wierzbicki [10])

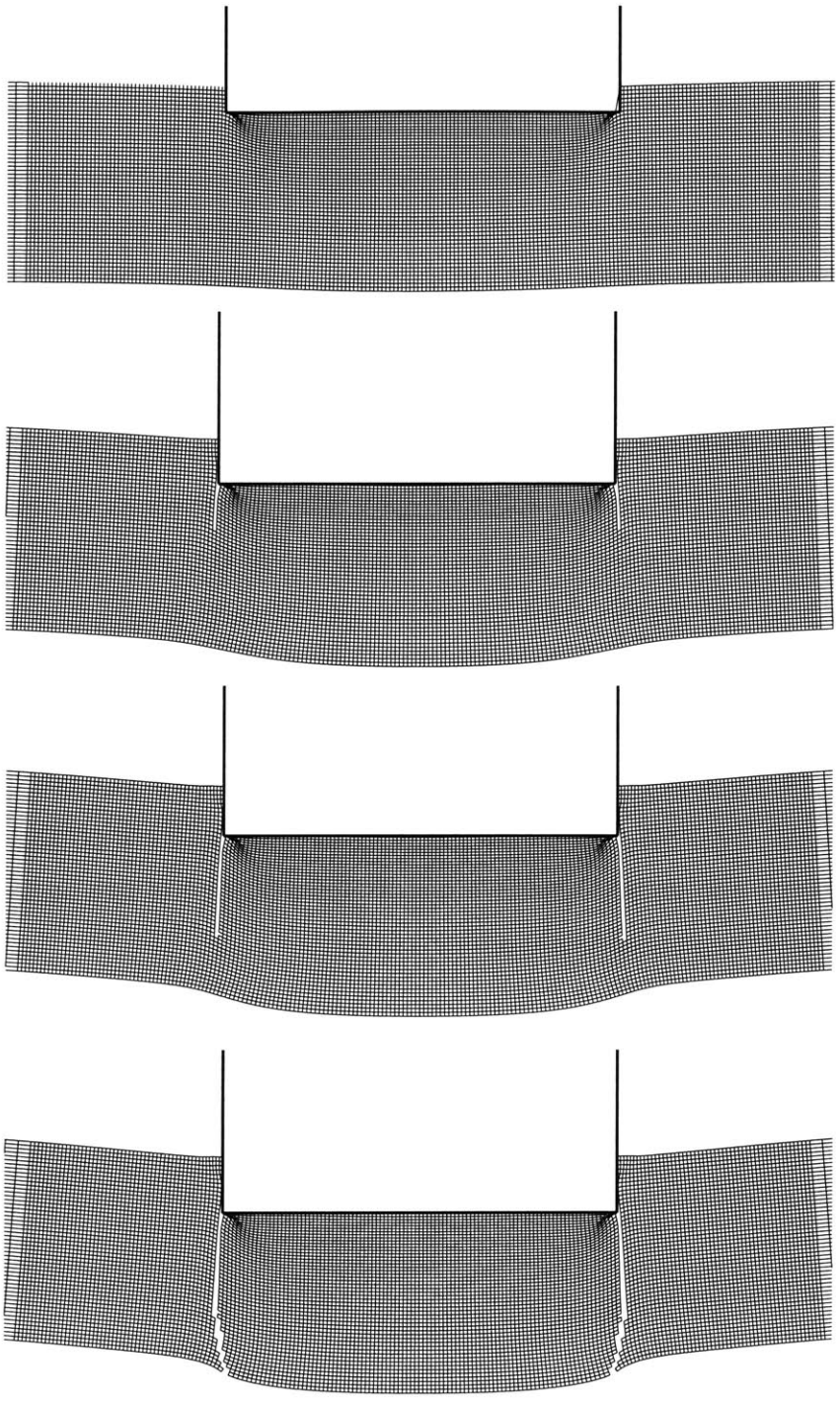

Fig. 8.16 Progressive formation of a shear crack in a beam struck by a flat-nose rigid projectile with the present approach
(after Teng and Wierzbicki [10])

8.6 Conclusion

A component validation of a solid aluminum beam with a smooth round notch under 3-point bending was carried out by the present author. Other applications of the crack formation condition developed in this thesis performed by my colleagues at the Impact and Crashworthiness Lab including an aluminum sandwich panel under 4-point bending, a thin steel plates under hemispherical punch, a steel double hull structure under static conical punch loading and penetration of a ductile aluminum beam by a rigid projectile were also reported. The present approach gave very good results on crack formation prediction (time and location) in not only aluminum but also steel structures. Although this approach is for ductile crack formation, good crack propagation patterns were obtained in all the applications. The prediction of force-displacement response in the steel double hull structure under static conical punch loading agreed also well with tests. The approach seems promising for industrial applications, especially in prediction of ductile crack formation. However, much work has to be done to put crack propagation on solid theoretical basis. The present approach and its interpretation is new and needs further validations for different materials at different labs.

Chapter 9

Conclusions and Recommendations

9.1 Conclusions

Experimental, numerical and analytical studies were carried out on the prediction of ductile crack formation. A methodology for predicting ductile crack formation suitable in industrial applications was developed based on the idea of introducing different weighting functions for different stress triaxiality ranges where different ductile crack formation mechanisms occur. The component validations preformed by the present author and other colleagues in the ICL clearly have shown the effectiveness of the method. The main accomplishment of the present thesis consists of the following points.

- A comprehensive test program on fracture of Al2024-T351 was completed.
- A well-defined procedure to determine fracture locus (calibration for fracture) was presented.
- A concept of a cut-off value for negative triaxialities was introduced.
- Two mechanisms of ductile crack formation and a transition mode were observed.
- Effects of seven variables controlling fracture were studied. Equivalent strain and stress triaxiality were found to be of utmost importance.

- A modified criterion was introduced for ductile crack formation under single reversals of strain.

A Comprehensive Testing Program

Tensile, compressive, shear and combined loading tests were performed for 2024-T351 aluminum alloy. Over 90 experiments were conducted on using seventeen different types of specimens. For the first time, a broad range of stress triaxialities were applied ranging from the lowest -0.26 all the way to the highest 0.95. The tests provided the global force-displacement relationship and individual components of stress and strain tensors could not be measured. Parallel numerical simulations were performed to determine the individual components of stress and strain tensors and their histories.

Determination of Fracture Locus under Monotonic Loadings

The point of the departure of our analysis is the fracture initiation criterion formulated in terms of accumulated plastic equivalent strain with the stress triaxiality as a weighting function. The criterion by itself is not new and has been proposed by many authors in the past and studied in the limited range of stress triaxialities. What is new in the present thesis is recognition that the fracture locus can not be described by one smooth monotonic function (as suggested by Johnson and Cook [74] and Borvik et al [120] etc.) but consists of three distinct branches for low, intermediate and high stress triaxialities. While the present failure envelope was determined in an empirical basis, there has been some important analytical development as well. In particular, we have developed a unified approach to fracture valid for both negative and positive stress triaxialities. Until now, the fracture criterion given by the plastic equivalent strain with suitable weighing functions was thought to be applicable only to the region of positive stress triaxialities. We have shown that the fracture envelope for negative triaxialities, formulated earlier in the space of principal strains can be in fact transformed to the same space of the

equivalent strain and stress triaxiality. For the correlation of experimental results and simulations, all three branches of the fracture envelope were uniquely determined in the case of 2024-T351 aluminum alloy. Even more importantly, we have determined a general procedure of calibrating a wide range of materials for fracture which we think could find a wide spread industrial applications.

Determination of Cut-Off Value

Considerable evidence was collected on the existence of limiting value of stress triaxialities below which fracture will never occur. This evidence comes from the detailed analysis of upsetting tests as well as from revisiting famous experimental program on the influence of the hydrostatic pressure on fracture performed by Bridgman in early fifties. The critical value of the stress triaxiality found in the thesis is $-1/3$. Even though the above finding now seems to be straightforward, no one has pointed out on this property.

Physical Mechanisms of Ductile Crack Formation

The complex mechanism of void nucleation, growth, and linkage, which occurs in the high stress triaxiality range, was reviewed extensively. Specimens that failed in the high stress triaxiality range as well as those that fractured under the negative stress triaxiality range were examined and studied by using SEM and polishing techniques. Besides the well-known void nucleation, growth, and linkage mechanism, which occurs in the high stress triaxiality, range, a different mechanism of "shear fracture" was observed in the negative stress triaxiality range. A combination of those two mechanisms occurs in the intermediate stress triaxiality range, which is essentially a transition range. The above micro mechanism observations serve as a justification of the existence of three distinct branches in the empirically found fracture envelope.

Dependence of Ductile Crack Formation on Other Effects

Other effects including stress and strain ratios, specimen size, and anisotropy were studied. The difference of equivalent strain to crack formation found in specimens with different cross section shapes can be explained by the large difference of the stress triaxiality. Similar equivalent strain to crack formation was found for specimens that have similar stress triaxiality but different stress and strain ratios. Furthermore, all test points fell well within a single fracture locus in the equivalent strain to crack formation and the stress triaxiality space. Similarly, the fracture points corresponding to plates with different thickness and diameters of holes were shown to fit well with the failure envelope. Small difference in compression on specimens machined in two different directions was found. It can be concluded that the equivalent strain and the stress triaxiality are the two most important parameters governing crack formation while others are probably of secondary importance.

Ductile Crack Formation under Single Reversals of Strain

A special design of a specimen and experiment setup for studying crack formation under compression-tension loadings was developed. Repeatable experimental results were obtained. It was found that the pre-compression plays an important role in crack formation. Linear superposition of damage accumulation failed to predict crack formation in compression-tension loadings. A simple criterion was developed to predict crack formation in this type of reverse loadings.

9.2 Future Studies

It is suggested that further research should be conducted on the following topics:

- More detailed study on physical mechanisms of "shear fracture" is needed to reveal the process of ductile crack formation. The transition of "shear fracture" to void nucleation, growth, and linkage should be also further investigated.

- Different types of specimens were designed for determination of weighting functions in the present thesis. Clearly developing a universe apparatus, which covers the entire stress triaxiality and also produces constant stress triaxiality at the critical location during whole deformation process will be a big step forward for a rapid industrial calibration process.

- Only a limited number of variables on crack formation were discussed in this thesis. Other factors such as surface/sub surface sites, stress and strain gradient, strain rate, temperature and other loading conditions such as torsion are good subjects for future studies.

- Only one type of reverse loading was performed. Other cases involving different stress and strain histories such as tension-compression, torsion-tension should be further investigated. Also studies on corresponding physical mechanisms are clearly needed.

- A generalization of the present concept of crack initiation into propagation is needed to many industrial applications. The effect of mesh size, stress and strain gradient, element deletion etc. should be carefully investigated.

- Most of conclusions were drawn based on the results obtained in Al 2024-T351. Different materials have different microstructures, hardening, strength, ductility,

response to temperature and rate, etc., which might change the behavior of ductile crack formation. Therefore, the applicability of the present methodology to other material should be studied.

- Limited component validations were presented in this thesis. The present approach to fracture should be further verified at other research centers on different materials and structures under different types of loadings.

Bibliography

1. Porter, D. A., Easterling, K. E., and Smith, G. D. W. (1978). Dynamic studies of tensile deformation and fracture of pearlite. *Acta Metallurgica* **26,** 1405-1422.
2. Bluhm, J. I., and Morrissey, R. J. (1964). Preliminary investigation of the fracture mechanism in a tensile speicmen. U.S. Army Materials Research Agency, Watertown, MA.
3. McClintock, F. A. (1968). A criterion of ductile fracture by the growth of holes. *Journal of Applied Mechanics* **35,** 363-371.
4. Hancock, J. W., and Mackenzie, A. C. (1976). On the mechanisms of ductile failure in high-strength steels subjected to multi-axial stress-states. *Journal of the mechanics and physics of solids* **24,** 147-169.
5. French, I. E., and Weinrich, P. F. (1975). The influence of hydrostatic pressure on the tensile deformation and fracture of copper. *Metallurgical Transactions A* **6A,** 785-790.
6. Kudo, H., and Aoi, K. (1967). Effect of compression test conditions upon fracturing of medium carbon steel. *Journal of Japanese Society of Technology and Plasticity* **18,** 17-27.
7. McClintock, F. A., and Zheng, Z. M. (1993). Ductile fracture in sheets under transverse strain gradients. *International Journal of Fracture* **64,** 321-337.
8. Zheng, L., and Wierzbicki, T. (2002). Numerical simulation of crush behavior of aluminum sandwich panels for train collision. Report 92. Impact & Crashworthiness Laboratory, MIT, Cambridge, MA.

9. Lee, Y. W., Woertz, J. C., and Wierzbicki, T. (2003). Fracture prediction of thin plates under hemispherical punch with calibration and experimental verification. Report 100. Impact and Crashworthiness Laboratory, MIT, Cambridge, MA.

10. Teng, X., and Wierzbicki, T. (2003). Effect of fracture criteria on high velocity perforation of thin beams. Report 98. Impact & Crashworthiness Laboratory, MIT, Cambridge, MA.

11. Tipper, C. F. (1949). The fracture of metals. *Metallurgia* **39,** 133-137.

12. Rogers, H. C. (1960). Tensile fracture of ducitle metals. *Trans. Metallurgical Society of AIME* **218,** 498-506.

13. Puttick, K. E. (1959). Ductile fracture in metals. *Philosophical Magazine, Series 8* **4,** 964-969.

14. Edelson, B. I. (1963). Strain concentrations and ductility. *Trans. Quarterly of ASM* **56,** 82-89.

15. Gurland, J., and Plateau, J. (1963). The mechanism of ductile rupture of metals containing inclusions. *Trans. quarterly of ASM* **56,** 442-454.

16. Beachem, C. D. (1963). An electron fractographic study of the influence of plastic strain conditons upon ductile rupture processes in metals. *Trans. Quarterly of ASM* **56,** 318-326.

17. Rice, J. R., and Tracey, D. M. (1969). On the ductile enlargement of voids in triaxial stress fields. *Journal of the Mechanics and Physics of Solids* **17,** 201-217.

18. McClintock, F. A., Kaplan, S. M., and Berg, C. A. (1966). Ductile fracture by hole growth in shear band. *International Journal of Fracture Mechanics* **2,** 614-627.

19. LeRoy, G., Embury, J. D., Edward, G., and Ashby, M. F. (1981). A model of ductile fracture based on the nucleation and growth of voids. *Acta Metallurgica* **29,** 1509-1522.

20. Tvergaard, V., and Hutchinson, J. W. (2002). Two mechanisms of ductile fracture: void by void growth versus multiple void interaction. *International Journal of Solids and Structures* **39,** 3581-3597.

21. Koplik, J., and Needleman, A. (1988). Void growth and coalescence in porous plastic solids. *International Journal of Solids and Structures* **24,** 835-853.

22. Bandstra, J. P., and Koss, D. A. (2001). Modeling the ductile fracture process of void coalescence by void-sheet formation. *Materials Science and Engineering A* **319-321,** 490-495.

23. Tvergaard, V. (1982). Ductile fracture by cavity nucleation between large voids. *Journal of the Mechanics and Physics of Solids* **30,** 265-286.

24. Bandstra, J. P., Goto, D. M., and Koss, D. A. (1998). Ductile fracture as a result of a void-sheet instability: experiment and computational modeling. *Materials Science and Engineering A* **249,** 46-54.

25. Gurson, A. L. (1977). Continuum theory of ductile rupture by void nucleation and growth: Part I-yield criteria and flow rules for porous ductile media. *Journal of Engineering Materials and Technology* **99,** 2-15.

26. Gurson, A. L. (1975). Plastic Flow and Fracture Behavior of Ductile Materials Incorporating Void Nucleation, Growth and Interaction. Brown University.

27. Tvergaard, V. (1981). Influence of voids on shear band instabilities under plane strain conditions. *International Journal of Fracture* **17,** 389-407.

28. Tvergaard, V. (1982). On localization in ductile materials containing spherical voids. *International Journal of Fracture* **17,** 389-407.

29. Tvergaard, V., and Needleman, A. (1984). Analysis of the cup-cone fracture in a round tensile bar. *Acta Metallurgica* **32,** 157-169.

30. Needleman, A., and Tvergaard, V. (1984). An analysis of ductile rupture in notched bars. *Journal of the Mechanics and Physics of Solids* **32,** 461-490.

31. Argon, A. S., and Im, J. (1975). Separation of second phase particles in spheroidized 1045 Steel, Cu-0.6PCT Cr alloy, and maraging steel in plastic straining. *Metallurgical Transactions* **6A,** 839-851.

32. Gurland, J. (1972). Observations on the fracture of cementite particles in a spheroidized 1.05%C steel deformed at room temperature. *Acta Metallurgica* **20,** 735-741.

33. Needleman, A., and Rice, J. R. (1978). Limits to ductility set by plastic flow localization. *In* "Mechnaics of Sheet Metal Forming" (D. P. Koistinen, Ed.), Plenym Publishing.

34. Chu, C. C., and Needleman, A. (1980). Void nucleation effects in biaxially stretched sheets. *Journal of Engineering Materials and Technology* **102,** 249-256.

35. Berdin, C., Dong, M. J., and Prioul, C. (2001). Local approach of damage and fracture toughness for nodular cast iron. *Engineering Fracture Mechanics*, 1107-1117.

36. Xia, L., and Shih, C. F. (1995). Ductile crack growth---I. A numerical study using computational cells with microstructurally-based length scales. *Journal of the Mechanics and Physics of Solids* **43,** 233-259.

37. Xia, L., and Shih, C. F. (1995). Ductile crack growth---II. Void nucleation and geometry effects on macroscopic fracture behavior. *Journal of the Mechanics and Physics of Solids* **43,** 1953-1981.

38. Xia, L., and Shih, C. F. (1996). Ductile crack growth---III. Transition to cleavage fracture incorporating statistics. *Journal of the Mechanics and Physics of Solids* **44,** 603-639.

39. Xia, L., Shih, C. F., and Hutchinson, J. W. (1995). A computational approach to ductile crack growth under large scale yielding conditions. *Journal of the Mechanics and Physics of Solids* **43**.

40. Faleskog, J., Gao, X., and Shih, C. F. (1998). Cell model for nonlinear fracture analysis---I. Micromechanics calibration. *International Journal of Fracture* **89,** 355-373.

41. Gao, X., Faleskog, J., and Shih, C. F. (1998). Cell model for nonlinear fracture analysis---II. Fracture-process calibration and verification. *International Journal of Fracture* **89,** 375-398.

42. Kachanov, L. M. (1958). Time of the rupture process under creep conditions. *IZV Akad Nauk S.S.R., Otd. Tekhn. Nauk* **8,** 26-31.

43. Rabotnov, Y. N. (1969). "Creep Problems of Structural Members," North-Holland, Amsterdam.

44. Lemaitre, J. (1971). Evaluation of dissipation and damage in metals submitted to dynamic loading. In "Proceedings ICM" Kyoto, Japan.

45. Lemaitre, J. (1985). A continuous damage mechanics model for ductile fracture. *Journal of Engineering Materials and Technology* **107,** 83-89.

46. Wang, T. J. (1992). Unified CDM model and local criterion for ductile fracture-I. Unified CDM model for ductile fracture. *Engineering Fracture Mechanics* **42,** 177-183.

47. Dhar, S., P.M., D., and Sethuraman, R. (2000). A continuum damage mechanics model for ductile fracture. *International Journal of Pressure Vessels and Piping* **77,** 335-344.

48. Barenblatt, G. I. (1962). The mathematical theory of equilibrium cracks in brittle fracture. *Advances in Applied Mechanics* **7,** 55-129.

49. Hillerborg, A., Modeer, M., and Petersson, P. E. (1976). Analysis of crack formation and crack growth in concrete by means of fracture mechanics and finite elements. *Cement Concrete Research* **6,** 773-782.

50. Needleman, A. (1990). An analysis of decohesion along an imperfect interface. *International Journal of Fracture* **42,** 21-40.

51. Roychowdhury, S., Roy, Y. D. A., and Dodds, R. H. (2002). Ductile tearing in thin aluminum panels:experiments and analyses using large-displacement, 3-D surface cohesive elements. *Engineering Fracture Mechanics* **69,** 983-1002.

52. Tvergaard, V., and Hutchinson, J. W. (1996). Effect of strain-dependent cohesive zone model on predictions of crack growth resistance. *International Journal of Solids and Structures* **33,** 3297-3308.

53. Tvergaard, V., and Hutchinson, J. W. (1992). The relation between crack growth resistance and fracture process parameters in elastic-plastic solids. *Journal of the Mechanics and Physics of Solids* **40,** 1377-1397.

54. Elices, M., Guinea, G. V., Gomez, J., and Planas, J. (2002). The cohesive zone model: advantages, limitations and challenges. *Engineering Fracture Mechanics* **69,** 137-163.

55. McClintock, F. A. (2003). Private communication.

56. Que, N. S., and Tin-Loi, F. (2002). Numerical evaluation of cohesive fracture paramters from a wedge splitting test. *Engineering Fracture Mechanics* **69,** 1269-1286.

57. Siegmund, T., and W., B. (1999). Prediction of the work of separation and implications to modeling. *International Journal of Fracture* **99,** 97-116.

58. Needleman, A. (1987). A continuum model for void nucleation by inclusion debonding. *Journal of Applied Mechanics* **54,** 525-531.

59. Needleman, A. (1990). An analysis of tensile decohesion along an interface. *Journal of the Mechanics and Physics of Solids* **38,** 289-324.

60. Tvergaard, V. (2001). Crack growth predctions by cohesive zone model for ductile fracture. *Journal of the Mechanics and Physics of Solids* **49,** 2191-2207.

61. Levy, A. J. (1994). Separation at a circular interface under biaxial loading. *Journal of the Mechanics and Physics of Solids* **42,** 1087-1104.

62. Siegmund, T., and Needleman, A. (1997). Numerical simulation of fast crack growth in brittle solids. *Journal of the Mechanics and Physics of Solids* **42,** 1397-1343.

63. Lin, G., Gornec, A., and Schwalbe, K. H. (1998). Three dimensional finite element simulation of crack extension in aluminum alloy 2024-FC. *Fatigue and Fracture of Engineering Materials and Structures* **21,** 1159-1173.

64. de-Andres, A., Perez, J. L., and Ortiz, M. (1999). Elastic-plastic finite elementanalusis of three-dimensional fatigue crack growth in aluminum shafts subjected to axial loading. *International Journal of of Solids and Structures* **36,** 2231-2258.

65. Repetto, E. A., Radovitzky, R., and Ortiz, M. (2000). Finite element simulation of dynamic fracture and fragmentation of glass rods. *Computer Methods in Applied Mechanics and Engineering* **183,** 3-14.

66. Scheider, I. (2001). Simulation of cup-cone fracture in round bars using the cohesive zone model. In "First MIT Conference on Computational Fluid and Solid Mechanics" (K. J. Bathe, Ed.) ELSEVIER, Boston, USA.

67. Fischer, F. D., Kolednik, O., Shan, G. X., and Rammerstorfer, F. G. (1995). A note on calibration of ductile failure damage indicators. *International Journal of Fracture* **73,** 345-357.

68. Cockcroft, M. G., and Latham, D. J. (1968). Ductility and the workability of metals. *Journal of the Institute of Metals* **96,** 33-39.

69. Brozzo, P., Deluca, B., and Rendina, R. (1972). A new method for the prediction of formability in metal sheet, Sheet Metal Forming and Formability. In "Proceedings of the 7th Biennial Conference of the IDDRG".

70. Clift, S. E., Hartley, P., Sturgess, C. E. N., and Rowe, G. W. (1990). Fracture prediction in plastic deformation processes. *International Journal of Mechanical Sciences* **32,** 1-17.

71. Norris, D. M., Reaugh, J. E., Moran, B., and Quinones, D. F. (1978). A plastic-strain, mean-stress criterion for ductile fracture. *Journal of Engineering Materials and Technology* **100,** 279-286.

72. Oyane, M., Sato, T., Okimoto, K., and Shima, S. (1980). Criteria for ductile fracture and their applications. *Journal of Mechanical Work and Technology* **4,** 65-81.

73. Atkins, A. G. (1981). Possible explanation for unexpeted departures in hydrostatic tension-fracture strain relations. *Metal Science* **15,** 81-83.

74. Johnson, G. R., and Cook, W. H. (1985). Fracture characteristics of three metals subjected to various strains, strain rates, temperatures and pressures. *Engineering Fracture Mechanics* **21,** 31-48.

75. Wilkins, M. L., Streit, R. D., and Reaugh, J. E. (1980). Cumulative -strain-damage model of ductile fracture: simulation and prediction of engineering fracture tests. UCRL-53058, Lawrence Livermore Laboratory, Livermore, California.

76. Atkins, A. G. (1997). Fracture mechanics and metalforming: Damage mechanics and the local approach of yesterday and today. *In* "Fracture Research in Retrospect, An Anniversary Volume in Honour of George R. Irwin's 90th Birthday" (H. P. Rossmanith, Ed.), A.A. Balkema/Rotterdam/Brookfield.

77. Atkins, A. G. (1996). Fracture in forming. *Journal of Materials Processing Technology* **56,** 609-681.

78. Bridgman, P. W. (1952). "Studies in Large Plastic Flow and Fracture," Harvard University Press, Cambridge, Massachusetts.

79. Mirza, M. S., Barton, D. C., and Church, P. (1996). The effect of stress triaxiality and strain-rate on the fracture characteristics of ductile metals. *Journal of Materials Science* **31**.

80. Argon, A. S., Im, J., and Safoglu, R. (1975). Cavity formation from inclusions in ductile fracture. *Metallurgical Transactions* **6A,** 825-837.

81. Argon, A. S. (1976). Formation of cavities from nondeformable second phase particles in low temperature ductile fracture. *Journal of Engineering Material Technology Transactions* **38 Series H,** 60-68.

82. Rosovsky, E., and Hahn, W. C. (1973). The behavior of particles during plastic deformation of metals. *Metallurgical Transactions* **4,** 927-930.

83. Gangulee, A., and Gurland, J. (1967). On the fracture of silicon particles in aluminum-silicon alloys. *Transactions of the Metall. Sec. Of the A.S.M.* **239,** 269-272.

84. Lindley, T. C., Oates, G., and Richards, C. E. (1970). A critical appraisal of carbide cracking mechanisms in ferried/carbide aggregates. *Acta Metallurgica* **18,** 1127-1136.

85. Easterling, K. E., Fischmeister, H. F., and Navara, E. (1973). The particle-to-matrix bond in dispersion-hardened austenitic and ferritic iron alloys. *Powder Metallurgy* **16,** 128-145.

86. Engel, L., and Klingele, H. (1981). "An Atlas of Metal Damage," Carl Hanser Verlag, Munich, Germany.

87. Thomason, P. F. (1990). "Ductile Fracture of Metals," Pergamon Press.

88. VanStone, R. H., and Psioda, J. A. (1975). Discussion of metallurgical factors affecting fracture toughness of aluminum alloys. *Metallurgical Transactions A* **6A,** 668-670.

89. Cox, T. B., and Low, J. R. (1974). An investigation of the plastic fracture of AISI 4340 and 18 Nickel-200 grade maraging steels. *Met. Trans* **5,** 1457-1470.

90. Henry, G., and Horstmann, D. (1979). "De Ferri Metallographia, vol. V: Fractography and Microfractography," Verlag Stahleisen m.b.H., Dusseldorf, Germany.

91. Brooks, C. R., and Choudhury, A. (1993). "Metallurgical Failure Analysis," McGraw-Hill, Inc., New York.

92. Treitler, R. (1996). Private communication.

93. Bridgman, P. W. (1964). "Studies in Large Plastic Flow and Fracture," Harvard University Press, Cambridge, Massachusetts.

94. Siebel, E., and Pomp, A. (1927). Dieermittlung der formanderungsfestigkeit von metallen durch den stauchversuch. *Mitt. K-W_Inst. Eisenforsch* **9,** 157.

95. Loizou, N., and Sims, R. B. (1953). The yield stress of pure lead in compression. *Journal of the Mechanics and Physics of Solids* **1,** 234-243.

96. Johnson, W. (1956). Experiments in plane-strain extrusion. *Journal of the Mechanics and Physics of solids* **4,** 269-282.

97. Johnson, W. (1956). The pressure for the cold extrusion of lubricated rod through square dies of moderate reduction at slow speeds. *Journal of the Institute of Metals* **85,** 403-408.

98. Johnson, W., and Mellor, P. B. (1962). "Plasticity for Mechanical Engineers," D. Van Nostrand Company LTD, London.

99. Cook, M., and Larke, E. C. (1945). Resistance of copper and copper alloys to homogeneous deformation in compression. *Journal of the Institute of Metals* **71,** 371.

100. Schey, J. A., Venner, T. R., and Takomana, S. L. (1982). The effect of friction on pressure in upsetting at low diameter-to-height ratios. *Journal of Mechanical Working Technology* **6,** 23-33.

101. McClintock, F. A., and Argon, A. S. (1965). "Mechanical Behavior of Materials," Addison-Wesley Publishing Company, Inc., Cambridge, MA.

102. Marshall, E. R., and Shaw, M. C. (1952). The determination of flow stress from a tensile specimen. *Trans. ASM* **44,** 705-725.

103. Parker, E. R., Davis, H. E., and Flanigan, A. E. (1946). A study of the tension test. *Proc. ASTM* **46,** 1159-1174.

104. Alves, M., and Jones, N. (1999). Influence of hydrostatic stress on failure of axisymmetric notched specimens. *Journal of the Mechanics and Physics of Solids* **47,** 643-667.

105. White, C. S., Bronkhorst, C. A., and Anand, L. (1990). An improved isotropic-kinematic hardening model for moderate deformation metal plasticity. *Mechanics of Materials* **10,** 127-147.

106. kuhn, H. A., and Dieter, G. E. (1977). Workability in bulk forming processes. In "Fracture" ICF4, Waterloo, canada.

107. Bao, Y., and Wierzbicki, T. (2001). Fracture calibration procedure from upsetting test for industrial applications. Report 57, Impact & Crashworthiness Laboratory, MIT, Cambridge, MA.

108. Wierzbicki, T. (1999). Calibration of ductile fracture from compression and tension tests. Report 21, Impact & Crashworthiness Laboratory, MIT, Cambridge, MA.

109. Bao, Y., and Wierzbicki, T. (2002). Determination of fracture locus for the 2024T351 Aluminum. Report 81, Impact and Crashworthiness Lab, MIT, Cambridge, MA.

110. Hooputra, H., Metzmacher, G., and Werner, H. (2001). Fracture criteria for crashworthiness simulation of wrought aluminum alloy components. In "11th Annual European Conference EuroPam" Heidelberg, German.

111. Hopperstad, O. S., Borvik, T., Langseth, M., Labibes, K., and Albertini, C. (2002). On the influence of stress triaxiality and strain rate on the behavior of a structural steel. Part I, Experiments. *The European Journal of Mechanics.*

112. Goldthorpe, B. D. (1997). A path dependent model for ductile fracture. *Journal De Physique IV* **C3,** 705-710.

113. Thomason, P. F. (1968). Tensile Plastic Instability and Ductile Fracture Criteria in Uniaxial Compression Tests. *International Journal of Mechanical Sciences* **11,** 187-202.

114. Thomason, P. F. (1968). The Use of Pure Aluminum as an Analogue for the History of Plastic Flow, in Studies of Ductile Fracture Criteria in steel Compression Specimens. *International Journal of Mechanical Sciences* **10,** 501-518.

115. Ganser, H. P., Atkins, A. G., Kolednik, O., Fischer, F. D., and Richard, O. (2001). Upsetting of cylinders: A comparison of two different damage indicators. *Journal of Engineering Materials and Technology* **123,** 94-99.

116. French, I. E., and Weinrich, P. F. (1973). The effect of hydrostatic pressure on the tensile fracture of a-brass. *Acta Metallurgica* **21,** 1533-1537.

117. French, I. E., Weinrich, P. F., and Weaver, C. W. (1973). Tensile fracture of free machining brass as a function of hydrostatic pressure. *Acta Metallurgica* **21,** 1045-1049.

118. Johnson, G. R., and Cook, W. H. (1983). A constitutive model and data for metals subjected to large strains, high strain rates and high temperatures. In "Proceedings of the seventh international symposium on ballistics" Hague, Netherlands.

119. Borvik, T., Langseth, M., Hopperstad, O., and Kalo, K. (1999). Ballistic penetration of steel plates. *International Journal of Impact Engineering* **22,** 855-886.

120. Borvik, T., Hopperstad, O., Berstad, T., and Langseth, M. (2002). Perforation of 12mm thick steel plates by 20mm diameter projectiles with flat, hemispherical and conical noses, Part II: numerical simulations. *International Journal of Impact Engineering* **27,** 37-64.

121. McClintock, F. A. (2002). Private communication.

122. Clausing, D. P. (1970). Effect of plastic strain state on ductility and toughness. *International Journal of Fracture Mechanics* **6,** 71-85.

123. Rice, J. R. (1968). A path independent integral and the approximate analysis of strain concentrations by notches and cracks. *Journal of Applied Mechanics* **35,** 379-386.

124. Hill, R. (1952). On discontinuous plastic states, with special reference to loclalized necking in thin sheets. *Journal of the Mechanics and Physics of Solids* **1,** 19-30.

125. Bluhm, J. I. (1961). A model for the effect of thickness on fracture toughness. *ASTM Proceeding* **61,** 1324-1331.

126. Taira, S., and Tanaka, K. (1979). Thickness effect of notched metal sheets on deformation and fracture under tension. *Engineering Fracture Mechanics* **11,** 231-249.

127. Chow, C. K., and Nho, K. H. (1997). Effect of thickness on the fracture toughness of irradiated Zr-2.5Nb pressure tubes. *Journal of Nuclear Materials* **246,** 84-87.

128. Pardoen, T., Marchal, Y., and Delannay, F. (1999). Thickness dependence of cracking resistance in thin aluminum plates. *Journal of the Mechanics and Physics of Solids* **47,** 2093-2123.

129. Pardoen, T., Marchal, Y., and Delannay, F. (2002). Essential work of fracture compared to fracture mechanics-towards a thickness independent plane stress toughness. *Engineering Fracture Mechanics* **69,** 617-631.

130. Minami, F., Toyoda, M., and Satoh, K. (1987). A probabilistic analysis on thickness effect in fracture toughness. *Engineering Fracture Mechanics* **26,** 433-444.

131. Okazawa, S., Usami, T., Noguchi, H., and Fujii, F. (2002). Three-dimensional necking bifurcation in tensile steel specimens. *Journal of Engineering Mechanics* **128,** 479-486.

132. Weibull, W. (1939). The phenomenon of rupture in solids. *Ingeniors Vetenskaps Akademien Handlingar* **153.**

133. McClintock, F. A., and Irwin, G. R. (1965). Plasticity Aspects of fracture mechanics. *In* "Fracture Toughness Testing and its Applications, ASTM STP 381" (W. F. Brown, Ed.), American Society for Testing and Materials, Philadelphia PA.

134. Minami, F., Bruckner_Foit, A., Munz, D., and Trolldenier, B. (1992). Estimation procedure for the weibull parameters used in the local approach. *International Journal of Fracture* **54,** 197-210.

135. Lesuer, D. R. (2000). Experimental investigation of material models for Ti-6Al-4V titanium and 2024 -T3 aluminum. Lawrence Livermore National Laboratory, Livermore, CA.

136. Dell, H., Gese, H., Kessler, L., Werner, H., and Hopputra, H. (2001). Continuous failure prediction model for nonlinear load paths in successive stamping and crash process. In "SAE 2001 World Congress" Detroit, Michigan.

137. McClintock, F. A. (1993). Uniaxial stress-strain relations for surface roughening. *In* "Behaviour of Defects at High Temperatures" (R. A. Ainsworth and R. P. Skelton, Eds.), Mechanical Engineering Publications, London.

138. Seok, C. S., Kim, Y. J., and Weon, J. I. (1999). Effect of reverse cyclic loading on the fracture resistance curve in C(T) speicmen. *Nuclear Engineering and Design* **191,** 217-224.

139. Harvey, D. P. (2000). Effects of strain precycling on the tensile fracture morphology of Nickel 270. In "Proceedings of the Tenth (2000) International Offshore and Polar Engineering Conference" The International Society of Offshore and Polar Engineers, Seattle, USA.

140. Cosham, A. (2001). A model of pre-strain effects on fracture toughness. *Journal of Offshore Mechanics and Arctic Engineering* **123,** 182-190.

141. Fields, B. A., and Miller, K. J. (1978). Fibrous crack initiation and propagation in pre-strained HY100 steel. In "Conference on Tolerance of Flaws in Pressurised Components" Institution of Mechanical Engineers, London, UK.

142. El-Fadaly, M. s., El-Sarrage, T. A., Eleiche, A. M., and Dahl, W. (1995). Fracture toughness of 20MnMoNi55 steel at different temperatures as affected by room-temperature pre-deformation. *Journal of Materials Processing Technology* **54,** 159-165.

143. Miyata, T., Tagawa, T., and Aihara, S. (1997). Influence of pre-strain of fracture toughness and stable crack growth in low carbon steels. *In* "Fatigue and Fracture Mechanics: Twenty Eighth Vol.," (J. H. Underwood, B. D. Macdonald, and M. D. Mitchell, Eds.), American Society for Testing and Materials, Philadelphia, PA.

144. Homma, K., Miki, C., and Yang, H. (1998). Fracture toughness of cold worked and simulated heat affected structural steel. *Engineering Fracture Mechanics* **59,** 17-28.

145. Hagiwara, N., Masuda, T., and Oguchi, N. (2000). Effects of prestrain on fracture toughness and fatigue crack growth of line pipe steels. In "Proc. Third

International Pipeline Conference (IPC 2000)" Amercian Society of Mechanical Engineers, Calgary, Alberta, Canada.

146. Chaboche, J. L. (1989). Constitutive equations for cyclic plasticity and cyclic viscoplasticity. *International Journal of Plasticity* **5,** 247-302.

147. Chaboche, J. L. (1989). Time independent constitutive theories for cyclic plasticity. *International Journal of Plasticity* **2,** 149-188.

148. Chun, B. K., Jinn, J. T., and Lee, J. K. (2002). Modeling the Bauschinger effect for sheet metals, part I: theory. *International Journal of Plasticity* **18,** 571-595.

149. Chun, B. K., Kim, H. Y., and Lee, J. K. (2002). Modeling the Bauschinger effect for sheet metals, part II: applications. *International Journal of Plasticity* **18,** 597-616.

150. Lee, Y. W., and Wierzbicki, T. (2003). Fracture prediction of doublehull under static conical punch loading. Report 106, Impact and Crashworthiness Lab, MIT, Cambridge, MA.

151. Yahiaoui, M., Patrick, M. B., and Trauth, K. A. (1994). Experimental Studies on Scale Models for Grounding. Report 18. Joint MIT-Industry Program on Tanker Safety, MIT, Cambridge, MA.

152. Griffith, A. A. (1924). The theory of rupture. In "Proceedings of the First International Congress of Applied Mechanics" Delft.

153. Griffith, A. A. (1920). The phenomena of rupture and flow in solids. *Philosophical Transactions of the Royal Society (London)* **A221,** 163-198.

154. Inglis, C. E. (1913). Stresses in a plate due to the presence of cracks and sharp corners. *Proc. Inst. Naval Arch.* **55,** 219-230.

155. Wieghardt, K. (1907). Über das Spalten und Zerreissen elastischer Körper. *Z Mathematik und Physik* **55,** 60-103.

156. Orowan, E. (1949). Fracture and strength of solids. *Reports on Progress in Physics* **12,** 185-232.

157. Orowan, E. (1945). Notch brittleness and the strength of metals. *Transactions, Institution of Engineers and Shipbuilders in Scotland* **89,** 165-215.

158. Irwin, G. R. (1948). Fracture dynamics. *In* "Fracturing of Metal" (F. Jonassen, W. P. Roop, and R. T. Bayless, Eds.), American Society for Metals, Cleveland OH.

159. Irwin, G. R. (1957). Analysis of stresses and strains near the end of a crack. *Journal of Applied Mechanics* **24,** 361-364.

160. Williams, M. L. (1957). On the stress distribution at the base of a stationary crack. *Journal of Applied Mechanics* **24,** 109-144.

161. Wells, A. A. (1961). Unstable crack propagation in metals:cleavage and fast fracture. In "Proceeding of Crack Propagation symposium".

162. Hutchinson, J. W. (1968). Singular behavior at the end of a tensile crack in a hardening material. *Journal of the Mechanics and Physics of Solids* **16,** 13-31.

163. Rice, J. R., and Rosengren, G. F. (1968). Plane strain deformation near a crack tip in a power law hardening material. *Journal of the Mechanics and Physics of Solids* **16,** 1-12.

164. O'Dowd, N. P., and Shih, C. F. (1991). Family of crack-tip fields characterized by a triaxiality parameter: Part I - structure of fields. *Journal of the Mechanics and Physics of Solids* **39,** 989-1015.

165. O'Dowd, N. P., and Shih, C. F. (1992). Family of crack-tip fields characterized by a triaxiality parameter: Part II - fracture applications. *Journal of the Mechanics and Physics of Solids* **40,** 939-963.

166. McClintock, F. A. (1971). Plasticity aspects of fracture. *In* "Fracture" (H. Liebowitz, Ed.), Academic Press, New York.

167. McClintock, F. A. (2002). Slip line fracture mechanics: a new regime of fracture mechanics. *In* "Fatigue and Fracture Mechanics: 33rd Volume, ASTM STP1417" (W. G. Reuter and R. S. Piascik, Eds.), American Society for Testing and Materials, West Conshohocken, PA.

168. Hao, S., Schwalbe, K. H., and Cornec, A. (2000). The effect of yield strength mis-match on the fracture analysis of welded joints: slip-line field solutions for pure bending. *International Journal of Solids and Structures* **37,** 5385-5411.

Appendix

Summary of "Classical"Fracture Mechanics

In 1920s, Griffith [152, 153] found that a simple critical stress or strain criterion was not appropriate to predict fracture by studying a uniformly loaded plate with an elliptical hole using Inglis's solution [154]. A similar result was observed in an earlier study by Wieghardt [155] who noticed that the stresses at the tip of a sharp crack in an elastic body were infinite after solving the problem of a linear elastic wedge subjected to an arbitrary concentrated force and pointed out that fracture did not occur when the stress exceeded a critical value at a point, but only when the stress over a small potion of the body exceeded a critical value. Griffith [152, 153] then turned to energy method and proposed that in order to propagate a crack, the corresponding surface energy must be balanced by elastic strain energy concept. Based on the energy balance, Griffith obtained the famous critical stress corresponding to fracture for a linear elastic brittle material as

$$\sigma_f = \sqrt{\frac{2E\gamma}{\pi a}} \tag{A.1}$$

where E is the Young's modulus, γ is the specific surface energy and a is the half crack length.

Orowan [156, 157] and Irwin [158] studied fracture behavior of metals and found independently that the plastic work at the crack front must be considered and in fact it

was far larger than the surface energy. It was concluded that Griffith's theory could be used if the surface energy is replaced by the plastic work for metals. Both Irwin [159] and Williams [160] found that the local stresses around the crack tip was governed by a single parameter K which is called now the stress intensity factor and is generally defined as

$$K = \sigma\sqrt{\pi a}\, F(a/W) \qquad \text{(A.2)}$$

where σ is a representative stress, W is the width of a plate, $F(a/W)$ is a function of the geometry.

Initial growth of a pre-crack occurs when the stress intensity factor K reaches a critical value K_c since the stress intensity factor determines the stress field of the region surrounding the crack tip. This is the essence of the linear elastic fracture mechanics (LEFM). Unfortunately, the critical value K_c depends not only on materials but also on geometries and loading modes. There are three typical modes studied in the literature, called mode I (pure opening), mode II (in-plane shearing) and mode III (tearing or antiplane shearing) (See Fig. A.1). Understanding of mode I fracture is relatively complete, analyses and data for mode I can be found in the handbook or standard, while for mode II, III and also possible mixed modes, analyses and data are rather scarce. Also, as pointed out by McClintock and Irwin [133], the K-concept only becomes valid when the K dominates annular region around the crack tip that is large compared to the plastic zone. Those facts clearly limit the application of the linear elastic fracture mechanics.

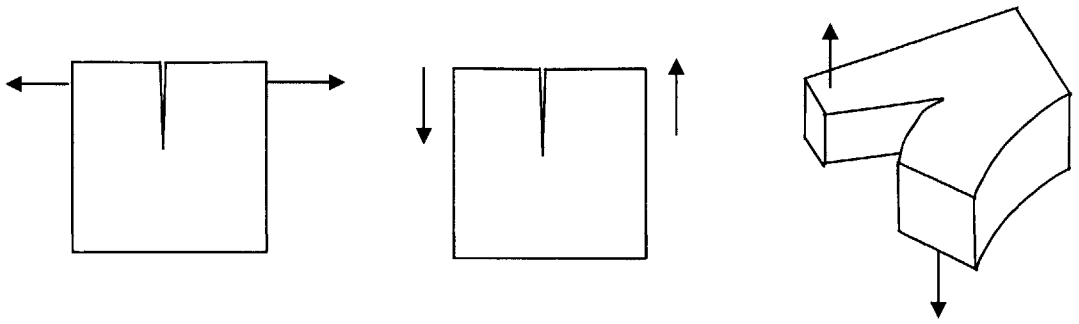

Fig. A.1 Three fracture modes

A practical need of dealing with fracture involving large plastic deformation leads to the development of the elastic-plastic fracture mechanics (EPFM). Well [161] introduced the

crack tip opening displacement (CTOD) concept to model fracture of structures with an initial sharp crack under conditions of large plastic deformation. It was assumed that a critical crack tip opening which controls crack growth exists. Later, a similar concept, the crack tip opening angle (CTOA) appeared in the literature. However, location where the displacement or angle should be measured as CTOD or CTOA is not clearly defined.

Another important concept in the elastic-plastic fracture mechanics (EPFM) is the J-integral

$$J = \int_{\Gamma} (Wdy - \vec{T}\frac{\partial \vec{u}}{\partial x} dl) \qquad (A.3)$$

where W is the strain energy density, $\vec{T}$ is the traction vector and $\vec{u}$ is the displacement vector, dl is element of the length of Γ.

Rice [123] has shown that in a non-linear elastic material, the line integral encircling the sharp crack tip is path independent and its value represents the energy release rate. Thus, fracture can be accurately predicted by taking J-integral as a measurement of fracture toughness for no-linear elastic materials. For plastic materials, however, it can be only approximately assumed that the crack growth is controlled by $J-$integral if the inner core of non-proportional loading is small compared to a specimen's uncracked ligament or the size of the $J-$controlled region since the concept of J is developed from no-linear elastic materials and is not valid in the plastic zone near the crack tip where loading is non-proportional for plastic materials.

Further studies on plastic materials have subsequently been performing by the fracture mechanics community. Many valuable results have been achieved. Among those, Hutchinson [162] and Rice and Rosengren [163] obtained the details of the singular behavior of stresses around the crack tip for a power law hardening material by assuming small plastic zone. On the basis of the Hutchinson-Rice- Rosengren stress field, O'dowd and Shih [164, 165] introduced a non-singular stress called $Q-$stress for large plastic deformation. They proposed that stresses near the crack tip under extensive yielding can be described by two parameters: the $J-$integral which is the HRR singular term, and the

non-singular $Q-$stress. However, the definition of the $Q-$stress is not clear. It depends on geometries and loading conditions and has limited data in the literature.

Besides the shortcomings described above, both the linear elastic fracture mechanics (LEFM) and the elastic plastic fracture mechanics (EPFM) including $J-Q$ have one common major limitation. They can only be used for structures with an initial sharp crack or sharp crack-like defect. Clearly, this method is not applicable in crack formation.

Slip line theory is another new regime of plastic fracture mechanics. In many cases of plan strain, field around crack tip can be approximately described by two symmetrical intense slip-lines (planes) (Mode I) or one line for asymmetry (mixed mode). For rigid-plastic, non-hardening and isotropic material, a number of solutions of slip line plasticity for different cases are available. A good summary of slip line fields can be found in a classic review of plasticity aspects of fracture by McClintock [166]. With the slip-line solution for a given geometry and loading, normal stress across the slip line, slip displacement across the line and the angle of the two slip lines (only for Mode I) which are called the crack tip driving parameters (CTDPs) can be found. The idea of slip line fracture mechanics (SLFM) is that within the region around crack tip described by CTDPs, crack responds in a material-dependent way by initial or continuing crack growth, as described by McClintock [167]. The crack tip response functions (CTRFs) (eg. displacement across the slip line, CTOD, CTOA) of the CTDPs are used to determine crack initiation and growth. The beauty of the SLFM comes from analytical prediction of crack initiation and growth even though it is restricted to limiting case of no strain hardening. It is certainly a great tool to validate finite element modeling of crack initiation and growth. However, as recommended by McClintock [167], various experiments and analyses are need to determine the validity range of the slip line fracture mechanics and to obtain values and means of determining the crack tip driving parameters (CTDPs) in terms of geometry and loading for specimens and structural components and to find values and means of determining the crack tip response functions (CTRFs) for different materials. Some interesting application of the slip line fracture mechanics in butt welds with mis-match can be found in Hao et al. [168].